Operational Modal Analysis (OMA) for wind turbines health monitoring

Ambroise Cadoret

To cite this version:

Ambroise Cadoret. Operational Modal Analysis (OMA) for wind turbines health monitoring. Mechanics [physics]. Université de Rennes, 2023. English. NNT : 2023URENS046 . tel-04382806

HAL Id: tel-04382806
https://theses.hal.science/tel-04382806

Submitted on 9 Jan 2024

HAL is a multi-disciplinary open access archive for the deposit and dissemination of scientific research documents, whether they are published or not. The documents may come from teaching and research institutions in France or abroad, or from public or private research centers.

L'archive ouverte pluridisciplinaire **HAL**, est destinée au dépôt et à la diffusion de documents scientifiques de niveau recherche, publiés ou non, émanant des établissements d'enseignement et de recherche français ou étrangers, des laboratoires publics ou privés.

THESE DE DOCTORAT DE

L'UNIVERSITE DE RENNES

ECOLE DOCTORALE N° 601
Mathématiques, Télécommunications, Informatique, Signal, Systèmes, Electronique
Spécialité : *Signal, Image, Vision*

Par
Ambroise CADORET

Analyse modale opérationnelle pour le suivi de santé structurelle des éoliennes

Operational Modal Analysis (OMA) for wind turbines health monitoring

Thèse présentée et soutenue à Rueil-Malmaison, le 22 septembre 2023
Unité de recherche : Centre Inria de l'Université de Rennes

Rapporteurs avant soutenance :

Joseph MORLIER	Professeur des universités, ISAE-SUPAERO
Roger SERRA	Professeur des universités, INSA Centre Val de Loire

Composition du Jury :

Président :	Julien WAEYTENS	Directeur de recherche, Université Gustave Eiffel
Rapporteurs :	Joseph MORLIER	Professeur des universités, ISAE-SUPAERO
	Roger SERRA	Professeur des universités, INSA Centre Val de Loire
Examinateurs :	Enora DENIMAL	Chargée de recherche, Inria centre de l'Université de Rennes
	Ilyes KHELF	Expert mécanique et méthodes, Engie Green
	Qinghua ZHANG	Directeur de recherche, Inria centre de l'Université de Rennes
Co-dir. de thèse :	Jean-Marc LEROY	Ingénieur de recherche, IFP Energies Nouvelles
Dir. de thèse :	Laurent MEVEL	Directeur de recherche, Inria centre de l'Université de Rennes

Invités

Jean CHARLETY	Ingénieur de recherche, IFP Energies Nouvelles
Jean-Lou PFISTER	Ingénieur de recherche, IFP Energies Nouvelles

TABLE OF CONTENTS

Remerciements **19**

Résumé en français **21**

Abstract **27**

Introduction **29**

I State of the art 33

1 Wind turbine **34**

1.1 Introduction 34

1.2 Wind turbine description 34

1.3 Common faults in wind turbine rotor 35

1.4 Wind turbine modeling 36

1.4.1 Wind modeling 36

1.4.2 Aerodynamic loads computation 38

1.4.3 Structural modeling of a wind turbine 39

1.4.4 Wind turbine controller 40

1.4.5 Wind turbine models used in the thesis 40

1.4.6 Conclusion 43

1.5 Modal analysis of linear time periodic systems 44

1.5.1 Dynamic model of an LTP system 44

1.5.2 Recall: modal analysis of an LTI system 45

1.5.3 Definition and presentation of a simple LTP system 45

1.5.4 Floquet theory 47

1.5.5 Coleman or Multi-Blade Coordinate (MBC) transformation 49

1.5.6 Example: MBC modes for rotor edge bending dynamics 51

1.5.7 Equivalence MBC-Floquet 54

1.5.8 Floquet modes computation with *OpenFAST* 55

1.6 Conclusion 56

2 Operational modal analysis and fault detection **57**

2.1 Introduction 57

2.2 Operational Modal Analysis (OMA) for LTI systems 57

2.2.1 Classical OMA assumptions 59

2.2.2 Stochastic Subspace Identification (SSI) 59

2.2.3 Uncertainty quantification 63

2.2.4 Conclusion . . . 65
2.3 OMA for wind turbine . . . 65
2.3.1 Frequency domain method . . . 66
2.3.2 Subspace methods . . . 67
2.3.3 SSI-LPTV method . . . 67
2.3.4 Application on operating structures . . . 70
2.3.5 Conclusion . . . 70
2.4 Stochastic subspace-based damage detection and localization . . . 71
2.4.1 Damage parametrization . . . 72
2.4.2 Standard residuals . . . 73
2.4.3 Statistical damage detection . . . 73
2.4.4 Fault localization . . . 77
2.4.5 Clustering of the redundant parameters . . . 79
2.4.6 Conclusion . . . 79
2.5 Fault detection of wind turbine . . . 80
2.5.1 Imbalance detection . . . 81
2.5.2 Rotor damage detection . . . 83
2.5.3 Conclusion . . . 84
2.6 Conclusion . . . 84

II LTI Approximation for Subspace Identification of LTP Systems Applied to Wind Turbines **85**

3 Theoretical approximation of LTP systems into LTI systems and associated state-space description **86**
3.1 Introduction . . . 86
3.2 Approximation of Floquet modes . . . 87
3.3 Validation of the approximation . . . 88
3.3.1 Example of the academic model . . . 88
3.3.2 Quantification of the approximation error . . . 90
3.4 Analysis of Floquet modes . . . 91
3.4.1 Floquet modes of the DTU 10MW . . . 91
3.4.2 Analysis of tower DOF . . . 92
3.4.3 Analysis of rotor DOF . . . 92
3.4.4 Mode shapes of the global structure . . . 93
3.5 State-space expression of the approximation . . . 94
3.6 Subspace Factorization . . . 97
3.7 Conclusion . . . 101

4 Validation of the identification of the approximation **102**
4.1 Introduction . . . 102
4.2 Validation of the uncertainty quantification method . . . 102
4.3 Identification: application to an academic model of wind turbine . . . 106

4.3.1 Case 1: constant rotational speed . . . 106
4.3.2 Case 2: variable rotational speed . . . 107
4.4 Identification: application to an aero-servo-elastic wind turbine model . . . 109
4.4.1 Frequency spectrum analysis . . . 110
4.4.2 Subspace identification . . . 110
4.5 Comparison with an existing method . . . 112
4.6 Conclusion . . . 115

III Fault detection 117

5 Rotor anisotropy tracking for fault detection 118
5.1 Introduction . . . 118
5.2 Modal analysis of a wind turbine with an anisotropic rotor . . . 119
5.2.1 Analysis of the effects of the anisotropy of stiffness on Fourier harmonics of the Floquet modes . . . 119
5.2.2 Difference between stiffness and mass anisotropy . . . 121
5.3 Uncertainties of phase shift and amplitude . . . 122
5.3.1 Definition: Sensitivity of phase shift . . . 123
5.3.2 Definition: Sensitivity of amplitude . . . 124
5.3.3 Validation . . . 124
5.4 Anisotropy tracking with operational modal analysis . . . 125
5.4.1 Method to detect rotor anisotropy . . . 125
5.4.2 Case 1: 5% of stiffness loss on one blade under white noise wind . . . 126
5.4.3 Case 2: 5% of stiffness loss on one blade under turbulent wind . . . 128
5.5 Conclusion . . . 129

6 Rotor fault detection based on the local approach 130
6.1 Introduction . . . 130
6.2 Definition of a new residual for the Stochastic Subspace-based Damage Detection and localization . . . 131
6.3 Application to the academic model of wind turbine . . . 133
6.3.1 Preliminary study . . . 133
6.3.2 Damage detection . . . 134
6.3.3 Damage localization . . . 135
6.3.4 Damage quantification . . . 136
6.4 Application to the DTU 10 MW wind turbine model, hub height wind . . . 137
6.4.1 Simulation parameters . . . 137
6.4.2 Preliminary study . . . 138
6.4.3 Damage detection . . . 139
6.4.4 Damage localization and quantification . . . 140
6.5 Application to the DTU 10 MW wind turbine model, full field wind . . . 142
6.5.1 Preliminary study . . . 142
6.5.2 Damage detection . . . 143

6.5.3 Damage localization and quantification . . . 144
6.6 Definition of the mean residual . . . 145
6.6.1 Residual distribution . . . 145
6.6.2 Application to the academic model of wind turbine . . . 146
6.6.3 Bootstrapping and moving average . . . 148
6.7 Modeling of a local loss of stiffness on the DTU 10MW wind turbine model . . . 150
6.7.1 Computation of the sensitivities . . . 150
6.7.2 Clustering of the redundant parameters . . . 152
6.8 Detection and localization of local losses of stiffness . . . 153
6.8.1 Damage detection . . . 154
6.8.2 Damage localization and quantification . . . 154
6.9 Alternative selection of sensors . . . 156
6.9.1 Parametrization and clustering . . . 156
6.9.2 Damage detection and localization . . . 157
6.10 Detection and localization of mass and pitch imbalance . . . 159
6.10.1 Mass imbalance . . . 159
6.10.2 Pitch imbalance . . . 162
6.11 Performance of the non-parametric test . . . 164
6.12 Conclusion . . . 165

7 Detection of damage of the rotor using measurement from the fixed frame 167
7.1 Introduction . . . 167
7.2 Search for sensitive damage indicators . . . 167
7.2.1 Floquet modes evolution . . . 168
7.2.2 Evolution of the modes shapes and frequencies of the DTU 10MW . . . 171
7.2.3 Additivity of the effects of the damage . . . 172
7.3 Use of the coherence to detect new Fourier harmonics . . . 173
7.3.1 Description of the method . . . 174
7.3.2 Distribution of the coherence . . . 175
7.3.3 Application: detection of a stiffness loss on one blade . . . 177
7.3.4 Application: detection of a addition of mass on one blade . . . 180
7.4 Damage detection based on the frequencies . . . 182
7.4.1 Definition of a residual . . . 182
7.4.2 Theoretical performance . . . 183
7.4.3 Application: detection of different damage scenarios . . . 184
7.5 Conclusion . . . 186

Conclusion and perspectives 189

IV Appendices 193

A Aerodynamic loads modelling with the BEM theory 194

B Lemma and theorem used **199**
B.1 Law of large numbers [30] 199
B.2 Central limit theorem [30] 199
B.3 Lemma 3 of [12] 199
B.4 Theorem: Convergence of finite sum 200

C Mathematical proofs **202**
C.1 Proof: Convergence of $o(1)$ 202
C.2 Proof of the convergence of $\frac{1}{N}\sum_{k=0}^{N} z_k z_k^T$ 204

D Proof: Moments and accelerations coupling with SSI **207**

E Extraction of the identified eigenmodes from the stabilization diagram **209**

Bibliography **211**

LIST OF FIGURES

1 Comparaison des fréquences de l'approximation (lignes en pointillées) et la densité de puissance spectrale d'un *decay test* du modèle 5DDL d'éolienne au niveau d'un DDL de rotor (ligne bleue) et d'un DDL de la nacelle (ligne rouge) – approximation définie avec ϕ_{min}=1% 23
2 Comparaison sur une période de la partie réelle de la déformée périodique du mode de Floquet de référence (ligne continue) avec différentes approximation (lignes en pointillées) pour différents facteurs de participation minimum – Premier mode de Floquet correspondant à des vibrations de Yaw 23
3 Diagramme de stabilisation obtenu pour une identification du modèle d'éolienne multi-physiques en utilisant des mesures de tour et de rotor, simulation avec un vent turbulent et une vitesse variable - (- - -) : fréquences de référence - (●) : fréquences identifiées 24
4 Évolutions du test de détection de défaut en utilisant le résidu moyen (nb_f = 10) pour différentes localisations de l'endommagement simulé, associés avec les histogrammes des différents tests (obtenues en utilisant le *bootstrapping*) 25
5 Histogrammes des tests de détection de défaut pour les différents endommagements simulés, utilisation du résidu moyen (nb_f = 10) et du *bootstrapping* (1000 combinaisons de résidus) 26
6 Installed wind power capacity in Europe, 2013-2022 [46] 29
7 Failure rates and associated downtime of the different components of a wind turbine [5] 30

1.1 Drawing of a wind turbine 35
1.2 Example of wind spectrum [19] 37
1.3 Example of a grid of wind speed used in *Turbsim* [74] 38
1.4 Comparison of wind speed grid, for two different spatial evolution modeling . . . 39
1.5 Example of a speed control curve 40
1.6 Workflow of *OpenFAST* for a floating wind turbine [94] 41
1.7 Wind turbine model [119] 42
1.8 Evolution of control parameters of the DTU 10MW wind turbine function of the wind speed 43
1.9 Power spectral density (PSD) of the acceleration of the Mathieu oscillator for two different simulations with $\omega_A = 0.8$ 46
1.10 Campbell diagram of the frequency and damping of the Mathieu oscillator . . . 47
1.11 Mode shapes of the first edge bending modes, after the inverse MBC transformation, - - -:= undeformed wind turbine, ──:= mode shape 51
1.12 Scheme of different bases in a wind turbine geometry 52

1.13 Comparison of normalized Fourier transforms of periodic mode shapes computed with different methods, academic model of wind turbine 54

2.1 Example of stabilization diagram, from an identification of a 3 DOF mass-spring model- (- - -): theoretical frequencies - (●): identified frequencies 62
2.2 Illustrative example of the uncertainty propagation, based on the original figure in [53] 64
2.3 Example of stabilization diagram, from an identification of a 3 DOF mass-spring model, with the estimation of the uncertainties- (- - -): theoretical frequencies - (●): identified frequencies and related standard deviations (error bars) 65
2.4 Examples of test distribution, function of the degree of freedom and the non-centrality parameter of the χ^2 function 76
2.5 Flowchart of the stochastic subspace-based damage detection and localization . . 80
2.6 Power Spectral Density (PSD) of Side-Side acceleration of the tower for two configurations of the rotor with the DTU 10MW model 81
2.7 Power Spectral Density (PSD) of Fore-Aft acceleration at mid-tower for two configurations of the rotor with the DTU 10MW model 82
2.8 Power Spectral Density (PSD) of acceleration at mid-tower for two configurations of the rotor with the DTU 10MW model, under turbulent wind ($\bar{u} = 6.7$ and $\sigma_u = 20\%$) 82
2.9 Polar plot of the evolution of mode shape of flap bending modes of the simple wind turbine, function of the stiffness of one blade. Each star corresponds to a loss of 5% of stiffness of the blade n°3 83

3.1 Comparison of the frequencies of the approximation from Table 3.1 (dashed lines and id number) and the Power Spectral Density (PSD) of a free decay of the 5DOF wind turbine of a rotor DOF (blue line) and a tower DOF (red line) – (ϕ_{min}) threshold of 1% 89
3.2 Comparison over a period of the real part of the periodic mode shape of the reference Floquet model (continuous line) with different approximations (dashed lines) for different values of the minimum participation factor (ϕ_{min}) – First Floquet mode corresponding to the Yaw motion 90
3.3 Campbell Diagram of the MBC modes principal frequencies ($|\mu_j|/2\pi$) of the DTU 10MW, only the frequencies from modes with a damping below 20% are displayed 92
3.4 Real part evolution of periodic mode shapes at tower DOF 93
3.5 Real part of the periodic mode shape of the backward edge at the rotor DOF . . 93
3.6 Real part of the periodic mode shape of the 1 Fore-Aft at the rotor DOF 94
3.7 Different mode shapes from the Floquet mode of Backward edge 94
3.8 Different mode shapes from the Floquet mode of 1 Fore-Aft 95

4.1 Histogram of the identified frequency and damping of the fourth Fourier harmonics of the approximation and the comparison of the 95% confidence interval 103

4.2 Histograms of MAC values for two Fourier harmonics with the empirical and estimated confidence interval, (- - -): Estimated 95% confidence interval, (-·-·): Empirical 95% confidence interval . . . 105
4.3 Stabilization diagram from acceleration measures of all DOF from a simulation with a constant rotational speed - (- - -): reference frequencies - (●): identified frequencies . . . 107
4.4 Evolution of the rotational speed during the simulation . . . 108
4.5 Stabilization diagram from acceleration measures of all DOF from a simulation with a variable rotational speed - (- - -): reference frequencies - (●): identified frequencies . . . 108
4.6 PSD of an acceleration of a rotor DOF (blue) and a tower DOF (red) of the academic model of a wind turbine with a variable rational speed, compared with the frequencies of the Fourier harmonics of the approximation . . . 109
4.7 Evolution of the wind speed (black) and the rotational speed (blue) during the simulation . . . 110
4.8 PSD of a blade root edge bending moment, with the comparison with the frequency of specific approximation modes . . . 111
4.9 PSD of the acceleration Side-Side at mid-tower, with the comparison with the frequency of specific approximation modes . . . 111
4.10 Stabilization diagram from an identification with all the data, from a simulation with a turbulent wind and a variable rotational speed- (- - -): reference frequencies - (●): identified frequencies . . . 112
4.11 Stabilization diagram computed with the H-OMA-TD method with all the DOF from a simulation with a constant rotational speed. The blue dashed line (- - -) corresponds to an approximation frequency and the red dashed lines (- - -) correspond to the modulation of this frequency - (●): identified frequencies . . . 113
4.12 Comparison of stabilization diagrams of two methods between 0.8 and 1.2 Hz . . . 113

5.1 Evolution of the polar plot of the edgewise bending mode shapes against the third blade stiffness . . . 120
5.2 PSD at mid-tower along Side-Side for different anisotropies, with the two dashed lines corresponding to the harmonics of the rotation (1P and 3P) . . . 122
5.3 Comparison of the identified phases shift and amplitudes with the estimated 99% confidence interval (CI) . . . 125
5.4 Comparison of the edgewise bending mode shapes between the reference state and the damaged state under a white noise wind . . . 127
5.5 Comparison of the edgewise bending mode shapes between the reference state and the damaged state under a turbulent wind . . . 128

6.1 Contribution of each identifiable Fourier harmonic to the damage detection of the academic model of wind turbine . . . 133
6.2 Comparison of the theoretical distributions and the histograms of the damage detection tests . . . 135

6.3 Box plot of the damage localization tests, for the two first simulated damages . . 136
6.4 Localization of the meteorological buoys of Météo-France with accessible data [92], the used buoy is circled 138
6.5 Wind speed values for the Gascogne buoy 138
6.6 Theoretical study of the damage detection applied to the DTU 10MW wind turbine model 139
6.7 Study of the performance of the damage detection test 140
6.8 Histograms of the damage detection test 141
6.9 Box plot of the damage localization for the two studied cases 141
6.10 Study of the performance of the damage detection test, full field wind simulated 142
6.11 Histograms of the damage detection test, full field wind modeling 143
6.12 Box plot of the damage localization for the two studied cases, full field wind modeling 144
6.13 Theoretical distribution of the damage detection test for $\Delta G_3 = -0.5\%$ and different values of nb_f 147
6.14 Comparison of the theoretical distributions and the histograms of the damage detection tests using the mean residual 147
6.15 Histograms of the damage detection test for the two system states, with different numbers of residuals to construct the mean residual with the bootstrapping . . . 149
6.16 Results of the damage detection using the mean residual and a moving average . 150
6.17 Absolute values of the sensitivities of the phase shift and amplitude of the edge bending modes shapes and the sensitivities of the associated frequencies against the damage location on the blade 151
6.18 Preliminary study using the full damage parametrization 152
6.19 Results of the clustering of the rotor stiffness parameters 153
6.20 Evolutions of the damage detection test using the mean residual ($nb_f = 10$) for the different simulated damages, associated with the histogram obtained using bootstrapping 155
6.21 Results of the localization and quantification on the parameters of the second blade, $\Delta K_{5,2} = -7.5\%$ 156
6.22 Results of the clustering of the rotor stiffness parameters, use of accelerations . . 157
6.23 Histograms of the damage detection tests, use of the blade accelerations, obtained using bootstrapping 158
6.24 Results of the damage localization and quantification for a loss of 7.5% of stiffness in the section 5 of the second blade, use of the accelerations 158
6.25 Histogram of the damage detection for an addition of mass, using the mean residual ($nb_f = 10$) and the bootstrapping 160
6.26 Histograms of the damage detection test for a pitch error, using the mean residual ($nb_f = 10$) and the bootstrapping 163

7.1 Evolution of the Backward flap Floquet against the stiffness of one blade, academic model of wind turbine 169

7.2 Participation factor of edge bending Floquet modes using only tower accelerations function of the stiffness of one blade . . . 170
7.3 Comparison of the PSD of the acceleration at mid-tower along Side-Side with accelerations from a model with an isotropic rotor and from a model where one blade has a loss of stiffness of 5%. Accelerations obtained from a simulation with a constant wind speed . . . 171
7.4 Evolutions of the frequencies of the Fourier harmonics sensitive to a rotor damage function of different stiffness losses in the rotor. 2b:= two damaged blades and 3b:= three damaged blades . . . 174
7.5 Visualization of the frequencies of interest in the original and modulated signal ($k = 2$), for an isotropic and anisotropic rotor (5% stiffness loss on one blade). •:= Frequency of a new Fourier harmonic or harmonic of the rotational speed that is appearing with anisotropy . . . 175
7.6 Mean coherence spectrum, with the 95% estimated confidence interval (- - -), 1024 values in the spectrum . . . 176
7.7 Histograms of the coherence for a frequency corresponding to a peak and a frequency corresponding to the noise, with a fit of a distribution . . . 176
7.8 Coherence between the acceleration tower-top along Side-Side and the modulated one, wind turbine model under white noise wind . . . 177
7.9 Coherence between the acceleration tower-top along Side-Side and the modulated one, wind turbine model under turbulent wind . . . 178
7.10 Mean Coherence spectrum of each rotor configuration, with the dashed lines corresponding to he frequencies of interest . . . 179
7.11 Histograms of the coherence around the frequencies of the Backward and Forward edge, 🟦 := histogram computed from accelerations of the reference rotor, 🟧:= histogram computed from accelerations of the damaged rotor . . . 180
7.12 Coherence between the acceleration tower-top along Side-Side and the modulated one, wind turbine model under turbulent wind with an addition of mass . . . 181
7.13 Coherence results using the tower-top acceleration along Side-Side, addition of mass on one blade . . . 182
7.14 Values of the Fisher matrix function of the considered residual . . . 183
7.15 Histogram of the damage detection test for the different simulated damage scenarios, using the mean residual ($nb_f = 10$) and bootstrapping (1000 combinations) 185

A.1 Stream tube of a wind turbine . . . 194
A.2 Tangential velocity across the rotor . . . 195
A.3 Blade element velocities . . . 196

E.1 Results of the extraction of the eigenmodes of the stabilization diagram, for the identification of the academic model at a constant rotational speed . . . 210

LIST OF TABLES

1.1 Common faults in a wind turbine blade and associated modeling 36

1.2 Parameter of the academic model of wind turbine 42

1.3 Characteristic values of the DTU 10MW wind turbine 43

3.1 Fourier harmonics of Floquet modes, with a minimum participation factor of 1%, for a rotational speed of 1.4 rad/s 89

4.1 Comparison of the empirical standard deviation ($\sigma_{\cdot\ MC}$) and the estimated standard deviation ($\sigma_{\cdot\ est}$) of the frequency and damping associated with there 95% confidence interval 103

4.2 Comparison of the empirical and estimated 5% quantile value of the MAC criterion between same mode shapes 105

4.3 Summary of the identification results, academic model of wind turbine at constant rotational speed 107

4.4 Summary of the identification results, academic model of wind turbine at variable rotational speed 109

4.5 Summary of the identification results, with the matching of the identified modes with the reference modes 112

4.6 Comparison of the identification results between the H-OMA-TD and the SSI . . 114

4.7 Clustering of the frequencies of the identified modes 114

4.8 Comparison of the identified participation factor with the H-OMA-TD with the theoretical ones and the classical SSI 115

5.1 Selected frequencies of the approximation function of the stiffness of the third blade 119

5.2 MAC values computed between the isotropic and the anisotropic mode shapes of the Fourier harmonics of edge bending for different anisotropy levels 121

5.3 MAC values computed between mode shapes of same Fourier harmonic with different type of anisotropy for different anisotropy levels 121

5.4 Comparison of the empirical and the estimated standard deviations for the phase shift and amplitude of two selected Fourier harmonics, with the associated 95% confidence interval 125

5.5 MAC criterion and respective uncertainties, under a white noise wind 127

5.6 MAC criterion and the respective uncertainties, under a turbulent wind 129

6.1 Minimum 95%-level detectable change ($\overline{\Delta\theta_{min}}$) and probabilities of detection (POD) function of the number of data sets used for the estimation of the reference (n_f) 134

6.2 Theoretical and empirical means of the damage detection tests, $\bar{t}_{th}$ and $\bar{t}_{emp}$ respectively . . . 135
6.3 Theoretical and empirical means of the damage localization tests, $\bar{t}_{h\ th}$ and $\bar{t}_{h\ emp}$ respectively, function of the tested parameters . . . 136
6.4 Mean values of the damage, associated with their 95% confidence interval . . . 137
6.5 Theoretical probability of detection (%) for different stiffness losses and different construction of the residual . . . 139
6.6 Mean values of the damage quantification with the associated 95% confidence intervals . . . 141
6.7 Theoretical probability of detection (%) for different stiffness loss and different construction of the residual . . . 143
6.8 Mean values of the damage quantification with the 95% confidence intervals, full field wind modeling . . . 144
6.9 Minimum detectable fault and probability of detection function of the number of files used in the mean residual (nb_f) . . . 146
6.10 Theoretical and empirical means of the damage detection tests using the mean residual, $\bar{t}_{th}$ and $\bar{t}_{emp}$ respectively . . . 148
6.11 Theoretical and empirical means of the damage localization and quantification tests using the mean residual, function of the tested parameters . . . 148
6.12 Empirical probability of detection . . . 154
6.13 Mean values of the localization and quantification tests, with the 95% confidence intervals for the quantification . . . 156
6.14 Theoretical POD of mass additions function of the number of files used to compute the residual . . . 160
6.15 Empirical POD of mass additions function of the sensitivities used to compute the test. Obtained using bootstrapping . . . 160
6.16 Mean values of the localization and quantification tests on data with simulations of additions of mass, with the 95% confidence intervals for the quantification . . . 161
6.17 Comparison of the mean values of the localization and quantification tests with two different sensitivity matrices, applied on data with an addition of 1% of mass 161
6.18 Empirical POD of a pitch error function of the sensitivities used to compute the test. Obtained using bootstrapping . . . 162
6.19 Mean values of the localization and quantification tests on data with simulation of pitch errors, with the 95% confidence intervals of the quantification . . . 163
6.20 Comparison of the mean values of the localization and quantification tests with two different sensitivity matrices, applied on data with a pitch error of 2° . . . 164
6.21 Empirical POD of the different simulated damages using the non-parametric test, compared to the probabilities obtained with the parametric test . . . 165

7.1 Fourier harmonics of Floquet modes, with a minimum participation factor of 1%, for a rotational speed of 1.4 rad/s using the nacelle DOF, academic model of a wind turbine with an isotropic rotor . . . 168

7.2 Fourier harmonics of Floquet modes, with a minimum participation factor of 1%, for a rotational speed of 1.4 rad/s using the nacelle DOF, academic model of wind turbine with a stiffness reduction of 5% one one blade 169
7.3 New harmonics identified function of the simulated stiffness of one blade, associated with the estimated standard deviation of the frequency (σ_f) 169
7.4 MAC between the mode shapes of the DTU wind turbine model with an isotropic rotor and the mode shapes of the DTU wind turbine model where a blade has a stiffness loss of 5%, identifiable Fourier harmonics using tower accelerations along Side-Side and Fore-Aft 171
7.5 Sensitivities of the frequencies of the identifiable Fourier harmonics using tower accelerations (Ω=6 rpm) 172
7.6 Frequencies of the identifiable Fourier harmonics using tower accelerations function of the rotational speed (Hz) 173
7.7 POD of different stiffness reductions of the tower or the rotor function of the definition of the residual 184
7.8 Damage localization and quantification results using the minmax test 186

REMERCIEMENTS

Je tiens tout d'abord à remercier l'IFP Énergie Nouvelles et Inria pour l'opportunité qui m'a été accordée de réaliser une thèse au sein de ces deux établissements.

Je souhaite sincèrement remercier mes encadrants. Ce fut un plaisir de travailler avec vous. Je suis très reconnaissant de la liberté que vous m'avez laissée dans mes recherches et des innombrables conseils que vous avez pu me donner. Particulièrement, je tenais à remercier Laurent Mevel, mon directeur de thèse, pour le temps que tu as pris pour travailler avec moi, pour toutes les connaissances et ton expertise que tu m'as transmises. Également, je remercie chaleureusement mon promoteur de thèse Jean-Marc Leroy, notamment pour les nombreuses discussions qui m'ont permis de prendre confiance en moi et de me redonner le moral pendant les périodes difficiles.

Je remercie également les rapporteurs de thèse Joseph Morlier et Roger Serra, ainsi que les membres du jury Ilyes Khelf et Quinghua Zhang et le président du jury Julien Waeytens, pour leurs commentaires avisés et leur intérêt pour mes travaux.

Je voudrais également remercier les doctorants d'IFPEN que j'ai eu le plaisir de rencontrer durant ma thèse et avec qui j'ai pu passer de nombreux bons moments. Et surtout Abhilash, Julie, Margaux et Judy, avec qui j'ai eu la chance de partager un bureau et toutes les discussions et les moments conviviaux qui vont avec. Merci de m'avoir supporté lorsque je m'énervais trop régulièrement sur mon ordinateur.

Enfin, je tiens à remercier ma famille, et plus particulièrement mes parents et ma sœur, pour leur soutien indéfectible durant ma thèse et même avant. Cela n'aurait pas été possible sans vous.

Ambroise

RÉSUMÉ EN FRANÇAIS

Introduction

Aujourd'hui de nouveaux parcs éoliens sont en construction et toutes les prévisions annoncent une forte hausse du nombre de parcs en France et en Europe pour les dix prochaines années. Il est donc important de mettre en place des méthodes de suivi de santé fiables et robustes pour assurer l'intégrité structurelle des éoliennes en utilisation. Les méthodes basées sur l'OMA (Analyse Modale Opérationnelle) sont une solution, puisqu'elles permettent de suivre l'évolution des propriétés modales de la structure (fréquences et déformées) au cours du temps à partir de données issues de capteurs. Ces méthodes ont été appliquées à de nombreuses structures notamment de génie civil, qui sont modélisées comme des systèmes linéaires temporellement invariants (LTI). Cependant, la rotation d'une éolienne empêche de modéliser une telle structure comme un système invariant, mais peut plutôt être modélisée comme un système linéaire temporellement périodique (LTP). Dès lors il est nécessaire d'étendre les méthodes OMA aux systèmes temporellement périodiques, pour permettre le suivi des propriétés modales des éoliennes.

Pour cela la thèse se décompose en trois axes. Tout d'abord un état de l'art sur la modélisation et l'analyse modale des éoliennes en rotation est effectué, avec l'objectif de déterminer le contenu des mesures vibratoires qui pourrait être retrouvé sur une éolienne. Par la suite, cet état de l'art est étendu aux méthodes d'identifications classiques et adaptées au problème éolien pour en comprendre les limitations. Le deuxième axe de la thèse est dédié au développement d'une méthode d'identification des éoliennes en rotation, basée sur l'analyse des vibrations des systèmes LTP et l'approximation des modes de Floquet. Cette nouvelle approche est alors validée avec un exemple d'identification d'éolienne opérationnelle, à partir de données simulées. Enfin, le troisième axe est dédié à la détection de défauts pour les rotors d'éoliennes en adaptant une méthode de la littérature, et en utilisant des capteurs positionnés au niveau des pales ou bien de la tour. Dans les deux cas, la méthode utilise les meilleurs indicateurs de défauts obtenus à partir de l'identification.

État de l'art

Pour débuter, l'état de l'art de l'analyse modale d'une éolienne en rotation et des systèmes LTP en général est réalisé. Il en découle que deux méthodes peuvent être utilisées, les transformations MBC (*Multi Blade Coordinates*) pour les systèmes tournants composés d'un rotor et la méthode de Floquet pour les systèmes LTP en général. Ces deux méthodes sont équivalentes pour un rotor isotrope (pales du rotor avec les mêmes propriétés matérielles et géométriques) et permettent d'obtenir les modes propres du système étudié. Ces modes propres appelés également modes de Floquet, sont composés d'une composante temporelle permettant d'obtenir une fréquence et un amortissement et d'une composante spatiale qui peut être interprétée comme une déformée périodique de la même période de rotation que le système. La différence entre ces modes propres et les modes propres d'un système LTI est la déformée qui est constante dans le cas d'un système LTI.

Pour continuer l'état de l'art, les méthodes OMA sont étudiées pour comprendre comment les paramètres modaux sont obtenus à partir des mesures. Les méthodes OMA ont été appliquées à de nombreuses structures réelles, notamment de génie civil. Ces structures peuvent être modélisées comme des systèmes LTI et d'après les hypothèses des méthodes OMA, ces dernières ne peuvent être appliquées qu'à ce type de systèmes. Par la suite, dans la littérature, des méthodes OMA ont été définies pour l'identification des systèmes LTP. Cependant elles ont toutes des inconvénients qui empêchent leur utilisation pour le suivi de structures réelles. En effet, les méthodes basées sur les fonctions de transferts harmoniques ont l'inconvénient de ne pas définir théoriquement le nombre de modulations qui doivent être effectuées, de plus ces modulations augmentent la dimension du signal, et donc le coup de calcul. Pour les méthodes basées sur un pré-traitement des données avec les transformations MBC, l'inconvénient est que ces transformations sont fausses dès lors que le rotor est anisotrope, ce qui est problématique pour un suivi de structure et pour la détection de défaut, car un défaut engendre de l'anisotropie. Enfin, la méthode SSI-LPTV, permet théoriquement d'identifier les modes de Floquet d'un système LTP. Cependant cette méthode converge en nombre de périodes et non en temps, ce qui fait qu'elle demande un temps de mesures trop important pour être utilisé en réalité dans le cas des éoliennes. Par conséquent, il faut définir une nouvelle approche pour identifier les éoliennes en rotation.

Pour conclure l'état de l'art, les méthodes de détection de défauts de rotor d'éolienne sont étudiées. De nombreuses méthodes basées sur la détection du déséquilibre du rotor existent. Ces méthodes permettent de détecter des défauts de pitch d'une pale ou bien des augmentations de masses liées à l'accumulation de glace, qui sont des défauts courants. Cependant, très peu de méthodes existent pour la détection de défauts structuraux des pales. Ainsi, une méthode de détection de défauts structuraux pour les pales d'éoliennes opérationnelles pourra être définie.

Approximation de la dynamique d'une éolienne opérationnelle et identification associée

Pour permettre l'identification des éoliennes opérationnelles et des systèmes LTP en général, il est choisi d'approximer les vibrations libres de ces systèmes, c'est-à-dire approximer les modes de Floquet. Cette approximation est basée sur la transformée de Fourier de la déformée périodique, où seulement les composantes non négligeables sont sélectionnées (en utilisant le facteur de participation). Cela entraîne une décomposition en modes propres équivalentes à celles des systèmes LTI, où dans ce cas les modes propres sont les harmoniques de Fourier des modes de Floquet. Cette approximation a pu être validée avec une application avec un modèle 5 degré de liberté (DDL) d'éolienne en rotation, où en Figure 1, la PSD d'un decay test du modèle est comparée avec les fréquences de l'approximation du système. Ainsi nous pouvons observer une concordance entre les pics de la PSD et les fréquences de l'approximation, ce qui confirme l'approximation. Ensuite, la convergence de l'approximation a pu être confirmée théoriquement, mais également avec un exemple sur le modèle 5 DDL d'éolienne. Dans la Figure 2, la déformée périodique théorique d'un mode de Floquet est comparée à des déformées reconstruites à partir de l'approximation, ainsi nous pouvons observer que l'approximation tend bien vers la valeur théorique, validant l'approximation.

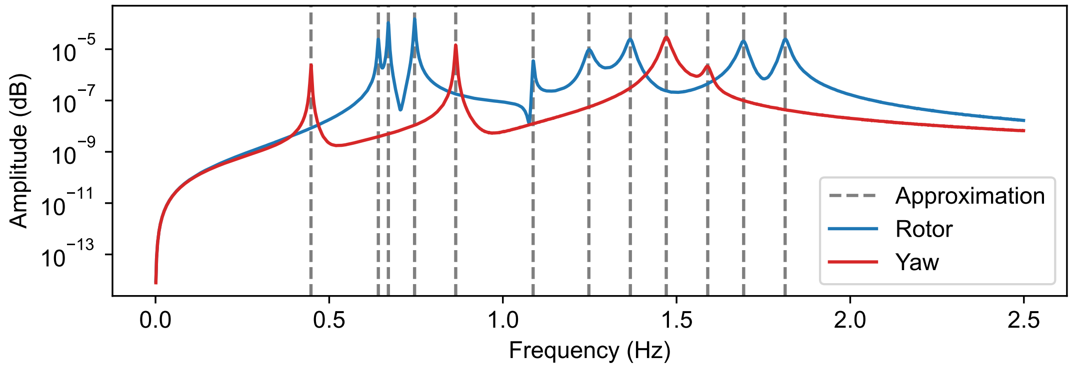

FIGURE 1 – Comparaison des fréquences de l'approximation (lignes en pointillées) et la densité de puissance spectrale d'un *decay test* du modèle 5DDL d'éolienne au niveau d'un DDL de rotor (ligne bleue) et d'un DDL de la nacelle (ligne rouge) – approximation définie avec ϕ_{min}=1%

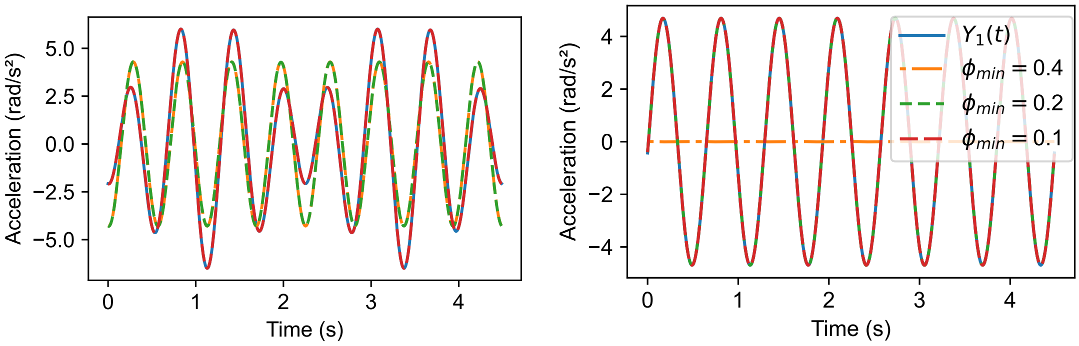

(a) Rotor

(b) Nacelle (Yaw)

FIGURE 2 – Comparaison sur une période de la partie réelle de la déformée périodique du mode de Floquet de référence (ligne continue) avec différentes approximation (lignes en pointillées) pour différents facteurs de participation minimum – Premier mode de Floquet correspondant à des vibrations de Yaw

Par la suite, il est démontré théoriquement qu'il est possible d'identifier les harmoniques de Fourier composant l'approximation peuvent bien être identifiées avec les méthodes OMA de l'état de l'art, en particulier les méthodes sous-espace. Ainsi, l'identification de l'approximation a notamment pu être validée avec un exemple d'identification du modèle d'éolienne multi-physique DTU 10MW en rotation, avec une simulation avec un vent turbulent et une rotation variable. En Figure 3, le diagramme de stabilité de l'identification est affiché et nous pouvons observer que les alignements de modes identifiés correspondent aux lignes en pointillée représentant les fréquences de l'approximation. Nous pouvons en conclure qu'il est bien possible d'identifier les harmoniques de Fourier des modes de Floquet. Par conséquent, il est possible de suivre l'état structurel d'une éolienne en rotation via l'identification des harmoniques de Fourier des modes de Floquet.

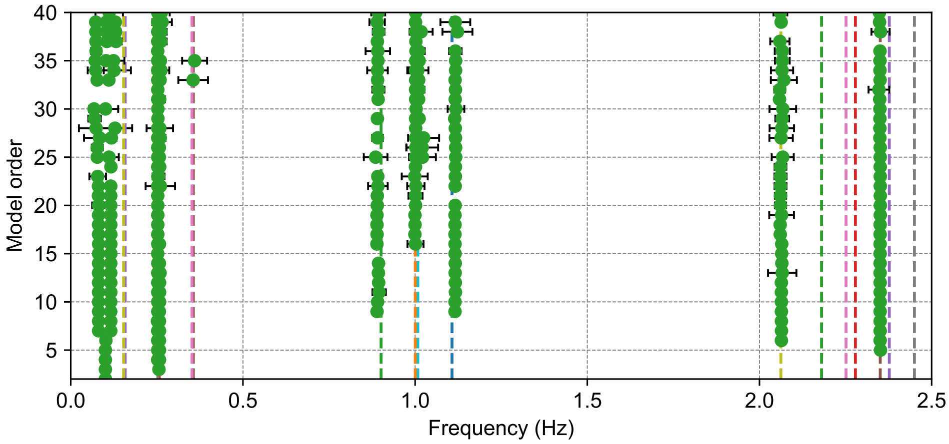

Figure 3 – Diagramme de stabilisation obtenu pour une identification du modèle d'éolienne multi-physiques en utilisant des mesures de tour et de rotor, simulation avec un vent turbulent et une vitesse variable - (- - -) : fréquences de référence - (●) : fréquences identifiées

Détection de défaut via la détection d'anisotropie du rotor

Pour effectuer de la détection de défaut structurel d'un rotor d'éolienne, il faut en premier lieu déterminer les meilleurs indicateurs de défaut qui peuvent être obtenus avec l'identification des harmoniques de Fourier des modes de Floquet. D'après la littérature, les défauts peuvent être détectés via le suivi d'anisotropie du rotor, dont les meilleurs indicateurs de défauts sont les phases et amplitudes des déformées des modes de flexion du rotor (edge ou flap). Ceci est confirmé avec le modèle de la DTU 10MW, où les phases et amplitudes des déformées des modes de flexion edge sont environ 10 fois plus sensibles à une baisse de raideur d'une pale que les fréquences de ces mêmes modes.

Une fois les indicateurs de défaut choisis, la méthode de détection de défaut peut être définie. Ici une méthode de la littérature est adaptée, à savoir la *Stochastic Subspace-based Damage Detection*. Cette méthode permet de détecter un changement dans le système étudié via le changement de distribution d'un test statistique basé sur un résidu construit à partir des mesures ou des résultats d'identification. Ainsi, un nouveau résidu est défini en fonction des phases et amplitudes des déformées des modes de flexion egde identifiés. De plus, comme la détectabilité des défauts est faible, il est décidé d'augmenter cette détectabilité avec l'utilisation d'un résidu moyen, permettant de réduire la covariance et donc d'augmenter la détectabilité des défauts. Pour valider cette méthode de détection de défaut, il est décidé d'appliquer la méthode à la détection de perte locale de raideur ΔK d'une pale du modèle d'éolienne DTU 10MW, où les harmoniques de Fourier sont identifiées à partir de mesures de moment en pied de pale. En Figure 4, les résultats de la détection de défauts des différents endommagements sont résumés, avec l'évolution des tests moyens et leurs histogrammes associés. En premier lieu nous pouvons observer avec les histogrammes (Figure 4d) que le test ne réagit pas de la même manière pour les différents défauts. Dans un second temps, il peut être conclu que le défaut est détecté dans les cas $\Delta K_{2,3}$ et $\Delta K_{5,2}$ ($\Delta K_{2,3}$: perte de raideur sur la troisième pale sur une section entre 10 et 20% de la longueur de la pale ; $\Delta K_{5,2}$: perte de raideur sur la deuxième pale sur une section entre 40 et 50% de la longueur de la pale). De plus, avec cette méthode il a été possible de trouver la pale endommagée, une fois le défaut détecté. Enfin, la détection d'autres types de défauts (ajout de masse et d'erreur d'angle de pitch) a également été testée.

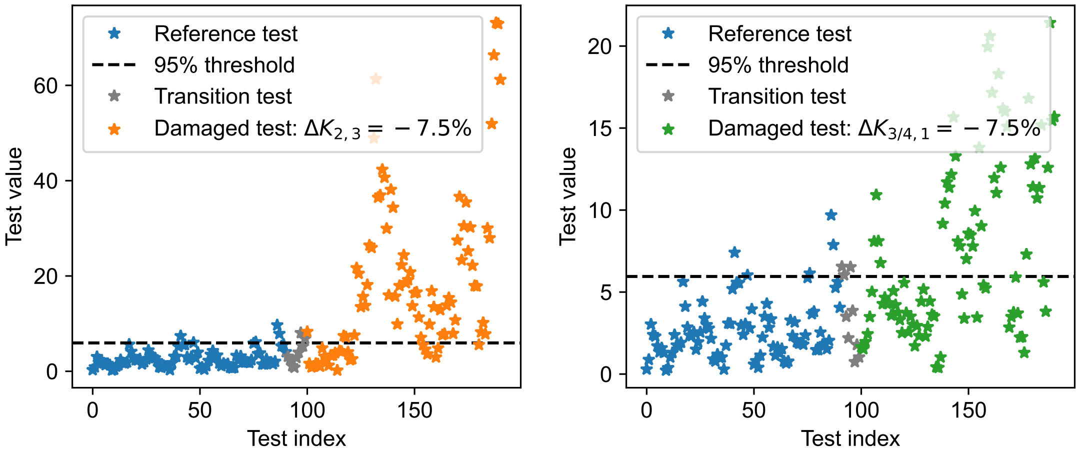

(a) Évolution du test : $\Delta K_{2,3}$ (b) Évolution du test : $\Delta K_{3/4,1}$

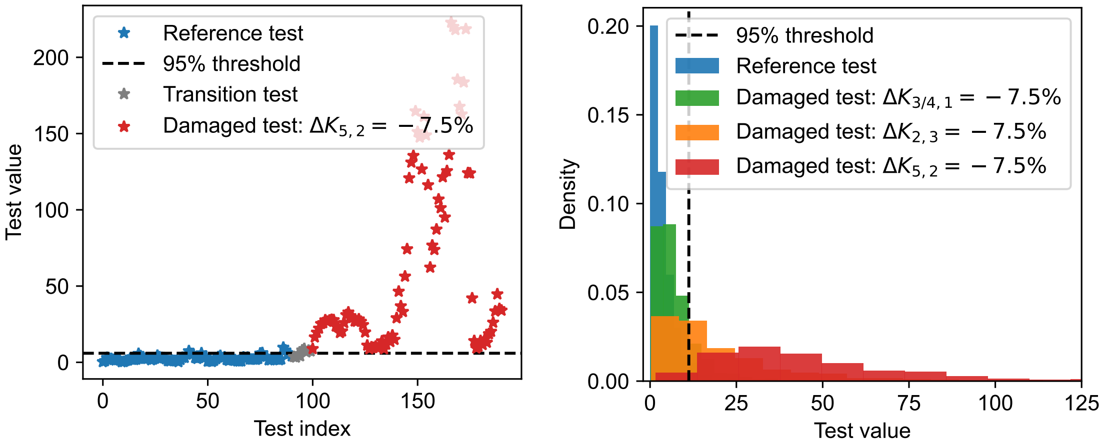

(c) Évolution du test : $\Delta K_{5,2}$ (d) Histogrammes des tests de détection de défaut

FIGURE 4 – Évolutions du test de détection de défaut en utilisant le résidu moyen ($nb_f = 10$) pour différentes localisations de l'endommagement simulé, associés avec les histogrammes des différents tests (obtenues en utilisant le *bootstrapping*)

La détection de défaut a été réalisée en utilisant des mesures provenant du rotor, or cette partie de l'éolienne est difficile à instrumenter. Ainsi, il est essayé d'effectuer de la détection de défaut du rotor en utilisant des mesures provenant de la tour ou de la nacelle (c.a.d provenant du *fixed frame*). Pour commencer, les indicateurs de défauts sont recherchés et parmi les plus sensibles aux défauts, les fréquences des harmoniques de Fourier de flexion suivant edge et Side-Side identifiables avec des mesures du *fixed frame* sont utilisées. Un résidu est construit en utilisant ces indicateurs, rendus pour certains indépendants de la vitesse de rotation du rotor. La détection de défaut est alors effectuée en utilisant une nouvelle fois la *Subspace-based Damage Detection method*. Pour valider cette méthode et le choix du résidu associé, elle est appliquée à la détection de différentes combinaisons de variations de raideurs globales du rotor et de la tour. Avec la Figure 5, les histogrammes des différents tests de détection de défauts effectués pour les différents endommagements sont affichés. Avec ces histogrammes, nous pouvons observer qu'il a été possible de détecter la présence d'un défaut dans tous les cas testés.

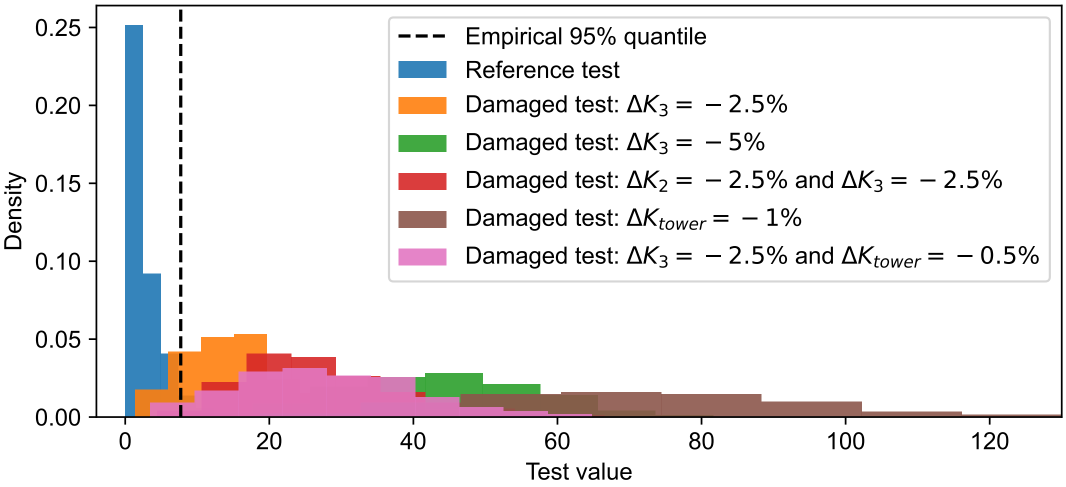

FIGURE 5 – Histogrammes des tests de détection de défaut pour les différents endommagements simulés, utilisation du résidu moyen ($nb_f = 10$) et du *bootstrapping* (1000 combinaisons de résidus)

Conclusion

Dans cette thèse, l'objectif était de surveiller une éolienne sans avoir à l'arrêter ni à interférer avec son fonctionnement. Ainsi, le problème de la surveillance des éoliennes par analyse modale opérationnelle a été traité. Le défi principal provient du fait qu'une éolienne en rotation entraîne un caractère périodique au système, ce qui empêche l'utilisation des méthodes d'identification des modes propres définie pour des structures temporellement invariantes telles que celles de génie civil.

Pour permettre l'identification des modes propres des systèmes périodiques, une étude de la dynamique des éoliennes en rotation a été réalisée. Ainsi, basée sur cette étude, une approximation des modes propres des éoliennes en rotation a pu être définie, où ces modes propres sont définis comme une somme de modes propres d'une structure invariante. Par la suite, il a été démontré théoriquement que les méthodes d'identification sous-espaces existantes peuvent identifier correctement l'approximation définie précédemment. Puis ces méthodes ont été validées avec différents exemples d'identifications utilisant des données simulées à partir de modèles d'éoliennes. Pour conclure le travail, la détection de défauts du rotor a été traitée, en utilisant des mesures du rotor ou bien de la tour. Pour ces deux cas, les paramètres obtenus par identification les plus sensibles aux défauts ont été recherchés et utilisés pour adapter une méthode de détection de défaut de l'état de l'art. Pour les deux situations, il a été possible de détecter une baisse de raideur d'une pale et de déterminer la pale endommagée lorsque des mesures du rotor sont utilisées.

Tous ces travaux pourront être poursuivis notamment avec l'application des méthodes à des données réelles, permettant de vérifier la robustesse des approches et surtout d'observer l'impact des conditions opérationnelles et environnementales sur les harmoniques de Fourier des modes de Floquet.

ABSTRACT

In this thesis, the objective is to monitor the wind turbine without stopping or interfering with its operation. Therefore, the monitoring of operating wind turbines is studied with Operational Modal Analysis (OMA). OMA methods aim to estimate the modal parameters of a structure based only on the outputs of an operating structure under ambient excitation such as wind and waves. After presenting the studied system and the associated physical modeling, the modal analysis of a rotating wind turbine is defined based on the Floquet modes, thanks to the modeling of an operating wind turbine as a linear time periodic system coming from the automatic field. Then, classical OMA methods used for invariant systems (for example civil engineering structures) are presented, to understand how the modal parameters are retrieved from the collected signals. Based on both studies, it is concluded that classical identification methods cannot be used for the monitoring of operating wind turbines. Moreover, the methods specifically designed for the rotating machines have drawbacks and also cannot be applied to operating wind turbines. Consequently, it is needed to define a new identification procedure, to adapt the classical OMA methods for the identification of the operating wind turbines. A second objective is to develop damage detection methods focus on the rotor. For the damage detection of wind turbine rotors, many methods have been developed for pitch and mass imbalance detection, but only a few methods exist for blade stiffness change detection. Therefore, a damage detection method from the literature needs to be adapted for the detection of stiffness changes in a wind turbine rotor.

To enable the monitoring of operating wind turbines, firstly, the dynamical behavior of the linear time periodic systems is approximated into linear time invariant systems under nonstationary inputs. This approximation is composed of the non-zero Fourier harmonics of the Floquet modes. The approximation is validated using an academic model of a rotating wind turbine, and a physical meaning of the approximation is given with an application on a multi-physics model of a wind turbine (the DTU 10MW wind turbine model on *OpenFAST*). Then, the state-space representation of the approximation is defined, and it is demonstrated that the approximation can be identified with a classical subspace method. Finally, the Stochastic Subspace Identification (SSI) method is used to identify the approximation of wind turbine models, particularly of the multi-physics model of a wind turbine under a turbulent wind and a variable rotational speed. In all identifications, the identified modes correspond to the Fourier harmonics of the Floquet modes defined by the approximation.

Secondly, based on the identification of the Fourier harmonics of the approximation, a damage detection method for wind turbine rotors based on rotor anisotropy tracking can be defined. To start, the damage sensitive parameters are searched and defined as the phase shift and amplitude of the Fourier harmonics of the edge (in the rotor plane) bending mode shapes. Also, the associated uncertainties are defined and validated. Then, a damage detection method from the literature, namely the Statistical Subspace-based Damage Detection is adapted to the studied problem by defining a residual using the phase shift and amplitude of the edge bending mode shapes. This method is applied with a gradually increasing difficulty, from the detection and localization of a loss of stiffness of one blade of the academic model to the detection and localization of a global loss of stiffness of one blade of the DTU 10MW wind turbine model under a realistic variable wind. To continue using measurements with a fixed or limited length and without concatenating the data, a mean residual is defined, conjointly with the associated positive impact on the covariance of the residual that improves the damage detectability. The mean residual is then used in a number of applications, and it is shown that it is possible to detect and localize local stiffness losses, mass additions, and pitch errors. The effect of the number of sensors, and their location, is also highlighted. However, since it may be difficult to monitor the rotor, damage detection is also performed using the more common tower and nacelle measurements. To do so, two methods are tested using new damage sensitive features. One method for the appearance of new Fourier harmonics is based on the coherence of a signal and its modulation with rotor speed. And one using the frequencies of the selected damage sensitive Fourier harmonics, with the adaptation of Stochastic Subspace-based Damage Detection method. With the latter, it is possible to detect smaller rotor stiffness losses than with the coherence and to distinguish rotor and tower faults.

INTRODUCTION

Wind power generation in Europe (EU+UK) in 2022 reaches new records in terms of absolute production (489 TWh) and for the share of onshore (14.1%) and offshore (3.2%) wind energy in electricity production [46], which is directly related to the increase of installed onshore and offshore capacity in Europe, which has doubled in the last decade (see Figure 6). Moreover, in the latest central scenario of Wind Europe [46], the wind power capacity in Europe is expected to increase by 129 GW in the next five years.

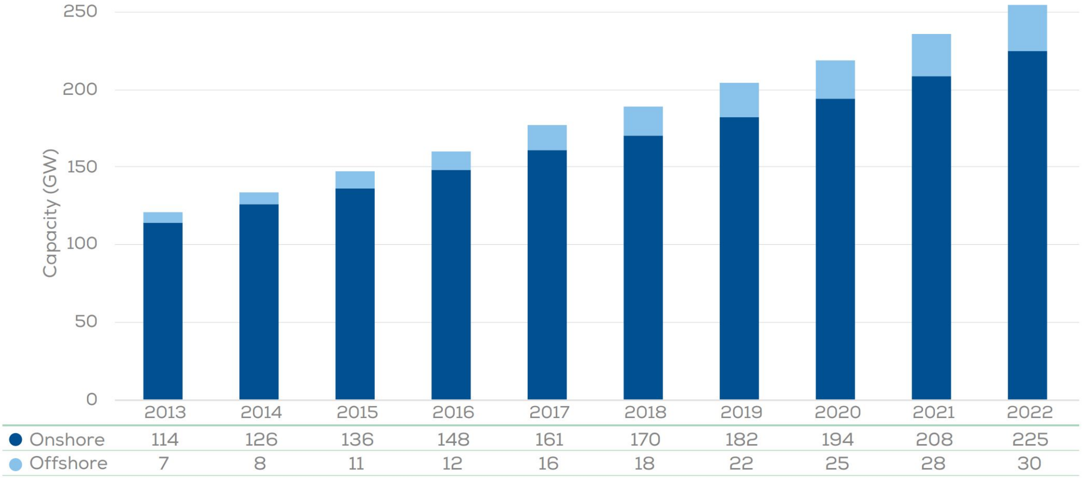

Figure 6 – Installed wind power capacity in Europe, 2013-2022 [46]

Regarding the actual installed capacity, given the prospects for growth in the number of wind farms in the coming years, and the continuing quest to reduce maintenance costs, it is important to implement reliable monitoring methods based on data collected during the operation of the wind turbines. In order to increase the lifetime of wind turbines and to improve the planning of maintenance operations. Operational Modal Analysis (OMA) methods are powerful methods for monitoring structural properties by identifying the modal signature. Many OMA methods have been developed for civil engineering applications, where the monitored structure can be accurately modeled by linear time invariant (LTI) systems [17]. However, the rotation of the rotor of a wind turbine breaks the LTI hypothesis, and these systems should rather be modeled as linear time periodic (LTP) systems. Since they no longer meet the basic assumptions of OMA, these LTI-based OMA methods need to be extended to LTP systems in order to enable the monitoring of the operating wind turbines.

The objective of this thesis is to develop an efficient identification approach for operating wind turbines and to develop damage detection methods with industrial applications. In this thesis, the damage detection will be designed to focus on the rotor blades. In [5], the authors give a review of different reliability studies. On average the hub and blades have a failure rate of around 7.5% and the highest downtime as it is shown in Figure 7. It shows that it is important to monitor this part of a wind turbine, even more knowing that damage on a blade can later lead to irreversible damage, for example, if a damaged blade hits the tower.

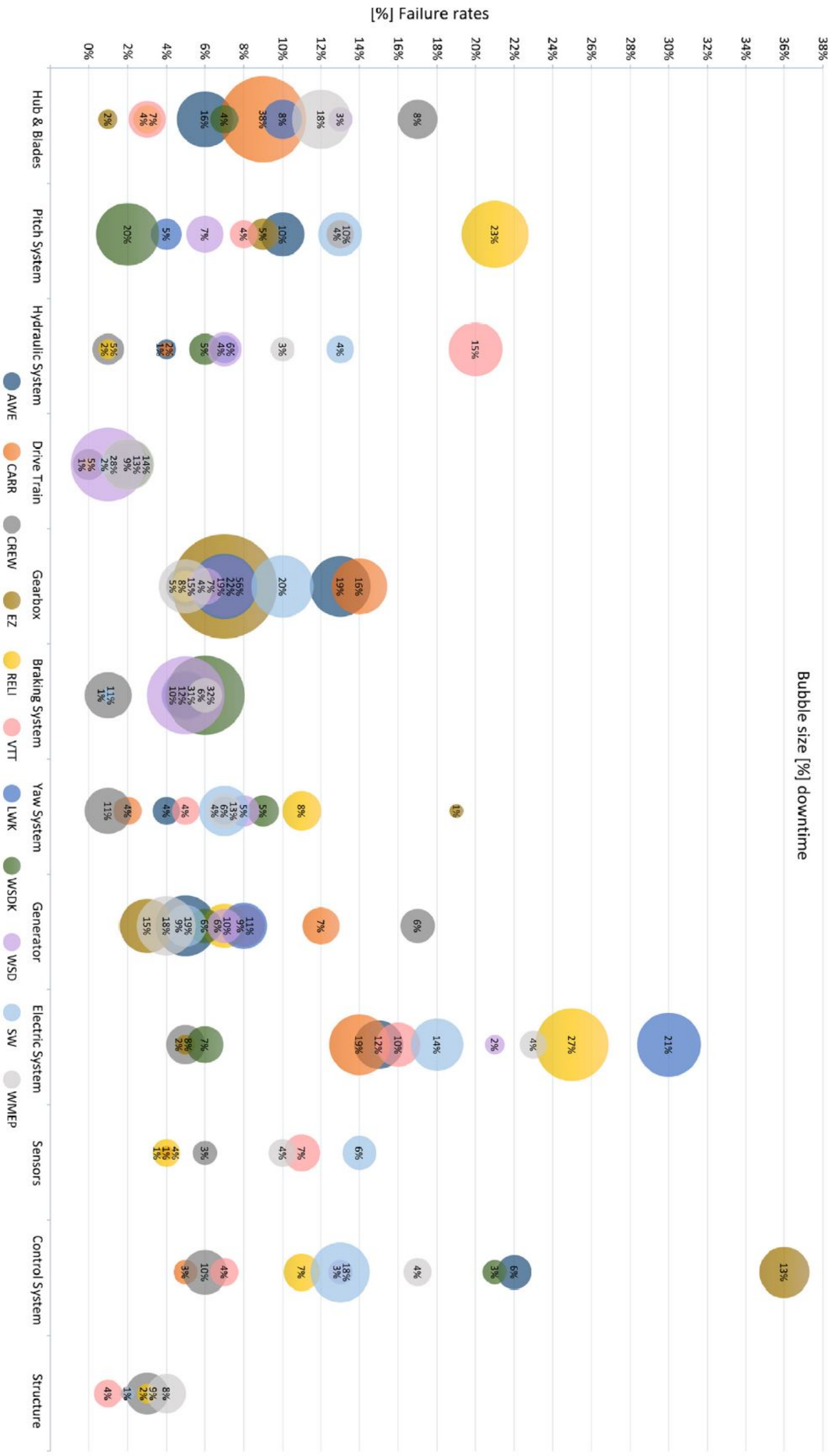

Figure 7 – Failure rates and associated downtime of the different components of a wind turbine [5]

The manuscript is organized as follows: the first Part is dedicated to the state of the art. In Chapter 1, the wind turbine modeling with the different involved physics is presented, as the models used in the thesis. Then, the modal analysis of the wind turbine and of the linear time periodic systems, in general, are presented. The objective is to understand the dynamics of a rotating wind turbine and what will compose the measurements. Then in Chapter 2, the OMA methods are presented. The main objective is to understand the purpose of the methods and why they can not be applied to rotating wind turbines. To continue, a brief review of the identification method designed for the rotating wind turbine is performed, to understand the choices made and the resulting drawbacks to develop a new approach. To finish a fault detection method based on the identification results is presented, as it should be possible to adapt it to the identification of operating wind turbines. Also, the damage sensitive parameters of the different rotor faults are presented, conjointly with some damage detection methods.

Secondly, the second Part develops the first contribution of the thesis, within Chapter 3 the definition of the approximation of the LTP system into an LTI system for subspace identification. With this new approach, the system is approximated based on the Floquet modes decomposition to be identified with the classical OMA methods. From the definition of the approximation, the use of a subspace method is demonstrated. Finally, in Chapter 4 the approach is validated with the identification of increasingly complex systems.

Finally, Part 3 develops the second contribution of the thesis, with fault detection based on the identification results. In Chapter 5 the damage sensitive parameters are searched, namely the phase shift and the amplitude of the rotor edge bending modes shapes. Then, the associated uncertainties are defined and validated. Finally, it is shown that these parameters can be used to detect rotor faults. Then, in Chapter 6, the Stochastic Subspace-based Damage Detection is adapted for the detection of rotor faults, using the aforementioned damage sensitive parameters. This method is validated on increasingly complex systems, to finally detect and localize a blade with a local loss of stiffness. Also, it is shown that the method can be performed using different kinds of measurements and that it is possible to detect different faults that can occur on a wind turbine rotor. Finally, in Chapter 7, the damage detection of rotor faults using measurements from the fixed frame (nacelle or tower) is assessed, where the objective is to determine if it is possible to perform such damage detection. From the nacelle and tower measurements, the new most damage sensitive features are searched and used in two damage detection methods.

PART I

State of the art

Chapter 1

Wind turbine

Abstract

In this Chapter, first, an introduction to the wind turbine area and the main elements of the modeling of each part of the multi-physics problem are given. Also, the two models that will be used in the thesis are presented. The first model is a phenomenological 5 degrees of freedom model of a wind turbine, used to test and validate the methods that will be developed in the thesis, with low simulation time. The second model is a more complex and realistic aero-servo-elastic model of a 10 MW wind turbine. Then, the modal analysis of the wind turbine and periodic systems, in general, is presented. Where the two methods that are used, the Floquet theory and the Multi-Blade-Coordinate transformation, are detailed. It is clear that the dynamical behavior of periodic systems is different from the one of time invariant systems. So, the modal parameters that will be searched in the signal of periodic systems will be different from those of invariant systems.

1.1 Introduction

The State of the art of the thesis is divided into two parts. With the first part dedicated to wind turbines. In this part, the modeling of wind turbine dynamics is introduced first. Then, the two models of different complexity used in the thesis are presented. The first model is a phenomenological model of 5 degrees of freedom of a rotating wind turbine, able to capture the main physical behavior of the problem. The second model is a complex multi-physics finite element model, to simulate realistic data. Finally, modal analysis for wind turbines is presented.

1.2 Wind turbine description

A schematic representation of a wind turbine is given in Figure 1.1 to introduce the main components of such structure as well as the basic terminology to describe their motion.

Some basic definitions are recalled here for the understanding of the thesis:

- Rated wind speed: Speed at which the turbine reaches its maximum power.
- Hub: Center of the rotor where all the blades are attached, illustrated in Figure 1.1
- Pitch angle: Angle to varies the angle of attack of the blade, illustrated in Figure 1.1. This variation of angle is used to reduce the aerodynamic efficiency of the rotor, when the wind speed is over the rated wind speed
- Yaw angle: The angle between the nacelle and a reference line (e.g. North-South axis), illustrated in Figure 1.1. This angle is adjusted so that the turbine is always in operation facing the wind.
- Tilt angle: The angle between the nacelle and the a horizontal line parallel to the ground, illustrated in Figure 1.1

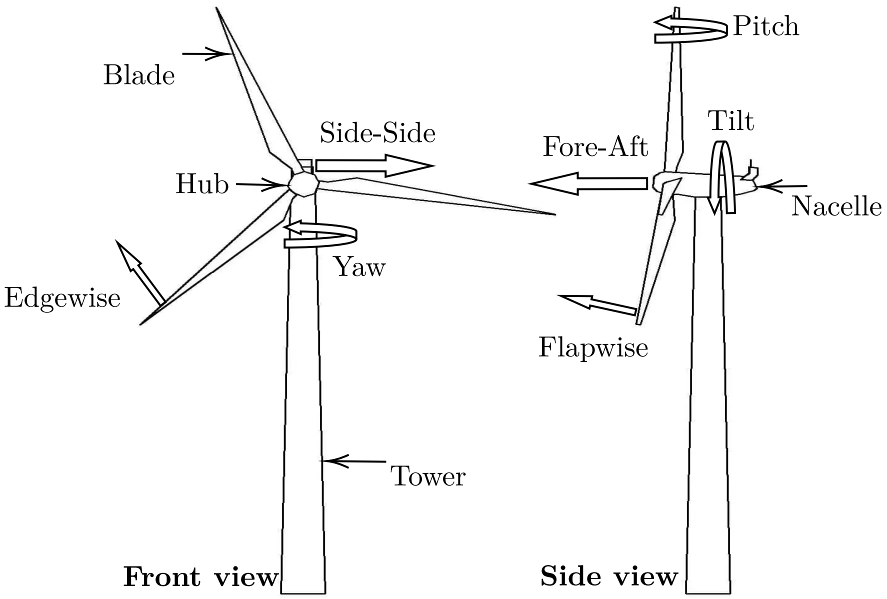

Figure 1.1 – Drawing of a wind turbine

- Azimuth angle: The angle that the rotor makes with respect to its original position, makes it possible to follow the blades position.
- Fore-Aft (FA) motion: Motion of the wind turbine in the wind direction, illustrated in Figure 1.1
- Side-Side (SS) motion: Motion of the wind turbine transverse to the wind direction, illustrated in Figure 1.1
- Edgewise (edge) displacement: Deflection of the blades in the rotor plane, illustrated in Figure 1.1
- Flapwise (flap) displacement: Deflection of the blades perpendicular to the rotor plane, illustrated in Figure 1.1

For the full description and characterisation of a wind turbine, the interested reader could refer to [19].

1.3 Common faults in wind turbine rotor

As said in the introduction, one of the objectives of the thesis is to perform damage detection with a focus on the wind turbine blades. The different kinds of faults and damages on the blades are then listed in Table 1.1. They impact the mechanical properties of the blades in different ways and so have different consequences on the dynamic behavior of the structure.

Thus, a fault in the rotor can be the consequence of a pitch misalignment. This leads to a change in the aerodynamic coefficients leading to a loss of power generation. Also, it changes the orientation of the blade, leading to a change in the mechanical properties along the flap and edge axis. It is also possible to observe an anisotropy in mass, that can be a consequence of ice accumulation on a blade [79, 93]. This can also lead to a loss of power generation and higher loads on shafts and bearings. Another fault is the anisotropy of stiffness, due for example to fatigue or lightning strike [80], leading to crack propagation, delamination, or debonding of the composite material.

Name	Modeling
Pitch error	Change of the aerodynamic coefficients and rotation of the structural properties
Ice accumulation	Addition of mass
Crack	Stiffness loss
Delamination	Stiffness loss
Debonding	Stiffness loss

Table 1.1 – Common faults in a wind turbine blade and associated modeling

1.4 Wind turbine modeling

A wind turbine is a complex rotating structure involving different physics that must be modeled. Many books, as [19, 66], give an overview of the modeling, performance and design of wind turbines. The main physics involved are briefly presented in the following.

Firstly, a modeling of the time and spatial evolution of the wind speed is presented. Secondly, the aerodynamic load computation methods are introduced. Afterward, the methods to model the mechanical part are presented. Then, the basics of wind turbine control are discussed. Finally, the wind turbine models that are used for the rest of the thesis are briefly presented.

1.4.1 Wind modeling

A wind turbine is subjected to variable wind, and the variability of the wind can be expressed in the frequency domain with a spectrum. In Figure 1.2, an example of the wind spectrum is displayed, with different peaks associated with different time scales. Synoptic variations (associated with the passage of weather system) and diurnal peaks (driven by local thermal effects) are important in prediction of wind and electricity power. The turbulent peak describes wind-speed variations on shorter time-scales (typically seconds to minutes). This peak has the main effect on the design and performance of a wind turbine. In general, only a few minutes or hours of time evolution of a wind turbine are simulated. So, looking at Figure 1.2, only the turbulent peak will have an impact on the time evolution of the wind. To define this turbulent peak, some models exist, where the two mains models of spectra are the the Kaimal [78] and von Karman [19], with the associated power spectra density defined as

$$\text{Kaimal: } S_k(f) = \frac{4\sigma_k^2 \frac{L_k}{\bar{u}}}{\left(1 + 6f\frac{L_k}{\bar{u}}\right)^{\frac{5}{3}}} \tag{1.1}$$

$$\text{von Karman: } S_k(f) = \frac{4\sigma_k^2 \frac{L_k}{\bar{u}}}{\left(1 + 70.8\left(f\frac{L_k}{\bar{u}}\right)^2\right)^{\frac{5}{6}}}. \tag{1.2}$$

Where f is the frequency, k the axis of the wind component (longitudinal, vertical or crosswise), L_k the Kaimal length scale, $\bar{u}$ the mean wind speed and σ_k the standard deviation of the wind speed. From [19], the von Karman spectrum gives a good description for turbulence in wind tunnels, although the Kaimal spectrum may give a better fit to empirical observations of atmospheric turbulence.

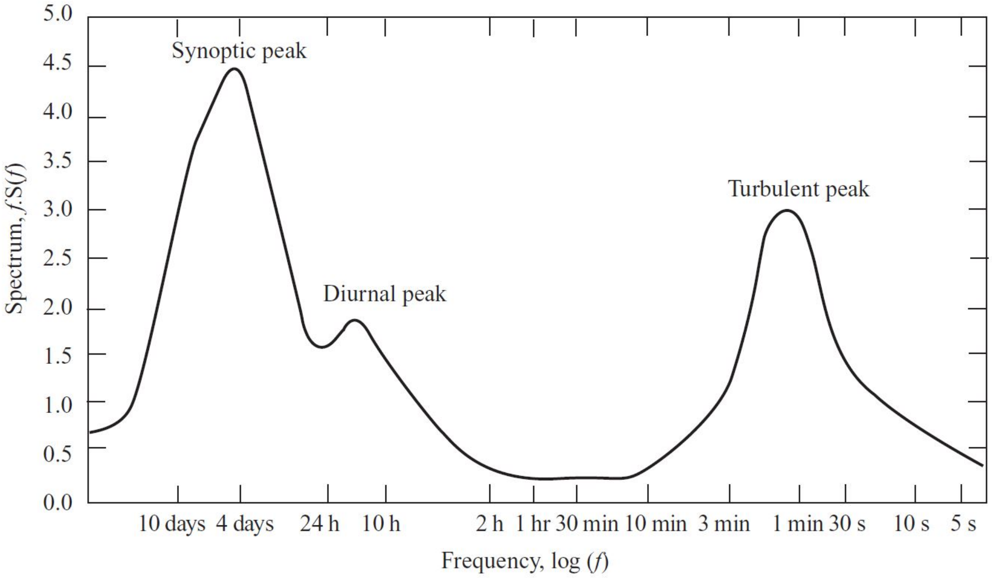

Figure 1.2 – Example of wind spectrum [19]

Once the spectrum of the wind has been defined, the time evolution can be computed. From the power spectra density the amplitude of the different frequencies can be obtained with $A(f) = \sqrt{S(f)2df}$, then the time evolution of the wind speed is obtained with the following Fourier series

$$U(t) = \bar{U} + \sum_{i=1}^{N} A(f_i) \cos\left(2\pi f_i t + \phi_i\right), \tag{1.3}$$

where ϕ_i is the phase shift associated with the frequency f_i, which is modeled as a random value, to have a stochastic wind speed.

However, to model the load on a wind turbine rotor due to the wind speed, a spatial evolution of the wind speed is needed, as it is displayed in Figure 1.3. To do so, the software *Turbsim* [74] can be used. To express the spatial evolution of the wind speed, two methods exist. The first one uses the wind speed evolution at the hub height from one of the previous spectra and vertical and horizontal shears. Those shears are expressing the evolution of the wind speed in the two main directions of the wind speed grid. Two possible distributions have been proposed to model this evolution due to ground roughness, respectively named logarithmic and power-law. The power law of the mean wind profile is defined as

$$\bar{u}(z) = \bar{u}\left(\frac{z}{z_{hub}}\right)^{\alpha}, \tag{1.4}$$

with z the altitude of the considered point, z_{hub} the altitude of the hub and α the vertical wind shear coefficient. For the horizontal shear, it is often set to zero, considering that there is no influence of the ground for example. A wind speed grid using a power law (called "Hub height" wind in *Turbsim*) is illustrated in Figure 1.4 (a).

Although, expressing the wind speed only with the hub height wind speed and the different

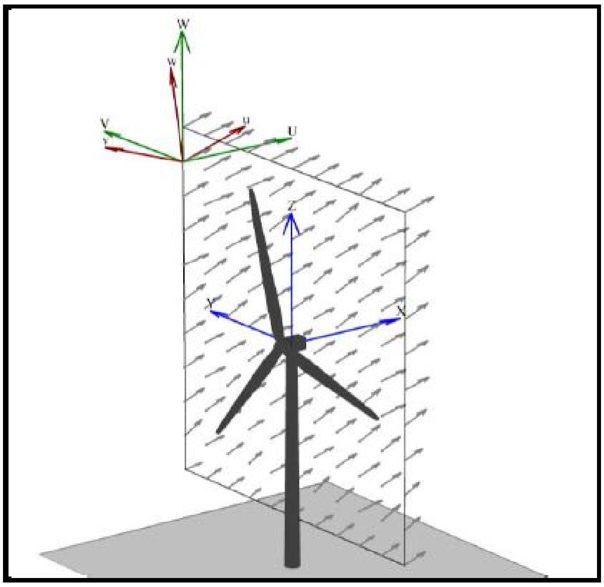

Figure 1.3 – Example of a grid of wind speed used in *Turbsim* [74]

shears is not representative of a real spatial distribution of the wind (called "Full field" wind in *Turbsim*), as represented in Figure 1.4 (b). So, the spatial variability can be expressed using the coherence between the spectra of all the points of a grid. The coherence between two points of a grid (i and j) is defined as

$$Coh_{ij}\left(f\right) = \frac{|S_{ij}(f)|}{\sqrt{S_{ii}(f)S_{jj}(f)}}, \tag{1.5}$$

with $S_{ij}(f)$ the cross-spectral density between the two points and $S_{ii}(f)$ and $S_{jj}(f)$ the spectral density defined previously. In *Turbsim*, the coherence for an IEC (International Electrotechnical Commission) [122] spectral model is defined as

$$Coh_{ij}\left(f\right) = \exp\left(-a\sqrt{\left(\frac{fr}{\bar{u}_{hub}}\right)^2 + \left(0.12\frac{r}{L_c}\right)^2}\right), \tag{1.6}$$

where r is the distance between the grid points, a is the coherence decrement and L_c is a coherence scale parameters. The values of the two last parameters are defined in [74], with $a = 12$ and $L_c = 2.45 \times \min\left(30, hubheight\right)$.

So, with this method commonly used in engineering, once the time and spatial evolution of the wind speed is modeled, the aerodynamic loads on the rotor due to the wind can be computed. In the next section, the main method to compute the aerodynamic loads will be presented.

1.4.2 Aerodynamic loads computation

To model the behavior of a wind turbine, the aerodynamic forces due to the wind applied to the structure have to be defined. This will also allow to determine the electrical power that a wind turbine can theoretically deliver. Different methods can be used to compute the aerodynamics loads on a wind turbine [61], with for example the Blade Element Momentum (BEM), the computational Fluid Dynamics (CFD) or the Vortex methods. The BEM theory is the most

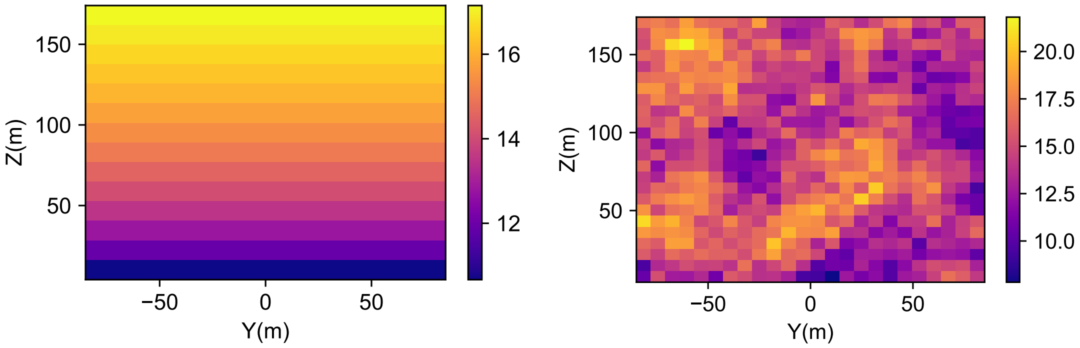

(a) "Hub height" wind

(b) Full field wind

Figure 1.4 – Comparison of wind speed grid, for two different spatial evolution modeling

common method used in the design modeling softwares, because it is the fastest of the mentioned methods, with a good level a accuracy. This method is described in the Appendix A.

1.4.3 Structural modeling of a wind turbine

Once the aerodynamic loads are defined, the structural part of the wind turbine must be modeled. Two major approaches are commonly employed for this modeling. A first method is the classical finite element method, widely used in the modeling of structures. The latter is used for example in the software *Deeplines Wind* [101], where the blades and the tower are modeled using 3D non-linear beams elements, with large transformation for the blades (around 50 beam elements per blade).

Another option is to reduce the problem size by projecting the wind turbine displacements on its linear eigenmodes through modal decomposition [121, 120, 64]. With such approach used in the software *OpenFAST* [94], where each part of the wind turbine is expressed through his eigenmodes. The modal decomposition aims to model a system from its eigenmodes, which can be used to express the displacements. Let us express the displacements $u(x,t)$ as a function of N eigenmodes:

$$u(x,t) = \sum_{i=1}^{N} A_i(x) q_i(t), \tag{1.7}$$

where $A_i(x)$ represents the spatial evolution of the mode shape i and $q_i(t)$ the time parameter associated to mode i. Therefore, the dynamic of the system is characterized by only N DOF. The main advantage of this method is that it allows us to obtain a large spatial discretization with few parameters, reducing drastically the problem size. The disadvantage is that the eigenmodes of the different parts of the structure must be known, which requires a preliminary study. Also, it is assumed that the linear eigenmodes of the components are sufficient to describe the dynamic of the whole wind turbine. To define a wind turbine model in *OpenFAST*, the eigenmodes of the tower and the blades are obtained with an eigenvalue decomposition, where both are modeled using 3D beam finite elements. To do so, the software *BModes* [14] can be used.

In *OpenFAST*, an onshore wind turbine is defined with the eigenmodes of the main components. For the blades, the two first flap bending modes and the first edge bending mode are used. For the tower, the two first bending modes along Side-Side and Fore-Aft are used. Blades and tower are supposed to be clamped respectively on the hub and on the ground. Finally, the first mode of torsional bending of the drive-train shaft is used. To those eigenmodes, the degree of freedom (DOF) of the generator can be added, for a total of 15 DOF for a three-bladed rotor.

1.4.4 Wind turbine controller

A wind turbine has three distinct control regions illustrated in Figure 1.5. They are characterized by the minimum and maximum allowed speeds of the wind turbine. The first region is when the wind speed is lower than the minimum speed of the turbine, then the turbine is stopped. The second region is when the wind speed is within the minimum and rated speed, in this region the controller will adjust the rotation speed to optimize the electrical power production. The last region is when the wind speed is above the rated speed. In this case, the wind turbine rotates at its maximum speed, the presented controller adjusts the angle of attack of the blades (pitch) to reduce the efficiency of the rotor and to have a constant power output. Other types of controllers exist and are based on passive stalling to limit power in the last region.

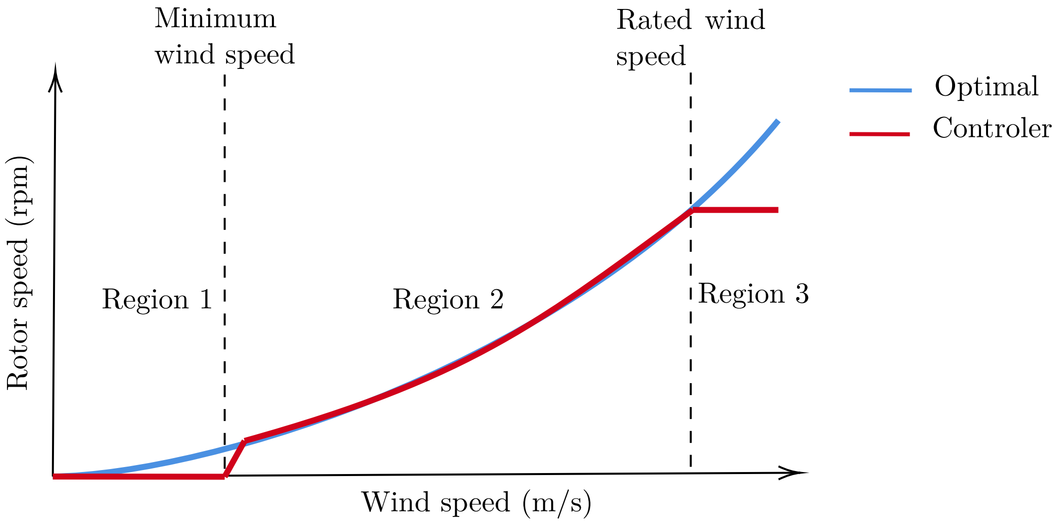

Figure 1.5 – Example of a speed control curve

The principles of wind turbine modeling have been introduced and the workflow of the coupling between all the physics is displayed in Figure 1.6, where the modeling of an offshore floating wind turbine is considered. The following Section is dedicated to the presentation of the wind turbine models used in the thesis. The first model is an academic model of a simplified wind turbine, able to mimic the main dynamic behaviors. The second model is a complex model of a real-world wind turbine.

1.4.5 Wind turbine models used in the thesis

Academic model of a wind turbine

In order to test and validate the OMA methods that are developed in the thesis, it is needed to have a simple model with low simulation time, but still able to represent the main dynamic behaviors. In this context, a phenomenological model of an onshore wind turbine is used, the latter is defined in [119] and represented in Figure 1.7. It has an isotropic rotor and a constant

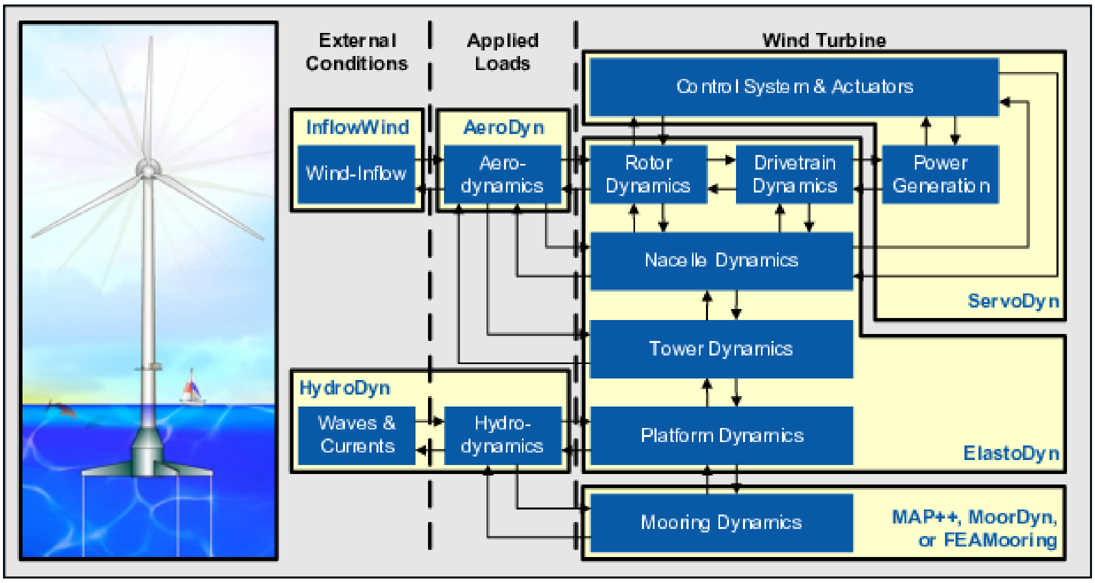

Figure 1.6 – Workflow of *OpenFAST* for a floating wind turbine [94]

rotational speed. This model is composed of 3 DOF representing the blade bending (one for each blade) perpendicular to the rotor plane, and two DOF of nacelle bending. To define the system equations, the Lagrange equations are used:

$$\mathcal{L} = T - V \tag{1.8}$$

$$\frac{d}{dt}\left(\frac{\partial \mathcal{L}}{\partial \dot{q}}\right) - \frac{\partial \mathcal{L}}{\partial q} = \delta W_q, \tag{1.9}$$

where $\mathcal{L}$ is called the Lagrangian, with T the kinetic energy and V the potential energy. δW_q represents the virtual work of the external forces with respect to the parameter q. Then these equations are resolved and linearized around the equilibrium solution (time t and azimuth angle ψ), considering small deflections. Thus, the mass, damping, and stiffness matrices can be computed, denoted $\mathcal{M}(t)$, $\mathcal{C}(t)$ and $\mathcal{K}(t)$, respectively, where

$$\mathcal{M}(t) = \begin{bmatrix} J_b & 0 & 0 & J_b\cos\psi_1 & -J_b\sin\psi_1 \\ 0 & J_b & 0 & J_b\cos\psi_2 & -J_b\sin\psi_2 \\ 0 & 0 & J_b & J_b\cos\psi_3 & -J_b\sin\psi_3 \\ J_b\cos\psi_1 & J_b\cos\psi_2 & J_b\cos\psi_3 & J_x + \frac{3}{2}J_b + J_0 & 0 \\ -J_b\sin\psi_1 & -J_b\sin\psi_2 & -J_b\sin\psi_3 & 0 & J_z + \frac{3}{2}J_b + J_0 \end{bmatrix}, \tag{1.10}$$

$$\mathcal{C}(t) = \begin{bmatrix} c_1 & 0 & 0 & -2\Omega J_b\sin\psi_1 & -2\Omega J_b\cos\psi_1 \\ 0 & c_2 & 0 & -2\Omega J_b\sin\psi_2 & -2\Omega J_b\cos\psi_2 \\ 0 & 0 & c_3 & -2\Omega J_b\sin\psi_3 & -2\Omega J_b\cos\psi_3 \\ 0 & 0 & 0 & c_x & -3\Omega J_b \\ 0 & 0 & 0 & 3\Omega J_b & c_y \end{bmatrix} \tag{1.11}$$

and

$$\mathcal{K}(t) = \begin{bmatrix} G_1 + \Omega^2 J_b & 0 & 0 & 0 & 0 \\ 0 & G_2 + \Omega^2 J_b & 0 & 0 & 0 \\ 0 & 0 & G_3 + \Omega^2 J_b & 0 & 0 \\ \Omega^2 J_b \cos\psi_1 & \Omega^2 J_b \cos\psi_2 & \Omega^2 J_b \cos\psi_3 & G_x & 0 \\ -\Omega^2 J_b \sin\psi_1 & -\Omega^2 J_b \sin\psi_2 & -\Omega^2 J_b \sin\psi_3 & 0 & G_z \end{bmatrix}. \tag{1.12}$$

Where, G_1, G_2, G_3 denotes the bending stiffness of each blade, J_b the inertia of the blades, J_0 the mass of the blades, G_x and G_z the stiffness of the motion of the nacelle with J_x and J_z the associated inertia. These matrices are periodic of period $T = \frac{2\pi}{\Omega}$, with Ω the rotational speed. The mechanical parameters are identical to those used by [119] and listed in Table 1.2 for the reference case (isotropic, i.e. roter where the three blades are identical).

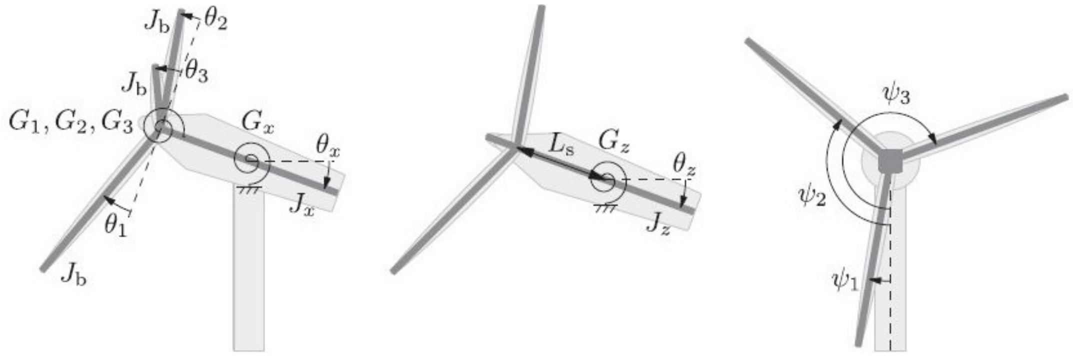

Figure 1.7 – Wind turbine model [119]

Blade moment of inertia about root	J_b	4×10^6 kg m^2
Nacelle/tower tilt moment of inertia	J_x	8×10^6 kg m^2
Nacelle/tower yaw moment of inertia	J_z	6×10^6 kg m^2
Blade stiffness	G_b	8×10^7 Nm
Nacelle/tower tilt stiffness	G_x	7×10^8 Nm
Nacelle/tower yaw stiffness	G_z	4×10^8 Nm
Blade damping	c_b	1×10^6 kg m^2 s^{-1}
Nacelle/tower tilt damping	c_x	1×10^6 kg m^2 s^{-1}
Nacelle/tower yaw damping	c_z	8×10^5 kg m^2 s^{-1}
Blade mass	m_b	12×10^3 kg
Distance from tower top to hub	L_s	4 m

Table 1.2 – Parameter of the academic model of wind turbine

With the presented model, it is also possible to define a wind turbine with different blade stiffness. However, to define a rotor with different blade mass and inertia, the Lagrange equation needs to be derived without the assumption that the mass and inertia of the blades are identical.

This model will be used for the development and validation of the OMA methods. However, the developed OMA methods must also be tested on a more realistic model. Thus, a second more complex and realistic model of a wind turbine is also considered in this thesis.

Reference wind turbine: DTU 10MW

In the rest of the thesis, the OMA methods will be also tested on complex numerical models of wind turbines, due to a non-access to real data. Because of confidentiality issues, the DTU 10MW reference wind turbine is employed, whose model is freely available (included the *OpenFAST* model) [32], with a detailed documentation of the structure [7] and the controller [65].

The DTU 10MW is a large wind turbine, with a size comparable to the wind turbines installed in the latest or under construction wind farms. The main properties of the wind turbine are given in Table 1.3, with two configurations, namely onshore and offshore on a jacket. The onshore version is used in this thesis. Figure 1.8 illustrates the behavior of the turbine, through some parameters defined with the controller, namely the rotational speed, the pitch angle and the electric power. These results highlight the different regions of the control. The first region is not displayed as the wind turbine is stopped below 4 m/s of wind speed. From 4 to 11 m/s, the power and the rotational speed are increasing with a pitch angle of 0°, corresponding to the region 2. Above 11 m/s, the power and the rotational speed are constant while the pitch angle increases in a similar way to the wind speed to reduce the efficiency of the rotor, corresponding to the region 3.

Maximum power	10 MW
Rotational speed	4 to 9.6 rpm
Rotor diameter	178.3 m
Hub height	119 m
Wind speed	minimal: 4m/s rated: 11.4 m/s maximal: 25 m/s

Table 1.3 – Characteristic values of the DTU 10MW wind turbine

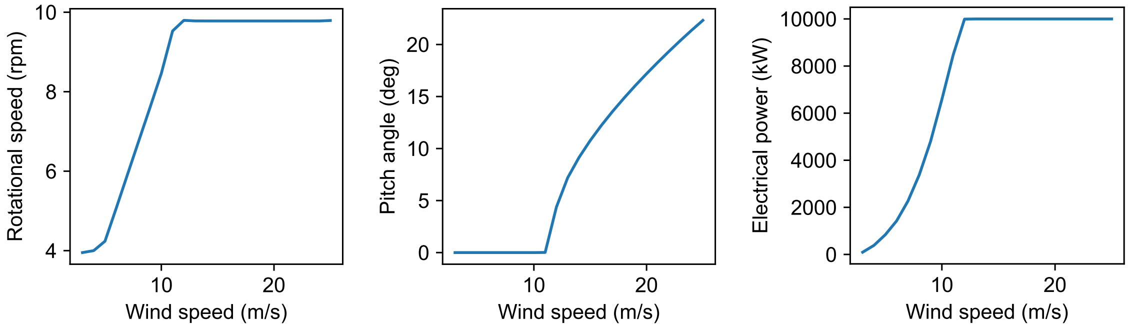

(a) Rotational speed (b) Pitch angle (c) Electrical power

Figure 1.8 – Evolution of control parameters of the DTU 10MW wind turbine function of the wind speed

1.4.6 Conclusion

First, the different physics involved in the modeling of a wind turbine has been described, namely the wind modeling, the aerodynamic loads from the wind speed evolution, the modeling of the structure, and finally the control. In the rest of the thesis, two models of wind turbines will be employed. The academic model is enough to understand the problem of OMA of wind turbines. The model of the theoretical wind turbine DTU 10MW, used with the software *OpenFAST* [94], allows a coupling of the various physics, with a modeling of the structure by modal decomposition and the aerodynamics loads computed with the BEM method. This complex model will allow to compute data close to what can bee seen on experimental measurements.

In the following, the modal analysis of wind turbine is introduced, and more precisely the modal analysis of linear time periodic systems with the Floquet theory. The objective is to understand the dynamical behavior of a wind turbine and LTP systems in general.

1.5 Modal analysis of linear time periodic systems

One of the objective of the thesis is to monitor the modal parameters of wind turbines, so it is needed to know them. A wind turbine with a constant rotational speed Ω can be modeled as a linear time periodic (LTP) system as it is commonly done in the automatic field, and the Floquet theory is the theory that enables to extend modal analysis for this type of system.

First, the dynamic model and the space-state representation of the LTP system are presented. Then, the modal analysis of linear time invariant (LTI) systems is recalled. After that, LTP systems and their specificities are introduced and illustrated with a simple model. Then, the dynamical model of an LTP system is defined, to express the associated state-space representation. Finally, the modal analysis of an LTP system is presented with the Floquet theory and the Multi-Blade Coordinate transformation.

1.5.1 Dynamic model of an LTP system

The motion of a wind turbine with a constant rotational speed Ω can be expressed as an LTP system,

$$\mathcal{M}(t)\ddot{u}(t) + \mathcal{C}(t)\dot{u}(t) + \mathcal{K}(t)u(t) = v(t), \tag{1.13}$$

where $u(t) \in \mathbb{R}^m$ represents the displacements of the structure at the DOF of the system, and $\mathcal{M}(t+T) = \mathcal{M}(t)$, $\mathcal{C}(t+T) = \mathcal{C}(t)$, $\mathcal{K}(t+T) = \mathcal{K}(t)$ are respectively the mass, damping and stiffness periodic matrices. $T = \frac{2\pi}{\Omega}$ represents the rotational period. $v(t)$ represents the load on the system. In the following, the mechanical system is expressed in a state-space form, from the definition of the state vector $x(t) \in \mathbb{R}^n$ where $n = 2m$. For the next sections, the observation $y(t) \in \mathbb{R}^r$ is also introduced.

$$x(t) = \begin{bmatrix} u(t) \\ \dot{u}(t) \end{bmatrix} \quad \text{and} \quad y(t) = C_a\ddot{u}(t) + C_v\dot{u}(t) + C_d u(t), \tag{1.14}$$

where C_a, C_v and C_d are selection matrices. A noise $w(t)$ can be added to the observation. $w(t)$ is assumed to be a Gaussian white noise. This leads to the following state-space expression:

$$\begin{cases} \dot{x}(t) = A_c(t)x(t) + B_c(t)v(t) \\ y(t) = C(t)x(t) + D(t)v(t) + w(t) \end{cases}, \tag{1.15}$$

with

$$\begin{aligned} A_c(t) &= \begin{bmatrix} 0 & I \\ -\mathcal{M}(t)^{-1}\mathcal{K}(t) & -\mathcal{M}(t)^{-1}\mathcal{C}(t) \end{bmatrix}, \\ C(t) &= \begin{bmatrix} C_d - C_a\mathcal{M}(t)^{-1}\mathcal{K}(t) & C_v - C_a\mathcal{M}(t)^{-1}\mathcal{C}(t) \end{bmatrix}, \\ B_c(t) &= \begin{bmatrix} 0 \\ -\mathcal{M}(t)^{-1} \end{bmatrix} \quad \text{and} \quad D(t) = C_a\mathcal{M}^{-1}(t). \end{aligned}$$

All matrices are periodic of period T, with $A_c(t) \in \mathbb{R}^{n\times n}$, $C(t) \in \mathbb{R}^{r\times n}$, $B_c(t) \in \mathbb{R}^{n\times m}$ and $D(t) \in \mathbb{R}^{r\times m}$.

1.5.2 Recall: modal analysis of an LTI system

Before describing the modal analysis of an LTP system, let us remind the modal analysis of an LTI system (like a stopped wind turbine). The dynamical behaviour of an LTI system is described by the homogeneous equation such that

$$\dot{x}_h(t) = Ax_h(t), \tag{1.16}$$

where $x_h(t) \in \mathbb{R}^n$ the state vector and $A \in \mathbb{R}^{n\times n}$ the state matrix. From this equation, the solution is

$$x_h(t) = \exp\left(At\right)x(t_0), \tag{1.17}$$

where $x(t_0)$ is the initial condition. Assuming that A is diagonalizable, an eigenvalue decomposition can be performed and the state vector can be expressed as

$$x_h(t) = \Psi\exp\left([\mu]t\right)\Psi^{-1}x(t_0), \tag{1.18}$$

where $\Psi \in \mathbb{R}^{n\times n}$ gather the n eigenvectors and $[\mu]$ a diagonal matrix with the associated eigenvalues. From this, it is possible to express the state vector as a sum of n eigenmodes composed of a spatial component, the eigenvector, and a time component, the eigenvalue.

$$x_h(t) = \sum_{i=1}^{n}\psi_i\exp(\mu_i t)q_i(t_0), \tag{1.19}$$

with ψ_i the i–th eigenvector (the i–th column of Ψ) and μ_i the i–th eigenvalue defining the i–th eigenmode. $q_i(t_0) = \psi_i' x(t_0)$ with ψ_i' the i–th row of Ψ^{-1} defines the initial conditions for each eigenmode.

The modal analysis of an LTI system has been introduced, now the modal analysis of an LTP system will be defined.

1.5.3 Definition and presentation of a simple LTP system

An LTP system is a system with time periodic coefficients. The simplest LTP system exhibiting an oscillatory behaviour is perhaps the well-known Mathieu oscillator, which is a one

DOF mass-spring system, with a periodic stiffness,

$$m\ddot{y}(t) + c\dot{y}(t) + (k_0 + k_1 \cos(\omega_A t))\, y(t) = v(t). \tag{1.20}$$

The stiffness of the system is periodic of period $\frac{2\pi}{\omega_A}$. In this section, the parameters are those used in [111], with $m = 1$, $k_0 = 1$, $k_1 = 1$, $c = 0.04$ and $\omega_A = 0.8$.

To study the dynamic of an LTP system, a frequency spectrum analysis of the Mathieu oscillator can be performed. In Figure 1.9a, the PSD of the free decay of the system is represented. Six peaks are observable in the PSD and marked with dashed lines. However, the system is composed of one DOF, so one should expect only one peak, to obtain a spectrum similar to what can be obtained with an LTI system. After analyzing the frequency peaks, it can be observed that all the peaks correspond to a modulation of the principal frequency. Indeed, the peak with the highest amplitude is observed at f=0.16 Hz. The other observed peaks correspond to $f + h\frac{\omega_A}{2\pi}$, where h is the modulation displayed in Figure 1.9a.

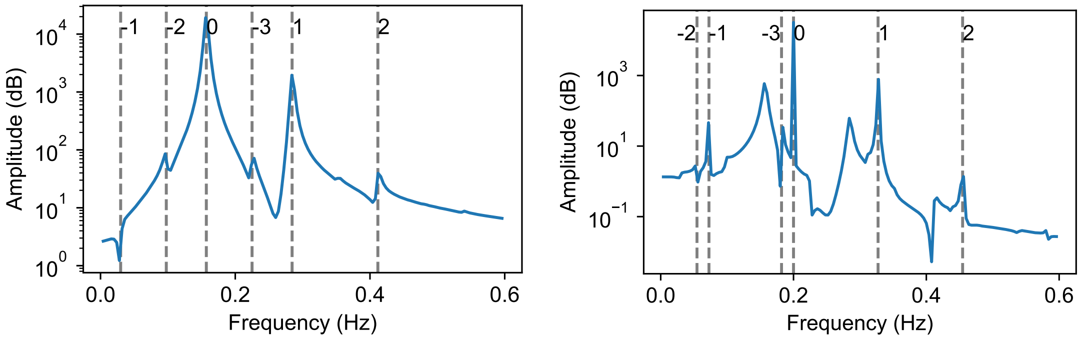

(a) Free decay, (- - -): different modulations of the Floquet mode frequency with their modulation number

(b) Input: harmonic with frequency of 0.2 Hz, (- - -): different modulations of the input frequency with their modulation number

Figure 1.9 – Power spectral density (PSD) of the acceleration of the Mathieu oscillator for two different simulations with $\omega_A = 0.8$

Then, another specificity of LTP systems is the modulation of the inputs. When the dynamic loading of the system ($v(t)$ in Equation (1.20)) is a pure harmonic excitation like $v(t) = A\cos(2\pi f t)$, the response of the system is composed of modulated harmonics. For LTP systems, the input frequency is modulated by the frequency of the system: $f + k\frac{\omega_A}{2\pi}$ (in the case of the Mathieu oscillator), where k is an integer. In Figure 1.9b, the PSD of the Mathieu oscillator obtained with an excitation frequency of 0.2 Hz is represented, with $\frac{\omega_A}{2\pi} = f_A = 0.127$ Hz. More peaks are present in this PSD with a harmonic excitation (Figure 1.9b) compared to the PSD of the free decay (Figure 1.9a). Compared to the decay test, a total of 6 new peaks can be found on the PSD, corresponding to the modulations 0, 1, -3, -2, 2, and -1 at the respective frequencies 0.2 (the input frequency), 0.33, 0.18, 0.05, 0.45 and 0.07 Hz. The second most important peak is around 0.33 Hz.

Finally, as the system depends on its period ω_A, the dynamic of the system vary regarding the rotational speed. This evolution is often displayed with a Campbell diagram, which represents the evolution of the natural frequencies with the rotational speed. As an example, Figure 1.10 shows the evolution of the frequency and damping of a peak (modulation $h = 0$) in the spectrum

Figure 1.9a. One can see the clear variation in frequency and damping of such systems when the rotational speed ω_A varies. Those Campbell diagrams can be used to check if the frequencies are not close to an eigenfrequency of other components of the system for some rotational speeds and so to avoid any resonance. Also, they can be used for stability analysis, verifying that the damping is positive.

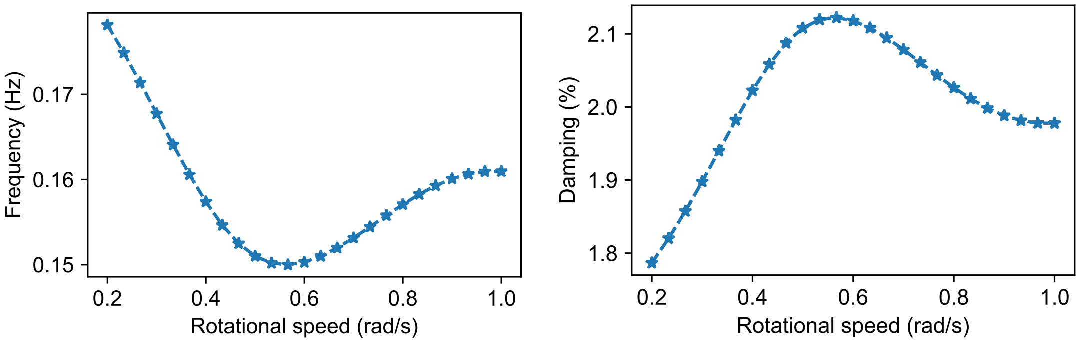

(a) Frequency (b) Damping

Figure 1.10 – Campbell diagram of the frequency and damping of the Mathieu oscillator

1.5.4 Floquet theory

The Floquet theory [49] is initially intended for the solving of linear differential equations of periodic coefficients. From this theory, it is possible to express the eigenmodes of an LTP system [116, 119, 118], with a spatial component and a time component.

The general solution of the differential equation (1.15) reads:

$$x(t) = \Phi(t, t_0)x(t_0) + \int_{t_0}^{t} \Phi(t, \tau)B_c(\tau)v(\tau)d\tau, \tag{1.21}$$

with $\Phi(t, t_0)$ the fundamental matrix solution of the homogeneous problem. Looking first at the homogeneous part of the differential equation:

$$\dot{x}_h(t) = A_c(t)x_h(t) \tag{1.22}$$

the fundamental matrix $\Phi(t, t_0)$ is the solution of this equation such that:

$$x_h(t) = \Phi(t, t_0)x(t_0). \tag{1.23}$$

To simplify Equation (1.23), the fundamental matrix can be expressed as $\Phi(t) := \Phi(t, t_0) = \Phi(t)\Phi(t_0)^{-1}$, with $\Phi(t_0) = \mathbf{I}$ the identity matrix. Also the monodromy matrix Q is defined by $Q = \Phi(T)$, where

$$\Phi(t + T) = \Phi(t)Q. \tag{1.24}$$

The eigenvalues of Q are called the characteristic multipliers (λ_i), with ψ_i the associated eigenvectors. The characteristic exponents (μ_i) are defined as

$$\lambda_i = \exp\left(\mu_i T\right). \tag{1.25}$$

The characteristic multipliers can be decomposed as $\lambda_i = \Re(\lambda_i) + \Im(\lambda_i) + ik\Omega$, with k an undetermined integer. The fundamental matrix can be factorized into a matrix of n independent periodic vectors $p(t)$ collected into the matrix $P(t)$

$$\Phi(t) = P(t) \exp(Rt), \tag{1.26}$$

with $R = \frac{1}{T}\log(Q)$. The matrix R can be diagonalized, using the characteristic exponents and the eigenvectors of Q,

$$R = \Psi [\mu] \Psi^{-1}. \tag{1.27}$$

So the matrix $\Phi(t)$ can be expressed with the characteristic exponents

$$\Phi(t) = P(t)\Psi \exp([\mu] t) \Psi^{-1}. \tag{1.28}$$

Finally using Equation (1.28) and Equation (1.23), the state vector is expressed as a sum of n Floquet modes

$$x_h(t) = \sum_{j=1}^{n} X_j(t) \exp(\mu_j t) q_j(t_0) \tag{1.29}$$

with $q_j(t_0) = \psi'_j x(t_0)$, ψ'_j the j–th row of the matrix Ψ^{-1} and $X_j(t) = P(t)\psi_j$ the T-periodic mode shape of the j–th Floquet mode.

The periodic mode shape can be expanded in a Fourier series,

$$X_j(t) = \sum_{l=-\infty}^{\infty} X_{j,l} \exp(il\Omega t) \tag{1.30}$$

Introduced in Equation 1.29, it leads to a new definition of the state

$$x_h(t) = \sum_{j=1}^{n} \sum_{l=-\infty}^{\infty} X_{j,l} \exp((\mu_j + il\Omega)t) q_j(t_0). \tag{1.31}$$

By comparing this definition to the definition of the state vector of an LTI system in Equation (1.19), it is clear that an LTP system can be seen as an LTI system with an infinite number of eigenmodes.

Practical computation of the Floquet modes Based on [118], a method to compute the Floquet modes of a system is proposed (when the matrix $A_c(t)$ is known):

1. **Determination of the fundamental matrix** $\Phi(t)$. Solve the differential Equation (1.22) for n different initial conditions. These initial conditions are a vector $x(0)$ full of zero except at index i where $x(0)(i) = 1$. Knowing that $x_h(t) = \Phi(t)x(0)$ and that $x(0)$ is full of zero except at index i, it comes

$$x(t) = \Phi(t)_{[i]} \tag{1.32}$$

   with $\Phi_{[i]}$ the i–th column of the fundamental matrix.

2. **Computation of the Floquet multipliers** using an eigenvalue decomposition of $Q =$

$\Phi(T)$

$$Q = \Psi \left[\lambda_i\right] \Psi^{-1} \tag{1.33}$$

3. **Computation of the Floquet exponents**

$$\mu_j = \frac{1}{T} \log\left(\lambda_j\right), \text{ with } \mu_j = -\xi_j \omega_j + i\omega_j \sqrt{1-\xi_j^2}. \tag{1.34}$$

where ω_j denotes the pulsation and ξ_j denotes the damping ratio.

4. **Computation of the periodic mode shapes** associated with each Floquet exponent from Equation (1.29)

$$x_j(t) = X_j(t) \exp\left(\mu_j t\right) q_j(0) \tag{1.35}$$

where $X_j(t)$ is defined such as:

$$X_j(t) = \Phi(t)\psi_j \exp\left(-\mu_j t\right) \tag{1.36}$$

where ψ_j is the j–th eigenvector of Q associated with the j–th eigenvalue.

1.5.5 Coleman or Multi-Blade Coordinate (MBC) transformation

To study the eigenmodes of an LTP system, according to the Floquet theory, it is possible to use a change of variables to express the LTP system as a time invariant system, which allows to use the theory of invariant systems. A common approach in the rotor dynamics community is to use the Multi-Blade-Coordinate transformation also called Coleman transformation, developed for rotors with a minimum of 3 equally spaced identical blades [27, 13, 119, 123]. This method enables an explicit definition of the change of variable. The difference between the Floquet method and the MBC transformation is detailed in Section 1.5.7. Here, the method developed in [13] is presented.

Let the LTP system be defined by the homogeneous equation:

$$\dot{x}_h(t) = A(t)x_h(t), \text{ with } \; A(t+T) = A(t), \tag{1.37}$$

$T = \frac{2\pi}{\Omega}$ the rotation period of the rotor, $x_h(t)$ the homogeneous part of the state vector, with $x_h(t) = \begin{bmatrix} u(t) \\ \dot{u}(t) \end{bmatrix}$. The displacement ($u(t)$) is defined with N_b DOF per blade and N_s DOF for the tower and the nacelle (defined as the fixed frame). Thus, for a 3-bladed rotor, the displacement vector follows this form

$$u(t) = \begin{bmatrix} (u^F)^T & u_1^1 & u_2^1 & u_3^1 & \dots & u_1^{N_b} & u_2^{N_b} & u_3^{N_b} \end{bmatrix}^T, \tag{1.38}$$

where u^F regroups the DOF of the fixed frame and u_k^j denotes the j–th DOF of the k–th blade. The Coleman transformation is defined by the following equation:

$$u(t) = T_1(t)u^{NR}(t), \tag{1.39}$$

with $u^{NR}(t)$ the new displacement vector,

$$u^{NR}(t) = \begin{bmatrix}(u^F)^T & q_0^1 & q_c^1 & q_s^1 & \dots & q_0^{N_b} & q_c^{N_b} & q_s^{N_b}\end{bmatrix}, \tag{1.40}$$

$$T_1(t) = \begin{bmatrix} I & & & \\ & \tilde{t}(t) & & \\ & & \ddots & \\ & & & \tilde{t}(t) \end{bmatrix} \in \mathbb{R}^{(N_s+3N_b)\times(N_s+3N_b)} \tag{1.41}$$

and

$$\tilde{t}(t) = \begin{bmatrix} 1 & \cos\psi_1(t) & \sin\psi_1(t) \\ 1 & \cos\psi_2(t) & \sin\psi_2(t) \\ 1 & \cos\psi_3(t) & \sin\psi_3(t) \end{bmatrix}, \tag{1.42}$$

where $\psi_k(t) = \Omega t + \frac{2\pi}{3}(k-1)$ denotes the azimuth angle of the k–th blade at the time instant t.

A physical signification can be given to these new coordinates, [62, 34]. The displacement of the the j–th DOF of the k–th blade is defined as

$$u_k^j(t) = q_0^j + q_c^j \cos(\psi_k(t)) + q_s^j \sin(\psi_k(t)). \tag{1.43}$$

If $u^j(t)$ denotes a DOF of flapwise bending, then q_0^j denotes the collective flap, q_c^j denotes the tilt motion and q_s^j denotes the yaw motion. The tilt and yaw motions are rotation of the rotor related to the tilt angle and the yaw angle (see Section 1.2). If $u^j(t)$ denotes a DOF of edgewise bending, then q_0^j denotes the collective edge, q_c^j denotes the horizontal motion and q_s^j denotes the vertical motion of the rotor.

The objective is to express a change of variables for the state vector. The derivative of the displacement is

$$\begin{aligned} \dot{u}(t) &= \frac{d}{dt}\left(T_1(t)u^{NR}(t)\right) && (1.44)\\ &= \dot{T}_1(t)u^{NR}(t) + T_1(t)\dot{u}^{NR}(t). && (1.45) \end{aligned}$$

So the change of variables of the state vector is defined by

$$x(t) = B(t)z_B(t) \tag{1.46}$$

with z_B the new state vector

$$z_B(t) = \begin{bmatrix} u^{NR}(t) \\ \dot{u}^{NR}(t) \end{bmatrix} \tag{1.47}$$

and

$$B(t) = \begin{bmatrix} T_1(t) & 0 \\ \dot{T}_1(t) & T_1(t) \end{bmatrix}. \tag{1.48}$$

Finally, the homogeneous equation of the system depending of the new coordinates can be expressed

$$\dot{z_B}(t) = A_B z_B(t), \text{ with } A_B = B(t)^{-1}\left(A(t)B(t) - \dot{B}(t)\right). \tag{1.49}$$

The A_B matrix is time invariant only if the rotor is isotropic. Therefore, the transformation is limited to an isotropic rotor. This limitation could be observed with measures on operational wind turbines, which will be discussed in the following sections.

Once the change of variables is done, the eigenvalue decomposition can be performed. Thus, using the results of the modal analysis of invariant systems

$$z_B(t) = V_B \exp\left(\Lambda_B t\right) V_B^{-1} z_B(0), \tag{1.50}$$

with V_B the eigenvectors of A_B and Λ_B the diagonal matrix gathering the eigenvalues of A_B. To recover the periodic mode shapes of MBC modes, the inverse transform on the eigenvectors must be performed

$$X_j(t) = B(t) V_j, \tag{1.51}$$

with V_j the j–th MBC eigenvector (also the j–th row of V_B). Finally, from the system matrices at one time instant t, it is possible to compute the MBC modes.

1.5.6 Example: MBC modes for rotor edge bending dynamics

Among all the MBC modes, a rotating wind turbine is characterized by three MBC modes of the first edge-bending, namely the backward, forward and collective, with their corresponding mode shapes in Figure 1.11. The specificity of backward and forward modes is that the corresponding frequency seen on the tower is not the same as the one seen on the rotor. The cause of this change of frequency will be presented by expressing the reaction forces due to the bending of the blades in the non-rotating frame using the disposition displayed in Figure 1.12.

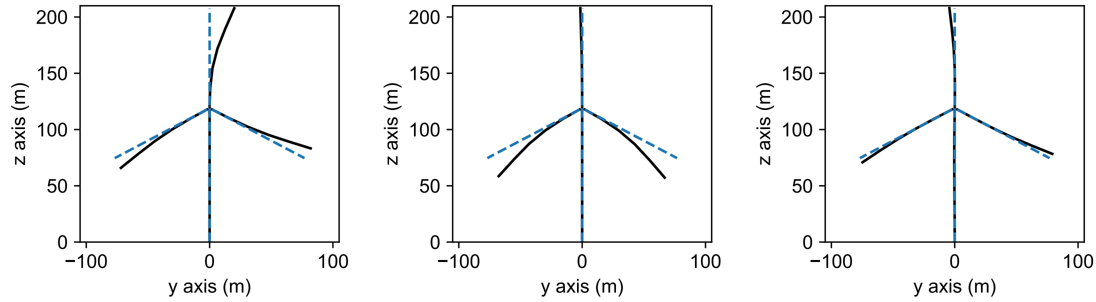

(a) Backward edge (b) Forward edge (c) Collective edge

Figure 1.11 – Mode shapes of the first edge bending modes, after the inverse MBC transformation, - - -:= undeformed wind turbine, —:= mode shape

Backward edge The Backward edge can be characterized by the phase shift between the bending of the blades, coming from the inverse transform of the MBC eigenvectors (Equation (1.51) and explained in [63]). With this mode, the bending of the second blade is late compared to the bending of the first, with a phase shift of $\frac{2\pi}{3}$. Then, the bending of the third blade is also late compared to the second, with also a phase shift of $\frac{2\pi}{3}$, which is equivalent to a phase shift $\frac{4\pi}{3}$ or $\frac{-2\pi}{3}$ with the bending of the first blade. Considering those phase shifts, the reaction force

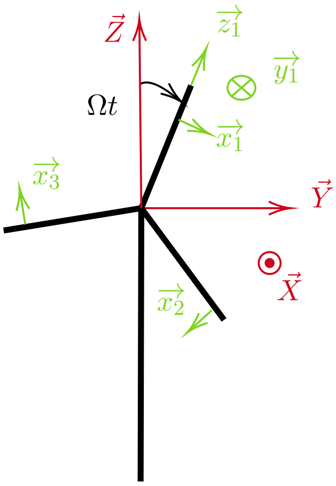

Figure 1.12 – Scheme of different bases in a wind turbine geometry

in the non-rotating frame for an isotropic rotor is

$$\vec{F}_{bck\ r} = A_{bck}\cos(\omega_{bck}t)\vec{x}_1 + A_{bck}\cos(\omega_{bck}t+\frac{2\pi}{3})\vec{x}_2 + A_{bck}\cos(\omega_{bck}t-\frac{2\pi}{3})\vec{x}_3, \tag{1.52}$$

where A_{bck} is the amplitude of the reaction for each blades and ω_{bck} the frequency of the backward edge on the rotor. From this equation, the reaction force in the non-rotating frame is

$$\vec{F}_{bck\ r} = A_{bck}\begin{cases} \cos(\omega_{bck}t)\cos(\Omega t)+\cos(\omega_{bck}t+\dfrac{2\pi}{3})\cos(\Omega t+\dfrac{2\pi}{3}) & \\ \qquad +\cos(\omega_{bck}t-\dfrac{2\pi}{3})\cos(\Omega t-\dfrac{2\pi}{3}) & \left(\vec{Y}\right) \\ \cos(\omega_{bck}t)\sin(\Omega t)+\cos(\omega_{bck}t+\dfrac{2\pi}{3})\sin(\Omega t+\dfrac{2\pi}{3}) & \\ \qquad +\cos(\omega_{bck}t-\dfrac{2\pi}{3})\sin(\Omega t-\dfrac{2\pi}{3}) & \left(\vec{Z}\right) \end{cases}. \tag{1.53}$$

Using trigonometric formulas, it can be simplified as

$$\vec{F}_{bck\ r} = A_{bck}\begin{cases} \dfrac{3}{2}\cos((\omega_{bck}-\Omega)t) & \left(\vec{Y}\right) \\ -\dfrac{3}{2}\sin((\omega_{bck}-\Omega)t) & \left(\vec{Z}\right) \end{cases}. \tag{1.54}$$

Consequently the frequency of the reaction force is $\frac{\omega_{bck}-\Omega}{2\pi}$.

Studying the reaction moment, it can be concluded that it is null, as $\cos(x)+\cos(x+\frac{2\pi}{3})+\cos(x+\frac{-2\pi}{3})=0,\ \forall\ x\in\ \mathbb{R}$. Thus, the frequency of the reaction of the bending corresponding to the backward edge in the tower is $\frac{\omega_{bck}-\Omega}{2\pi}$, which corresponds to what is obtained with the MBC transformation [63].

Forward edge Analogously to the Backward edge, the bendings of the blade of the Forward edge are out of phase. Where the bending of the second blade is in advance of the bending of the first, with a phase shift of $\frac{-2\pi}{3}$. And the bending of the third blade is in advance of the bending of the second, the phase shift to the bending of the first blade is $\frac{2\pi}{3}$. Thus, the reaction force corresponding to the blades bending in the rotational frame is

$$\vec{F}_{fw\ r} = A_{fw}\cos(\omega_{fw}t)\vec{x}_1 + A_{fw}\cos(\omega_{fw}t - \frac{2\pi}{3})\vec{x}_2 + A_{fw}\cos(\omega_{fw}t + \frac{2\pi}{3})\vec{x}_3, \tag{1.55}$$

where A_{fw} is the amplitude of the reaction for each blades and ω_{bck} the frequency of the forward edge on the rotor. For the forward edge, the phase shift are the opposite of the backward edge. From this equation, the reaction force in the non-rotating frame is

$$\vec{F}_{fw\ r} = A_{fw}\begin{cases}\cos(\omega_{fw}t)\cos(\Omega t) + \cos(\omega_{fw}t - \frac{2\pi}{3})\cos(\Omega t + \frac{2\pi}{3}) \\ \qquad + \cos(\omega_{fw}t + \frac{2\pi}{3})\cos(\Omega t - \frac{2\pi}{3}) & \left(\vec{Y}\right) \\ \cos(\omega_{fw}t)\sin(\Omega t) + \cos(\omega_{fw}t - \frac{2\pi}{3})\sin(\Omega t + \frac{2\pi}{3}) \\ \qquad + \cos(\omega_{fw}t + \frac{2\pi}{3})\sin(\Omega t - \frac{2\pi}{3}) & \left(\vec{Z}\right)\end{cases}. \tag{1.56}$$

Using trigonometric formulas, it can be simplified as

$$\vec{F}_{fw\ r} = A_{fw}\begin{cases}\frac{3}{2}\cos((\omega_{fw} + \Omega)t) & \left(\vec{Y}\right) \\ \frac{3}{2}\sin((\omega_{fw} + \Omega)t) & \left(\vec{Z}\right)\end{cases}. \tag{1.57}$$

Consequently the frequency of the reaction force is $\frac{\omega_{fw}+\Omega}{2\pi}$.

Once again, studying the reaction moment, it can be concluded that it is null. Thus, the frequency of the reaction of the bending corresponding to the forward edge in the tower is $\frac{\omega_{fw}+\Omega}{2\pi}$, which again, corresponds to what is obtained with the MBC transformation [63].

Collective edge Finally, the Collective edge is the mode where the blades are bending in phase, so, there is no phase shift between the bendings. Consequently, the reaction force of the bending of the blade corresponding to the collective edge is

$$\vec{F}_{col\ r} = A_{col}\cos(\omega_{col}t)\vec{x}_1 + A_{col}\cos(\omega_{col}t)\vec{x}_2 + A_{col}\cos(\omega_{col}t)\vec{x}_3, \tag{1.58}$$

where A_{col} is the amplitude of the reaction for each blades and ω_{col} the frequency of the collective edge on the rotor. Expressed in the non-rotating frame

$$\vec{F}_{col_r} = A_{col}\begin{cases}\cos(\omega_{col}t)\cos(\Omega t) + \cos(\omega_{col}t)\cos(\Omega t + \frac{2\pi}{3}) + \cos(\omega_{col}t)\cos(\Omega t - \frac{2\pi}{3}) & \left(\vec{Y}\right) \\ \cos(\omega_{col}t)\sin(\Omega t) + \cos(\omega_{col}t)\sin(\Omega t + \frac{2\pi}{3}) + \cos(\omega_{col}t)\sin(\Omega t - \frac{2\pi}{3}) & \left(\vec{Z}\right)\end{cases}, \tag{1.59}$$

leading to

$$\vec{F}_{col_r} = A_{col}\begin{cases}0 & \left(\vec{Y}\right) \\ 0 & \left(\vec{Z}\right)\end{cases} \tag{1.60}$$

Thus, the reaction force is null.

By expressing the reaction moment in the rotating and then in the non-rotating frame

$$\vec{M}_{col\ r} = M_{col}\cos(\omega_{col}t)\vec{y}_1 + M_{col}\cos(\omega_{col}t)\vec{y}_2 + M_{col}\cos(\omega_{col}t)\vec{y}_3 \tag{1.61}$$

$$= 3M_{col}\cos(\omega_{col}t)\vec{X}. \tag{1.62}$$

So the reaction moment of the blades for the collective edge has the same frequency on the tower as on the rotor, which again, corresponds to what is obtained with the MBC transformation.

Finally, with the simple analysis of the reactions of the edge bending modes of the rotor, it has been demonstrated why the frequency are not the same looking at the tower or the rotor. Also, it has been shown why the three edge bending modes does not have the same change of frequency between the tower and the rotor.

1.5.7 Equivalence MBC-Floquet

In [119], it has been proven that the modes computed with the Floquet theory are identical to the modes computed with the MBC transform for a system with an isotropic rotor. In this example, the academic model of wind turbine is used to show again the equivalence between the two approaches.

One way to compare the Floquet modes and the MBC modes is to compare the eigenvalues and the associated periodic mode shapes obtained with each method. As the imaginary part of the eigenvalue is undetermined (Equation (1.25)), the integer k should be identical between the two methods. But, if the eigenvalues are changed, then the periodic mode shapes must also be changed. Using Equation (1.36), the new periodic mode shape due to the addition of $k\Omega$ on the imaginary part of the j–th eigenvalue is

$$\tilde{X}_j(t) = X_j(t)\exp\left(-ik\Omega t\right), \tag{1.63}$$

with $\tilde{X}_j(t)$ the new periodic mode shape associated with the new eigenvalue $\tilde{\lambda}_j = \lambda_j + ik\Omega$.

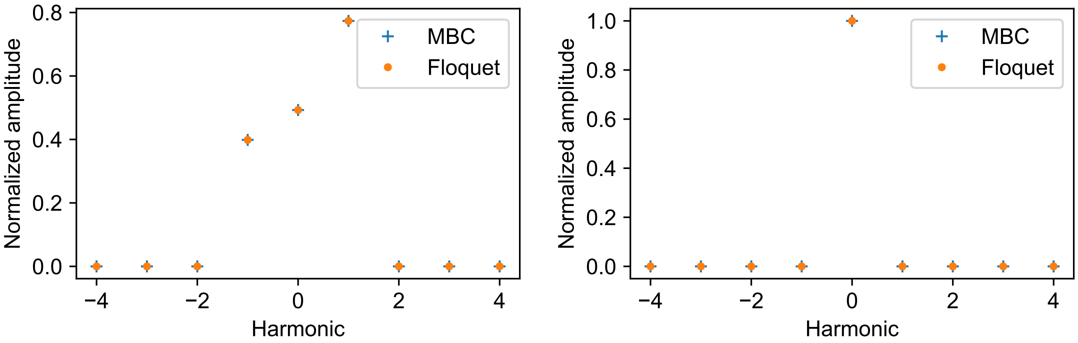

(a) First Floquet mode

(b) Fourth Floquet mode

Figure 1.13 – Comparison of normalized Fourier transforms of periodic mode shapes computed with different methods, academic model of wind turbine

To compare two periodic mode shapes, a way is to compare their normalized Fourier transforms. Figure 1.13 the normalized Fourier transforms of two Floquet modes of the academic model of wind turbine presented previously, computed with the MBC and the Floquet method.

For all the Floquet modes, the mean gap between the Fourier transforms is lower than 10^{-5}, which might be the consequence of the integration error during the computation of $\Phi(t)$. Comparing the eigenvalues, the relative gap has an order of magnitude lower than 10^{-8}.

Then the same study is performed but with a model where the stiffness of one blade is reduced by 1%, the mean gap between the Fourier transforms is around 10^{-4} for some Floquet modes, and the relative gap between the eigenvalues is also around 10^{-4} for some Floquet modes. So, there is an increase in the gap between the periodic modes shapes and the eigenvalues computed with the Floquet method or the MBC method.

From this example, it can be concluded that for an isotropic rotor, the Floquet modes obtained from the Floquet theory or by the MBC transformation are the same. Consequently, for a system with an isotropic rotor, the Floquet modes can be computed using the MBC transformation, which is easier compare to computing them using the Floquet theory, as it is not needed to perform a time integration with the MBC transformation. However, for a system with an anisotropic rotor, the only choice is to use the Floquet theory.

1.5.8 Floquet modes computation with *OpenFAST*

For a model of a wind turbine on *OpenFAST*, it is possible to compute the Floquet modes of the structure. To begin, let us start with the MBC approach, as it was done in [13] on a model of the NREL 5MW wind turbine. The first step is to obtain the matrices $A(t)$ and $C(t)$ (Defined in Equation (1.15)). In *OpenFAST* it is possible to linearize the equations around an operating point, with the theory described in [75]. To perform the linearization, the wind turbine will be simulated under a constant wind speed (so with a constant rotational speed), then after the stabilization of the wind turbine (around 10 to 25 periods/rotations), the linearization can be computed, which gives the matrices $A(t)$ and $C(t)$ at the time step of linearization. Then from the matrix $A(t)$ the MBC/Floquet modes can be estimated using the methods defined in Section 1.5.5. To have the periodic mode shapes defined as

$$Y_j(t) = C(t)X_j = C(t)B(t)V_j, \tag{1.64}$$

it is needed to compute the observation matrix ($C(t)$) along a period, so along a rotor rotation. Also to have a better estimation of the eigenmodes the mean matrix A_B can be computed using several linearizations, for example, the ones used for the computation of C(t).

As said before, if the rotor is anisotropic the MBC method can not be used to compute the Floquet modes of a wind turbine. To compute the Floquet modes, the fundamental matrix is needed, so, as described in Section 1.5.4 it is needed to solve the differential Equation (1.22) for different initial conditions. To do so, still using the *OpenFAST* linearization, the matrix $A(t)$ has to be computed along a discretized period. Then, with those matrices, a time integration method such as Euler or Runge-Kutta can be used. Then, the method described in Section 1.5.4 can be used. Finally, the periodic mode shape associated with the Floquet modes can be computed using the matrices $C(t)$ obtained conjointly with $A(t)$. Another method has been defined in [113], where the exponential integrator is used.

1.6 Conclusion

In this Chapter, first, wind turbine basics have been described, and the common faults of a wind turbine rotor have been presented. Then, the two wind turbine model used in the thesis have been defined. To finish, the modal analysis of the wind turbine has been defined, with the different methods available, one using the Floquet theory and the other using the MBC transformation. The modal analysis of wind turbines modeled as linear time periodic systems gives us an overview of the specificities of such systems and the difference in the dynamical behavior compared to the linear time invariant systems.

The next part of the state of the art is dedicated to operational modal analysis of wind turbines, which is the main subject of this thesis. First, the operational modal analysis for invariant systems (civil engineering structures for example) is introduced, with a description of the stochastic subspace identification method and the presentation of the associated uncertainty computation method. Secondly, operational modal analysis dedicated to wind turbines is presented, with the main existing methods. Then, a damage detection and localization method for time invariant system is defined. Finally, fault detection for wind turbine rotors is introduced, with an overview of the existing method to detect those faults.

Chapter 2

OPERATIONAL MODAL ANALYSIS AND FAULT DETECTION

Abstract

In this second part of the state of the art, the Operational Modal Analysis methods used for invariant systems (civil engineering structures for example) are presented first, to understand how the modal parameters are retrieved from the signal. The Stochastic Subspace Identification (SSI) covariance-driven method used in this thesis is especially detailed, with the associated uncertainty quantification of identified parameters. It is shown that the assumptions of those methods cannot be respected when they are used for the identification of wind turbines. Then, a review of the Operational Modal Analysis methods designed for operating wind turbines points out that they all have drawbacks and cannot be used for real structures. Consequently, it will be required to define a new approach. To finish, as one of the objectives of the thesis is to perform damage detection, a state-of-the-art damage detection method based on identification results is presented, namely the stochastic subspace-based damage detection and localization. Also, a brief review of the damage detection method of wind turbine rotors is presented, showing that many methods have been developed for pitch and mass imbalance detection, but only a few methods exist for the detection of changes in blade stiffness.

2.1 Introduction

The second part of the state of the art is dedicated to operational modal analysis of wind turbines, which is the main focus of this thesis. First, the operational modal analysis for invariant systems (civil engineering structures for example) is introduced, with a description of the stochastic subspace identification method and the presentation of the associated uncertainty computation method. Secondly, operational modal analysis dedicated to wind turbines and rotating structures is presented, with a brief review of the existing methods. Then, a damage detection and localization method for time invariant system using the operational modal analysis framework is defined. Finally, fault detection for wind turbine rotors is introduced, with an overview of the faults that can occur and the existing method to detect those faults.

2.2 Operational Modal Analysis (OMA) for LTI systems

In the previous Chapter, the modal analysis of the linear time invariant and time periodic systems has been presented. The modal analysis gives us information on the dynamic of the studied system, but how can it be possible to retrieve that information on a real structure? To do so, the Experimental Modal Analysis (EMA) [115, 47] is wildly employed since decades and used in many fields such as on an aircraft [15] or on a wind turbine blade [35]. With those methods, the modal parameters of the structure are estimated using the loads and a few measurements of the structure. Where the measurements of the structure dynamics can be accelerations, velocities, displacements, or strains for the civil engineering structures.

However, those methods require to apply and measure the loads/inputs and it is not always possible to apply/measure them especially on operating structures. So, Operational Modal Analysis (OMA) method, also called output-only modal analysis, aims to estimate the modal parameters of a system based on the outputs of a structure under ambient excitation sources such as wind, traffic, and waves.

There are two classes of OMA methods, namely methods in the time domain and methods in the frequency domain. The reader can refer to [17] for an introduction to those methods and to [105] for a complete review. For the frequency domain methods, the simplest method is the peak picking on the Fourier transform, where the eigenmodes of the studied system are identified with the peaks of the Fourier transform of the outputs, with the frequency of the eigenmodes corresponding to the frequency of the peaks and the mode shape is the amplitude of the Fourier transform. The method has been extended to multiple measurements with the Frequency Domain Decomposition (FDD) [18], using the Singular Value Decomposition of the Power Spectral Density. Other frequency domain methods retrieve the system modal parameters based on a fitting of a common denominator model to the Frequency Response Function (FRF), such that the Least-Squares Complex Frequency (LSCF) domain method [60] or the Polymax method [100]. In the time domain identification methods, there are many subspace methods that originate from the system identification field in automatic control. Such as the Eigensystem Realization Algorithm (ERA) [76], converted into the Natural Excitation Technique (NExT) method [68] and the Stochastic Subspace Identification (SSI) [135, 99, 134] that identifies the studied system as a state-space from the outputs. Two main versions of the SSI method exist, the SSI data-driven based and the SSI covariance-driven (often name SSI-cov). Both versions are based on the same theory, but they differ in the estimation of the system matrices. The SSI data-driven uses the definition of the Kalman filter state to retrieve the system matrices from the outputs whereas the SSI-covariance driven uses the correlations.

The OMA methods has been used in many fields, especially in civil engineering. Indeed, since civil engineering structures are large, it is not possible to measure the external loading, making OMA methods particularly relevant. Many applications of subspace methods applied to bridges [109, 39, 17] or pylons [99, 108] can be found in the literature. Moreover, OMA is also used in industry, as with the software *ARTeMIS Modal* of the company *Structural Vibration solution*, to carry out OMA with the FDD method and the SSI method.

Finally, OMA methods rely on several assumptions regarding the statistical properties of the excitation and the properties of the structure being identified. These assumptions will be detailed in the next paragraph. Then, the subspace method called Stochastic Subspace identification (SSI) used for this thesis will be presented. So, a method that estimated the uncertainty of the identified modes from the empirical uncertainties of the correlations is introduced.

2.2.1 Classical OMA assumptions

Since the loading is unknown, its form must be assumed. In the OMA formalism, the loading is considered as a white noise of zero mean and uncorrelated. This assumption is necessary to remove the impact of the load in the identification results (Equation (2.8)). However, for real structures, the load is never a real white noise. For example, in a wind turbine the main load is the wind. But as the spectra of the wind are almost flat, it can be approximated as a white noise [138]. However, as a wind turbine rotor is rotating, the spectrum of a blade load is no more flat, with peaks with frequencies related to the rotational speed [127]. But if a harmonic is in the load spectra, it will be identified as a system eigenmode jointly with the system eigenmodes. To deal with this problem, it exists many methods to remove harmonics in signal, with a method defined for subspace method in [54]. Moreover, in [12], it is demonstrated that the estimation of the modal parameters with a subspace method is consistent for the identification of a system under non-stationary noise excitation.

Another assumption concerns the behavior of the system: indeed, it is considered as a linear time invariant. This important assumption is used to retrieve the eigenmodes of the studied system. However, an invariant system can be non-linear but it can be supposed as linear if it behaves around an operating point. So, for an operating wind turbine modeled as a time periodic system, the identified eigenmodes will not correspond to the Floquet modes. So, the method can not retrieve these modal parameters from the outputs.

2.2.2 Stochastic Subspace Identification (SSI)

In this thesis, the SSI covariance-driven is used, with a Hankel matrix defined as a product of the matrix gathering the outputs (see Equation (2.14)). This particular method is used as the eigenmodes are estimates using only the outputs correlations. Also, this method can be used conjointly with related methods, such that an efficient computation method [41], an uncertainty computation [40], and a damage detection method [11].

Let an LTI system be defined by the quadruplet of matrices (A_c, B_c, C, D), evolving under a stationary Gaussian white noise excitation $v(t)$

$$\begin{cases} \dot{x}(t) = A_c x(t) + B_c v(t) \\ y(t) = C x(t) + D v(t) \end{cases} . \tag{2.1}$$

With $x(t) \in \mathbb{R}^n$ and $y(t) \in \mathbb{R}^r$. The solution of the system is

$$x(t) = \exp\left(A_c t\right) x_0 + \int_0^t \exp\left(A_c(t-\tau)\right) B_c v(\tau) d\tau. \tag{2.2}$$

Subspace methods exploit only outputs, so it is needed to express the system as a discrete time state-space. Considering the time step of the output Δt with the discrete time state vector x_k (with $k = \frac{t}{\Delta t}$), the solution of the system at a discrete time instant k is

$$x_k = \exp\left(A_c k \Delta t\right) x_0 + \sum_{i=1}^{k} \int_{(i-1)\Delta t}^{i\Delta t} \exp\left(A_c(k\Delta t - \tau)\right) B d\tau v_{i-1}, \tag{2.3}$$

considering the zero-order hold hypothesis on the load. Then, it is possible to express the state vector at the index $k+1$ as a function of x_k

$$x_{k+1} = \exp\left(A_c \Delta t\right) x_k + \int_{k\Delta t}^{(k+1)\Delta t} \exp\left(A_c((k+1)\Delta t - \tau)\right) B_c d\tau v_k. \tag{2.4}$$

Finally, the full discrete state-space can be expressed

$$\begin{cases} x_{k+1} = Ax_k + B\mathbf{v}_k \\ \quad y_k = Cx_k + D\mathbf{v}_k \end{cases}, \tag{2.5}$$

with $A = \exp(A_c\Delta t)$ and $B = \int_0^{\Delta t} \exp\left(A_c(\Delta t - \tau)\right) B_c d\tau {=} \left(A - I\right) A_c^{-1} B_c$.

The SSI [135] aims to identify the eigenmodes of the system through the sample correlations. The first step is to construct a Hankel matrix filled by correlations. A correlation matrix can be expressed as a function of the system matrices, with

$$\begin{aligned} R_i &= \mathbb{E}\left(y_{k+i} y_k^T\right) && (2.6)\\ &= \lim_{N\to\infty} \frac{1}{N} \sum_{k=0}^{N-1} \left(y_{k+i} y_k^T\right) && (2.7)\\ &= \lim_{N\to\infty} \frac{1}{N} \sum_{k=0}^{N-1} \left(\left(Cx_{k+i} + Dv_{k+i}\right) y_k^T\right), && (2.8) \end{aligned}$$

where v_k is independent of the past and is a Gaussian process of zero mean, consequently $\lim\limits_{N\to\infty} \frac{1}{N}\sum_{k=0}^{N-1}\left(Dv_{k+i}y_k^T\right) = 0$, for $i > 0$. Let us express x_{k+i} function of x_{k+1}

$$R_i = \lim_{N\to\infty} \frac{1}{N} \sum_{k=0}^{N-1} \left(\left(CA^{i-1}x_{k+1} + \sum_{j=1}^{i-1} A^{j-1} B v_{k+i-j}\right) y_k^T\right). \tag{2.9}$$

Analogously as before

$$\begin{aligned} R_i &= \lim_{N\to\infty} \frac{1}{N} \sum_{k=0}^{N-1} \left(\left(CA^{i-1}x_{k+1}\right) y_k^T\right) && (2.10)\\ &= CA^{i-1}G, && (2.11) \end{aligned}$$

with

$$\begin{aligned} G &= \lim_{N\to\infty} \frac{1}{N} \sum_{k=0}^{N-1} \left(x_{k+1} y_k^T\right) && (2.12)\\ &= A\Sigma C^T + S. && (2.13) \end{aligned}$$

Where the covariance matrix of the state vector $\Sigma = \mathbb{E}\left(x_k x_k^T\right) = A\Sigma A^T + Q$ is defined by a Lyapunov equation and $S = \mathbb{E}\left(Bv_k v_k^T D^T\right)$ and $Q = \mathbb{E}\left(Bv_k v_k^T B^T\right)$ function of the covariance matrix of the input.

From the previous equations, it is clear that the correlations of the outputs depend on the system matrices A and C, which contain the modal parameters of the studied system. So, the objective of the method is to estimate the matrices A and C from the Hankel matrix of the correlations. The Hankel matrix can be constructed directly from matrices gathering the data

$$\hat{H} = \mathcal{Y}^{+} \left(\mathcal{Y}^{-}\right)^{T}. \tag{2.14}$$

Where $\mathcal{Y}^{+} \in \mathbb{R}^{(p+1)r \times N}$ and $\mathcal{Y}^{-} \in \mathbb{R}^{qr \times N}$ such that

$$\mathcal{Y}^{+} = \frac{1}{\sqrt{N}} \begin{bmatrix} y_{q+1} & y_{q+2} & \cdots & y_{q+N} \\ y_{q+2} & y_{q+3} & \cdots & y_{q+N+1} \\ \vdots & \vdots & \ddots & \vdots \\ y_{q+p+1} & y_{q+p+2} & \cdots & y_{q+p+N} \end{bmatrix} \text{ and } \mathcal{Y}^{-} = \frac{1}{\sqrt{N}} \begin{bmatrix} y_{q} & y_{q+1} & \cdots & y_{q+N-1} \\ y_{q-1} & y_{q} & \cdots & y_{q+N-2} \\ \vdots & \vdots & \ddots & \vdots \\ y_{1} & y_{2} & \cdots & y_{N} \end{bmatrix}. \tag{2.15}$$

p and q are the size parameters of the Hankel matrix with often $p+1=q$ to have a square matrix. Those parameters have to be set regarding the model order of the identified system, or the number of eigenmodes that can be identified in the studied frequency range. $\hat{H}$ can be seen as the Hankel matrix filled with the estimate of correlations $\hat{R}_i$,

$$\hat{H} = \begin{bmatrix} \hat{R}_1 & \hat{R}_2 & \dots & \hat{R}_q \\ \hat{R}_2 & \hat{R}_3 & \dots & \hat{R}_{q+1} \\ \vdots & \vdots & \ddots & \vdots \\ \hat{R}_{p+1} & \hat{R}_{p+2} & \dots & \hat{R}_{p+q} \end{bmatrix}. \tag{2.16}$$

The Hankel matrix can be factorized such that $\hat{H} = O_p C_q$, where O_p denotes the observability matrix and C_q the controllability matrix, with $\hat{G}$ a consistent estimate of G.

$$O_p = \begin{bmatrix} C \\ CA \\ \vdots \\ CA^{p} \end{bmatrix} \text{ and } C_q = \begin{bmatrix} \hat{G} & A\hat{G} & \dots & A^{q-1}\hat{G} \end{bmatrix}. \tag{2.17}$$

In the LTI case, O_p is full column rank and C_q is full row rank. The observability matrix is obtained from a thin singular value decomposition of $\hat{H}$ and its truncation at the correct model order n

$$\hat{H} = USV^{T} = \begin{bmatrix} U_1 & U_2 \end{bmatrix} \begin{bmatrix} S_1 & 0 \\ 0 & S_2 \end{bmatrix} \begin{bmatrix} V_1^{T} \\ V_2^{T} \end{bmatrix}, \tag{2.18}$$

$$O_p = U_1 S_1^{1/2}, \tag{2.19}$$

where S_1 contains the first n singular values and U_1 the n first columns of U.

Then, the observation matrix C is identified as the first block row of O_p and the state transition matrix A is identified in a least-squares sense

$$A = O_{p\ (1:p)}^{\dagger} O_{p\ (2:p+1)}, \tag{2.20}$$

with $O_{p\ (1:p)}$ the first p blocks rows of O_p, $O_{p\ (2:p+1)}$ the p last blocks rows and $(\cdot)^{\dagger}$ denotes the Moore-Penrose pseudo inverse. Then, the eigenmodes can be computed with the eigenvalue decomposition of A

$$A = \Psi \left[\lambda_i\right] \Psi^{-1}. \tag{2.21}$$

The continuous time eigenvalues μ_i are found from the discrete time eigenvalues λ_i by

$$\mu_i = \frac{\log(\lambda_i)}{\Delta t}. \tag{2.22}$$

Then the frequency (f_i in Hz) and the damping (ξ_i in %) of the associated mode are defined such that

$$f_i = \frac{|\mu_i|}{2\pi} \quad \text{and} \quad \xi_i = -100.\frac{\Re\left(\mu_i\right)}{|\mu_i|}. \tag{2.23}$$

The observed mode shape matrix is found from

$$\Phi = C\Psi. \tag{2.24}$$

Finally, from the outputs, it is possible to identify the eigenmodes of the underlying system that can be identified with the selected sensors. There is also a variant with an efficient computation [41] based on the QR decomposition of the observability matrix, which is used for the rest of the thesis. Now let us present some applications on real structures and the uncertainty quantification of the identified modes.

One of the challenges of the method is to asses the system order n, as it is not necessarily known, especially for real structures where the system order depends on the number of DOF which is infinite theoretically. In the method, the system order corresponds to the number of eigenmodes that the signal contains, but some identified eigenmodes can correspond to the noise/inputs. The eigenmodes of the noise can be detected by their damping value that can be negative (a stable system has all its eigenvalues with positive damping), also those eigenmodes depend on the value of the system order.

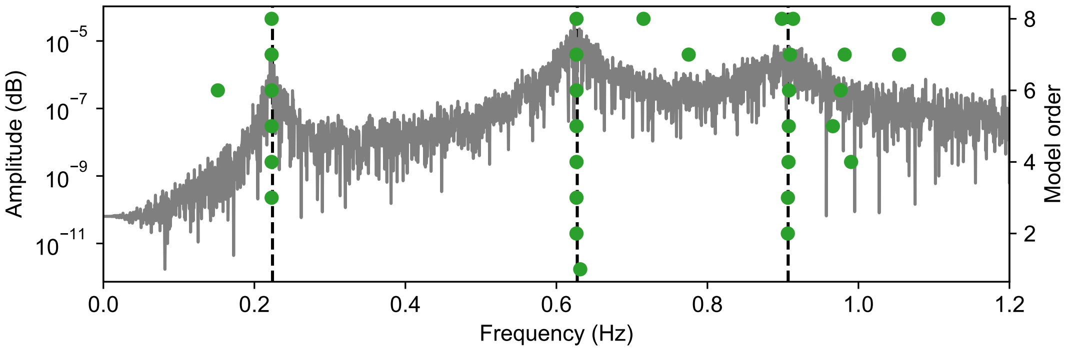

Figure 2.1 – Example of stabilization diagram, from an identification of a 3 DOF mass-spring model- (- - -): theoretical frequencies - (●): identified frequencies

To determine the order of the system, a stabilization diagram is used [99], where the eigenmodes are computed for different model orders. An example of a stabilization diagram is given in Figure 2.1, obtained from the identification of a simple 3 DOF mass-spring model, conjointly with the PSD of one DOF. One can see that the peaks of the PSD are corresponding to alignments of frequencies of identified modes. So, with the stabilization diagram, the eigenmodes of the system are detected with the alignments. Thus, at $n = 3$ (the theoretical model order) the three identified eigenmodes are corresponding to the system eigenmodes. But as the model order increases, other eigenmodes are identified, see 0.18 Hz at order 6 and 0.7 at order 7 for example. They are corresponding to the noise. But they can be detected as they are not stable as the model order increases, in contrast to the system eigenmodes. Also, the eigenmodes corresponding to the noise can be detected and removed from the stabilization diagram using the associated uncertainties, as they are much more uncertain than the eigenmodes of the structure.

2.2.3 Uncertainty quantification

The identification of structural modes with OMA is based on a stochastic modeling, so identified modes are uncertain. Consequently, it can be an added value to estimate the associated uncertainties of an identified mode during the monitoring of the structure.

The objective of the method is to compute the uncertainties of frequency, damping, and mode shape of the modes identified from the collected data with a subspace method. The uncertainty computation method is introduced in [108] using the first-order delta method, with an application to a real structure in [107]. This method can be used with input-output and output-only subspace methods [83, 84] and has been applied to different real structures [39, 108]. For all the applications during the present thesis, an efficient version presented in [40] is used. In this section, some key points of the method are presented.

Consider X and Y two matrices, with $X = f(Y)$. The distribution of the estimation Y ($\hat{Y}$), resp. of X ($\hat{X}$), follow a Gaussian process. Let us consider that $\hat{X}$ is close enough to X such that $\Delta X = \hat{X} - X$ expresses a small perturbation of X (similarly with Y). Using the first-order Taylor approximation, the definition of the perturbation ΔX is

$$\mathrm{vec}(\Delta X) = \mathcal{J}_{X,Y}\mathrm{vec}(\Delta Y) + o(\Delta Y). \tag{2.25}$$

where $\mathrm{vec}(x)$ denotes the vectorization of the matrix x and $\mathcal{J}_{X,Y} = \frac{\partial \mathrm{vec}(X)}{\partial \mathrm{vec}(Y)}$ is the sensitivity of X in relation to a change in Y.

Now, let us express the covariance matrix of $\hat{X}$ (Σ_X)

$$\Sigma_X = \frac{1}{n-1}\sum_{j=1}^{n}\left(\hat{X}_j - X\right)\left(\hat{X}_j - X\right)^T \tag{2.26}$$

$$= \frac{1}{n-1}\sum_{j=1}^{n}\mathrm{vec}\left(\Delta X\right)_j \mathrm{vec}\left(\Delta X\right)_j^T . \tag{2.27}$$

Then, using Equation (2.25)

$$\Sigma_X = \frac{1}{n-1}\sum_{j=1}^{n}\mathcal{J}_{X,Y}\mathrm{vec}\left(\Delta Y\right)_j \mathrm{vec}\left(\Delta Y\right)_j^T \mathcal{J}_{X,Y}^T. \tag{2.28}$$

Finally, the covariance matrix of X is expressed as

$$\Sigma_X = \mathcal{J}_{X,Y}\Sigma_Y\mathcal{J}_{X,Y}^T, \tag{2.29}$$

where Σ_Y is the covariance matrix of Y. This formula can be retrieved using the delta method [95]. With this idea illustrated in Figure 2.2, a perturbation on the correlations can be transported to the identified mode parameters.

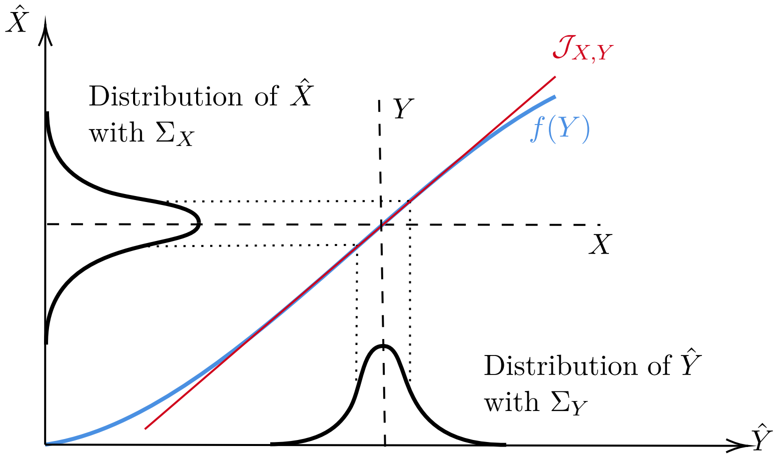

Figure 2.2 – Illustrative example of the uncertainty propagation, based on the original figure in [53]

To compute the uncertainties of the identified parameters computed with the SSI-cov, the covariance matrix of the Hankel matrix is needed. In [40], using the formula of the variance of the sample mean, the estimation of the covariance matrix of the Hankel matrix of correlations is defined as

$$\hat{\Sigma}_H = \frac{1}{n_b(n_b-1)} \sum_{j=1}^{n_b} \left(h_j - \bar{h}\right) \left(h_j - \bar{h}\right)^T . \tag{2.30}$$

where h_j is the vectorized Hankel matrix computed with the j–th of n_b block of data and $\bar{h}$ the vectorized mean Hankel matrix. The Hankel matrix is filled of estimations of correlations, so from the central limit theorem, it can be described by a Gaussian process. So the covariance of the Hankel matrix is the start of the uncertainty computation, from this and the sensitivity of all the steps of the SSI, the covariance matrices of the identified modes can be computed,

$$\widehat{\mathrm{cov}}(f_i) = \mathcal{J}_{f_i,H} \hat{\Sigma}_H \mathcal{J}_{f_i,H}^T, \ \widehat{\mathrm{cov}}(\xi_i) = \mathcal{J}_{\xi_i,H} \hat{\Sigma}_H \mathcal{J}_{\xi_i,H}^T, \ \widehat{\mathrm{cov}}(\phi_i) = \mathcal{J}_{\phi_i,H} \hat{\Sigma}_H \mathcal{J}_{\phi_i,H}^T. \tag{2.31}$$

The sensitivities of the modal parameters regarding the Hankel matrix are obtained based on the mathematical operations performed in the SSI method (Equation (2.18) to Equation (2.24)). With all the steps to compute those sensitivities detailed in the aforementioned papers.

Once the uncertainties are computed for all the identified eigenmodes, they can be used to remove the eigenmodes of the noise in the stabilization diagram. In Figure 2.3, the stabilization diagram obtained with an identification of a 3 DOF mass-spring model is once again displayed, but this time the uncertainties of the identified eigenmodes are computed and only the eigenmodes with a relative standard deviation below 2.5% are displayed. Then compared to the stabilization diagram in Figure 2.1, only the alignments that are corresponding to the system eigenmodes remain. So, with the estimated uncertainties, the stabilization diagram has been "cleaned" of the noise eigenmodes. This example shows that the estimation of the uncertainties can be a helpful tool for system identification.

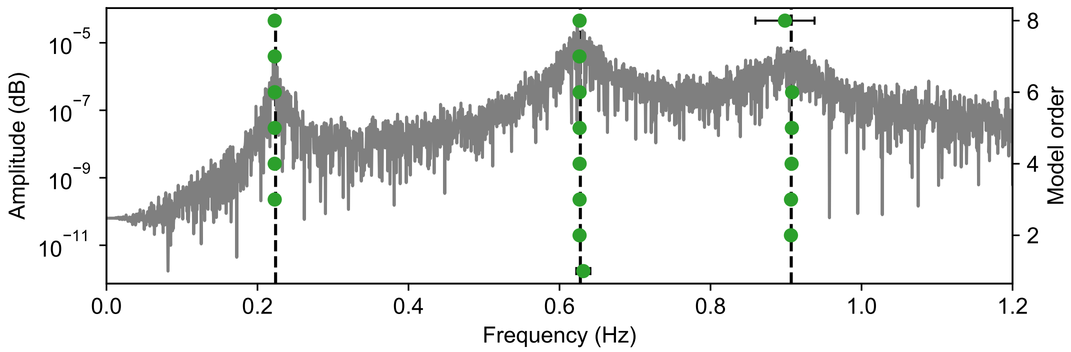

Figure 2.3 – Example of stabilization diagram, from an identification of a 3 DOF mass-spring model, with the estimation of the uncertainties- (- - -): theoretical frequencies - (●): identified frequencies and related standard deviations (error bars)

After performing an identification, it can be useful to compare the identified modes with references modes and quantify the uncertainty of this comparison. The Modal Assurance Criterion (MAC) [98] is a metric between 0 and 1, assessing the likelihood of two mode shapes being equal

$$MAC(\phi,\psi) = \frac{\left|\phi^H\psi\right|^2}{\left(\phi^H\phi\right)\left(\psi^H\psi\right)}. \tag{2.32}$$

The MAC criterion has boundaries, 0 and 1, as a consequence when the mean value of the MAC is near a boundary the criterion is not following a Gaussian law. In [58], where the uncertainty quantification of the MAC criterion is studied, this problem was treated with the use of inverse shifted chi-square distribution when the MAC criterion is near the upper boundary, i.e. when the mode shapes are equal. In this case, the first-order delta method can not be used, so a second order development is used to express the uncertainty of the MAC criterion. When the mode shapes are different, the MAC criterion is described with a Gaussian distribution, enabling the use of the first-order delta method.

The first-order delta method can be also used to compute the input and transfer matrix [56] for an input-output method and the Modal Phase Collinearity (MPC) of the identified mode shapes [55], and in general to all the quantities obtained from the identification of the modal parameters.

2.2.4 Conclusion

Now that the principles of OMA for LTI systems as well as some methods to obtain modal parameters and their uncertainties have been introduced, it has to be determined why the existing methods are not transferable to wind turbines and have a better understanding of what changes are needed to suit those methods for the identification of LTP systems.

2.3 OMA for wind turbine

Previous works have addressed the problem of OMA applied to wind power and rotating machines in general [117, 69, 34]. In parallel, other research works have treated the subject of LTP system identification for the control of wind turbines with input-output identification methods with the consideration of MIMO (Multiple Input Multiple Output) system [133] and [110].

To apply an OMA method to wind turbines, some assumptions must be verified. First, the loading must be an uncorrelated white noise. [127] showed with correlations of measurements on a blade that the loading is not a white noise. Indeed, the loading is a sum of a white noise and harmonics of the rotor rotation, which is not in agreement with the assumption. The second assumption is that the system must be linear and time invariant, but when a wind turbine is operational and the rotor is in motion, it behaves like an LTP system (see Section 1.5).

In this section, some OMA methods allowing to treat LTP systems are presented, but it is assumed that the loading follows the classic assumption of OMA methods. First, the main frequency domain method is presented. Second, two time domain methods are presented, one that pre-processes the data and one that is a modification of a subspace method.

2.3.1 Frequency domain method

To identify an LTP system, there is a method called the HPS method (Harmonic Power Spectrum) or HTF (Harmonic Transfer function) [3, 130, 111]. This approach was originally defined for control purposes in [142, 143], to create a map between the inputs and outputs of an LTP system. It is based on the Fourier transform and on a modulation of the measures.

Taking equation (1.29), it is possible to express each Floquet mode as an infinite sum of modes. To do this, the periodic mode shape of the modes is expressed in Fourier series.

$$x(t) = \sum_{m=-\infty}^{\infty} \sum_{j=1}^{n} X_{j,m} \exp\left(im\Omega t\right) \exp\left(\mu_j t\right) x_0. \tag{2.33}$$

By expressing the measure and performing a Fourier series decomposition of the observation matrix, one gets:

$$y(t) = C(t)x(t) = \sum_{j=1}^{n} C(t) X_j(t) \exp\left(\mu_j t\right) x_0 \tag{2.34}$$

$$= \sum_{l=-\infty}^{\infty} \sum_{j=1}^{n} Y_{j,l} \exp\left((\mu_j + il\Omega)t\right) x_0. \tag{2.35}$$

To study a periodically variable system of period $T = \frac{2\pi}{\Omega}$ with the HPS method, the measures are modulated with the harmonics of the rotation. The m^{th} modulated signal is given by:

$$y_m(t) = y(t) \exp\left(-im\Omega t\right), \tag{2.36}$$

with $i = \sqrt{-1}$. The Fourier transform of the modulated signals is defined as

$$Y(\omega) = \begin{bmatrix} \dots & y_{-1}(\omega)^T & y_0(\omega)^T & y_1(\omega)^T & \dots \end{bmatrix}. \tag{2.37}$$

Finally, analogous to a power spectrum of an LTI system, the Harmonic Power Spectrum is defined by:

$$S_{YY}(\omega) = \mathbb{E}\left(Y(\omega)Y(\omega)^H\right), \tag{2.38}$$

with $(\cdot)^H$ denotes the Hermitian transpose. Rewritten in term of eigenmodes:

$$S_{YY}(\omega) = \sum_{r=1}^{2N} \sum_{l=-\infty}^{\infty} \frac{\bar{C}_{r,l} W(\omega)_{r,l} \bar{C}_{r,l}^H}{\left[i\omega - (\mu_r - il\Omega)\right]\left[i\omega - (\mu_r - il\Omega)\right]^H}, \tag{2.39}$$

with all the terms involved defined in [3]. Thus, from the Equation (2.39), it can be seen that the power spectrum will have peaks at the Floquet exponents $(\mu_r - il\Omega)$.

This method allows the identification of the Fourier components of the Floquet modes of an LTP system, using the peak picking method or the Frequency Domain Decomposition (FDD) method. However, this method has the drawback of not giving the theoretical number of modulations needed for a proper identification, which does not make the method suitable for automation.

2.3.2 Subspace methods

As said in the introduction, it is not possible to apply a classical subspace method to an LTP system. Many methods have been implemented to adapt the classical subspace methods to the LTP system.

The first method developed consists in using the MBC transformation as a data pre-processing. It leads to the identification of the eigenmodes of the transformed systems, i.e the eigenvalues and eigenvectors of A_B in Equation (1.49). However the MBC transformation is defined with the assumption of isotropic rotors. In Section 2.3.4, it will be seen that this assumption is not valid for real applications.

Tcherniak proposes a pre-processing of the data before the application of a classical subspace method [130], the H-OMA-TD method (Harmonic OMA Time Domain), using results of the harmonic power spectrum method. In fact, the same modulation of the signal with the harmonics of the rotation is used, to then use a subspace method on the signal. However, this method suffer of the same drawbacks than the HPS method.

Finally, Jhinaoui proposes a modification of the SSI method, with an identification of the monodromy matrix of the system, called the SSI-LPTV method [71, 70]. This method identifies LTP systems without approximation and without assumptions on the shape of the state matrices. In the next section, this method is detailed, to understand how an LTP system can be fully identified and the resulting drawbacks of this identification technique.

2.3.3 SSI-LPTV method

First, let us define the Lyapunov-Floquet transformation that expresses the state vector as a time invariant system

$$x(t) = \Phi(t)e^{-Rt}z(t), \text{ with } \dot{z}(t) = Rz(t), \tag{2.40}$$

where $\Phi(t)$ is the fundamental matrix and $Q = \Phi(T)$ is the monodromy matrix and $R = \frac{1}{T}\log(Q)$. So the new expression of the state-space is

$$\begin{cases} \dot{z}(t) = Rz(t) + L(t)^{-1}w(t) \\ y(t) = \tilde{C}(t)z(t) + v(t) \end{cases} \tag{2.41}$$

with $L(t) = \Phi(t)\exp(-Rt)$ and $\tilde{C} = C(t)L(t)$.

Discretization

Let $t = k\Delta t$ with Δt be the time step of the measures, the discrete state system is then defined as:

$$\begin{cases} z_{k+1} = Fz_k + \tilde{w}_k \\ y_k = \tilde{C}_k + v_k \end{cases} \tag{2.42}$$

with $F = \exp(R\Delta t)$, $\tilde{C}_k = \tilde{C}(k\Delta t)$, $v_k = v(k\Delta t)$ and $\tilde{w}_k = \int_{k\Delta t}^{(k+1)\Delta t} \exp(Q(k+1)\Delta t - s) \left(L(s)^{-1}w(s)\right) ds$.

Parameters to identify

The objective is to identify the discrete exponents of Floquet (the eigenvalues of F)

$$\mu_i = \exp(\lambda\Delta t). \tag{2.43}$$

Then, the periodic eigenvectors must be identified. The vectors of the matrix F and of the matrix R are identical to ϕ_{λ_i}. Then the mode shapes are obtained with $\tilde{C}_k$:

$$\psi_{k,i} = \tilde{C}_k\phi_{\lambda_i}. \tag{2.44}$$

Construction of the Hankel matrix

In the same way as the SSI-cov method, the matrices of the system are identified from correlations, with the construction of a Hankel matrix (see Section 2.2.2). Let $T_d = \frac{T}{\Delta t}$ be the period of the discrete signal, with T the period of the system (the period must be known).

The variables z_{j+iT_d} and y_{j+iT_d} have the same dynamic behavior for the same j. Let us define the Hankel matrix of covariances for the sequence j:

$$\hat{H}^j_{p,q} = \frac{1}{N_T}\sum_{i=0}^{N_T-1} Y^+_{j+iT_d}(Y^-_{j+iT_d})^T, \tag{2.45}$$

where N_T is the number of discrete period in the signal, and

$$Y^+_{j+iT_d} = \begin{bmatrix} y^T_{j+iT_d} & \dots & y^T_{j+p+iT_d} \end{bmatrix} \text{ and } Y^-_{j+iT_d} = \begin{bmatrix} y^T_{j-1+iT_d} & \dots & y^T_{j-q+iT_d} \end{bmatrix}. \tag{2.46}$$

In the same way the covariance matrix with a lag time is defined:

$$\hat{H}_{p,q}^{j+1} = \frac{1}{N_T} \sum_{i=0}^{N_T-1} Y_{j+iT_d}^{+} (Y_{j+(i+1)T_d}^{-})^T. \tag{2.47}$$

Then, the global Hankel matrix is:

$$\hat{H}_{p,q} = \begin{bmatrix} \hat{H}_{p,q}^{j} \\ \hat{H}_{p,q}^{j+1} \end{bmatrix}. \tag{2.48}$$

Estimation of the observability matrix and the system matrices

Once the Hankel covariance matrix has been constructed, the observability matrix can be identified using an SVD:

$$\hat{H}_{p,q} = U_n S_n V_n^T \tag{2.49}$$

$$\hat{O}_p^j = U_n S_n^{\frac{1}{2}}. \tag{2.50}$$

The observability matrix is defined as:

$$O_p^j = \begin{bmatrix} \tilde{C}_j \\ \tilde{C}_{j+1} F \\ \vdots \\ \tilde{C}_{j+1} F^{j+p} \end{bmatrix}. \tag{2.51}$$

Consequently:

$$O_p^{\uparrow} F^{T_d} = O_p^{\downarrow} \tag{2.52}$$

with $O_p^{\uparrow}$ the p+1 first bloc rows and $O_p^{\downarrow}$ the p+1 last bloc rows. So it is possible to identify the matrix F:

$$\hat{F} = \left(O_p^{\uparrow\,\dagger} O_p^{\downarrow} \right)^{\frac{1}{T_d}}. \tag{2.53}$$

The matrix $\tilde{C}^j$ is identified as the first bloc rows of the observability matrix.

Finally the Floquet exponents are obtained with an eigenvalue decomposition of $\hat{F}$ and the physical eigenmodes are obtained from the Floquet exponents.

Conclusion

This method allows to identify the Floquet exponents associated with the amplitude of the mode shapes at time j in the calculation of the correlations. Therefore, by repeating the method for all discrete times of a period, it would be possible to identify the periodic mode shapes. Thus, the Floquet modes can be completely identified. Based on this method, an associated uncertainty computation method [73] and a fault detection method for rotor instability monitoring [72] have been developed.

A disadvantage of this method is that it converges with the number of measured periods. The authors recommend more than 2000 periods and at least 10 000 periods for a good estimation.

Obtaining 2000 periods with a large wind turbine would require more than three hours of measurements, with a constant rotational speed, which is not applicable. This method is more suitable for structures with a high and constant rotational speed, such as helicopter rotors.

2.3.4 Application on operating structures

Once the OMA methods have been defined, it is necessary to be able to verify if the assumptions used are true. For this purpose, many wind turbines have been instrumented to apply the methods, in particular the Multi-Blade-Coordinate method.
In a first step, applications to parked wind turbines or only to tower measures are presented, which means studying time-invariant systems. In a second step, results of application of OMA methods to operational wind turbines are presented.

Tower and parked rotor

The easiest way is to start by instrumenting a stopped wind turbine, which removes the problem of studying LTP systems. To continue using classical OMA methods with an operational wind turbine, one solution is to instrument only the tower (or the foundation for an offshore wind turbine). Thus it is possible to follow the evolution of the natural frequencies of the structure, as it has been performed on onshore [97, 96] and offshore [140, 139] wind turbines. This allows to study the influence of the rotation speed on the identified eigenmodes. In [137], the authors give a review on the identification of the operating offshore wind turbine, with a focus on the identification using measurements from the tower for the identification of the damping.

Operating wind turbines

As mentioned in the introduction, many wind turbines have been instrumented, most of them to use the Coleman transformations [36, 37, 104, 33]. As said before, the Coleman transformations assume an isotropic rotor but the applications show that the real structures do not verify this assumption. Moreover, the transformations are sensitive to the placement of the sensors [128, 146], which increases the difficulty to stay under the assumption of isotropic rotor.

When applying the MBC method to an anisotropic rotor, it is observed that the transformations do not filter the harmonics of the rotor rotation. This means that the OMA methods will identify the rotation harmonics as modes.

2.3.5 Conclusion

So, it can be stated that the current methods of identification of linear periodically variable systems are not applicable to wind turbines. Indeed, the MBC transformations cannot be applied to wind turbines because the isotropy hypothesis is not respected [146]. For frequency methods such as HPS (Harmonic Power Spectrum) [3, 111], the application seems difficult because of the number of modulations to be performed. Theoretically, it is necessary to have an infinite number of modulations, the authors advise two to three modulations. In the same way for the H-OMA-TD method [126], the theoretical number of modulations is not applicable, moreover, it is difficult to compare the results, because the subspace method identifies a lot of modes, compared to the theory. And, the modulation of the signal involves a large amount of data, which makes the identification expensive in terms of computation time. Finally, despite the possibility of fully identifying the Floquet modes without any assumptions on the rotor and pre-processing, the SSI-LPTV cannot be used with operating wind turbines due to the convergence rate of the identified parameters.

It shows us, that existing methods are not applicable to operating wind turbines and more generally for LTP systems. It points out the need to develop OMA methods for operating wind turbines. From the state of the art, two approaches seem promising. Develop an OMA method for the LTP system based on Floquet theory or use a pre-processing of the data to treat an invariant system, allowing the use of a classical OMA method. These two approaches will be explored in the next part of the thesis.

To finish the state of art, the damage detection will be treated, with the presentation of an identification based method designed for LTI systems and different existing methods for the fault detection for wind turbine.

2.4 Stochastic subspace-based damage detection and localization

When a system is identified and monitored, the next step is to perform damage detection. The idea behind the procedure is that the change in the structure (such as the stiffness, the mass, or the structure configuration) will have an impact on the identified parameters. Among all the damage detection methods in the literature, two categories can be listed, namely the data-driven methods and the model-based methods. For data-driven methods, few methods perform damage detection using the time series or the spectra, with the drawback to dealing with damage features of high dimension, which needs to use reduction techniques such that the Principal Component Analysis (PCA) [129]. Others are based on the identified modal parameters [4]. For example, the identified mode shape curvature can be monitored [29], which requires to have several sensors along the structure. Also, the data-driven method can be based on machine learning to link the signal or the modal parameters to a structural state [48, 6]. The machine learning methods are powerful, however, they can be considered as black-box and need many training data to be implemented. Then among the model-based methods, model updating is one of the most used. The purpose of the method is to update the parameters of a model (for example a finite elements model) by minimizing the distance between the model and the data. This distance can be a function of the identified parameters [57] or directly on the data (with pre-processing) [52, 51]. To do so, it is needed to have a model that can be run quickly, as it is called many times during the minimization, which is not the case for the computation of the Floquet modes for the two models used in the thesis. As an indication, it takes 10 seconds for the academic model and more than 1 hour for the DTU 10MW model (because the system matrices are obtained with linearizations).

In this thesis, it is chosen to use the stochastic subspace-based damage detection and localization based on the local approach defined in [11]. This method is a data-driven method that links changes in the monitored features to changes in the system using model information, i.e.

the sensitivities of the damage feature regarding the system parameters. Also, this method gives a statistical framework that enables to assess *a priori* the performance of the damage detection. Moreover, the possibility to isolate any change in the parametrization can be assessed [10], i.e. the damaged element can be localized. Also, this method has been applied to real structures with the example of road bridges [42, 39].

To present the damage detection method, first, the damage parametrization based on the local approach is described. Then the different possible damage features are presented. To continue, the damage detection and the associated statistical framework are defined. After that, two damage localization approaches are described. Finally, a method to regroup the redundant parameters is presented.

2.4.1 Damage parametrization

The objective of the fault detection method is to detect a change in the system parameters, represented as the vector $\theta \in \mathbb{R}^h$ (for example it can regroups the stiffness or mass of the elements of the structure), with behavior assumed as

$$\begin{aligned} H_0 &: \theta = \theta_0 && \text{(reference system)}, \\ H_1 &: \theta = \theta_0 + \frac{\delta}{\sqrt{N}} && \text{(damaged system)}, \end{aligned} \tag{2.54}$$

where $\delta = \sqrt{N}\,(\theta - \theta_0)$ is unknown but fixed. The definition of the change vector for statistical analysis δ is for mathematical convenience, as it allows for the distribution of the residual to be characterized in the following. It also implies that smaller changes in the monitoring parameters θ can be detected with increasing the length of the signal (N), as $\Delta\theta = \theta - \theta_0 = \delta/\sqrt{N}$.

The change in the parameters will be sought through a so-called Gaussian residual vector $\zeta \in \mathbb{R}^l$, estimated from a subspace identification using a signal of length N. The impact of a change in the structure parameters on the residual can be modeled as a change in the mean of the residual based on the central limit theorem and using the first-order Taylor approximation [43], such that

$$\zeta \sim \begin{cases} \mathcal{N}\left(0, \Sigma\right) : H_0 \\ \mathcal{N}\left(\mathcal{J}\delta, \Sigma\right) : H_1 \end{cases}, \tag{2.55}$$

where $\delta \in \mathbb{R}^h$ is related to the unknown change under H_1, $\mathcal{J} = \frac{\partial \zeta}{\partial \theta}\frac{1}{\sqrt{N}} \in \mathbb{R}^{l \times h}$ the sensitivity matrix of the residual with respect to the parameters and Σ the covariance matrix of the residual under both H_0 and H_1. The sensitivity matrix can be defined theoretically, with some definition depending on the chosen residual in [85] or empirically using the first-order Taylor approximation.

As the first-order Taylor approximation is used, it is assumed that the change in the parameter is small (i.e. the local approach). Then to compute the sensitivity matrix $\mathcal{J}$ it is needed to have a model corresponding to the structure. Consequently, it might be needed to first fit the model to the data in H_0.

2.4.2 Standard residuals

To perform the damage detection, a residual must be defined first. Among many possibilities among the possible Gaussian residuals, the residual was previously defined in [9] as

$$\zeta = \sqrt{N}\text{vec}\left(U_2^T \hat{H}\right), \tag{2.56}$$

with $\hat{H}$ in Equation (2.18) and U_2 the left null part of $\hat{H}$. The issue with this residual is that the associated test is not robust to the environmental conditions [42]. So, later in [42] a new residual robust to the environmental conditions (as it is not a function of the covariance of the inputs/noise) has been defined, such that

$$\zeta = \sqrt{N}\text{vec}\left(S\left(\theta_0\right)^T \hat{U}_1\right), \tag{2.57}$$

with $\hat{U}_1$ the non-null left part of $\hat{H}$ and $S\left(\theta_0\right)^T$ the left null space of $O_p\left(\theta_0\right)$. Moreover, To be robust to environmental conditions and take advantage of the identification of an identified estimate of the modes, a residual has also been defined directly with the identified modal parameters. For example in [59], the residual is defined with the identified frequencies and mode shapes,

$$\zeta = \sqrt{N}\left(\hat{z} - z\left(\theta_0\right)\right), \tag{2.58}$$

with

$$\hat{z} = \begin{bmatrix} \hat{f}_1 & \dots & \hat{f}_m & \Re\left(\hat{\phi}_1\right)^T & \dots & \Re\left(\hat{\phi}_m\right)^T & \Im\left(\hat{\phi}_1\right)^T & \dots & \Im\left(\hat{\phi}_m\right)^T \end{bmatrix}^T, \tag{2.59}$$

the identified modal parameters and $z\left(\theta_0\right)$ the modal parameters of the reference system.

To choose the residual to perform the damage detection, first, a residual robust to the environmental conditions is needed. Then, a simple residual can be selected, to have an easier computation of the residual and the sensitivity matrix. Finally, to improve the damage detection a residual defined with the most damage sensitive features can be defined. Thereafter the choice and the computation of a residual, the damage detection can be performed, based on a statistical test.

2.4.3 Statistical damage detection

To detect a change in the residual distribution defined in Equation (2.55), the Generalized Likelihood Ratio (GLR) is used,

$$GLR\left(\zeta\right) = -2\log\frac{\sup_{\theta\in H_0} p\left(\zeta|\theta_0\right)}{\sup_{\theta\in H_1} p\left(\zeta|\theta\right)}, \tag{2.60}$$

with the Gaussian distribution of the residual ($\zeta \in \mathbb{R}^l$) defined as

$$p(\zeta) = \frac{1}{(2\pi)^l \det(\Sigma)^{1/2}} \exp\left(-\frac{1}{2}\left(\zeta - \mathcal{J}\delta\right)^T \Sigma^{-1}\left(\zeta - \mathcal{J}\delta\right)\right). \tag{2.61}$$

From Equation (2.60) and the definition of the residual distribution, the GLR is defined as [11]

$$GLR = t = \zeta^T \Sigma^{-1} \mathcal{J} \left(\mathcal{J}^T \Sigma^{-1} \mathcal{J} \right)^{-1} \mathcal{J}^T \Sigma^{-1} \zeta, \tag{2.62}$$

with $\delta^* = \left(\mathcal{J}^T \Sigma^{-1} \mathcal{J} \right)^{-1} \mathcal{J}^T \Sigma^{-1} \zeta$ the value that maximise the GLR test.

Proof. Let us proof Equation (2.62). First, Equation (2.61) can be inserted in Equation (2.60), leading to

$$GLR(\zeta) = -2 \log \frac{\sup_{\theta \in H_0} \exp \left(-\frac{1}{2} \zeta^T \Sigma^{-1} \zeta \right)}{\sup_{\theta \in H_1} \exp \left(-\frac{1}{2} \left(\zeta - \mathcal{J}\delta \right)^T \Sigma^{-1} \left(\zeta - \mathcal{J}\delta \right) \right)}.$$

By simplifying the previous equation

$$\begin{aligned} GLR(\zeta) &= \sup_{\theta \in H_0} \left(\zeta^T \Sigma^{-1} \zeta \right) + \sup_{\theta \in H_1} \left(- \left(\zeta - \mathcal{J}\delta \right)^T \Sigma^{-1} \left(\zeta - \mathcal{J}\delta \right) \right) \\ &= \sup_{\theta \in H_1} \zeta^T \Sigma^{-1} \zeta - \left(\zeta - \mathcal{J}\delta \right)^T \Sigma^{-1} \left(\zeta - \mathcal{J}\delta \right) \\ &= \sup_{\theta \in H_1} \zeta^T \Sigma^{-1} \mathcal{J}\delta + \left(\mathcal{J}\delta \right)^T \Sigma^{-1} \zeta - \left(\mathcal{J}\delta \right)^T \Sigma^{-1} \mathcal{J}\delta \\ &= \sup_{\theta \in H_1} f(\delta) \end{aligned}$$

because log is an increasing function and $\theta \in H_0 = \theta_0$. To assess the maximum of the GLR, let us find δ such that $\frac{\partial f(\delta)}{\partial \delta} = 0$. Thus,

$$\begin{aligned} & \frac{\partial f(\delta)}{\partial \delta} = 0 \\ & \Leftrightarrow 2 \zeta^T \Sigma^{-1} \mathcal{J} - 2 \left(\mathcal{J}\delta \right)^T \Sigma^{-1} \mathcal{J} = 0 \\ & \Leftrightarrow \left(\mathcal{J}\delta \right)^T \Sigma^{-1} \mathcal{J} = \zeta^T \Sigma^{-1} \mathcal{J} \\ & \Leftrightarrow \delta^T = \zeta^T \Sigma^{-1} \mathcal{J} \left(\mathcal{J}^T \Sigma^{-1} \mathcal{J} \right)^{-1} \\ & \Leftrightarrow \delta = \left(\mathcal{J}^T \Sigma^{-1} \mathcal{J} \right)^{-1} \mathcal{J}^T \Sigma^{-1} \zeta \end{aligned}$$

Finally, the GLR is defined as

$$\begin{aligned} GLR(\zeta) = & \zeta^T \Sigma^{-1} \mathcal{J} \left(\mathcal{J}^T \Sigma^{-1} \mathcal{J} \right)^{-1} \mathcal{J}^T \Sigma^{-1} \zeta + \left(\mathcal{J} \left(\mathcal{J}^T \Sigma^{-1} \mathcal{J} \right)^{-1} \mathcal{J}^T \Sigma^{-1} \right)^T \Sigma^{-1} \zeta \\ & - \left(\mathcal{J} \left(\mathcal{J}^T \Sigma^{-1} \mathcal{J} \right)^{-1} \mathcal{J}^T \Sigma^{-1} \right)^T \Sigma^{-1} \mathcal{J} \left(\mathcal{J}^T \Sigma^{-1} \mathcal{J} \right)^{-1} \mathcal{J}^T \Sigma^{-1} \zeta \end{aligned}$$

The Equation (2.62) is obtained

$$GLR(\zeta) = t = \zeta^T \Sigma^{-1} \mathcal{J} \left(\mathcal{J}^T \Sigma^{-1} \mathcal{J} \right)^{-1} \mathcal{J}^T \Sigma^{-1} \zeta.$$

□

From this test, the Fisher matrix can be defined

$$F = \mathcal{J}^T \Sigma^{-1} \mathcal{J}. \tag{2.63}$$

This matrix can be seen as a ratio between the sensitivity and the covariance of the residual, where the diagonal terms give the detectability of each parameter component and the non-diagonal terms quantify the impact of one parameter component on the others and vice versa. With this matrix, it is possible to assess the impact of a change in each parameter component on the residual.

From the theory of the GLR, the statistical test is following a χ^2 distribution [11] such as

$$t \sim \begin{cases} \chi^2(\nu, 0) : H_0 \\ \chi^2(\nu, \lambda) : H_1 \end{cases}, \tag{2.64}$$

where ν is the number of degrees of freedom of the distribution equal to the dimension of the parameter space, and λ is the non-centrality parameter such that

$$\lambda = \delta^T F \delta. \tag{2.65}$$

Based on the properties of the χ^2 distribution, the mean of the test denoted as $\bar{t}$, will be $\bar{t} = \nu$ under H_0 and $\bar{t} = \nu + \lambda$ under H_1.

For some applications, the sensitivity matrix might not be available, so theoretically, it is not possible to perform the damage detection test. However in [42], the non parametric test has been defined, replacing the sensitivity matrix with the identity matrix ($\mathcal{J} = \mathcal{I}$). So, the non parametric test is defined as

$$t_{np} = \zeta^T \Sigma^{-1} \zeta \tag{2.66}$$

and is equivalent to the square of the Mahalanobis distance and is defined with the following distribution

$$t_{np} \sim \begin{cases} \chi^2(\nu, 0) : H_0 \\ \chi^2(\nu, \lambda_{np}) : H_1 \end{cases}, \tag{2.67}$$

where the degree of freedom is the size of ζ and $\lambda_{np} = \delta^T \Sigma^{-1} \delta$.

From the theoretical distribution of the test (under both H_0 and H_1), it is possible *a priori* to assess the minimal change that will be detected based on a given confidence level, here 95% is considered. To do so, the method defined in [87] is used. First, the upper bound of the interval that contains 95% of the reference test $[0, t_{crit}]$ (leading to a probability of false alarm of 5%) is computed, with

$$\int_0^{t_{crit}} f_{\chi^2}(\nu, 0)(t) dt = 0.95. \tag{2.68}$$

Then, the minimum non-centrality parameter (λ_{min}) is defined such that

$$\int_0^{t_{crit}} f_{\chi^2}(\nu, \lambda_{min})(t) dt = 0.05 \tag{2.69}$$

and estimated by minimizing the following function

$$g(\lambda) = \left| \int_0^{t_{crit}} f_{\chi^2}(\nu, \lambda)(t)dt - 0.05 \right|. \tag{2.70}$$

Then, from Equation (2.65) the associated minimum statistical change can be assessed and for one parameter component

$$\delta_{h\ min} = \sqrt{\lambda_{min}/F_{hh}}, \tag{2.71}$$

where F_{hh} corresponds to the contribution of the h–th parameter component in the Fisher matrix. From the minimum 95%-level detectable statistical change, the associated minimum 95%-level detectable change in the h–th parameter component is

$$\Delta\theta_{h\ min} = \frac{\delta_{h\ min}}{\sqrt{N}}. \tag{2.72}$$

Also, from the value t_{crit} it is possible to compute the probability of detection of a statistical change δ and the associated change $\Delta\theta$ in the physical parameter θ ($\Delta\theta = \theta - \theta_0$). From the distribution of the test and the non-centrality parameter associated with the change (Equation (2.65)), the probability of detection (POD) is defined by

$$\text{POD}\,(\Delta\theta) = \int_{t_{crit}}^{\infty} f_{\chi^2}\left(\nu, N\Delta\theta^T F \Delta\theta\right)(t)dt. \tag{2.73}$$

Different distributions of the damage detection test are displayed in Figure 2.4. The impact of the number of degrees of freedom on the distribution is illustrated in Figure 2.4a and an example of distribution shift due to a parameter change in Figure 2.4b.

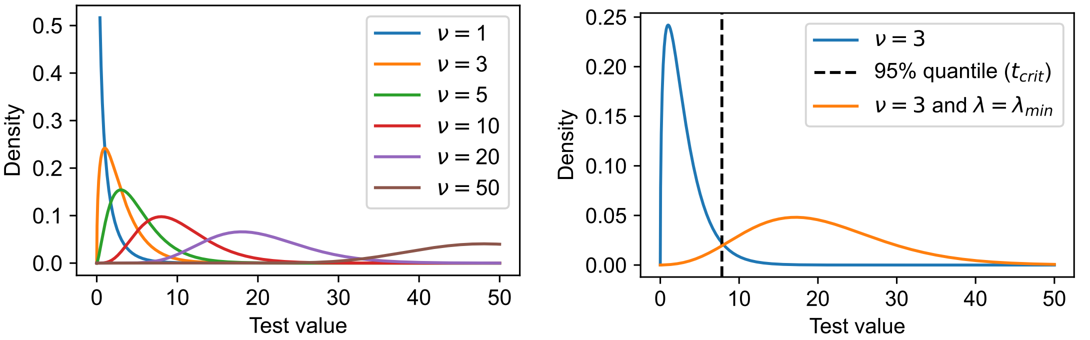

(a) Test distributions with different number of degrees of freedom (ν) and $\lambda = 0$

(b) Impact of the non-centrality parameter (λ) on the test distribution

Figure 2.4 – Examples of test distribution, function of the degree of freedom and the non-centrality parameter of the χ^2 function

In practical application, the covariance or sensitivity matrices can be badly conditioned, leading to numerical errors during the computation. To avoid this, in [43] a numerical efficient computation has been defined based on a QR decomposition of the normalized sensitivity matrix,

$$\tilde{\mathcal{J}} = \Sigma^{-1/2}\mathcal{J} = QR. \tag{2.74}$$

Then, the damage detection test become

$$
\begin{aligned}
t &= \zeta^T \Sigma^{-1/2} Q Q^T \Sigma^{-1/2} \zeta && (2.75)\\
&= \alpha^T \alpha, && (2.76)
\end{aligned}
$$

with $\alpha = Q^T \Sigma^{-1/2} \zeta$. The other advantage is the computational cost, if the QR decomposition is performed before the test computation, there are fewer operations in Equation (2.76) than in Equation (2.62).

2.4.4 Fault localization

Once the damage has been detected, the next step is to assess which parameter has changed. To do so, the sensitivities are used as they link the change in the residual mean to a change in the system parameters.

Direct localization

To localize a fault, the direct localization/isolation test [9] is evaluated first, where each parameter component is individually tested for change. This test assumes that the change is restricted to one statistical change component δ_h ($\mathcal{J}\delta = \mathcal{J}_h \delta_h$), where $\mathcal{J}_h$ corresponds to the sensitivity of the parameter component of index h, leading to

$$
t_h = \zeta^T \Sigma^{-1} \mathcal{J}_h \left(\mathcal{J}_h^T \Sigma^{-1} \mathcal{J}_h \right)^{-1} \mathcal{J}_h^T \Sigma^{-1} \zeta, \tag{2.77}
$$

with the following distribution

$$
t_h \sim \begin{cases} \chi^2(1,0) : H_0 \\ \chi^2(1,\lambda) : H_1 \end{cases}. \tag{2.78}
$$

For the direct test on the other parameter components (that have not changed), their respective distribution is $t_{\bar{h}} \sim \chi^2 \left(1, \bar{\lambda}\right)$ under H_1, with $\bar{\lambda}$, the non centrality parameter defined as [43]

$$
\bar{\lambda} = \delta_h^2 F_{h\bar{h}} F_{\bar{h}\bar{h}}^{-1} F_{h\bar{h}}^T, \tag{2.79}
$$

where $F_{h\bar{h}} = \mathcal{J}_h^T \Sigma^{-1} \mathcal{J}_{\bar{h}}$ and $F_{\bar{h}\bar{h}} = \mathcal{J}_{\bar{h}}^T \Sigma^{-1} \mathcal{J}_{\bar{h}}$. It means that under H_1, when the changed parameter component is tested, the test mean (denoted as $\bar{t_h}$) will be $\bar{t_h} = 1 + \lambda$, whereas $\bar{t_h} = 1 + \bar{\lambda}$ when an unchanged parameter component is tested.

From the direct localization test, it is possible to compute a quantification test, based on the relation between the change of the mean of the residual and the fault. So, from [43] the fault quantification test is defined as

$$
\hat{\delta}_h = \left(\mathcal{J}_h^T \Sigma^{-1} \mathcal{J}_h \right)^{-1} \mathcal{J}_h^T \Sigma^{-1} \zeta. \tag{2.80}
$$

Under H_1 and with $\mathcal{J}\delta = \mathcal{J}_h \delta_h$ the distribution of the test is

$$
\hat{\delta}_h \sim \mathcal{N} \left(\delta_h, F_{hh}^{-1} \right). \tag{2.81}
$$

Otherwise, if the tested parameter is not the actual changed parameter, the quantification follow

$$\hat{\delta}_h \sim \mathcal{N}\left(F_{hh}^{-1} F_{h\bar{h}} \delta_{\bar{h}}, F_{hh}^{-1}\right), \tag{2.82}$$

see [43] for more details.

So, the associated fault quantification can be used jointly with the localization test to assess the false positive. Indeed, if the considered parameters are the stiffness of a structure, the damage will reduce those parameters. So, if a parameter has a non-negligible localization test but the associated fault is positive, then it will be considered as a false positive; because the change in the parameter has no physical meaning.

Minmax localization

The main issue with the previous damage localization method is that a test on a non-damaged parameter can have a non-negligible test value for the localization and the quantification. To avoid that, the minmax test has been defined in [8] and explained in [43]. In this test the parameters are tested on the orthogonal space of the others, to avoid any assumptions about the change of the non-tested parameters, which leads to a robust localization test. To begin, the partial residuals are defined as:

$$\zeta_h = \mathcal{J}_h^T \Sigma^{-1} \zeta \tag{2.83}$$

$$\zeta_{\bar{h}} = \mathcal{J}_{\bar{h}}^T \Sigma^{-1} \zeta, \tag{2.84}$$

then, the robust residual of h against $\bar{h}$ is

$$\zeta_h^* = \zeta_h - F_{h\bar{h}} F_{\bar{h}\bar{h}}^{-1} \zeta_{\bar{h}}. \tag{2.85}$$

The Fisher matrix associated with the robust residual is then defined as

$$F_h^* = F_{hh} - F_{h\bar{h}} F_{\bar{h}\bar{h}}^{-1} F_{\bar{h}h}. \tag{2.86}$$

Finally, the minmax localization test is defined as

$$t_{mm} = \zeta_h^{*\,T} F_h^{*\,-1} \zeta_h^*, \tag{2.87}$$

with the following distribution

$$t_{mm} \sim \begin{cases} \chi^2(1, 0) : H_0 \\ \chi^2(1, \lambda_{mm}) : H_1 \end{cases}. \tag{2.88}$$

where $\lambda_{mm} = \delta_h^T F_h^* \delta_h$ is the non-centrality parameter associated with the test, which is independent of $\delta_{\bar{h}}$.

As for the direct localization test, it is possible to compute an associated damage with the minmax localization test.

$$\hat{\delta}_h^{mm} = \left(F_h^*\right)^{-1} \zeta_h^*. \tag{2.89}$$

Associated with the following distribution

$$\hat{\delta}_h^{mm} \sim \mathcal{N}\left(\delta_h, (F_h^*)^{-1}\right). \tag{2.90}$$

Clearly, this damage quantification is theoretically an unbiased estimator.

However, it has to be noted that the invertibility of all matrices in the computation is guaranteed only when $\mathcal{J}$ has full column rank and Σ is positive definite. Consequently, it might not be possible to perform the minmax test for some system parametrization, so, before performing the test, the rank of the sensitivity matrix should be assessed.

2.4.5 Clustering of the redundant parameters

In a considered system parametrization, some parameters can have similar sensitivity, with collinear sensitivity vectors, leading to a sensitivity matrix not full rank. Consequently, to perform the minmax test presented in the previous section, the parametrization has to be reduced. Also, with the direct localization test Equation (2.77), parameters with similar sensitivities will have the same values, and it will not be possible to assess the true damage localization. In [2, 86, 85], a method to regroup into clusters the parameters with similar sensitivities has been defined, based on the hierarchical clustering. To perform this clustering, the following distance is used

$$d_{i,j} = 1 - \frac{\tilde{\mathcal{J}_i}^T \tilde{\mathcal{J}_j}}{\|\tilde{\mathcal{J}_i}\|\|\tilde{\mathcal{J}_j}\|}, \tag{2.91}$$

where $\tilde{\mathcal{J}_i} = \Sigma^{-1/2}\mathcal{J}_i$ is the normalized sensitivity of the i–th parameter component. Once the clusters have been defined, the associated sensitivities can be defined as the cluster center, with

$$\tilde{\mathcal{J}}_k^c = \frac{1}{m_k} \sum_{i \in C_k} \tilde{\mathcal{J}}_i, \tag{2.92}$$

the sensitivity of the k–th cluster (C_k) composed of m_k parameters.

As the sensitivities of the clusters are normalized, the tests definition have to be adapted. Consequently, the damage detection, localization and quantification tests function of normalized sensitivities are defined such that

$$t = \zeta^T \Sigma^{-1/2} \tilde{\mathcal{J}} \left(\tilde{\mathcal{J}}^T \tilde{\mathcal{J}}\right)^{-1} \tilde{\mathcal{J}}^T \Sigma^{-1/2} \zeta \tag{2.93}$$

$$t_h = \zeta^T \Sigma^{-1/2} \tilde{\mathcal{J}}_h \left(\tilde{\mathcal{J}}_h^T \tilde{\mathcal{J}}_h\right)^{-1} \tilde{\mathcal{J}}_h^T \Sigma^{-1/2} \zeta \tag{2.94}$$

$$\hat{\delta}_h = \left(\tilde{\mathcal{J}}_h^T \tilde{\mathcal{J}}_h\right)^{-1} \tilde{\mathcal{J}}_h^T \Sigma^{-1/2} \zeta. \tag{2.95}$$

2.4.6 Conclusion

Consequently, with this method, based on data processing and model sensitivities, it is possible to detect changes in system parameters and even more localize those changes. In Figure 2.5 a flowchart summarizes the presented method.

This damage detection method has been extended on LTP systems, based on the SSI-LPTV identification method [72], and applied to simulated data of a helicopter on the ground. But as the SSI-LPTV method, it is not possible to apply this method to a wind turbine, because it uses estimates that converge depending on the number of rotations in the signal. So, to apply this method to a wind turbine, this method has to be adapted to the problem, similarly to the identification method.

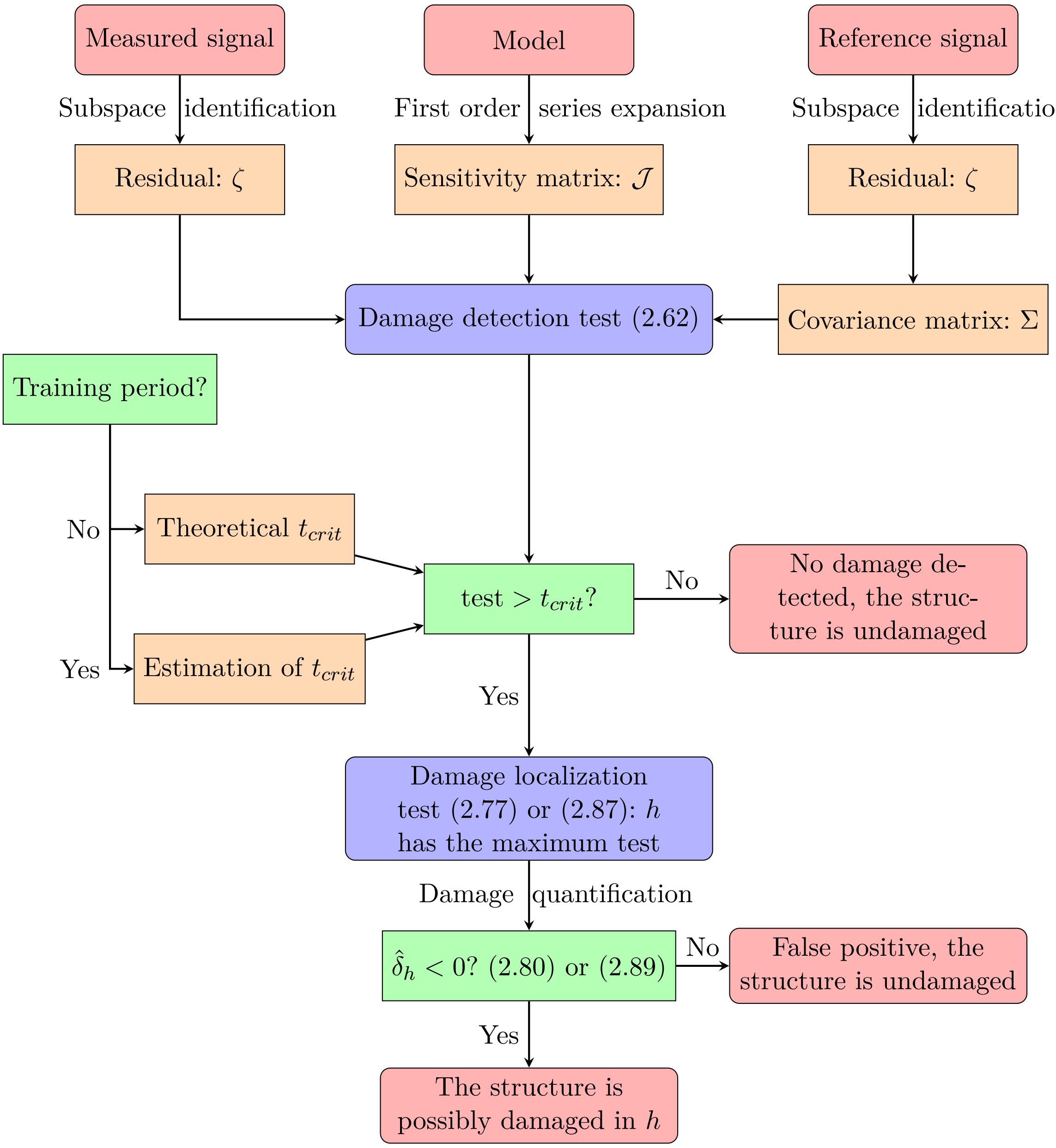

Figure 2.5 – Flowchart of the stochastic subspace-based damage detection and localization

2.5 Fault detection of wind turbine

As it was said in the previous section, one of the objectives of OMA is to detect damage or fault on a structure, looking at a change in the eigenmodes, i.e. a change in frequency, damping, or mode shape. Previous papers and thesis [132] deal with the problem of damage detection for a wind turbine. In this thesis, the focus will be on the rotor faults that are presented in Section 1.3, but other structural parts can be damaged, such as the tower and the substructure for the offshore wind turbines. In [103], detection of scour of a fixed offshore wind turbine has been performed, based on the tracking of the frequencies of the first bending modes of the tower, with an application to real measurements. For the offshore wind turbines, the jacket is a crucial part to monitor, several works have been done to explore the available techniques [82, 26], with an application to simulated data. Finally, the damage detection of a wind turbine can be performed based only on the SCADA measurement, i.e. based on the electricity production and on the environmental conditions. With those methods, it is studied if the wind turbine is producing the electricity that it should produce, with a review in [124]. It has also been used for the damage detection of an offshore wind turbine jacket based on machine learning in [25]. Those SCADA data can be also used for fatigue estimation as in [38, 31].

In [44], the type of damage that occurs on a wind turbine rotor and damage detection methods have been explored. It has been shown that to monitor wind turbine rotor faults, a solution is to monitor the anisotropy or the imbalance (mass or pitch anisotropy). This approach will be exploited in the following of the thesis. First, the type of damages and faults leading to an anisotropy of the rotor are introduced. Then, two methods based on two consequences of stiffness anisotropy and imbalance are presented.

2.5.1 Imbalance detection

The detection of pitch misalignment and added mass called imbalance detection has been treated in several papers. In [79] the imbalance is detected with the PSD of the electrical power, then the nature and the severity are determined using blade measurements. In [20] the focus is on pitch errors, based on tower measurements, where the detection localization and quantification is performed using a multi-layer perceptron. In [67] the PSD of the rotational speed is used as the damage feature and the support vector machine is chosen to perform mass imbalance detection and quantification. All the cited works are performed on simulated data. But in [144] the impact of icing on a blade on the PSD of tower accelerations is shown on real measurements.

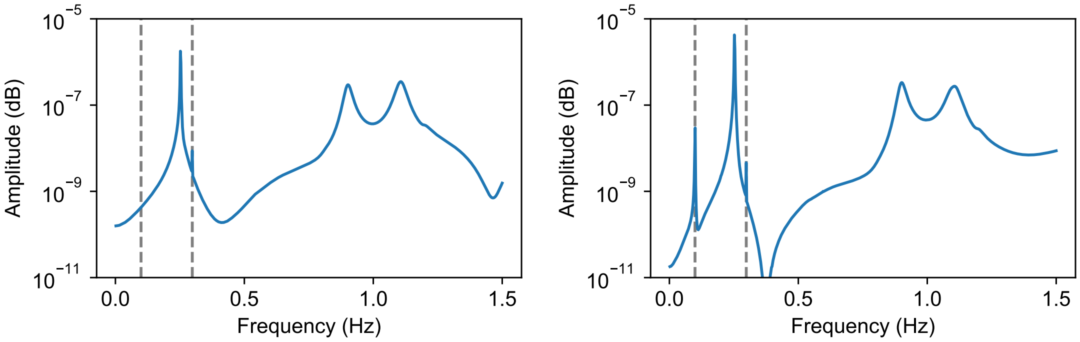

(a) isotropic rotor (b) 1% of mass added on one blade

Figure 2.6 – Power Spectral Density (PSD) of Side-Side acceleration of the tower for two configurations of the rotor with the DTU 10MW model

In all those papers the detection of rotor imbalance is based on the apparition of the first harmonic of the rotation (called the 1P) in the fixed frame, namely the tower and the nacelle. In Figure 2.6, PSD of tower accelerations along Side-Side for two configurations are displayed, one with an isotropic rotor and one with a rotor imbalance, where 1% of mass added is simulated. This figure shows that a new peak appears with mass anisotropy. This new peak corresponds to the first dashed line, which is the 1P ($\frac{\Omega}{2\pi}$), and the second dashed line corresponds to the 3P. Similar behavior can be seen along Fore-Aft with a pitch misalignment of one blade, where a misalignment of 2° is simulated in Figure 2.7.

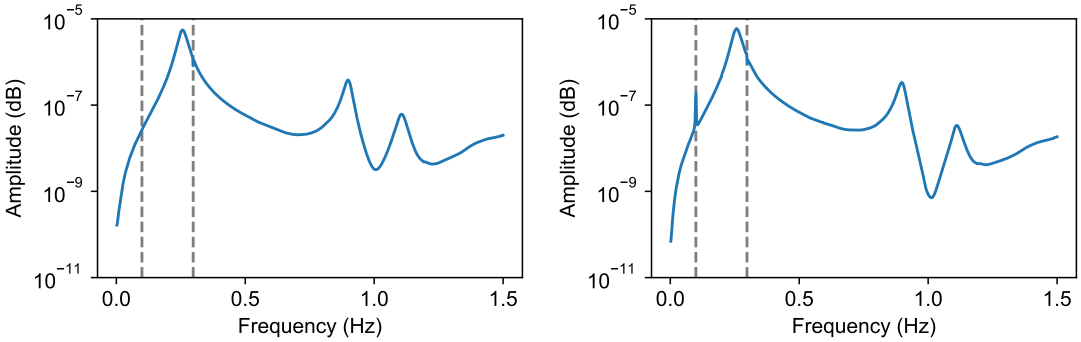

(a) isotropic rotor

(b) 2° of pitch offset of one blade

Figure 2.7 – Power Spectral Density (PSD) of Fore-Aft acceleration at mid-tower for two configurations of the rotor with the DTU 10MW model

However, the previous figures were obtained from simulations with a constant wind speed and consequently a constant rotational speed. For a real wind turbine, the wind is turbulent and consequently, the rotational speed is variable. In Figure 2.8, the PSD of the Side-Side and Fore-Aft acceleration for respectively an add of mass and a pitch offset are displayed (both under a turbulent wind).With a variable rotational speed, the frequencies of the harmonics are varying during the simulation, or a PSD is averaging the frequencies. So, the intensity of the peaks is lower and the peaks are wider. This can be seen in Figure 2.8, where for the addition of mass the 1P peak has almost disappeared and totally disappears for the pitch offset. Consequently, for real external conditions it is much more difficult to detect rotor imbalance and much more sophisticated methods have to be used as in the methods presented at the beginning of the section.

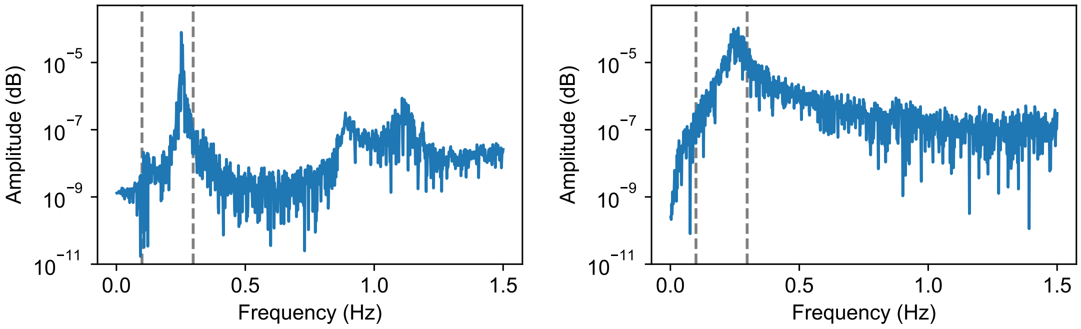

(a) Side-Side acceleration: 1% of mass added on one blade

(b) Fore-Aft acceleration: 2°of pitch offset of one blade

Figure 2.8 – Power Spectral Density (PSD) of acceleration at mid-tower for two configurations of the rotor with the DTU 10MW model, under turbulent wind ($\bar{u} = 6.7$ and $\sigma_u = 20\%$)

2.5.2 Rotor damage detection

In the literature, some methods defined for the detection of structural rotor faults can be found for example in [131, 129], with detection of trailing edge opening on one blade of a small wind turbine (225 kW). In those papers, the cross-covariance of rotor sensors is used as a damage feature through a Mahalanobis distance. The issue with this method is its sensitivity to the operational conditions that must be mitigated, as it is done in [112, 90, 50]. Also, this approach does not provide localization information. Finally, in all the cited papers, a mechanical actuator is installed on the monitored blade. So, it gives a signal with low covariance and constant external conditions, which is not relevant to the real external conditions of a wind turbine blade.

The rotor faults can be seen as the apparition of anisotropy of stiffness, this kind of anisotropy leads to a change in the mode shapes of whirling modes, i.e. the bending modes of the rotor along flap and edge. In [126, 34], it has been shown that the anisotropy leads to a change in the phase shift between blades and the amplitudes of bending. The phase shift is 10 times more sensitive than the frequency, which makes it a very promising indicator to monitor wind turbines. Figure 2.9 illustrates with polar plots the evolution of the phase shift and the amplitude of periodic modes shape of the simple wind turbine model. On the polar plots, each star represents a DOF of the considered mode shape, with the coordinates of the star defined by the amplitude and the phase shift of the DOF. In this example, the stiffness of the third blade varies from 100% to 75%. When compared to the first blade (chosen as the reference blade), the phase shift of the second blade can vary by 60°. Differences between blades can be used for damage detection.

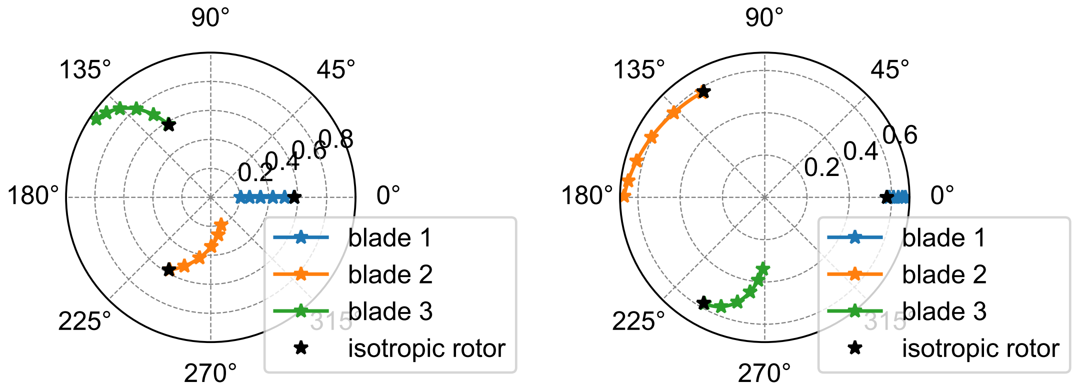

(a) Third Floquet mode

(b) Fifth Floquet mode

Figure 2.9 – Polar plot of the evolution of mode shape of flap bending modes of the simple wind turbine, function of the stiffness of one blade. Each star corresponds to a loss of 5% of stiffness of the blade n°3

The stiffness anisotropy has also consequences on the fixed frame (nacelle and tower). The apparition of the first harmonic of the rotation in the PSD due to a pitch misalignment or an added mass has been mentioned previously, but the anisotropy (any type) leads also to the apparition of new Fourier components in the Floquet modes for the whirling modes on the tower. It has been treated in [125] for the stiffness anisotropy detection on a simple model of a wind turbine (with three edge bending DOF and two nacelle DOF).

2.5.3 Conclusion

Fault detection methods for wind turbine rotors have been introduced, with two main parts, mass and pitch imbalance detection, which has been widely treated, and rotor damage detection. For the latest, it has been shown that the stiffness anisotropy leads to significant changes in the whirling mode shapes, with the example of the evolution of these modes of the academic model of a wind turbine.

Consequently, the study of the evolution of mode shapes needs to be carried on, especially with the analysis of the dynamical behavior changes of large wind turbines such as the model of the DTU 10MW wind turbine. And might be used jointly with stochastic subspace-based damage detection. But, to perform damage detection, the identification of the operating wind turbines has to be performed.

2.6 Conclusion

To conclude, with the presentation of the Operational Modal Analysis methods designed for the invariant systems, it has been understood that it is not theoretically possible to identify the modal parameters of the time periodic systems with these methods, considering that one of the main assumptions of the methods is that the system is time invariant. Then, with the brief review of the OMA methods for the time periodic systems, it has been concluded that all the existing methods have nonnegligible drawbacks and they can not be used to monitor real structures. Consequently, a new identification procedure designed for the linear time periodic system needs to be developed, where two approaches can be studied: develop an OMA method for the LTP system based on Floquet theory or use a pre-processing of the data to treat an invariant system, allowing the use of a classical OMA method.

To continue, a damage detection method that is using identification results has been presented. Using the hypothetical results of the identification of the operating wind turbines, it should be possible to adapt this method to perform damage detection. Then, fault detection methods designed for wind turbines are presented, conjointly with the damage indicators of the different types of damage. For the detection of rotor imbalance (mass or pitch), some methods have been already defined and tested. However, the detection of structural faults in the blades has not been addressed as much. Consequently, damage detection will focus mainly on the detection of structural faults in the blades.

In the next part, the problem of the identification of the linear time periodic systems will be treated, based on the approximation of the Floquet modes as a sum of invariant modes.

PART II

Linear Time Invariant Approximation for Subspace Identification of Linear Periodic Systems Applied to Wind Turbines

Chapter 3

THEORETICAL APPROXIMATION OF LTP SYSTEMS INTO LTI SYSTEMS AND ASSOCIATED STATE-SPACE DESCRIPTION

Abstract

In this Chapter, the dynamical behavior of the linear time periodic systems is approximated into linear time invariant systems under nonstationary inputs. This approximation is based on the Floquet theory coupled with a Fourier decomposition. The approximation is firstly validated on the academic model of a wind turbine and illustrated on the DTU 10MW wind turbine model. Then, the state-space representation of the approximation is defined, and it is demonstrated that the approximation can be identified with a classical subspace method.

3.1 Introduction

In the previous chapter, the dynamic behavior of a wind turbine and the Operational Modal Analysis has been presented. More precisely, existing OMA methods for wind turbines have been introduced and their limitations highlighted. The objective here is to propose an identification method able to deal with rotating machines and operating wind turbines, more precisely a method without any assumption on the rotor isotropy. The method proposed here is based on the LTP modeling of the eigenmodes and relies on the existing OMA methods presented in Section 2.2.

To achieve such objectives, it is proposed to approximate an LTP system as an LTI system based on the Floquet theory (see Section 1.5.4) coupled with a Fourier decomposition. Once this decomposition is performed, it is demonstrated that state-of-the-art OMA methods for LTI systems can be employed for the Floquet-Fourier decomposition of LTP systems.

The chapter is organized as follows: the first section of the chapter is dedicated to the approximation of LTP systems into LTI systems based on the study of the Floquet modes. Secondly, the approximation is validated with a study on the academic model of wind turbine and theoretically. Then, the physical meaning of the approximation is assessed. Finally, the state representation of the approximation is defined to demonstrate that the approximation can be identified with the SSI method.

3.2 Approximation of Floquet modes

To begin let us recall the Floquet decomposition of the homogeneous part of an LTP system of period T (fully described in Section 1.5.4). The solution of the homogeneous equation is

$$x_h(t) = \Phi(t)x(t_0), \tag{3.1}$$

with $\Phi(t)$ the fundamental matrix such as $\Phi(t+T) = \Phi(t)Q$ and $x(t_0)$ the initial conditions. This fundamental matrix can be decomposed as

$$\Phi(t) = P(t)\exp\left(Rt\right), \tag{3.2}$$

with $P(t)$ a T-periodic matrix and $R = \frac{1}{T}\log\left(Q\right)$. The matrix R can be diagonalized, using the characteristic exponents (μ)and the eigenvectors (Ψ) of Q, leading to

$$\Phi(t) = P(t)\Psi\exp\left(\left[\mu\right]t\right)\Psi^{-1}. \tag{3.3}$$

Then it is possible to express the homogeneous part of the state vector ($x_h(t)$) as a sum of modes, namely the Floquet modes:

$$x_h(t) = \sum_{j=1}^{n} X_j(t)\exp\left(\mu_j t\right)q_j(t_0) \tag{3.4}$$

with $q_j(t_0) = \psi_j' x(t_0)$, ψ_j' the j–th row of the matrix Ψ^{-1} and $X_j(t) = P(t)\psi_j$ the T-periodic mode shape of the j–th Floquet mode.

Once the Floquet mode decomposition is done, the objective is to express the observation vector as a finite sum of eigenmodes to obtain the description of a time invariant system (Equation (1.19)). The Floquet mode decomposition of the observation $y_h(t)$ (associated with the observation matrix $C(t)$) is

$$y_h(t) = C(t)\sum_{j=1}^{n} X_j(t)\exp\left(\mu_j t\right)q_j(t_0) \tag{3.5}$$

$$= \sum_{j=1}^{n} Y_j(t)\exp\left(\mu_j t\right)q_j(t_0), \tag{3.6}$$

where $Y_j(t) = C(t)X_j(t)$ is the mode shape of the j–th Floquet mode, a periodic vector of period $T = \frac{2\pi}{\Omega}$, which can then be expanded into a Fourier series:

$$Y_j(t) = \sum_{l=-\infty}^{\infty} Y_{j,l}\exp\left(il\Omega t\right) \tag{3.7}$$

By combining Equations (3.6) and (3.7), the observation vector can be expressed as an infinite sum of terms:

$$y_h(t) = \sum_{j=1}^{n}\sum_{l=-\infty}^{\infty} Y_{j,l}\exp\left(\left(\mu_j + il\Omega\right)t\right)q_j(t_0) \tag{3.8}$$

Most relevant components of the expansion of $y_h(t)$ are determined by the participation factor (modified compared to [16]), defined as:

$$\phi^y_{j,l} = \frac{\|Y_{j,l}\|^2}{\sum_{k=-\infty}^{\infty} \|Y_{j,k}\|^2}. \tag{3.9}$$

By defining a minimal participation factor (ϕ^y_{min}), an approximation of the observation ($\hat{y}_h(t)$) is constructed by truncating the series by keeping only terms with the highest participation factor,

$$\hat{y}_h(t) = \sum_{(j,l),\phi^y_{j,l} \geq \phi^y_{min}} Y_{j,l} \exp\left((\mu_j + il\Omega)\, t\right) q_j(0). \tag{3.10}$$

$\hat{y}_h(t)$ can then be expressed as a sum of $\tilde{n}$ modes

$$\hat{y}_h(t) = \sum_{p=1}^{\tilde{n}} Y_p \exp\left(\bar{\mu}_p t\right) q_p(t_0), \tag{3.11}$$

where each index p corresponds to a pair (j, l), and $\bar{\mu}_p = \mu_j + il\Omega$ and $\tilde{n}$ is the number of modes with a participation factor superior to the minimum threshold ϕ^y_{min}. Finally, the Floquet modes of an LTP system have been approximated by a finite number of eigenmodes identical to those of an LTI system (see Equation (1.19)), that are the Fourier harmonics of the Floquet modes. Consequently, the dynamical behavior of an LTP system can be approximated by the behavior of an LTI system, as it was illustrated in [1] with the Mathieu oscillator. Now, this approximation will be validated using an academic model of a wind turbine.

3.3 Validation of the approximation

3.3.1 Example of the academic model

The previously defined approximation is applied on an example of an LTP system. Firstly, a frequency analysis is performed to verify that the frequencies obtained with the approximation model fit the frequencies of the real model. Secondly, the error of the approximation looking at the periodic mode shapes is computed. Here, an academic model of a wind turbine is used [119] as described in Section 1.4.5, with a rotational speed of 1.4 rad/s and an isotropic rotor. For this example, the approximation is computed with a minimum participation factor (ϕ^y_{min}) of 1%. A summary of the approximation is given in Table 3.1, where the Floquet modes are computed using the method presented in Section 1.5.4. For example, the yaw motion Floquet mode is composed of three Fourier harmonics with l=8, 7 and 6 for the id Number 1, 2 and 3 respectively, with $\mu_j = -0.0734 + 0.5616i$.

The objective is to verify that the frequencies of the model approximation modes ($\frac{|\bar{\mu}_p|}{2\pi}$) are fitting those of the wind turbine model. The observable frequencies of the wind turbine are obtained based on a decay test (non-zero initial displacements and zero load). Precisely, these frequencies are obtained by analysing the frequency peaks in PSD of the response. This comparison is illustrated for the 5 DOF wind turbine (presented in Section 1.4.5) in Figure 3.1, where the PSD of the accelerations of one rotor DOF and one tower DOF are represented. The frequencies obtained from the approximation given in Table 3.1 are represented with dashed

Floquet mode	id Number	Participation factor (ϕ^y)	Frequency (Hz)	Damping (%)	Sum of ϕ^y
Yaw motion	1	0.598	1.693	0.690	$> 1 - 10^{-5}$
	2	0.243	1.470	0.794	
	3	0.159	1.248	0.936	
Pitch/tilt motion	4	0.409	1.813	0.598	$> 1 - 10^{-5}$
	5	0.300	1.590	0.682	
	6	0.291	1.367	0.794	
Forward flap	7	0.632	0.641	0.324	$> 1 - 10^{-5}$
	8	0.233	0.864	0.240	
	9	0.134	1.087	0.191	
Collective flap	10	1.000	0.746	0.267	1.000
Backward flap	11	0.990	0.670	0.230	$> 1 - 10^{-5}$
	12	0.010	0.448	0.344	

Table 3.1 – Fourier harmonics of Floquet modes, with a minimum participation factor of 1%, for a rotational speed of 1.4 rad/s

lines and referred by their id number.

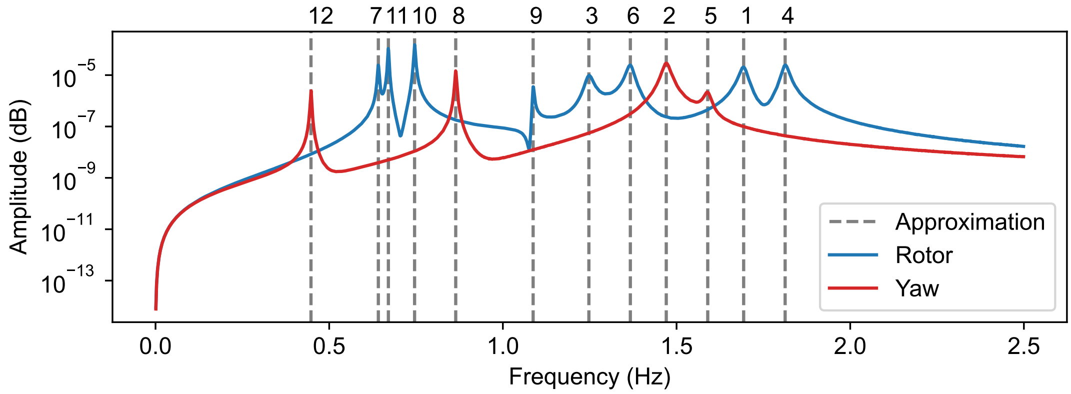

Figure 3.1 – Comparison of the frequencies of the approximation from Table 3.1 (dashed lines and id number) and the Power Spectral Density (PSD) of a free decay of the 5DOF wind turbine of a rotor DOF (blue line) and a tower DOF (red line) – (ϕ_{min}) threshold of 1%

As seen in Figure 3.1, each peak in the PSD spectrum corresponds to one frequency among the model approximation modes. And vice versa, all model approximation modes are observable in the PSD. Moreover, a good alignment between the frequency peaks and the approximation is observable. As a conclusion, approximating the homogeneous part of an LTP-system as an LTI-system is plausible.

Then, a method to evaluate the approximation error is developed to compare the exact periodic mode shapes with those reconstructed with the approximation. To reconstruct the approximated periodic mode shape denoted $\hat{Y}_j$, an inverse Fourier transform is performed on a Fourier series composed of zeros except on the components of the approximation. For the approximation (presented in Table 3.1), the relative approximation error ($\frac{\|Y_j(t)-\hat{Y}_j(t)\|}{\|Y_j(t)\|}$) over the period is below 0.05%, for all the DOF and for all the Floquet modes. So, in this example, the Floquet modes are well approximated.

In Figure 3.2, the first reconstructed periodic mode shape is compared to the exact one on two DOF, one of the rotor and one of the tower. To illustrate the impact of the truncation on the approximation, different minimum participation factor thresholds ϕ^y_{min} are considered. It is clear that the lower the participation factor and the higher number of retained modes, the better the approximation. Indeed, when ϕ^y_{min} is lower, more Fourier coefficients are retained in the approximation and so a higher accuracy is reached. In the present case, a minimum participation factor of 0.1 is required to obtain an accurate approximation. This can be confirmed with an analysis of the participation factors values in Table 3.1.

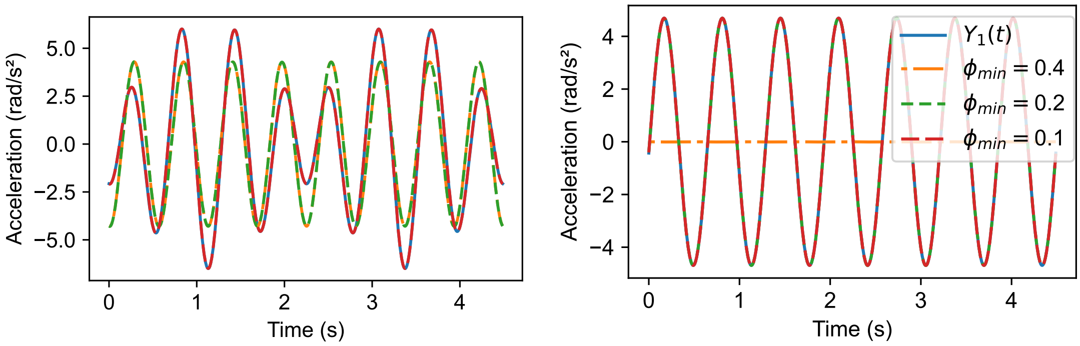

(a) Rotor (b) Tower (Yaw)

Figure 3.2 – Comparison over a period of the real part of the periodic mode shape of the reference Floquet model (continuous line) with different approximations (dashed lines) for different values of the minimum participation factor (ϕ_{min}) – First Floquet mode corresponding to the Yaw motion

From this study, it can be concluded that the approximation of the Floquet modes as a finite number of Fourier harmonics selected based on the participation factor should be able to describe the dynamical behavior of an LTP-system as long as the minimum participation is carefully chosen.

3.3.2 Quantification of the approximation error

To wrap up the theoretical study, this approximation error will be quantified function of the minimum participation factor. Precisely, the error on the periodic mode shape will be quantified. First, with $\hat{Y}_j(t)$ the approximation of the periodic mode shape of the j–th Floquet mode, the Fourier series decomposition of the gap between the periodic mode shape and the approximation writes

$$Y_j(t) - \hat{Y}_j(t) = \sum_{l=-\infty}^{\infty} Y_{j,l} \exp(il\Omega t) - \sum_{l,\phi^y_{j,l} \geq \phi^y_{min}} Y_{j,l} \exp(il\Omega t) \tag{3.12}$$

$$= \sum_{l,\phi^y_{j,l} < \phi^y_{min}} Y_{j,l} \exp(il\Omega t), \tag{3.13}$$

With the identity of Parseval, it comes

$$\|Y_j(t) - \hat{Y}_j(t)\| = \frac{1}{T} \int_{-T/2}^{T/2} \|Y_j(t) - \hat{Y}_j(t)\|^2 dt = \sum_{l,\phi^y_{j,l} < \phi^y_{min}} \|Y_{j,l}\|^2. \tag{3.14}$$

With Equation (3.9)

$$\|Y_{j,l}\|^2 = \phi^y_{j,l} \sum_{k=-\infty}^{\infty} \|Y_{j,k}\|^2, \tag{3.15}$$

leading to

$$\|Y_j(t) - \hat{Y}_j(t)\| = \sum_{l,\phi^y_{j,l}<\phi^y_{min}} \phi^y_{j,l} \left(\sum_{k=-\infty}^{\infty} \|Y_{j,k}\|^2 \right). \tag{3.16}$$

Furthermore,

$$\sum_{l,\phi^y_{j,l}<\phi^y_{min}} \phi^y_{j,l} = 1 - \sum_{l,\phi^y_{j,l}\geq\phi^y_{min}} \phi^y_{j,l}, \tag{3.17}$$

as the sum of all the participation factors of a Floquet mode is 1. Consequently,

$$\|Y_j(t) - \hat{Y}_j(t)\| \leq \left(1 - \sum_{l,\phi^y_{j,l}\geq\phi^y_{min}} \phi^y_{j,l} \right) \sum_{k=-\infty}^{\infty} \|Y_{j,k}\|^2. \tag{3.18}$$

With the identity of Parseval $\sum_{k=-\infty}^{\infty} \|Y_{j,k}\|^2 = \|Y_j(t)\|$, so the second term of the previous equation is constant. Also,

$$\lim_{\phi^y_{min}\to 0} \sum_{l,\phi^y_{j,l}\geq\phi^y_{min}} \phi^y_{j,l} = 1, \tag{3.19}$$

so

$$\lim_{\phi^y_{min}\to 0} \|Y_j(t) - \hat{Y}_j(t)\| = 0, \ \forall\ j \in [1:n] \text{ and } t \in \mathbb{R}^+. \tag{3.20}$$

As a conclusion, the approximation error should tend to zero similarly to the minimum participation factor. Now, the Floquet modes of the DTU 10MW wind turbine will be analysed to understand the meaning of the approximation on a realistic model.

3.4 Analysis of Floquet modes

The objective of this section is to give insights into the physical meaning and representation of Floquet modes and describe the associated approximation. Here, some Floquet modes of the DTU 10MW wind turbine (defined in Section 1.4.5) are presented considering an isotropic rotor. The periodic mode shapes are studied using different outputs. For the tower, four displacements are used, along Fore-Aft (in the wind direction) and Side-Side (transverse to the wind direction) directions at mid-tower and at tower top. For the rotor, the displacements from the undeflected blade along flap (perpendicular to the rotor plane) and edge (in the rotor plane) directions for each blade at mid-blade are used.

3.4.1 Floquet modes of the DTU 10MW

Before starting the study of the periodic mode shapes, the evolution of the Floquet modes frequencies versus the rotational speed can be studied. As described in Section 1.5.8, from the linearized matrices, the Floquet modes can be computed with the MBC transformation, as the rotor is isotropic. Then, the modal analysis can be performed using the method described in Section 1.5.5. Here, each simulation is performed with a constant wind speed of 7 m/s. The evolution of the frequencies can be displayed with a Campbell diagram.

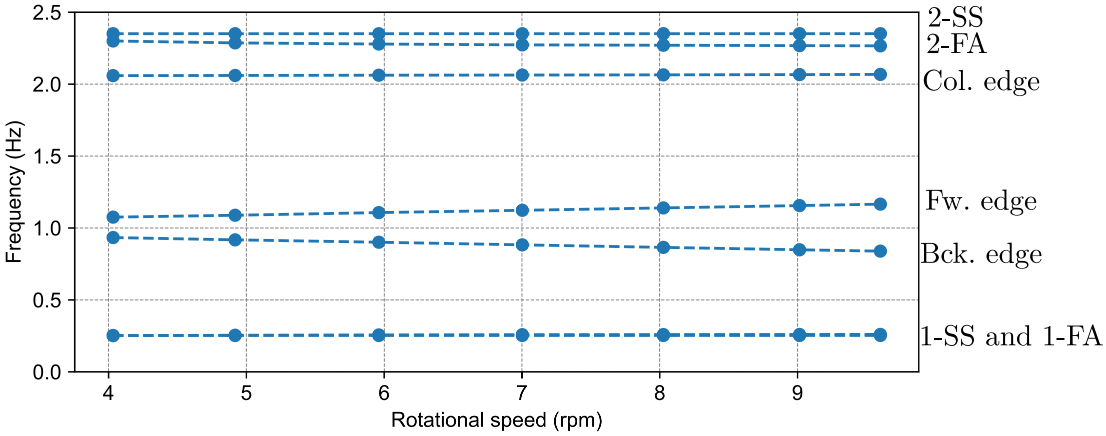

Figure 3.3 – Campbell Diagram of the MBC modes principal frequencies ($|\mu_j|/2\pi$) of the DTU 10MW, only the frequencies from modes with a damping below 20% are displayed

In Figure 3.3, the evolutions of the frequencies of some MBC modes are displayed and named according to the mode shapes. It can be seen that almost all the frequencies are constant regarding the rotational speed. Also, this Campbell diagram gives an explanation for the names of the edge-bending eigenmodes. The forward edge denotes the eigenmodes where the frequency increases with the rotational speed and the backward edge denotes the eigenmodes where the frequency decreases. The frequencies of those two eigenmodes are separated by $2\frac{\Omega}{2\pi}$, with for this model a central frequency around 1 Hz.

In the next sections, the studied system will be the DTU 10MW wind turbine rotating at 6 rpm.

3.4.2 Analysis of tower DOF

Theoretically, a Fourier transform of a periodic mode shape using only the components of the tower DOF is composed of a single harmonic, if the rotor is isotropic. This harmonic corresponds to the associated MBC mode, as it was introduced in [119]. In Figure 3.4, the periodic mode shapes of the backward edge and the 1-Fore-Aft on tower DOF are displayed, with constant values along the period. These mode shapes evolutions confirm that the periodic mode shapes on the tower are composed of a single harmonic.

For the backward edge and the first Fore-Aft, the frequency of the associated eigenvalue is 0.9001 Hz and 0.257 Hz respectively. As a recall, the eigenvalue of a Floquet mode is defined with $\pm k\Omega$ in the imaginary part, where k is an undetermined integer (see Section 1.5.4). So if the periodic mode shape is constant, the frequency of the associated Fourier component is the frequency of the Floquet mode, computed with the characteristic exponent.

3.4.3 Analysis of rotor DOF

Here, the previous analysis is performed on the DOF of the rotor. In Figures 3.5 and 3.6, the periodic mode shapes of the backward edge and the 1 Fore-aft on rotor DOF are displayed

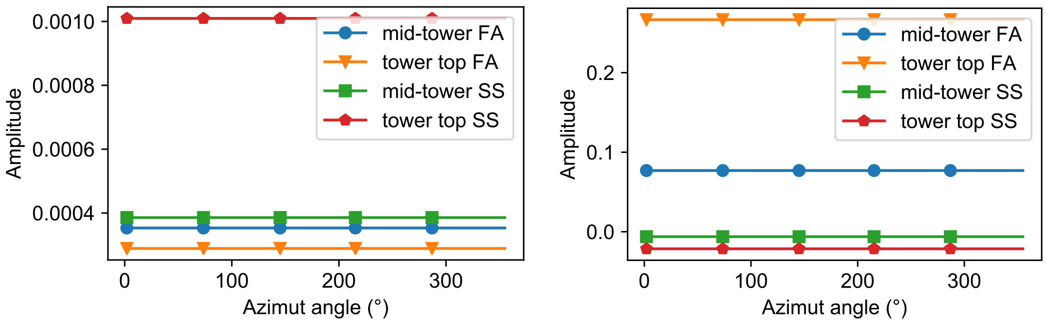

(a) Bck. edge - 0.9001 Hz

(b) 1-FA - 0.257 Hz

Figure 3.4 – Real part evolution of periodic mode shapes at tower DOF

with their associated Fourier transform. Figures 3.5.a and 3.6.a show that the periodic mode shapes are not constant with the azimuth angle. For each mode the harmonics involved in the Fourier transform are different. For the backward edge, only the harmonic $h = 1$ has a significant contribution (amplitude of 0.85). This means that one Fourier component composes this periodic mode shape at the rotor DOF, with a frequency equal to $0.9001 + \frac{\Omega}{2\pi}$=1.000 Hz. For the 1 Fore-Aft mode, three different harmonics (h=-1,0,1) are involved with an amplitude of 0.2, 0.45, and 0.3 respectively. It means that three different Fourier harmonics will compose the approximation, and one is the same as the one seen with the tower DOF (h=0).

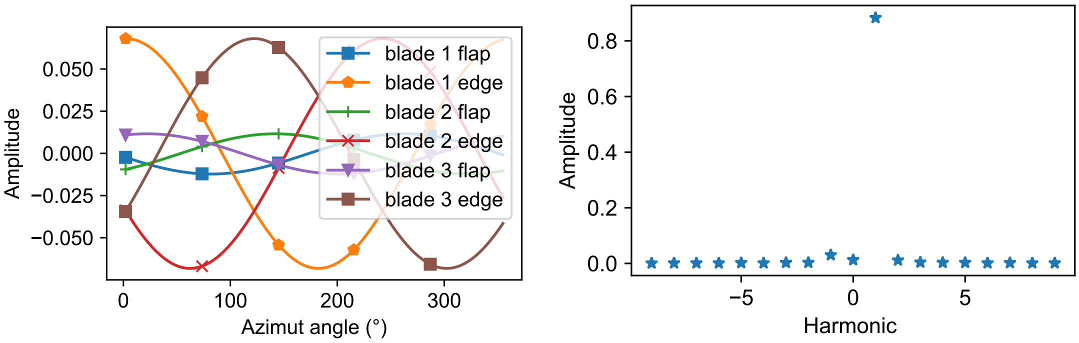

(a) Evolution of the mode shape real part

(b) Associated normalized Fourier transform

Figure 3.5 – Real part of the periodic mode shape of the backward edge at the rotor DOF

3.4.4 Mode shapes of the global structure

With the analysis of the periodic mode shapes through different DOF, it is clear that the harmonics contributing to a Floquet mode depend on the DOF considered. Using those analyses, the mode shapes of the Fourier harmonics are displayed on the global structure.

In Figures 3.7 and 3.8, the mode shapes of the Fourier harmonics of two Floquet modes are displayed, namely the backward edge harmonics ($h = -1$ and $h = 0$) and the first Fore-Aft ($h = -1$, $h = 0$ and $h = 1$) . It has to be noted that the rotor is rotating, so the mode shapes are given at one specific azimuth angle and the mode shapes of the structure are given with the undeflected structure as reference. To have a better view it is needed to consider the vibrations and the rotation together (the animations can be seen in `https://mybox.inria.fr/`

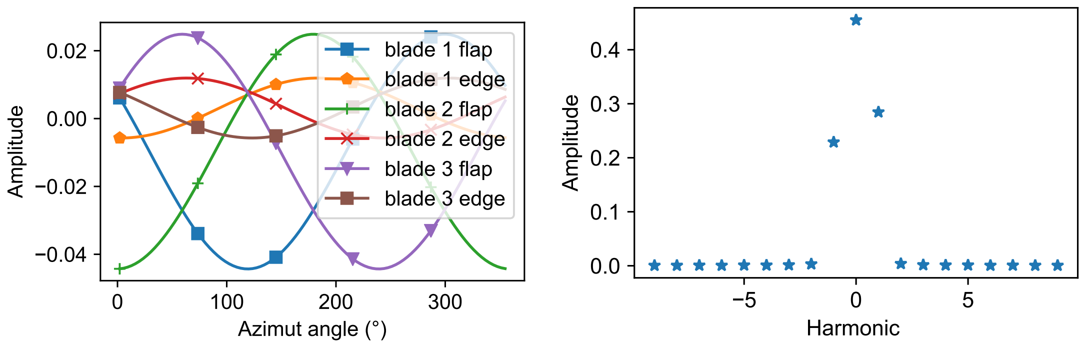

(a) Evolution of the mode shape real part (b) Associated normalized Fourier transform

Figure 3.6 – Real part of the periodic mode shape of the 1 Fore-Aft at the rotor DOF

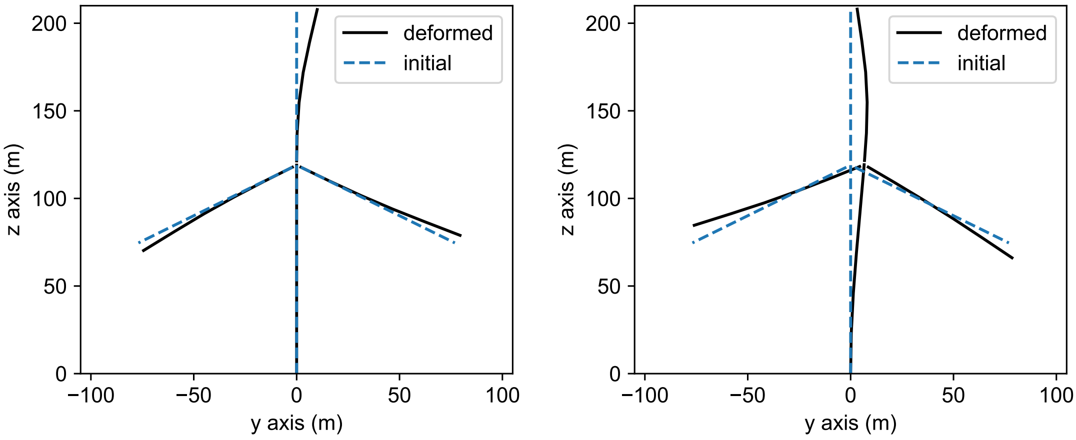

(a) f=1.000 Hz, h=1 (b) f=0.901 Hz, h=0

Figure 3.7 – Different mode shapes from the Floquet mode of Backward edge

`d/8c10b338c23a4a82a9ed/`).

3.5 State-space expression of the approximation

The objective of this section is to express the state-space representation of the approximation. Once these matrices are defined, they can be inserted in the state-space defined for an LTP system (Equation (1.15)).

Equation (3.11) shows that the shape of the approximation of the observation $\hat{y}(t)$ is the same as the observation of an LTI system (only for the homogeneous part). So there must exist a state-space composed of some state vector $z(t) \in \mathbb{R}^{\tilde{n}}$ and the approximation of the observation $\hat{y}(t)$ such that the homogeneous part reads

$$\begin{cases} \dot{z}_h(t) = \tilde{A} z_h(t) \\ \hat{y}_h(t) = \tilde{\mathbf{C}} z_h(t) \end{cases}, \tag{3.21}$$

with $\tilde{A}$ and $\tilde{\mathbf{C}}$ the transition and observation matrices of the approximation and $z_h(t)$ of the

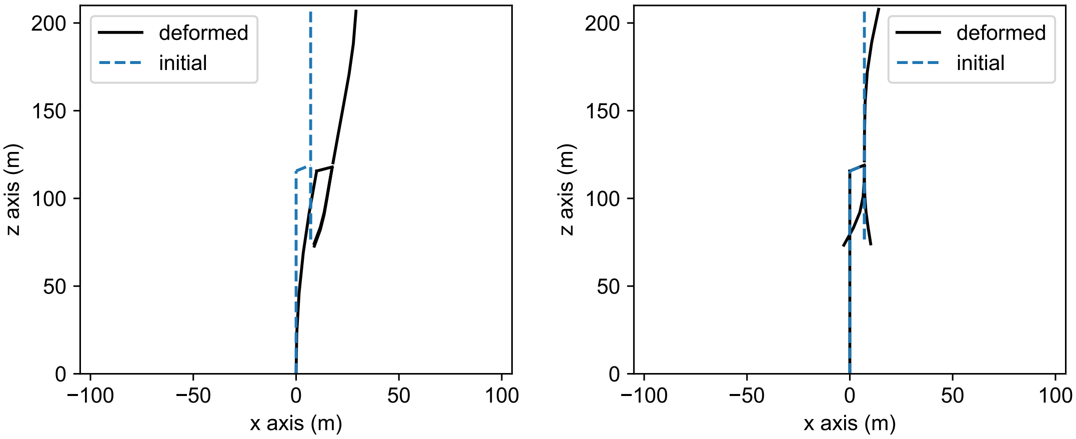

(a) f=0.257 Hz, h=0

(b) f=0.158 Hz, h=-1

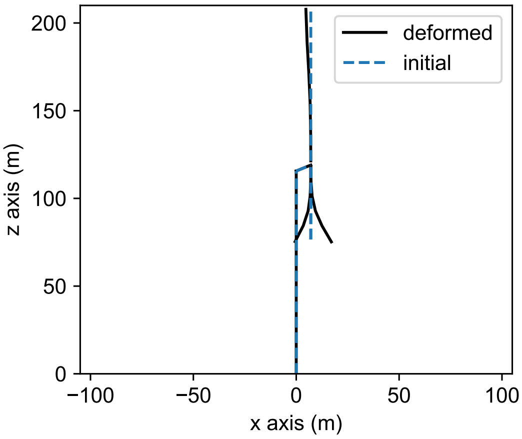

(c) f=0.356 Hz, h=1

Figure 3.8 – Different mode shapes from the Floquet mode of 1 Fore-Aft

form

$$z_h(t) = \sum_{p=1}^{\tilde{n}} Z_p \exp\left(\bar{\mu}_p t\right) q_p(t_0). \tag{3.22}$$

By injecting Equation (3.22) into Equation (3.21) and setting t_0 to 0 (for a better readability) it comes

$$\sum_{p=1}^{\tilde{n}} Z_p \bar{\mu}_p \exp\left(\bar{\mu}_p t\right) q_p(0) = \tilde{A} \sum_{p=1}^{\tilde{n}} Z_p \exp\left(\bar{\mu}_p t\right) q_p(0), \tag{3.23}$$

and by expressing the sums in matrix form

$$\mathcal{Z}\left[\bar{\mu}\right] \exp(\left[\bar{\mu}\right] t) q(0) = \tilde{A} \mathcal{Z} \exp(\left[\bar{\mu}\right] t) q(0), \tag{3.24}$$

with $\mathcal{Z} \in \mathbb{R}^{\tilde{n} \times \tilde{n}}$ regrouping the amplitudes of the state vector Z_p (one vector per column), $[\bar{\mu}]$ a diagonal matrix containing the eigenvalues of the approximation and $q(0) \in \mathbb{R}^{\tilde{n}}$ regrouping the scalar $q_p(0)$. So, the transition matrix is defined as

$$\tilde{A} = \mathcal{Z}\left[\bar{\mu}\right] \mathcal{Z}^{-1} \in \mathbb{R}^{\tilde{n} \times \tilde{n}}. \tag{3.25}$$

With the observation matrix of the approximation ($\tilde{\mathbf{C}}$) in Equation (3.21), and Equations (3.11) and (3.22), it comes

$$\sum_{p=1}^{\tilde{n}} Y_p \exp\left(\bar{\mu}_p t\right) q_p(0) = \tilde{\mathbf{C}} \sum_{p=1}^{\tilde{n}} Z_p \exp\left(\bar{\mu}_p t\right) q_p(0). \tag{3.26}$$

Or, in a matrix form

$$\tilde{\Phi} \exp\left(\left[\bar{\mu}\right] t\right) q(0) = \tilde{\mathbf{C}} \mathcal{Z} \exp\left(\left[\bar{\mu}\right] t\right) q(0) \tag{3.27}$$

with $\tilde{\Phi} \in \mathbb{R}^{r \times \tilde{n}}$ regrouping the amplitudes of the observations modes. The observation matrix $\tilde{\mathbf{C}}$ is expressed as

$$\tilde{\mathbf{C}} = \tilde{\Phi} \mathcal{Z}^{-1} \in \mathbb{R}^{r \times \tilde{n}}. \tag{3.28}$$

To express the full discrete state-space, the discrete transition matrix and the input matrix are needed. First of all, let us define the observation of the state-space using Equation (1.21)

$$y(t) = C(t)\Phi(t)x(0) + C(t)\Phi(t) \int_0^t \Phi(\tau)^{-1} B_c(\tau) v(\tau) d\tau. \tag{3.29}$$

Using the approximation of the observation of the homogeneous part (Equation (3.11)) and Equations (3.27), the approximation of $C(t)\Phi(t)$ is defined in matrix form

$$C(t)\Phi(t) \simeq \tilde{\Phi} \exp\left(\left[\bar{\mu}\right] t\right) \tilde{\Psi}, \tag{3.30}$$

with $\tilde{\Psi}$ such that $q(0) = \tilde{\Psi} x(0)$. To express the approximation of $\Phi(\tau)^{-1}$, the approximation of the homogeneous part of the state-space is needed. With the same Fourier harmonics as $\hat{y}_h(t)$

$$\hat{x}_h(t) = \sum_{p=1}^{\tilde{n}} X_p \exp\left(\bar{\mu}_p t\right) q_p(0), \tag{3.31}$$

leads to the approximation

$$\Phi(\tau) \simeq \mathcal{X} \exp\left(\left[\bar{\mu}\right] \tau\right]) \tilde{\Psi}, \tag{3.32}$$

with $\mathcal{X} \in \mathbb{R}^{n \times \tilde{n}}$ regrouping the vectors X_p. For simplicity, if one assumes $t = k\Delta t$ (k an integer), the approximation of the observation in discrete time is defined as

$$\hat{y}_k = \tilde{\Phi} \exp\left(\left[\bar{\mu}\right] k\Delta t\right) q(0) + \tilde{\Phi} \exp\left(\left[\bar{\mu}\right] k\Delta t\right) \sum_{i=1}^{k} I_i v_{i-1}, \tag{3.33}$$

with

$$I_i = \int_{(i-1)\Delta t}^{i\Delta t} \exp\left(-\left[\bar{\mu}_p\right] \tau\right) \mathcal{X}^{\dagger} B_c(\tau) d\tau, \tag{3.34}$$

where $(\cdot)^{\dagger}$ denotes the Moore-Penrose pseudo inverse and with the hypothesis of a zero-order hold on $v(t)$. With Equation (3.28), it is possible to express the observation matrix into $\hat{y}_{k+1}$ such that

$$\hat{y}_{k+1} = \tilde{\mathbf{C}} \mathcal{Z} \exp\left(\left[\bar{\mu}\right] (k+1)\Delta t\right) q(0) + \tilde{\mathbf{C}} \mathcal{Z} \exp\left(\left[\bar{\mu}\right] (k+1)\Delta t\right) \sum_{i=1}^{k+1} I_i v_{i-1}. \tag{3.35}$$

The state vector in discrete time z_k at time index $k+1$ is expressed as

$$z_{k+1} = \mathcal{Z}\exp\left(\left[\bar{\mu}\right](k+1)\Delta t\right)q(0) + \mathcal{Z}\exp\left(\left[\bar{\mu}\right](k+1)\Delta t\right)\sum_{i=1}^{k+1} I_i v_{i-1}. \tag{3.36}$$

Using the definition of z_k

$$z_{k+1} = \tilde{\mathbf{A}} z_k + \mathbf{B}_k v_k. \tag{3.37}$$

with $\tilde{\mathbf{A}} = \exp\left(\tilde{A}\Delta t\right)$ and $\mathbf{B}_k = \mathcal{Z}\exp\left(\left[\bar{\mu}\right](k+1)\Delta t\right) I_{k+1}$.

Finally, adding the term of the excitation in the observation leads to the discrete state-space of the approximation defined as

$$\begin{cases} z_{k+1} = \tilde{\mathbf{A}} z_k + \mathbf{B}_k v_k \\ \quad y_k = \tilde{\mathbf{C}} z_k + \mathbf{D}_k v_k + \tilde{w}_k \end{cases}, \tag{3.38}$$

with $\tilde{w_k} = w_k + \varepsilon_{y,\,k}$, where $\varepsilon_{y,\,k}$ is the approximation error of the observation (supposed to be with zero mean, independent with moments of same order as the noises). $\mathbf{B}_k$ and $\mathbf{D}_k = D(k\Delta t)$ are periodic matrices of period $T_d = \frac{T}{\Delta t}$. Assume $\tilde{\mathbf{A}}$ has all non zero distinct eigenvalues with modulus less than 1.

Proof. let us prove the T_d periodicity of $\mathbf{B}_k$. Using Equations (3.33) and (3.34)

$$\mathbf{B}_k = \mathcal{Z}\exp\left(\left[\bar{\mu}\right](k+1)\Delta t\right) I_{k+1}. \tag{3.39}$$

Let us express $\mathbf{B}_{k+T_d}$, so

$$\mathbf{B}_{k+T_d} = \mathcal{Z}\exp\left(\left[\bar{\mu}\right](k+1)\Delta t\right)\exp\left(\left[\bar{\mu}\right]T_d\Delta t\right) I_{k+T_d+1}, \tag{3.40}$$

moreover

$$I_{k+T_d+1} = \int_{(k+T_d)\Delta t}^{(k+T_d+1)\Delta t} \exp\left(-\left[\bar{\mu}\right]\tau\right)\mathcal{X}^{\dagger}B_c(\tau)d\tau \tag{3.41}$$

$$= \int_{(k)\Delta t}^{(k+1)\Delta t} \exp\left(-\left[\bar{\mu}\right](\tau+T_d)\right)\mathcal{X}^{\dagger}B_c(\tau+T_d)d\tau. \tag{3.42}$$

But $B_c(\tau)$ is a periodic matrix, so $B_c(\tau+T_d) = B_c(\tau)\ \forall\tau\in\mathbb{R}^+$, thus

$$I_{k+T_d+1} = \exp\left(-\left[\bar{\mu}\right]T_d\Delta t\right) I_{k+1}. \tag{3.43}$$

Finally $\mathbf{B}_k = \mathbf{B}_{k+T_d}$ □

The state-space expression of the approximation has been defined, now it will be demonstrated that a subspace method can be used to identify the matrices $\tilde{\mathbf{A}}$ and $\tilde{\mathbf{C}}$.

3.6 Subspace Factorization

The objective is to prove that a subspace method can be used to identify the Fourier harmonics of the Floquet modes of the approximation defined in Equation (3.38). As, the Fourier harmonics can be retrieved in the matrices $\tilde{\mathbf{A}}$ and $\tilde{\mathbf{C}}$, those two matrices need to be estimated with the subspace method. Here the SSI covariance driven presented in Section 2.2.2 is used. The first step is the computation of the Hankel matrix of correlations defined by

$$\hat{H} = \mathcal{Y}^{+} \left(\mathcal{Y}^{-}\right)^{T}. \tag{3.44}$$

Let us define the submatrices $\hat{H}_{m,n}$ of $\hat{H}$ by restriction to indices (m, n) $m \in [1 : p + 1]$ and $n \in [1 : q]$ by

$$\hat{H}_{m,n} = \mathcal{Y}^{+}_{m} \left(\mathcal{Y}^{-}\right)^{T}_{n} \ , \tag{3.45}$$

with $\mathcal{Y}^{+}_{m}$ the m–th block line of $\mathcal{Y}^{+}$ and $\left(\mathcal{Y}^{-}\right)^{T}_{n}$ the n–th block column of $\left(\mathcal{Y}^{-}\right)^{T}$.

$$\begin{aligned}
\mathcal{Y}^{+}_{m} &= \begin{bmatrix} y_{q+m} & y_{q+m+1} & \dots & y_{q+N+m-1} \end{bmatrix} \\
\left(\mathcal{Y}^{-}\right)^{T}_{n} &= \begin{bmatrix} y^{T}_{q+1-n} & y^{T}_{q+2-n} & \dots & y^{T}_{q+N+1-n} \end{bmatrix}^{T}
\end{aligned}$$

Let $k_m = q + m + k$ and $k_n = q + 1 - n + k$ with $k_m = k_n + m + n - 1$, it yields

$$\hat{H}_{m,n} = \frac{1}{N} \sum_{k=0}^{N-1} \left(\tilde{\mathbf{C}} z_{k_m} + \mathbf{D}_{k_m} v_{k_m} + \tilde{w}_{k_m}\right) \left(\tilde{\mathbf{C}} z_{k_n} + \mathbf{D}_{k_n} v_{k_n} + \tilde{w}_{k_n}\right)^{T}. \tag{3.46}$$

Let us define z_{k_m} function of z_{k_n}

$$z_{k_m} = \tilde{\mathbf{A}}^{m+n-1} z_{k_n} + \sum_{j=1}^{m+n-1} \tilde{\mathbf{A}}^{j-1} \mathbf{B}_{k_m-j} v_{k_m-j}. \tag{3.47}$$

From this expression, the submatrix of the Hankel matrix can be defined as

$$\begin{aligned}
\hat{H}_{m,n} = {} & \tilde{\mathbf{C}} \tilde{\mathbf{A}}^{m+n-2} \frac{1}{N} \sum_{k=0}^{N-1} \left(\tilde{\mathbf{A}} z_{k_n} z^{T}_{k_n} \tilde{\mathbf{C}}^{T} + \tilde{\mathbf{A}} z_{k_n} v^{T}_{k_n} \mathbf{D}^{T}_{k_n} + \tilde{\mathbf{A}} z_{k_n} \tilde{w}^{T}_{k_n}\right) \\
& + \frac{1}{N} \sum_{k=0}^{N-1} \sum_{j=1}^{m+n-1} \tilde{\mathbf{C}} \tilde{\mathbf{A}}^{j-1} \left(\mathbf{B}_{k_m-j} v_{k_m-j} z^{T}_{k_n} \tilde{\mathbf{C}}^{T} + \mathbf{B}_{k_m-j} v_{k_m-j} v^{T}_{k_n} \mathbf{D}^{T}_{k_n} + \mathbf{B}_{k_m-j} v_{k_m-j} \tilde{w}^{T}_{k_n}\right) \\
& + \frac{1}{N} \sum_{k=0}^{N-1} \left(\mathbf{D}_{k_m} v_{k_m} z^{T}_{k_n} \tilde{\mathbf{C}}^{T} + \mathbf{D}_{k_m} v_{k_m} v^{T}_{k_n} \mathbf{D}^{T}_{k_n} + \mathbf{D}_{k_m} v_{k_m} \tilde{w}^{T}_{k_n}\right) \\
& + \frac{1}{N} \sum_{k=0}^{N-1} \left(\tilde{w}_{k_m} z^{T}_{k_n} \tilde{\mathbf{C}}^{T} + \tilde{w}_{k_m} v^{T}_{k_n} \mathbf{D}^{T}_{k_n} + \tilde{w}_{k_m} \tilde{w}^{T}_{k_n}\right).
\end{aligned} \tag{3.48}$$

Leading to

$$\begin{aligned}
\hat{H}_{m,n} = {} & \tilde{\mathbf{C}}\tilde{\mathbf{A}}^{m+n-2}\frac{1}{N}\sum_{k=0}^{N-1}\left(\tilde{\mathbf{A}} z_{k_n} z_{k_n}^T \tilde{\mathbf{C}}^T + \tilde{\mathbf{A}} z_{k_n} v_{k_n}^T \mathbf{D}_{k_n}^T + \tilde{\mathbf{A}} z_{k_n} \tilde{w}_{k_n}^T\right) \\
& + \tilde{\mathbf{C}}\tilde{\mathbf{A}}^{m+n-2}\frac{1}{N}\sum_{k=0}^{N-1}\left(\mathbf{B}_{k_n} v_{k_n} z_{k_n}^T \tilde{\mathbf{C}}^T + \mathbf{B}_{k_n} v_{k_n} v_{k_n}^T \mathbf{D}_{k_n}^T + \mathbf{B}_{k_n} v_{k_n} \tilde{w}_{k_n}^T\right) \\
& + \frac{1}{N}\sum_{k=0}^{N-1}\sum_{j=1}^{m+n-2}\tilde{\mathbf{C}}\tilde{\mathbf{A}}^{j-1}\left(\mathbf{B}_{k_m-j} v_{k_m-j} z_{k_n}^T \tilde{\mathbf{C}}^T + \mathbf{B}_{k_m-j} v_{k_m-j} v_{k_n}^T \mathbf{D}_{k_n}^T + \mathbf{B}_{k_m-j} v_{k_m-j} \tilde{w}_{k_n}^T\right) \\
& + \frac{1}{N}\sum_{k=0}^{N-1}\left(\mathbf{D}_{k_m} v_{k_m} z_{k_n}^T \tilde{\mathbf{C}}^T + \mathbf{D}_{k_m} v_{k_m} v_{k_n}^T \mathbf{D}_{k_n}^T + \mathbf{D}_{k_m} v_{k_m} \tilde{w}_{k_n}^T\right) \\
& + \frac{1}{N}\sum_{k=0}^{N-1}\left(\tilde{w}_{k_m} z_{k_n}^T \tilde{\mathbf{C}}^T + \tilde{w}_{k_m} v_{k_n}^T \mathbf{D}_{k_n}^T + \tilde{w}_{k_m} \tilde{w}_{k_n}^T\right).
\end{aligned} \tag{3.49}$$

Finally

$$\hat{H}_{m,n} = \tilde{\mathbf{C}}\tilde{\mathbf{A}}^{m+n-2}\hat{G}_n + o(1), \tag{3.50}$$

with $o(1)$ a matrix converging to zero with N, the demonstration is developed in Appendix C.1. Applying Lemma 3 of [12] under the moment hypotheses presented in Appendix B.3, then

$$\hat{G}_n(N) = \frac{1}{N}\sum_{k=0}^{N-1}\tilde{\mathbf{A}} z_{k_n} z_{k_n}^T \tilde{\mathbf{C}}^T + \mathbf{B}_{k_n} v_{k_n} v_{k_n}^T \mathbf{D}_{k_n}^T. \tag{3.51}$$

Firstly, assume that N is a multiple of T_d,

$$\hat{G}_n(N) = \frac{1}{N}\tilde{\mathbf{A}}\sum_{k=0}^{N-1}\left[z_{k_n} z_{k_n}^T\right]\tilde{\mathbf{C}}^T + \frac{1}{T_d}\sum_{j=1}^{T_d}\mathbf{B}_j \frac{T_d}{N}\sum_{\tilde{k}_j}\left[v_{\tilde{k}_j} v_{\tilde{k}_j}^T\right]\mathbf{D}_j^T, \tag{3.52}$$

where $\tilde{k}_j$ denote the indices corresponding to the specific instants of the period and where $\mathbf{B}_j$ and $\mathbf{D}_j$ are periodic matrices. Let us demonstrate that $\hat{G}_n$ and $\hat{H}_{m,n}$ converge.

Let $l \in [1; T_d[$ an integer, the matrix $\hat{G}_n$ estimated with $N+l$ data is defined as

$$\begin{aligned}
\hat{G}_n(N+l) = {} & \frac{1}{N+l}\tilde{\mathbf{A}}\sum_{k=0}^{N+l-1}\left[z_{k_n} z_{k_n}^T\right]\tilde{\mathbf{C}}^T + \frac{1}{T_d}\sum_{j=1}^{T_d}\mathbf{B}_j \frac{T_d}{N+l}\sum_{\tilde{k}_j}\left[v_{\tilde{k}_j} v_{\tilde{k}_j}^T\right]\mathbf{D}_j^T \\
& + \frac{1}{N+l}\sum_{k=N}^{N+l-1}\mathbf{B}_{k_n} v_{k_n} v_{k_n}^T \mathbf{D}_{k_n}^T.
\end{aligned} \tag{3.53}$$

The input and feedthrough matrices are bounded finite matrices and v_k is bounded in moments, $\sup_{k\geq 0}\mathbb{E}\left(\|\mathbf{B}_k v_k v_k^T \mathbf{D}_k\|^2\right) \leq C < \infty$. So, with the theorem from Appendix B.4

$$\lim_{N\to\infty}\frac{1}{N+l}\sum_{k=N}^{N+l-1}\mathbf{B}_{k_n} v_{k_n} v_{k_n}^T \mathbf{D}_{k_n}^T = 0, \tag{3.54}$$

also

$$\lim_{N\to\infty}\frac{1}{T_d}\sum_{j=1}^{T_d}\mathbf{B}_j\frac{T_d}{N+l}\sum_{\tilde{k}_j}\left[v_{\tilde{k}_j}v_{\tilde{k}_j}^T\right]\mathbf{D}_j^T=\lim_{N\to\infty}\frac{1}{T_d}\sum_{j=1}^{T_d}\mathbf{B}_j\frac{T_d}{N}\sum_{\tilde{k}_j}\left[v_{\tilde{k}_j}v_{\tilde{k}_j}^T\right]\mathbf{D}_j^T. \tag{3.55}$$

In Appendix C.2 it is proven that $\frac{1}{N}\tilde{\mathbf{A}}\sum_{k=0}^{N-1}\left[z_{k_n}z_{k_n}^T\right]\tilde{\mathbf{C}}^T$ converges to a unique limit. Consequently, $\hat{G}_n(N)$ converges.

Let us express $\hat{G}_{n+1}(N)$. $\hat{G}_{n+1}(N)$ is $\hat{G}_n(N)$ shifted to the past. Precisely, $\hat{G}_n(N)$ is defined with the index from $q+1-n$ to $q+N+1-n$ while $\hat{G}_{n+1}(N)$ is defined with the index from $q-n$ to $q+N-n$. So, $\hat{G}_{n+1}(N)$ can be expressed in function of $\hat{G}_n(N)$

$$\begin{aligned}\hat{G}_{n+1}(N)-\hat{G}_n(N)=&\frac{1}{N}\sum_{k=0}^{N-1}\tilde{\mathbf{A}}z_{k_{n+1}}z_{k_{n+1}}^T\tilde{\mathbf{C}}^T+\mathbf{B}_{k_{n+1}}v_{k_{n+1}}v_{k_{n+1}}^T\mathbf{D}_{k_{n+1}}^T\\&-\frac{1}{N}\sum_{k=0}^{N-1}\tilde{\mathbf{A}}z_{k_n}z_{k_n}^T\tilde{\mathbf{C}}^T+\mathbf{B}_{k_n}v_{k_n}v_{k_n}^T\mathbf{D}_{k_n}^T\end{aligned} \tag{3.56}$$

In Appendix C.2, it has been proven that the initial index had no impact on the limit of the first term, consequently

$$\hat{G}_{n+1}(N)-\hat{G}_n(N)=\frac{1}{N}\left(\mathbf{B}_{q+N+1-n}v_{q+N+1-n}v_{q+N+1-n}^T\mathbf{D}_{q+N+1-n}^T-\mathbf{B}_{q-n}v_{q-n}v_{q-n}^T\mathbf{D}_{q-n}^T\right) \tag{3.57}$$

$\sup_{k\geq 0}\mathbb{E}\left(\|\mathbf{B}_k v_k v_k^T\mathbf{D}_k^T\|^2\right)\leq C<\infty$, finally, with the theorem from Appendix B.4

$$\lim_{N\to\infty}\left(\hat{G}_{n+1}(N)-\hat{G}_n(N)\right)=0. \tag{3.58}$$

Analogously for all i and all n such that $1\leq n<n+i\leq q$, $\lim_{N\to\infty}\left(\hat{G}_{n+i}(N)-\hat{G}_n(N)\right)=0$. Finally, $\lim_{N\to\infty}\hat{G}_n(N)=G$ is invariant regarding the index n.

From the previous result, the matrix $\hat{H}$ can be expressed term by term as

$$\lim_{N\to\infty}\hat{H}=\begin{bmatrix}\tilde{\mathbf{C}}G & \tilde{\mathbf{C}}\tilde{\mathbf{A}}G & \dots & \tilde{\mathbf{C}}\tilde{\mathbf{A}}^{q-1}G\\ \tilde{\mathbf{C}}\tilde{\mathbf{A}}G & \tilde{\mathbf{C}}\tilde{\mathbf{A}}^2G & \dots & \tilde{\mathbf{C}}\tilde{\mathbf{A}}^qG\\ \vdots & \vdots & \ddots & \vdots\\ \tilde{\mathbf{C}}\tilde{\mathbf{A}}^pG & \tilde{\mathbf{C}}\tilde{\mathbf{A}}^{p+1}G & \dots & \tilde{\mathbf{C}}\tilde{\mathbf{A}}^{p+q-1}G\end{bmatrix}. \tag{3.59}$$

The Hankel matrix can be factorized such that $\hat{H}=O_pC_q$, where O_p denotes the observability matrix and C_q the controllability matrix,

$$O_p=\begin{bmatrix}\tilde{\mathbf{C}}\\ \tilde{\mathbf{C}}\tilde{\mathbf{A}}\\ \vdots\\ \tilde{\mathbf{C}}\tilde{\mathbf{A}}^p\end{bmatrix}\quad\text{and}\quad C_q=\begin{bmatrix}G & \tilde{\mathbf{A}}G & \dots & \tilde{\mathbf{A}}^{q-1}G\end{bmatrix}. \tag{3.60}$$

The observability matrix and the controllability matrix are somewhat similar to those in

Equation (2.17) derived under the usual LTI assumptions. Thus, the Fourier harmonics of the approximation can be computed with the method used in the stochastic subspace identification (Section 2.2.2). It implies that the computation of Gaussian confidence intervals is possible, similar to what was presented in Section 2.2.3.

3.7 Conclusion

To enable the identification of the rotating wind turbines, defined as LTP systems, it has been chosen to approximate them to perform identification with state-of-the-art methods. First, it has been proposed to express an LTP system as an LTI system of finite size (under nonstationary inputs). It is observed that only a few Fourier harmonics contribute to the Floquet modes, so only a limited number of harmonics can be retained. If illustrated on a wind turbine model, this description is valid for any LTP system. The LTI approximation and the impact of the truncation have been tested and validated on an academic model of a wind turbine, as well as the DTU 10MW wind turbine model. On the latter, Floquet modes are illustrated. After that, the state-space expression of the approximation has been defined and the use of a subspace method and the uncertainty computation has been demonstrated. A part of this work has been presented during the conference Safeprocess [21].

To continue, the method of uncertainty quantification will be validated using an identification of the academic model of wind turbine. Then the identification of the LTP systems approximation will be tested on rotating wind turbine models.

Chapter 4

VALIDATION OF THE IDENTIFICATION OF THE APPROXIMATION

Abstract

This Chapter is dedicated to the validation and the application of the identification of the approximation. To begin, the application of the uncertainty quantification method on the approximation of an LTP system is validated, with an example of identification on the academic model of a wind turbine. Then, the SSI method is used to identify the approximation of wind turbine models with a gradual complexity. Precisely, from the identification of the academic model with a constant rotational speed, to the identification of the DTU 10MW model under a turbulent wind and a variable rotational speed. In all identifications, the identified modes correspond to the Fourier harmonics of the Floquet modes defined by the approximation. Finally, it is shown that an existing identification method can also identify the approximation, but with a higher computational cost and complexity.

4.1 Introduction

In the previous Chapter, an approximation of the free vibrations of LTP systems has been defined, through the approximation of the Floquet modes as a sum of the non-zero Fourier harmonics. This approximation has been validated theoretically and with a study of the academic model of wind turbine. Then, it has been demonstrated that theoretically the Stochastic Subspace Identification can be used to identify the Fourier harmonics that compose the approximation. So, the next step is to apply and validate the identification of the approximation of LTP systems.

To do so, first, the uncertainty quantification from an identification of the approximation of an LTP system is validated with a Monte Carlo simulation using the academic model of wind turbine, as the uncertainties will be computed in every example of identification. Finally, the method is validated on different examples with a gradually increasing difficulty, with a comparison between the identified modes and the modes from the approximation.

4.2 Validation of the uncertainty quantification method

In the previous Chapter, it was demonstrated that the uncertainty quantification method can be used in addition to the identification of LTP system approximation, now let us validate it. Here, a Monte Carlo simulation is performed on the academic model of a wind turbine (with the same conditions presented in Section 3.3) to compare the estimated uncertainties with the empirical uncertainties. The model is identified using only the measurement of the accelerations of the rotor DOF. 1000 runs are performed for the Monte Carlo simulation to get enough points and estimate accurately enough the order of magnitudes of the uncertainties. The stochastic parameters of the simulations are the inputs generated with the same Gaussian law. The generated data from the simulation are sampled at 25 Hz during 600 s. For each Monte Carlo run, the identification of the wind turbine model is made in the same order, equal to 8. This choice is made as it represents the number of Fourier harmonics in the approximation seen through the rotor DOF (i.e. the number of peaks in the PSD in Figure 3.1). Also, the identifications are performed with the same Hankel matrix size (q+1=p=100). From the 1000 Monte Carlo runs, the average values and standard deviations are deduced for the frequency and damping of each Fourier harmonic. They are compared to the average standard deviation values computed with the uncertainty methods (denoted as estimation in the following). As these values are also uncertain, 100 runs are performed and the average values. Results are summarized in Table 4.1 and illustrated in Figure 4.1 for the fourth Fourier harmonic.

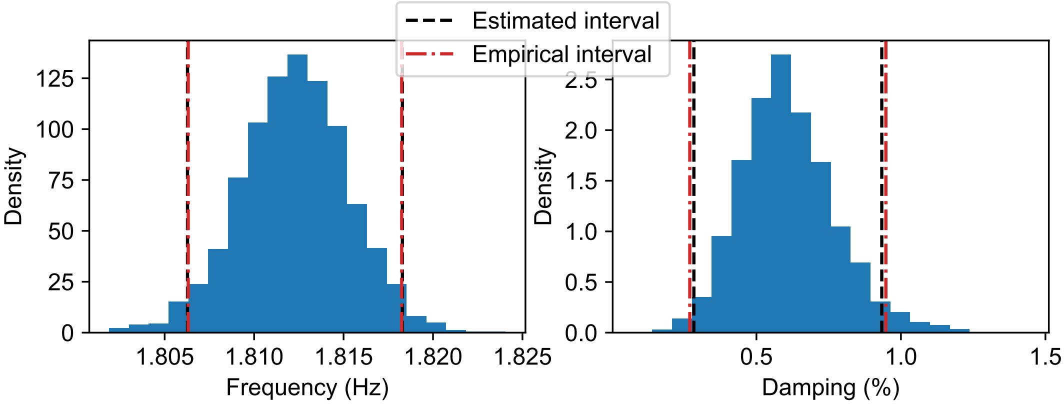

Figure 4.1 – Histogram of the identified frequency and damping of the fourth Fourier harmonics of the approximation and the comparison of the 95% confidence interval

In Figure 4.1, the histograms are obtained from the Monte Carlo simulation and the empirical 95% confidence interval (in red) based on the uncertainties of the identified frequencies and damping. The estimated 95% confidence interval (in black) are computed based on the mean of the estimated standard deviation. With this figure, it can be seen that for the studied Fourier harmonic, the confidence intervals are close.

	Frequency (Hz)			Damping (%)		
Id Number	f	$\sigma_{f\ MC}$ $\times 10^{-3}$	$\sigma_{f\ est}$ $\times 10^{-3}$	ξ	$\sigma_{\xi\ MC}$ $\times 10^{-1}$	$\sigma_{\xi\ est}$ $\times 10^{-1}$
1	1.693	2.44 ± 0.10	2.25 ± 0.10	0.712	1.42± 0.06	1.32 ± 0.05
3	1.247	2.73 ± 0.12	2.53 ± 0.10	0.959	1.97± 0.09	2.06 ± 0.09
4	1.812	2.98 ± 0.13	3.00 ± 0.14	0.609	1.70± 0.07	1.63 ± 0.08
6	1.367	2.71 ± 0.12	2.52 ± 0.12	0.813	1.85± 0.08	1.85 ± 0.10
7	0.641	0.90 ± 0.04	0.77 ± 0.04	0.369	1.48± 0.06	1.29 ± 0.07
9	1.088	3.04 ± 0.13	2.44 ± 0.28	0.258	2.49± 0.11	2.40 ± 0.24
10	0.746	0.82 ± 0.04	0.79 ± 0.04	0.301	1.16± 0.05	1.08 ± 0.06
11	0.670	0.75 ± 0.04	0.70 ± 0.04	0.269	1.29± 0.06	1.00 ± 0.05

Table 4.1 – Comparison of the empirical standard deviation ($\sigma_{.\ MC}$) and the estimated standard deviation ($\sigma_{.\ est}$) of the frequency and damping associated with there 95% confidence interval

In Table 4.1, the standard deviations values of the frequency and damping of all the Fourier harmonics can be compared, but as the values are uncertain, the confidence interval should be compared instead. Using the central limit theorem (remind in Appendix B.2), the estimated confidence interval of the estimated standard deviation is computed using the standard deviation of the estimation, such that

$$CI_{est}\left(95\%\right) = 4\frac{\sigma}{\sqrt{n}}, \tag{4.1}$$

for n estimations of the standard deviation used to compute the mean estimation ($\sigma_{\cdot\ est}$). Then, the confidence interval of the empirical standard deviation ($\sigma_{\cdot\ MC}$) is based on the theorem of Cochran

$$\frac{\left(n-1\right)\hat{\sigma}^2}{\chi^2_{1-\alpha/2,n-1}} \leq \sigma^2 \leq \frac{\left(n-1\right)\hat{\sigma}^2}{\chi^2_{\alpha/2,n-1}}, \tag{4.2}$$

where $\hat{\sigma}^2$ is the estimation of the variance σ^2 using a n random sample, α the parameter of the confidence interval ($\alpha = 0.05$ for a 95% confidence interval), $\chi^2_{\alpha/2,n-1}$ and $\chi^2_{1-\alpha/2,n-1}$ are the appropriate left-hand and right-hand values respectively of a chi-square distribution with $n-1$ degrees of freedom. The inequality leads to the following confidence interval

$$CI_{emp}\left(95\%\right) = \sqrt{\frac{\left(n-1\right)\hat{\sigma}^2}{\chi^2_{0.025,n-1}}} - \sqrt{\frac{\left(n-1\right)\hat{\sigma}^2}{\chi^2_{0.975,n-1}}}. \tag{4.3}$$

So, as for the fourth Fourier harmonic, the empirical and estimated standard deviations are close for the frequency and damping of all the identified Fourier harmonics. Then, the associated 95% confidence intervals can be compared, and one can see that all the confidence intervals are crossing each other, except for a couple of frequencies (7 and 9) and damping (7 and 11). Those results are similar to those described in [108] with an application to a steel beam. As a conclusion, estimated uncertainties match with the empirical uncertainties, validating the uncertainty computation associated with the identification of the approximation of LTP systems.

To continue the validation of the uncertainties of the identified modes, the uncertainties of the mode shapes need to be validated. To do so, the uncertainty of the MAC is used, as it is directly related to the mode shapes. As said in Section 2.2.3, the MAC follows a Gaussian distribution when the mode shapes are different and an inverse shifted chi-square distribution when the mode shapes are equal. To compare the Gaussian process, the standard deviation is used, whereas for the chi square process, the lower bound of the 95% quantile is used (as the upper bound is equal to 1).

Here the MAC (Equation (2.32)) is computed between the mode shapes of successive identification, meaning that the MAC matrix is computed 999 times ($MAC(n, n+1)$, $n \in [0, 999]$). First, the mean MAC matrix is analyzed and it is composed of values close to 1 or 0 because the mode shapes of the different identified Fourier harmonics are identical or completely orthogonal. Consequently, there are no MAC values that can be described with a Gaussian distribution and this case cannot be studied with the selected example. So the MAC values that will be studied will only be described with an inverse shifted chi-square distribution.

To validate the estimations of the uncertainties of the MAC, the diagonal values of the MAC matrix are studied, as those MAC values are computed between the same mode shapes. Similarly to the frequency and damping, empirical 95% confidence intervals are deduced from the 1000

Monte Carlo runs and compared with the estimated 95% confidence interval obtained with the means of 100 uncertainty computation. In Figure 4.2, the empirical and estimated lower bounds of the 95% confidence intervals are displayed jointly with the histogram of the MAC values, for two Fourier harmonics. Firstly, as expected, the shape of the histograms is close to the shape of an inverse shifted chi-square distribution described in [58].

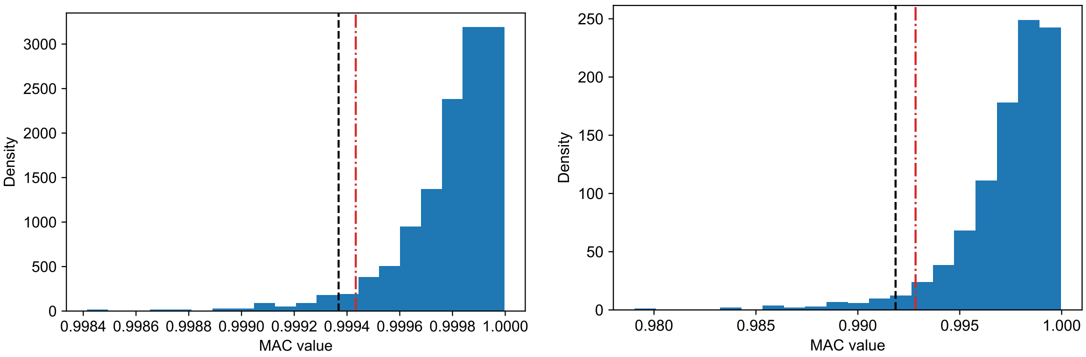

(a) 10–th Fourier harmonic (b) 11–th Fourier harmonic

Figure 4.2 – Histograms of MAC values for two Fourier harmonics with the empirical and estimated confidence interval, (- - -): Estimated 95% confidence interval, (-·-·): Empirical 95% confidence interval

Secondly, the empirical and estimated lower bounds are close, 0.9994 for both the empirical and the estimated for the 10–th Fourier harmonic, 0.9928 for the empirical and 0.9919 for the estimated for the 11–th Fourier harmonic. But, as the estimations of the lower bounds are also uncertain, the associated confidence intervals are needed. In Table 4.2, all the empirical and estimated lower bounds of the confidence intervals are reported, with also the upper and lower bounds of the estimated ones. For all the studied MAC values, the empirical lower bounds are in the confidence interval of the estimated lower bounds, which validates the uncertainty computation of the MAC (in the configuration of identical mode shapes, which validates also the uncertainty quantification of the modes shape.

id Number	MAC	$1-\text{quant}_{MC}(5\%)$	$1-\text{quant}_{est}(5\%)$	lower bound $1-\text{quant}_{est}(5\%)$	upper bound $1-\text{quant}_{est}(5\%)$
1	0.9998	$6.06{\cdot}10^{-4}$	$6.59{\cdot}10^{-4}$	$4.29{\cdot}10^{-4}$	$9.91{\cdot}10^{-4}$
3	0.9997	$8.87{\cdot}10^{-4}$	$1.02{\cdot}10^{-3}$	$5.59{\cdot}10^{-4}$	$2.17{\cdot}10^{-3}$
4	0.9995	$1.48{\cdot}10^{-3}$	$1.86{\cdot}10^{-3}$	$8.35{\cdot}10^{-4}$	$3.56{\cdot}10^{-3}$
6	0.9996	$1.16{\cdot}10^{-3}$	$1.45{\cdot}10^{-3}$	$7.81{\cdot}10^{-4}$	$3.15{\cdot}10^{-3}$
7	0.9933	$1.84{\cdot}10^{-2}$	$1.89{\cdot}10^{-2}$	$1.01{\cdot}10^{-2}$	$3.87{\cdot}10^{-2}$
9	0.9848	$4.55{\cdot}10^{-2}$	$3.93{\cdot}10^{-2}$	$1.70{\cdot}10^{-2}$	$8.03{\cdot}10^{-2}$
10	0.9998	$5.67{\cdot}10^{-4}$	$6.32{\cdot}10^{-4}$	$3.08{\cdot}10^{-4}$	$1.07{\cdot}10^{-3}$
11	0.9973	$7.17{\cdot}10^{-3}$	$8.15{\cdot}10^{-3}$	$3.00{\cdot}10^{-3}$	$3.39{\cdot}10^{-2}$

Table 4.2 – Comparison of the empirical and estimated 5% quantile value of the MAC criterion between same mode shapes

4.3 Identification: application to an academic model of wind turbine

The identification method has been defined, now the method will be validated comparing the identified modal parameters (frequencies, dampings and mode shapes) with the corresponding approximated values computed with the system matrices. To compare the identified parameters, the previously validated uncertainty computation method will be used.

In this section, the identified system is the academic model of a wind turbine with the same configuration that is used in Section 3.3. The simulated outputs are the accelerations of all the DOF sampled at 25 Hz during 600 s. Two cases will be considered, first with the simulation of the system at a constant rotational speed ($\Omega = 1.4$ rad/s), and second with a simulation with a variable rotational speed. Theoretically, the approximation and the identification are defined for a system with a constant period, so using data computed with a simulation with a variable rotational speed, it will be seen if it is possible to identify the approximation associated with the studied system.

The approximation of the academic model of wind turbine is computed with a minimal participation factor of 5%, and the rotational speed used to compute the Floquet modes is the mean rotational speed of the simulation for each case.

4.3.1 Case 1: constant rotational speed

The identification is performed using simultaneously the acceleration corresponding to the five DOF of the wind turbine model and the Hankel matrix is defined with $p = 75$. As said in Section 2.2.2, the model order of the identified system is supposed to be unknown, so a stabilization diagram is used to overcome this problem. The stabilization diagram of the identification is presented in Figure 4.3, where the frequencies of the identified modes computed for order 2 to order 20 are displayed. Here, only the physical identified modes are displayed, with a criteria on the damping: it should be positive (because the system is stable) and below 10% (a user parameter defined from the studied system). Also, the uncertainties of the frequencies are added to the diagram with error bars, which correspond to the standard deviations. Only the identified modes with a standard deviation of frequency below 0.05 Hz are displayed in the diagram. The dashed lines in the diagram represent the frequencies of the Fourier harmonics of the approximation setting the reference frequencies.

It can be seen from Figure 4.3 that the alignment of the identified frequencies are corresponding to the dashed lines. To extract the modal parameters of the stabilization diagram, a clustering method described in Appendix E is used. Then, the identified parameters are compared with the approximation in Table 4.3, where $(\cdot)_{ap}$ denotes a quantity of the approximation modes and $(\cdot)_{iden}$ a quantity of the identified modes. In this comparison, the modes are paired using the MAC criterion and the gap of frequency. For all modes, the identified frequencies are close to the approximation, where almost all the approximation values are in the 99% confidence interval defined as: $f_{iden} - 3\sigma_f < f_{ap} < f_{iden} + 3\sigma_f$. The same is seen for the damping. As all the MAC values are 1, the mode shapes are also corresponding. Consequently, it can be concluded that the identified modes are the modes defined in the approximation.

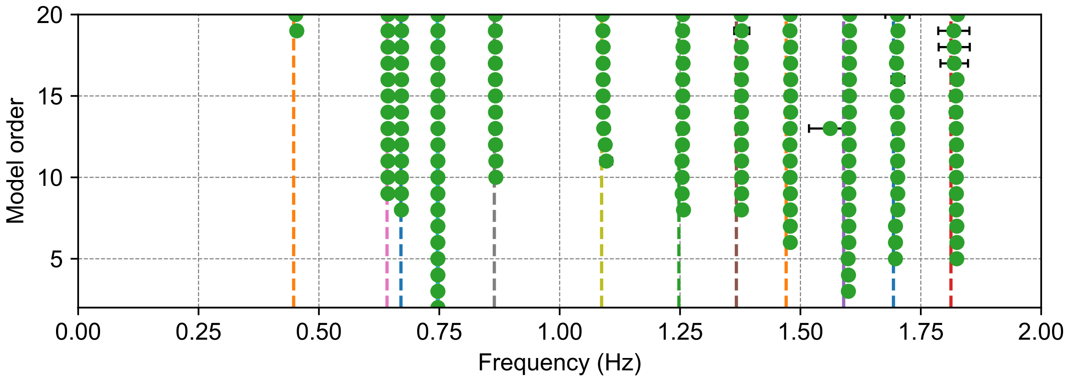

Figure 4.3 – Stabilization diagram from acceleration measures of all DOF from a simulation with a constant rotational speed - (- - -): reference frequencies - (●): identified frequencies

f_{ap} (Hz)	f_{iden} (Hz)	σ_f (Hz)	ξ_{ap} (%)	ξ_{iden} (%)	σ_ξ (%)	MAC
1.693	1.698	0.003	0.690	0.833	0.173	0.999
1.470	1.479	0.003	0.794	1.160	0.188	0.995
1.248	1.256	0.003	0.936	1.295	0.260	1.000
1.813	1.825	0.003	0.598	0.627	0.142	0.999
1.590	1.600	0.003	0.682	0.498	0.096	0.998
1.367	1.378	0.002	0.794	0.585	0.124	0.998
0.641	0.643	0.001	0.324	0.714	0.179	0.989
0.864	0.867	0.002	0.240	0.431	0.156	0.986
1.087	1.092	0.007	0.191	0.578	0.630	0.988
0.746	0.747	0.001	0.267	0.329	0.098	1.000
0.670	0.671	0.001	0.230	0.270	0.093	1.000
0.448	0.453	0.005	0.344	1.399	0.734	0.995

Table 4.3 – Summary of the identification results, academic model of wind turbine at constant rotational speed

Now we will continue with outputs computed from a simulation with a variable rotational speed, to be closer to real measures. Consequently, there will be much noise in the measurements compared to the previous simulation. Also, the modal signature of the system will vary, which should lead to an increase in the covariance of the identified values.

4.3.2 Case 2: variable rotational speed

The objective of this section is to perform the identification method on more realistic data, so a simulation of the academic model of a wind turbine with a variable rotational speed is performed. The rotational speed has a mean value of 1.807 rad/s, and the time series is computed from a spectrum obtained with aero-servo-elastic wind turbine model (see Figure 4.4). This variable rotational speed is directly injected if the system equations to simulate the wind turbine dynamic.

The same identification presented in the previous section is performed using the new simulated outputs. Once again, the objective is to compare the identified modal parameters with the corresponding values of the Fourier harmonics of the approximation computed with the system matrices.

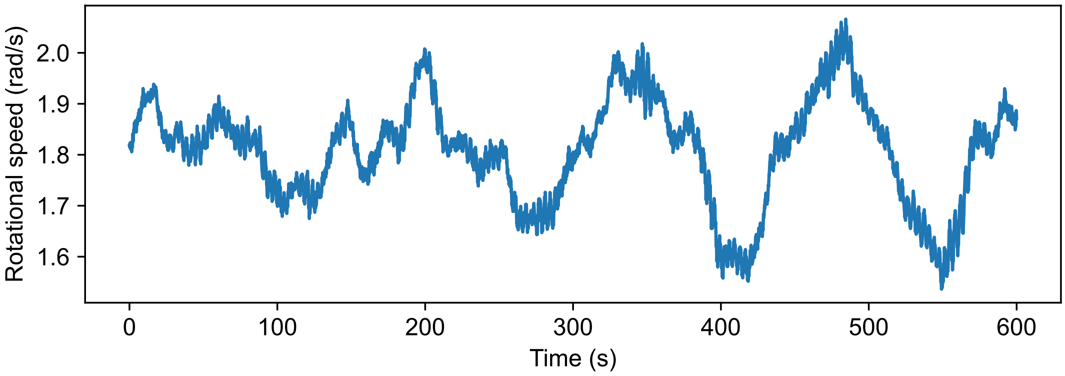

Figure 4.4 – Evolution of the rotational speed during the simulation

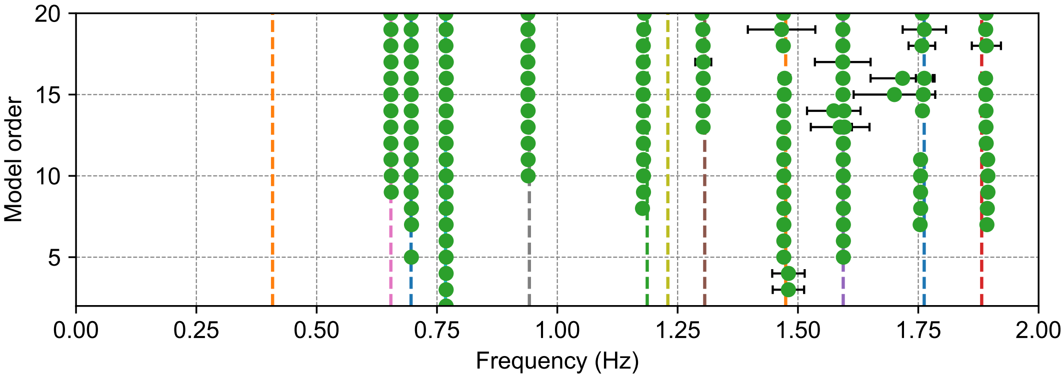

Figure 4.5 – Stabilization diagram from acceleration measures of all DOF from a simulation with a variable rotational speed - (- - -): reference frequencies - (●): identified frequencies

To begin with, the stabilization diagram in Figure 4.5 can be compared with the previous one (Figure 4.3). The error bars are wider compared to the previous identification, which is particularly visible for the identified modes with the highest frequencies. Also, two Fourier harmonics of the approximation are not identified in this example at about 0.4 Hz and about 1.22 Hz. The first one is the Fourier harmonic with the lowest frequency, corresponding to tower displacements (see frequency n°12 in Figure 3.1). The other non-identified Fourier harmonic, with a frequency around 1.2 Hz associated with rotor bending. Looking at the PSD of accelerations used for the identification in Figure 4.6, the amplitude of the first PSD peak is much lower compared to the others, explaining why this Fourier harmonic is not identified. One way to identify it would be to use only tower data. The other non-identified Fourier harmonic is not identified due to the high level of noise. Indeed, in Figure 4.6, no peak is seen around the corresponding frequency.

The comparison between the identified modes and the Fourier harmonics of the approximation is summarized in Table 4.4, where once again the modal parameters are extracted using the method described in Appendix E. As in the case with a constant rotational speed, the identified frequencies and dampings are close to those of the Fourier harmonics of the approximation, with the values of the approximation inside the 99% confidence intervals of the estimated values (excepted for the damping of the Fourier harmonics at 1.762 Hz, first line in Table 4.4). Also, the standard deviations are higher but with the same order of magnitude compared to the previous

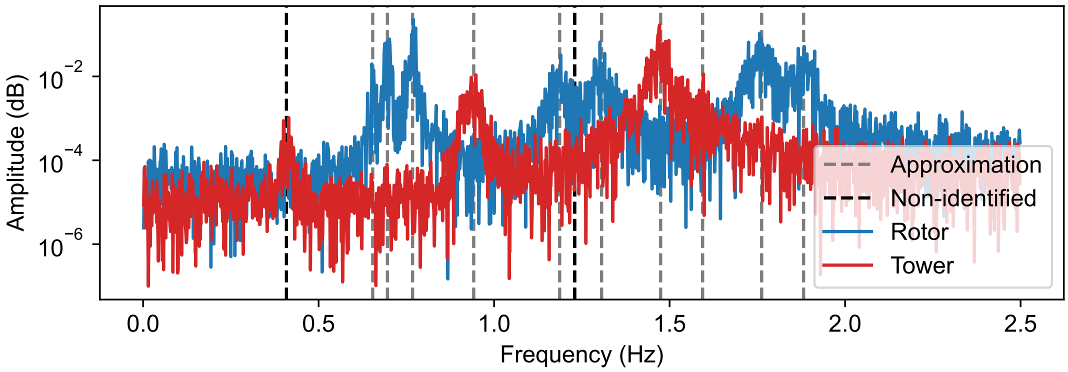

Figure 4.6 – PSD of an acceleration of a rotor DOF (blue) and a tower DOF (red) of the academic model of a wind turbine with a variable rational speed, compared with the frequencies of the Fourier harmonics of the approximation

identification. This is also the case for the MAC criterion between approximation and identified mode shapes.

f_{ap} (Hz)	f_{iden} (Hz)	σ_f (Hz)	ξ_{ap} (%)	ξ_{iden} (%)	σ_ξ (%)	MAC
1.762	1.754	0.005	0.659	1.152	0.190	1.000
1.475	1.471	0.002	0.787	0.911	0.143	0.999
1.187	1.178	0.004	0.978	1.047	0.284	0.999
1.882	1.893	0.005	0.570	0.881	0.294	1.000
1.594	1.594	0.002	0.673	0.590	0.130	0.999
1.306	1.303	0.005	0.821	1.490	0.414	0.999
0.654	0.655	0.001	0.352	0.344	0.180	1.000
0.942	0.939	0.004	0.244	1.318	0.267	0.998
0.768	0.769	0.001	0.259	0.405	0.113	1.000
0.696	0.697	0.002	0.217	0.432	0.117	1.000

Table 4.4 – Summary of the identification results, academic model of wind turbine at variable rotational speed

Finally, it can be concluded that the modes of the approximation can be identified, even with a variable rotational speed. Now let us test the method on much more realistic outputs, computed with an aero-servo-elastic wind turbine model.

4.4 Identification: application to an aero-servo-elastic wind turbine model

In this section, an identification of an aero-servo-elastic wind turbine model is performed. Precisely, the data are simulated based on a model of the DTU 10MW wind turbine presented in Section 1.4.5 with an isotropic rotor. The simulation is performed with a turbulent wind and a rotational speed controlled by an external controller (Figure 4.7). The objective is to confirm that the identified modes obtained with the current method are those computed with the approximation, with data close to real measurements.

In the simulation, the rotor has a mean rotational speed of 6 rpm, so the approximation is computed, as in Section 3.4, by assuming a constant rotational speed of 6 rpm. A minimum participation factor of 5% is applied to construct the approximation from the Floquet modes.

The data used in the identification are the Fore-Aft (FA) and Side-Side (SS) accelerations of the mid-tower and tower top, and the flap and edge blade root bending moments. These two sets of quantities do not have the same order of magnitude, so the data are normalized with the norm of their time evolution before the identification. Once the identification is performed, the mode shapes are re-normalized to come back to physical quantities. The data are sampled at 50 Hz during 600 s.

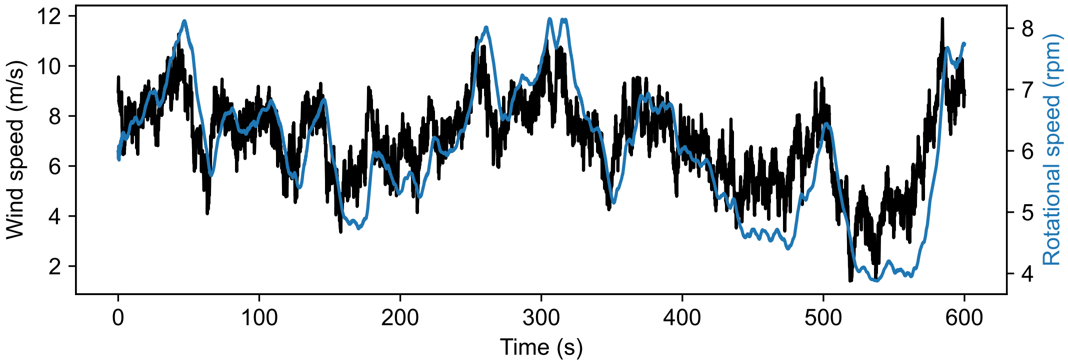

Figure 4.7 – Evolution of the wind speed (black) and the rotational speed (blue) during the simulation

4.4.1 Frequency spectrum analysis

The frequency analysis is composed of the study of the PSD of the different outputs, which are displayed in Figure 4.8 for a blade root edge bending moment and in Figure 4.9 for a tower acceleration along Side-Side. On these PSD, the frequencies of some Fourier harmonics of the approximation are added, namely the two first Side-Side bending modes of the tower and the harmonics of the three different Floquet modes corresponding to the bending of the blade along edge (backward, forward and collective). It can be seen that frequency peaks in the PSD are well estimated by the approximation. This illustrates once again the capacity of the method to approximate accurately the dynamic of the turbine even though the system is more complex and the rotational speed is varying.

With a frequency analysis some modes of the approximation have been identified, now a subspace identification with uncertainty quantification will be performed, to finish the validation and compare the identified modes with the approximation modes.

4.4.2 Subspace identification

In this last section, the identification of the DTU 10 MW wind turbine modal properties is performed using the blade root bending moments and tower accelerations together, with $p = 200$ and an order from 2 to 40. The proof of the use of the moments in the SSI is developed in Appendix D.

The identified modes are displayed in Figure 4.10 using a stabilization diagram, comparing the frequencies of the identified modes at different increasing orders and the frequencies of the

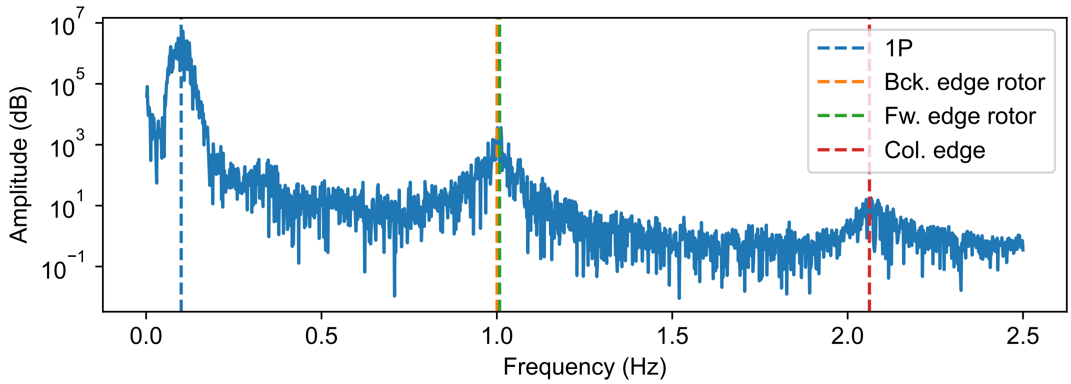

Figure 4.8 – PSD of a blade root edge bending moment, with the comparison with the frequency of specific approximation modes

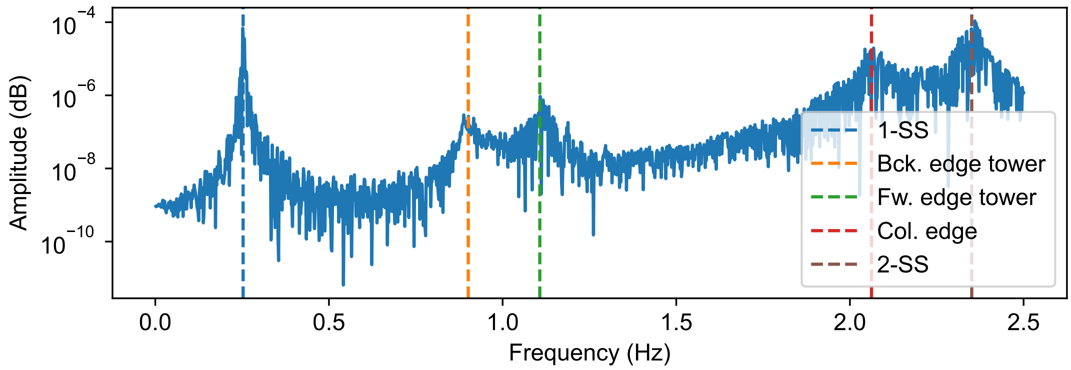

Figure 4.9 – PSD of the acceleration Side-Side at mid-tower, with the comparison with the frequency of specific approximation modes

approximation (dashed lines), defining the reference. It can be seen in Figure 4.10, that the modes obtained by the frequency spectrum analysis are properly identified. Once the modes are identified and extracted with the method of Appendix E, they are matched with the approximation modes using the MAC, with a minimum matching value of 0.7. The modes are matched twice, once using only the tower DOF, once using only the rotor DOF. Finally, eight identified modes are matched with the approximation modes. They are reported in Table 4.5, where $(\cdot)_{ap}$ denotes a quantity of the approximation modes and $(\cdot)_{iden}$ a quantity of the identified modes. Some approximation modes, like the mode 2-FA and the flap bending modes, are not identified due to their high damping ratios (more than 30% for the flap bending modes and around 13% for the mode 2-FA).

The relative gap between the identified modes from the data and the approximation modes computed from the model is lower than 1% for all the identified modes. It can be concluded that the identified modes are corresponding to the approximation modes. So, for a realistic case, the approximation modes can be identified with a classical OMA method.

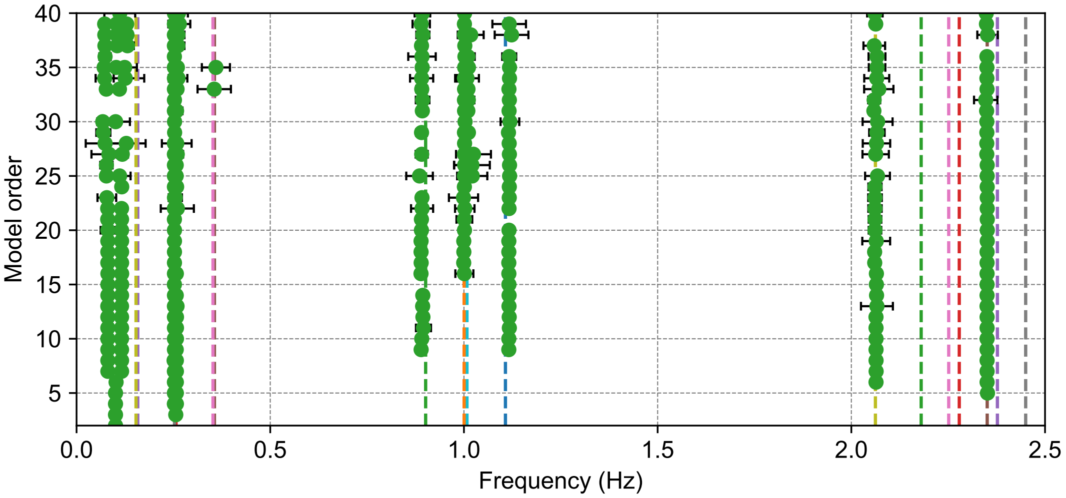

Figure 4.10 – Stabilization diagram from an identification with all the data, from a simulation with a turbulent wind and a variable rotational speed- (- - -): reference frequencies - (●): identified frequencies

	f_{ap} (Hz)	f_{iden} (Hz)	σ_f (Hz)	ξ_{ap} (%)	ξ_{iden} (%)	σ_ξ (%)	MAC	Names
Tower	2.349	2.351	0.003	0.869	0.987	0.124	1.000	2-SS
	2.061	2.064	0.006	1.778	1.732	0.280	1.000	Col. edge
	1.108	1.116	0.004	2.066	2.715	0.436	0.907	Fw. edge tower
	0.901	0.892	0.006	1.908	2.252	0.274	0.975	Bck. edge tower
	0.257	0.258	0.004	7.776	7.502	1.204	0.998	1-FA
	0.253	0.253	0.001	0.275	0.352	0.277	0.744	1-SS
Rotor	2.061	2.064	0.006	1.778	1.732	0.280	0.969	Col. edge
	1.008	1.010	0.011	2.269	1.771	1.184	0.759	Fw. edge rotor
	1.001	1.001	0.005	1.719	1.792	0.417	0.915	Bck. edge rotor
	0.257	0.258	0.004	7.776	7.502	1.204	0.983	1-FA

Table 4.5 – Summary of the identification results, with the matching of the identified modes with the reference modes

4.5 Comparison with an existing method

As mentioned in Section 2.3, there are already some existing OMA methods developed for wind turbines. Here, one existing subspace method is tested, the H-OMA-TD [130]. This method is the closest to what has been done in this chapter. To compare the results of this method, the data used in Section 4.3.1 are selected, namely the academic model of wind turbine with a constant rotational speed.

This method is composed of two steps. First, the signal is modulated (extending the spatial space of the data)

$$y_m(t) = y(t)\exp\left(-im\Omega t\right) \in \mathbb{R}^{r\times N} \tag{4.4}$$

and

$$Y(t) = \left[y_{-m}(t)^T \quad \dots \quad y_0(t)^T \quad \dots \quad y_m(t)^T\right]^T \in \mathbb{R}^{(2m+1)r\times N} \tag{4.5}$$

is the modulated data. Secondly, these data are used to perform a subspace identification.

In this example, the modulation parameter is set to $m = 2$, so the spatial space is five times larger compared to the original data space. Consequently, the identifications deal with five time more data, which significantly increases the computational time, from few seconds for the original data to around 100 seconds using the modulated data.

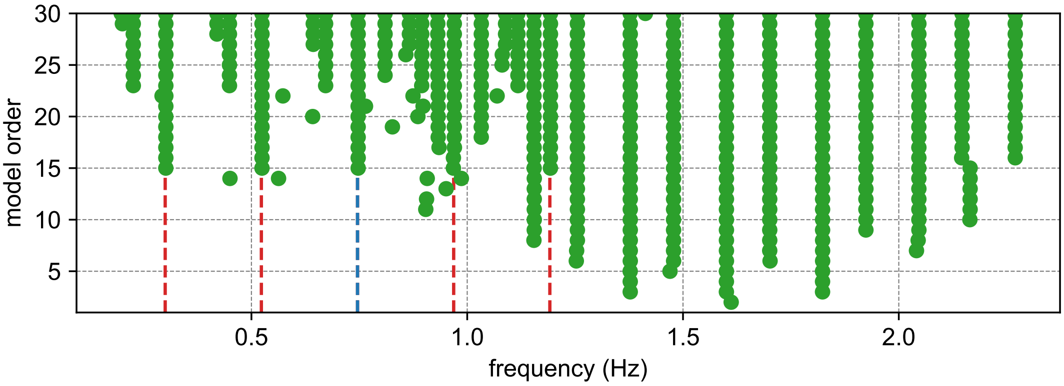

Figure 4.11 – Stabilization diagram computed with the H-OMA-TD method with all the DOF from a simulation with a constant rotational speed. The blue dashed line (- - -) corresponds to an approximation frequency and the red dashed lines (- - -) correspond to the modulation of this frequency - (●): identified frequencies

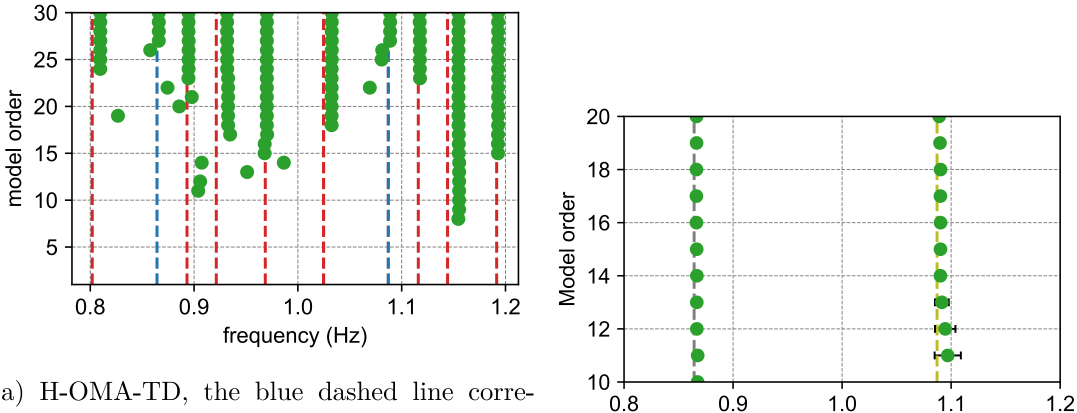

(a) H-OMA-TD, the blue dashed line corresponds to approximation frequencies and the red dashed lines correspond to the modulated frequencies

(b) Classical SSI

Figure 4.12 – Comparison of stabilization diagrams of two methods between 0.8 and 1.2 Hz

In Figure 4.11, the stabilization diagram from the identification of the modulated signal is displayed. In Figure 4.12, a zoom of this stabilization diagram is compared with the same zoom of the stabilization diagram from the identification with the original signal (Figure 4.3). These two figures show that much more modes are identified with H-OMA-TD method. This is the result of the modulation. With the chosen number of modulations, the theoretical number of identified modes should be 5 times the number of identified modes obtained in Section 4.3.1. This leads to a difficult analysis of the stabilization diagram. It must be noted that an uncertainty computation method is not used here, since the increase of the spatial dimension by the modulation leads to a higher computational cost, preventing the practical use of the method.

It is interesting to study how the modes appear in Figure 4.11. In fact, the identified modes appear depending of their energy, and the modulated modes have the same energy as corresponding non-modulated mode. That is why modes appear by groups in the stabilization diagram, with an example at the order 15, where the approximation modes and the corresponding modulation (the modes corresponding to the dashed lines) are identified at the same order. This leads to a problem as the modes in a group have the same modal information, so it is needed to identify the system at a higher order (order 30) compared to the classical SSI (order 20) to get the same modal information (see Figure 4.12).

The identified modes corresponding to the approximation modes can be compared, selecting the DOF corresponding to modulation 0 ($y_0(t)$ in Equation (4.5)). In table 4.6, the identification results of the H-OMA-TD method and the SSI method are compared, with a comparison of the gap to the Fourier harmonics of the approximation. Consequently, it can be concluded that the two methods can identify with the same accuracy the approximation, as the order of magnitude of the gap and the MAC are the same.

f_{ap} (Hz)	Δ_f (%) H-OMA-TD	Δ_f (%) SSI	ξ_{ap} (%)	Δ_ξ (%) H-OMA-TD	Δ_ξ (%) SSI	MAC H-OMA-TD	MAC SSI
1.693	0.5%	0.2%	0.690	0.241	0.098	0.999	0.999
1.470	0.5%	0.1%	0.794	0.281	0.084	0.996	0.995
1.248	0.6%	0.0%	0.936	0.314	0.044	1.000	1
1.813	0.6%	0.1%	0.598	0.132	0.161	1.000	0.999
1.590	0.7%	0.0%	0.682	0.153	0.031	0.995	0.998
1.367	0.8%	0.0%	0.794	0.159	0.048	0.998	0.998
0.642	0.2%	0.0%	0.324	0.352	0.037	0.993	0.989
0.864	0.2%	0.1%	0.240	0.242	0.052	0.985	0.986
1.087	0.2%	0.3%	0.191	0.154	0.232	0.990	0.988
0.746	0.2%	0.0%	0.267	0.102	0.040	1.000	1
0.670	0.2%	0.1%	0.230	0.033	0.006	1.000	1
0.448	0.3%	0.9%	0.344	0.049	1.005	0.995	0.995

Table 4.6 – Comparison of the identification results between the H-OMA-TD and the SSI

As mentioned before, there is a lot of identified modes due to the modulation. In Table 4.7, the identified frequencies are clustered function of the modulation with the approximation frequency as reference, with a total of 29 different harmonics of the approximation modes identified.

f (Hz)	$f - \frac{\Omega}{2\pi}$ (Hz)	$f - 2\frac{\Omega}{2\pi}$ (Hz)	$f + \frac{\Omega}{2\pi}$ (Hz)	$f + 2\frac{\Omega}{2\pi}$ (Hz)
1.7009	1.4780	1.2554	1.9237	2.1465
1.4780	1.2554	1.0326	1.7009	1.9237
1.2554	1.0326	0.8096	1.4780	1.7009
1.8234	1.6006	1.3776	2.0465	2.2699
1.6006	1.3776	1.1547	1.8234	2.0465
1.3776	1.1547	0.9318	1.6006	1.8234
0.6431	0.4201	0.1983	0.8659	1.0888
0.8659	0.6431	0.4201	1.0888	
1.0888	0.8659	0.6431		
0.7473	0.5245	0.3017	0.9701	1.1929
0.6719	0.4490	0.2262	0.8946	1.1174
0.4490	0.2262		0.6719	0.8946

Table 4.7 – Clustering of the frequencies of the identified modes

Finally, this method aims also to identify the participation factors of the identified modes

(Equation (3.9)), to recompute the periodic mode shapes of the Floquet modes. To compute this participation factor, the amplitude of the different modulations of the identified mode shapes is used (as it is done with the Fourier transform). In Table 4.8, the identified participation factors are compared to the theoretical ones, and the participation factor is computed with the classical SSI. To compute the participation factor with the classical SSI, the amplitude of the mode shapes corresponding to the harmonics of the same Floquet mode are compared. From this study, it can be concluded that the two approaches give equivalent results, with a mean gap of 0.015 for the H-OMA-TD and 0.013 for the classical SSI. However, it is easier to compute the participation factor with the H-OMA-TD (as the harmonics of the same Floquet mode are regrouped in one identified mode shape).

f_{iden} (Hz)	part. fact. H-OMA-TD	part. fact. SSI	theoretical par. fact.	gap H-OMA-TD	gap SSI
1.701	0.450	0.430	0.465	0.015	0.034
1.478	0.291	0.324	0.296	0.005	0.028
1.255	0.240	0.245	0.239	0.000	0.006
1.823	0.364	0.339	0.371	0.007	0.031
1.601	0.310	0.341	0.317	0.007	0.024
1.378	0.307	0.320	0.312	0.005	0.007
0.643	0.474	0.480	0.483	0.010	0.004
0.866	0.266	0.296	0.294	0.027	0.002
1.089	0.185	0.224	0.223	0.038	0.002
0.747	0.960	1.000	1.000	0.040	0.000
0.672	0.884	0.902	0.908	0.024	0.006
0.449	0.092	0.098	0.092	0.000	0.007

Table 4.8 – Comparison of the identified participation factor with the H-OMA-TD with the theoretical ones and the classical SSI

As a conclusion, this method does not give much more information as the developed approach in this chapter. With the drawback to need much more computational time and the increasing difficulty to post process the identification results. But the participation factors can be assessed easily with the H-OMA-TD. So, this method could be interesting for specific applications requiring the participation factors. However, the identified modes are not theoretically defined with this method, as is it mentioned in the paper [130]. To have a better understanding of what is identified, the background theory of the method need to be defined.

4.6 Conclusion

Before this study, it was understood that the LTP nature of the wind turbine modeling would result in developing adequate LTP methods to extract relevant features. As such, many methods have been developed in the literature with advantages and drawbacks. The output of this chapter is that it is also adequate to perform classical LTI system identification approaches on LTP systems. The resulting modes are the Fourier harmonics of the Floquet modes, and they can be used to characterize the wind turbine properties based on sensor data. It has the advantage of relying on the well studied SSI approach with all the benefits of the extensive background on such methods for LTI systems.

Then, after validating the uncertainty computation, the identification of the approximation has been performed on data from different simulations of rotating wind turbines. For all the identifications, the identified modes are corresponding to the modes defined with the approximation of the Floquet modes. Consequently, the classical OMA methods can be used to monitor the eigenmodes of an operating wind turbine. The results obtained in Section 4.4 has been presented during the conference EWSHM [23].

Finally, the identification approach has been compared to an existing identification method, the H-OMA-TD. The existing method is similar to the defined approach, with just a modulation of the data before the subspace identification. The results obtained with our new approach and the existing method are similar, but the results of the new approach are simpler to analyze and this new approach is less costly in terms of computational time. Consequently, the developed approach should be preferred, except for specific applications where the estimation of the participation factor is mandatory.

In the following, the identification approach that has been defined will be used for fault detection on a wind turbine rotor.

Part III

Fault detection

Chapter 5

ROTOR ANISOTROPY TRACKING FOR FAULT DETECTION

Abstract

To perform damage detection on a wind turbine rotor, it is needed to first find the most relevant damage indicators. In this Part, it is chosen to perform damage detection of a wind turbine rotor based on the tracking of rotor anisotropy due to a reduction of stiffness or an augmentation of mass of a blade. From the literature, the phase shift and amplitude of the edge bending modes shape are the most sensitive parameters to these variations. This is confirmed here with the example of the DTU 10MW wind turbine model. Then, the uncertainties associated with the amplitude and phase shift of the mode shape are defined and validated. To finish the chapter, a damage detection based on the comparison of the identified amplitudes and phase shift jointly with their confidence intervals is defined. This method is applied for the detection of a stiffness of 5% of one blade of the DTU 10MW wind turbine model, which shows that the chosen damage indicators can be used for the detection of rotor faults.

5.1 Introduction

In the previous part, an approach for the identification of wind turbines has been defined and validated on a realistic numerical example. Now, the objective is to exploit this approach to develop a fault detection method, designed for the monitoring of wind turbines rotor. Precisely, the detection of faults in the rotor will be studied based on the detection of rotor anisotropy. As said in Section 1.3, the fault can be a reduction of stiffness, an augmentation of mass, or a pitch angle error on a blade, all leading to rotor anisotropy. In this Chapter and in this Part in general, the method will be developed considering a stiffness anisotropy. But, the validity of the method for the detection of mass and pitch anisotropy will be discussed in Section 6.10. To begin damage detection, it is proposed that the developed method will focus on the modal parameters that are the most sensitive to rotor anisotropy. As mentioned in Section 2.5.2, those parameters are the phase shift and the amplitude of the edgewise bending mode shapes.

The objective is to monitor a change in the dynamical behavior by comparing the identified values for different states. As previously introduced in Section 2.2.3, the identified modes are uncertain so comparisons have to consider the uncertainties of each monitored parameter.

The chapter is organized as follows. Firstly, the evolution of the Fourier harmonics regarding the anisotropy is assessed for the model of the DTU 10MW wind turbine. Secondly, the uncertainties of the phase shift and the amplitude will be defined and validated. Finally, an OMA-based fault detection method using the statistical change of phase shift and amplitude is defined and tested on two tests cases of increasing complexity.

5.2 Modal analysis of a wind turbine with an anisotropic rotor

As presented in Section 2.5.2, the anisotropy of a wind turbine rotor leads to important variations in the mode shape of the whirling Floquet modes (i.e. the edgewise bending modes). In this Section, the objective is to assess the changes in the edgewise bending Fourier harmonics of the DTU 10MW wind turbine model. Here, a model with a rotational speed of 6 rpm is studied and an approximation defined with a minimum participation factor of 5 % is considered. This approximation is defined using the same outputs used in Section 4.4, namely the Fore-Aft (FA) and Side-Side (SS) accelerations of the mid-tower and tower top, and the flap and edge blade root bending moments.

Beforehand, the Floquet modes of the model must be computed. However, as the rotor is anisotropic the MBC transformation cannot be used. To compute the Floquet modes the homogeneous equation (Equation (1.22)) is integrated with different initial conditions, with the same method presented in Section 1.5.4. Precisely, the homogeneous equation is integrated with the Runge-Kutta order 4 method (RK4) using 500 linearized matrices from a rotating period.

5.2.1 Analysis of the effects of the anisotropy of stiffness on Fourier harmonics of the Floquet modes

To assess a change in the Fourier harmonics, the approximation is computed for three different global stiffness reductions of the third blade, namely 1%, 2.5% and 5%.

First, the change in the frequencies of the Fourier harmonics can be assessed. In Table 5.1, the evolution of frequencies of the Fourier harmonics identified in Section 4.4 is summarized depending on the stiffness loss of the damaged blade. Looking at the results, one can see that whatever the loss in stiffness is, the frequency changes are small. Indeed, the difference of frequencies between the structural states has a maximum of 0.015 Hz of difference for the Collective edge. This order of magnitude is not significant enough to track such change in a real structure, where the effects of varying environmental conditions will be important [45]. So, the change in the mode shapes due to the anisotropy will be assessed, as it was introduced in Section 2.5.2.

Name	Isotropic	99% of stiff	97,5% of stiff	95% of stiff.
2-SS	2.349 Hz	2.348 Hz	2.348 Hz	2.348 Hz
Col. Edge	2.061 Hz	2.058 Hz	2.054 Hz	2.046 Hz
Fw. Tower	1.108 Hz	1.107 Hz	1.106 Hz	1.105 Hz
Fw. Rotor	1.008 Hz	1.007 Hz	1.006 Hz	1.005 Hz
Bck. Rotor	1.001 Hz	0.999 Hz	0.995 Hz	0.988 Hz
Bck. Tower	0.901 Hz	0.899 Hz	0.896 Hz	0.888 Hz
1-FA	0.257 Hz	0.257 Hz	0.257 Hz	0.257 Hz
1-SS	0.253 Hz	0.253 Hz	0.253 Hz	0.253 Hz

Table 5.1 – Selected frequencies of the approximation function of the stiffness of the third blade

Figure 5.1 represents the evolution of the amplitude and the phase shift between the blades on a polar plot for the different considered stiffness reductions, where each subfigure corresponds to a different mode. First, it has to be noted that the first blade defines the reference, with an amplitude always equal to 1 and a phase to 0. The choice of the reference blade will have an

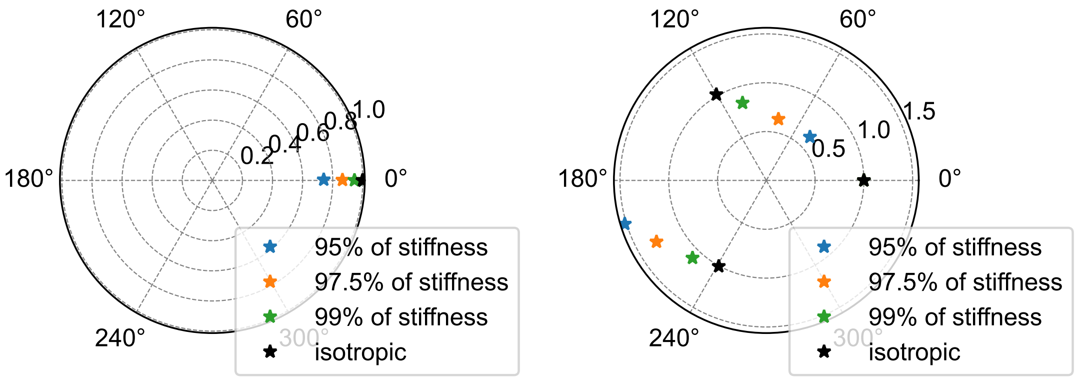

(a) Collective

(b) Backward

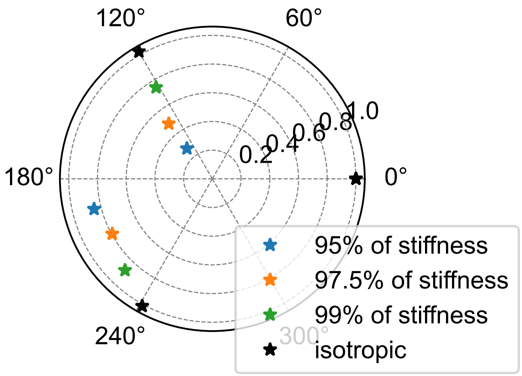

(c) Forward

Figure 5.1 – Evolution of the polar plot of the edgewise bending mode shapes against the third blade stiffness

impact on the values of phase shift and amplitude, but the global change compared to the isotropic state is the same if another blade is taken as reference. Figures 5.1b and 5.1c show that there is an important evolution of the phase shift for the Backward and Forward edge bending modes coupled with an important evolution of their amplitude. Indeed, for the isotropic state, the phase shift between each blade is 120° and the amplitude is equal to 1 for each blade. For a stiffness loss of 5%, the phase shift decreases to about 50° and 190° for the 2nd and 3rd blades for the Backward edge bending mode respectively, whereas the vibration amplitude decreases for the 2nd blade and increases for the third one. Considering the Forward edge bending mode (2nd at 240° and 3rd blade at 120° for the isotropic state), the amplitudes for each blade decrease, but it decreases substantially for the 3rd blade (to about 0.2). The phase shift of the 3rd blade remains somewhat constant and equal to 120°, whereas it decreases for the 2nd blade. The mode shape of the Collective edge has a different evolution compared to the two others (see Figure 5.1a). Indeed, only the amplitude of the damaged blade is evolving with a reduction of the amplitude according to the loss of stiffness. All these results illustrate the high sensitivity of the phase shift and amplitude to rotor anisotropy and the relevance of tracking these parameters to monitor a wind turbine.

Table 5.2 summarizes the MAC between the mode shapes of the isotropic state and the anisotropic states. It confirms the graphical analysis, since a larger evolution of the MAC is observed for the Backward and Forward edge mode shapes, meaning that the mode shape changes

Mode	Stiff. 99%	Stiff. 97.5%	Stiff. 95%
Col.	0.999	0.996	0.982
Bck.	0.968	0.846	0.691
Fw.	0.973	0.849	0.704

Table 5.2 – MAC values computed between the isotropic and the anisotropic mode shapes of the Fourier harmonics of edge bending for different anisotropy levels

are higher for those Fourier harmonics. It can be concluded that the mode shapes of the Backward and the Forward edge have a similar sensitivity to anisotropy. The mode shape of the Collective edge is less affected globally by the change scenarios since only the amplitude of the damaged blade is affected by the rotor anisotropy.

To conclude, due to the high sensitivity regarding the anisotropy of the mode shapes of the Fourier harmonics of edge bending, those mode shapes can be used to detect a stiffness loss on one blade. Now, the difference due to mass or stiffness anisotropy will be presented. To find out if it is possible to differentiate those two types of damage.

5.2.2 Difference between stiffness and mass anisotropy

The objective is to identify a structural fault from the dynamical behavior. In this section, the differences in the dynamical behavior between an addition of mass and a loss of stiffness are assessed. One question is whether the mode shapes of wind turbines are affected differently depending on whether there is a mass addition or a loss of stiffness in one blade. To do so, the MAC is used to compare the mode shapes of the Fourier harmonics of edge bending of the system with mass anisotropy and the system with stiffness anisotropy.

Here, the modes from models with a stiffness decrease or with a mass increase in one blade are compared. As the frequencies are usually too close to make the difference between the two types of faults, the objective is to see if the mode shapes can be used to make this distinction. Therefore, the mode shapes are compared thanks to the MAC. To simplify this analysis, it is chosen to compare the mode shapes obtained with a ratio k/m almost equal, with k (resp. m) the stiffness (resp. the mass) variation, as it translates roughly the expected frequency variation. In this study, the mass anisotropy in the model is defined by a change of the density of the third blade.

Stiffness anisotropy	Mass anisotropy	Col.	Bck.	Fw.
k=99 %	m=101 %	1	0.9998	0.9996
k=97.5 %	m=102.5 %	0.9999	0.9998	0.9998
k=95 %	m=105 %	0.9993	0.9993	0.9997

Table 5.3 – MAC values computed between mode shapes of same Fourier harmonic with different type of anisotropy for different anisotropy levels

Table 5.3 summarizes the MAC computed between the mode shapes of the Fourier harmonics of edge bending of the system with mass anisotropy and the mode shapes of the system with stiffness anisotropy. From Table 5.3, it can be seen that for the similar ratio stiffness/mass, the mode shapes are very similar as the MAC criterion is very close to 1. The error might be due to the difference in the ratio ($\frac{1}{1.05} \neq 0.95$) and can also be the result of the integration error in the computation of the Floquet modes. From this study, it can be concluded that it is not possible to know if the anisotropy arises from a loss of stiffness or an addition of mass when analysing the rotor mode shapes.

If the difference in the anisotropy cannot be seen with the rotor mode shapes, it might be seen on the tower. First, the PSD at mid tower of the acceleration along Side-Side will be compared, they are represented in Figure 5.2 for two different anisotropies.

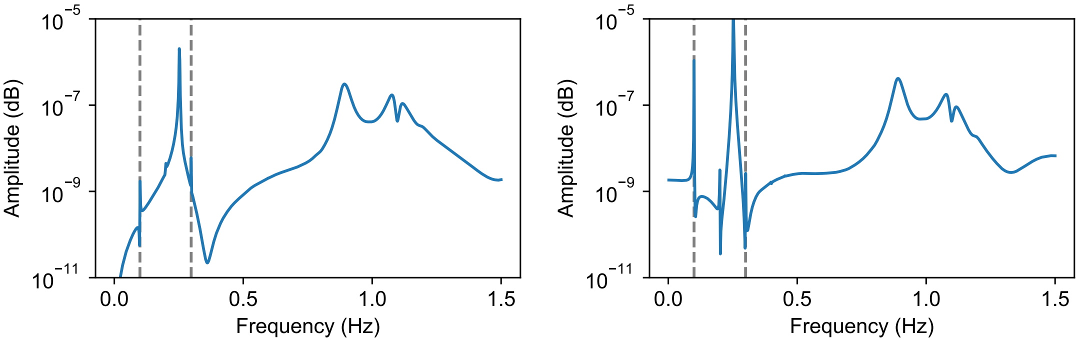

(a) 95% of stiffness (b) 105% of density

Figure 5.2 – PSD at mid-tower along Side-Side for different anisotropies, with the two dashed lines corresponding to the harmonics of the rotation (1P and 3P)

In Figure 5.2, it can be seen that the first peak of the PSD (the 1P) does not have the same amplitude, with an amplitude of about 10^{-6} dB for the mass anisotropy, equivalent to the 1SS peak, and a negligible amplitude of about 10^{-9} dB for the stiffness anisotropy. Consequently, the anisotropy in mass and stiffness can be differentiated with an analysis of the amplitude of the 1P peak along Side-Side, as it was presented in Section 2.5.1.

The impact of the anisotropy on the dynamical behavior has been assessed for the model of the DTU 10MW, with the confirmation that the anisotropy has an important impact on the phase shift and the amplitude of edgewise bending mode shapes. Also, it has been shown that the mass and stiffness anisotropies have a similar impact on the mode shapes, but these two anisotropies can be distinguished using the amplitude of the 1P harmonic in the frequency domain.

Now the uncertainties of the phase shift and the amplitude will be defined, to asses a more precise change of the values obtained with the identification method, i.e. identified value and the associated confidence interval.

5.3 Uncertainties of phase shift and amplitude

To assess the change in the identified edgewise bending mode shapes with the analysis of the phase shift and the amplitude, the respective uncertainties are needed. In this Section, the uncertainty quantification of the phase shift and the amplitude of the identified mode shapes is defined, using the first-order delta method presented in Section 2.2.3. Since the method of the literature enables the estimation of the uncertainties of the identified mode shapes, to compute the uncertainties of the phase shift and the amplitude only the associated sensitivities regarding the mode shape are needed, with

$$\Sigma_{P_i} = \mathcal{J}_{P,\phi}\Sigma_{\phi_i}\mathcal{J}_{P,\phi}^T \text{ and } \Sigma_{a_i} = \mathcal{J}_{a,\phi}\Sigma_{\phi_i}\mathcal{J}_{a,\phi}^T \tag{5.1}$$

for the i–th identified eigenmode.

5.3.1 Definition: Sensitivity of phase shift

First, let us define the phase shift P_j of a mode shape $\phi \in \mathbb{R}^r$ at the DOF j. The mode shape at the DOF j can be defined as

$$\begin{aligned}\phi_j &= a_j \exp(iP_j)\\ &= a_j \cos(P_j) + ia_j \sin(P_j),\end{aligned}$$

where a_j denotes the amplitude. From this expression, the phase shift can be defined as

$$P_j = \arctan\left(\frac{\Im(\phi_j)}{\Re(\phi_j)}\right). \tag{5.2}$$

As it was introduced in Section 2.2.3, to estimate the uncertainty of a quantity, its sensitivity from another quantity has to be defined. So, the sensitivity of the phase shift regarding the mode shape is defined as

$$\mathcal{J}_{P,\phi} = \begin{bmatrix}\frac{\partial P}{\partial \Re(\phi)} & \frac{\partial P}{\partial \Im(\phi)}\end{bmatrix} \in \mathbb{R}^{r\times 2r}. \tag{5.3}$$

First

$$\begin{aligned}\frac{\partial P_j}{\partial \Re(\phi_j)} &= -\frac{\Im(\phi_j)}{\Re(\phi_j)^2}\frac{1}{1+\left(\frac{\Im(\phi_j)}{\Re(\phi_j)}\right)^2} && (5.4)\\ &= \frac{-\Im(\phi_j)}{\Re(\phi_j)^2+\Im(\phi_j)^2} && (5.5)\\ &= \frac{-\Im(\phi_j)}{|\phi_j|^2}, && (5.6)\end{aligned}$$

analogously

$$\begin{aligned}\frac{\partial P_j}{\partial \Im(\phi_j)} &= \frac{1}{\Re(\phi_j)}\frac{1}{1+\left(\frac{\Im(\phi_j)}{\Re(\phi_j)}\right)^2} && (5.7)\\ &= \frac{\Re(\phi_j)}{\Re(\phi_j)^2+\Im(\phi_j)^2} && (5.8)\\ &= \frac{\Re(\phi_j)}{|\phi_j|^2}. && (5.9)\end{aligned}$$

Finally, the definition of $\mathcal{J}_{P,\phi}$ is

$$\mathcal{J}_{P,\phi} = \begin{bmatrix}\begin{bmatrix}\frac{-\Im(\phi_k)}{|\phi_k|^2}\end{bmatrix} & \begin{bmatrix}\frac{\Re(\phi_k)}{|\phi_k|^2}\end{bmatrix}\end{bmatrix}, \tag{5.10}$$

with $\begin{bmatrix}\frac{\Im(-\phi_k)}{|\phi_k|^2}\end{bmatrix} \in \mathbb{R}^{r\times r}$ a diagonal matrix, as for $\begin{bmatrix}\frac{\Re(\phi_k)}{|\phi_k|^2}\end{bmatrix}$.

$\mathcal{J}_{P,\phi}$ is defined and non-zero if ϕ is non-zero for all degrees of freedom. This condition is verified if the associated mode shape is seen through all the sensors. Actually, if a mode shape is not seen on a sensor, it is not useful to compute the phase-shift and the associated uncertainty.

5.3.2 Definition: Sensitivity of amplitude

The amplitude (a_i) of the DOF i of the mode shape ϕ is defined as

$$a_i = |\phi_i| = \sqrt{\Re(\phi_i)^2 + \Im(\phi_i)^2}. \tag{5.11}$$

Analogously as previously, the sensitivity of the amplitude regarding the mode shape has to be defined,

$$\mathcal{J}_{a,\phi} = \begin{bmatrix} \frac{\partial a}{\partial \Re(\phi)} & \frac{\partial a}{\partial \Im(\phi)} \end{bmatrix} \in \mathbb{R}^{r \times 2r}. \tag{5.12}$$

First

$$\frac{\partial a_i}{\partial \Re(\phi_i)} = \frac{\Re(\phi_i)}{|\phi_i|}, \tag{5.13}$$

and

$$\frac{\partial a_i}{\partial \Im(\phi_i)} = \frac{\Im(\phi_i)}{|\phi_i|}. \tag{5.14}$$

Finally, the sensitivity matrix ($\mathcal{J}_{a,\phi}$) is defined as

$$\mathcal{J}_{a,\phi} = \begin{bmatrix} \begin{bmatrix} \frac{\Re(\phi_k)}{|\phi_k|} \end{bmatrix} & \begin{bmatrix} \frac{\Im(\phi_k)}{|\phi_k|} \end{bmatrix} \end{bmatrix}, \tag{5.15}$$

with $\begin{bmatrix} \frac{\Re(\phi_k)}{|\phi_k|} \end{bmatrix} \in \mathbb{R}^{r \times r}$ a diagonal matrix, as for $\begin{bmatrix} \frac{\Im(\phi_k)}{|\phi_k|} \end{bmatrix}$.

Like $\mathcal{J}_{P,\phi}$, $\mathcal{J}_{a,\phi}$ is defined and non-zero if ϕ is non-zero for all DOF. When the amplitude at a sensor is zero , the associated distribution is not a Gaussian distribution, but may be a χ^2 distribution as for the MAC when the value is 1.

5.3.3 Validation

To validate the definition of those new uncertainties, a Monte Carlo simulation is performed to compare the estimated uncertainties with the empirical uncertainties. The validation here is performed on the academic model, using the identification parameters from Section 4.2 for the Monte Carlo simulation. To assess the distribution of the phase shift and amplitude, each identified mode shape needs to have the same normalization and the same DOF setting the reference. Here, it is chosen to divide the mode shape by one of its components

$$\phi' = \frac{\phi}{\phi_j}, \tag{5.16}$$

where ϕ' is the normalized mode shape and j is the index of the component setting the normalization. In this case, j is also the index for the reference phase. In the presented example the blade one will be the DOF of reference, with a phase equal to 0 and an amplitude equal to 1.

In Figure 5.3, the identified mode shapes of two Fourier harmonics are displayed, with one dot corresponding to one identification of the Monte Carlo simulation. This figure shows that for the two displayed Fourier harmonics, the identified mode shapes are in the 99% confidence

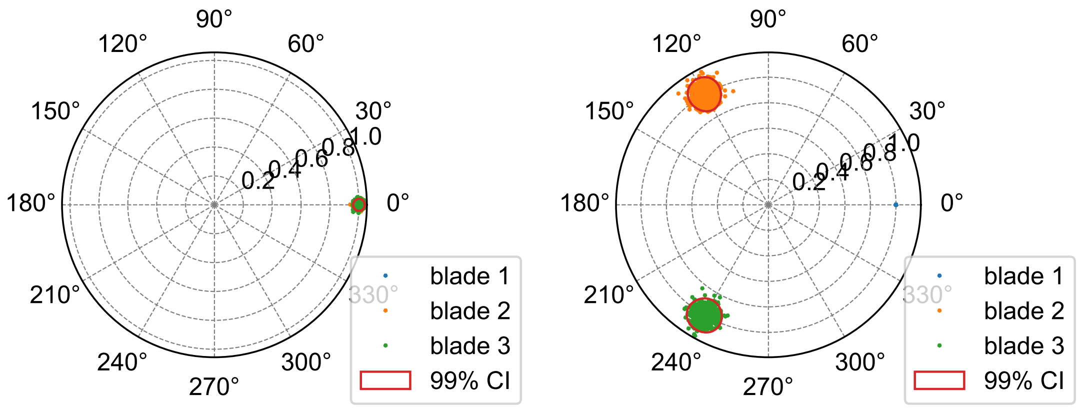

(a) 10–th Fourier harmonic

(b) 11–th Fourier harmonic

Figure 5.3 – Comparison of the identified phases shift and amplitudes with the estimated 99% confidence interval (CI)

interval. To have a better comparison, the empirical and estimated standard deviations are compared in Table 5.4, with the mean values associated with their 95% confidence intervals. The latter shows that the empirical and the estimated uncertainties are similar, with the same order of magnitude. Then, one can see that the confidence intervals are crossing each other for all the phase shifts and amplitudes presented. Finally, it can be noted that the 10–th harmonic had less uncertainties on the phase shift and the amplitude compared to the 11–th harmonic.

With the same arguments used in Section 4.2 it can be concluded that the estimation of the estimated uncertainties of the phase shift and the amplitude is validated. They will now be used for anisotropy tracking and fault detection.

Id Number and blade	Phase (°)	$\sigma_{p\ MC}$	$\sigma_{p\ est}$	Amplitude	$\sigma_{a\ MC}$ $\left(10^{-2}\right)$	$\sigma_{a\ est}$ $\left(10^{-2}\right)$
10, blade 2	0	0.73±0.03	0.74±0.10	1	1.26±0.06	1.28±0.17
10, blade 3	0	0.74±0.03	0.73±0.09	1	1.23±0.05	1.28±0.19
11, blade 2	120	2.52±0.11	2.41±0.66	1	4.41±0.19	4.30±0.86
11, blade 3	-120	2.54±0.11	2.41±0.55	1	4.48±0.20	4.30±0.98

Table 5.4 – Comparison of the empirical and the estimated standard deviations for the phase shift and amplitude of two selected Fourier harmonics, with the associated 95% confidence interval

5.4 Anisotropy tracking with operational modal analysis

The effects of the anisotropy on the Fourier harmonics has been presented and the uncertainty computation of the key parameters has been defined. Now, a method to detect anisotropy based on the identification of the edgewise bending modes is presented.

5.4.1 Method to detect rotor anisotropy

As told in the previous section, the identified modes obtained are uncertain. Thus, to determine if a mode shape has changed, it is necessary to compare the identified values taking into account the associated uncertainties. The MAC criterion can be used to determine if two mode shapes are statistically distinct. As presented in Section 2.2.3, in [58] it has been shown that the MAC follows different statistical laws depending on the compared mode shapes. If the compared mode shapes are identical, the criterion follows a χ^2 law and if the mode shapes are different, it follows a Gaussian law. For the χ^2 law, the confidence interval is defined with the lower bound of the 95% quantile as the upper bound is 1. For the Gaussian law, the confidence interval is computed based on the standard deviation.

The objective of the method is to assess changes in the mode shapes. To achieve such a goal, an actual set of identified modes has to be compared to a reference set. Precisely, a change in the rotor isotropy is sought through changes in the edgewise bending modes. The method to detect anisotropy changes is composed of the following steps:

1. Identification of the reference state using only the blade root edge-moment: uncertainty computation of the reference mode shape, amplitude and phase shift
2. Identification of the current state (potentially damaged) using only the blade root edge-moment: uncertainty computation of the current mode shape, amplitude and phase shift
3. Comparison of the edgewise bending mode shapes and their associated uncertainties on a polar plot. The compared estimated mode shapes are not corresponding to the same state if the 95% confidence intervals do not cross each other
4. Computation of the MAC criterion and the associated uncertainties. If the MAC follows a χ^2 law, the mode shapes correspond to the same state, whereas if the MAC follows a Gaussian law the mode shapes are corresponding to different states and anisotropy is detected.

Now, this method will be tested, with a change scenario in the DTU 10MW rotor isotropy.

5.4.2 Case 1: 5% of stiffness loss on one blade under white noise wind

To start, the method is performed on an ideal case, with data from simulations where the wind is defined with a Gaussian process. The objective is to be as close as possible to the assumptions of the OMA-method and to have a simulation with a rotational speed close to a constant rotational wind. The wind and the rotational speed of the wind turbine are given in Figure 5.4a.

The method previously defined is used where the reference system is the wind turbine model with an isotropic rotor and the damaged system is the same except that the third blade has a reduction of 5% of global stiffness, as it was done in Section 5.2.

Figure 5.4(b-d) gathers the results from the identification and the estimated 95% CI of the identified modes shapes of the edge bending modes. It can be seen that for all those modes, the CI are separated by an important distance between them. This important variation in terms of amplitude and phase shift tends to demonstrate that the mode shapes between the reference and damaged configurations have substantially changed. It implies that the mode shape variations are large enough to get the certitude that the mode shapes are different between the two states, and so that a fault appeared in the system. In other words, the signature of the fault on this mode shape is strong enough to ensure its detection with certitude.

In Table 5.5, the MAC and the uncertainties of each identified mode are summarized. For all those modes, the identified value of the MAC is below the lower bounds of the 95% quantile

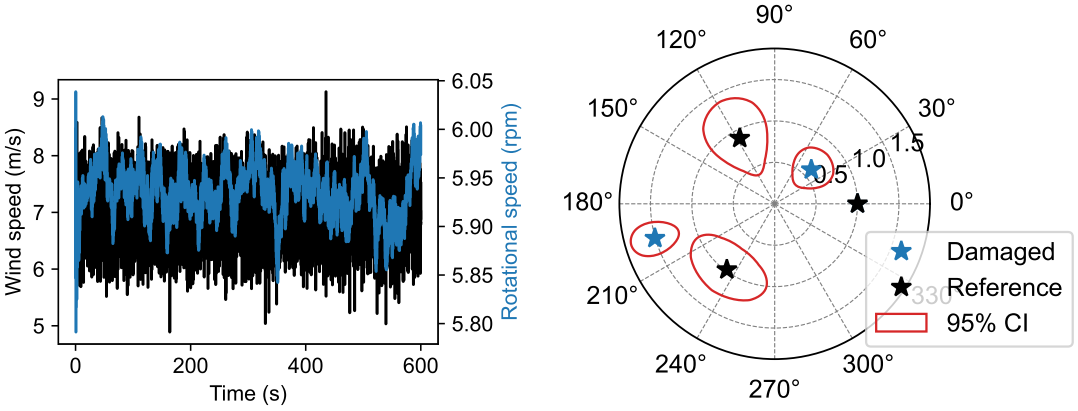

(a) Evolution of the wind speed and rotational speed during the simulation

(b) Backward - identified mode shape and 95% CI

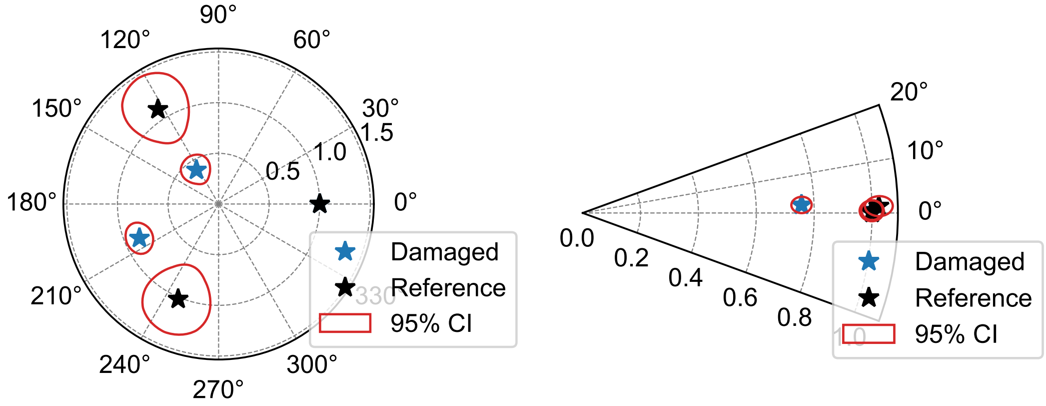

(c) Forward - identified mode shape and 95% CI

(d) Collective - identified mode shape and 95% CI

Figure 5.4 – Comparison of the edgewise bending mode shapes between the reference state and the damaged state under a white noise wind

defined with the chi-square law (last column of Table 5.5). As it was developed in [58] and introduced in Section 2.2.3, it can be concluded that the mode shapes used for the computation of the MAC are different. It can be concluded that the graphical analysis of the confidence intervals and the analysis of the MAC give the same result for the mode shape comparison.

Finally, from the analysis of the change of the mode shapes, it can be concluded that the new state is damaged. Also, looking at the amplitude of the Collective edge mode shape, the damage is localized on the third blade, as this blade is the only blade associated with a loss of amplitude.

Name	MAC value	σ_{MAC}	95% quantile lower bound
Col.	0.9817	0.0030	0.9987
Bck.	0.7328	0.1245	0.8598
Fw.	0.7541	0.1018	0.8589

Table 5.5 – MAC criterion and respective uncertainties, under a white noise wind

5.4.3 Case 2: 5% of stiffness loss on one blade under turbulent wind

The fault detection method was able to successfully detect and localize the damage on the previous case. Now, let us try the method on more realistic data computed with a simulation with a turbulent wind, where the reference and damaged states are identical to the previous ones. Figure 5.5a represents the wind speed and the rotational speed of the rotor. Compared to the previous case (see Figure 5.4a) the wind variation is much more important in this case, as for the rotational speed. In Figures 5.5b, 5.5c and 5.5d, the phase shift and amplitudes for the reference and damaged cases are represented for the three considered modes with their CI.

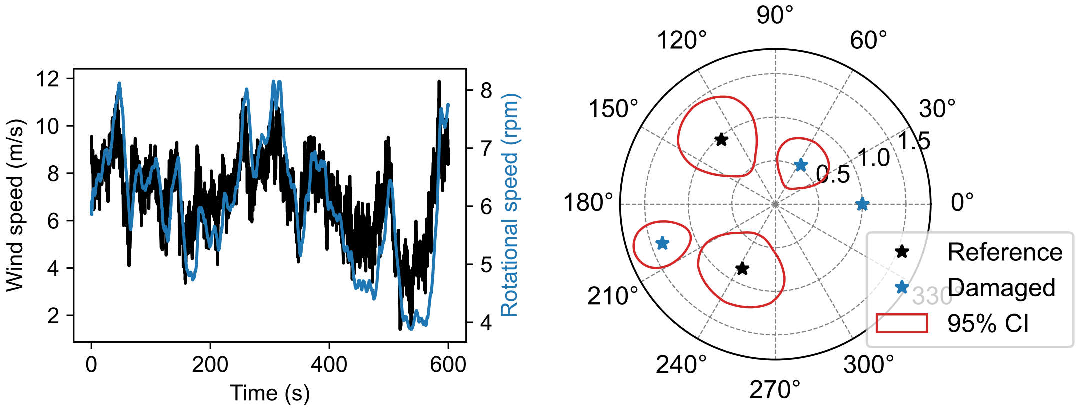

(a) Evolution of the wind speed and rotational speed during the simulation

(b) Backward - identified mode shape and 95% CI

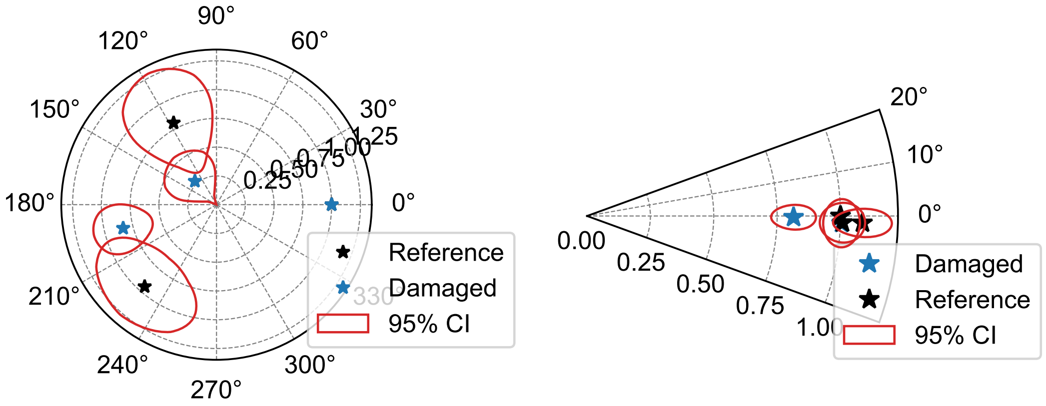

(c) Forward - identified mode shape and 95% CI

(d) Collective - identified mode shape and 95% CI

Figure 5.5 – Comparison of the edgewise bending mode shapes between the reference state and the damaged state under a turbulent wind

Figures 5.5b and 5.5d show that the CI are bigger compared to the previous case (see Figures 5.4d and 5.4b). Despite a larger uncertainty in the identification, the confidence intervals of the Collective and Backward edge modes are not crossing each other. However, due to the increase in the CI, the gap between them has been reduced. For the Forward edge mode (Figure 5.5c), the confidence intervals are crossing each other, which means that it can not be stated that this mode shape has changed. From this graphical analysis, it can be concluded that the Collective and Backward edge mode shapes of the damaged state are different from those in the reference state.

Name	MAC value	σ_{MAC}	95% quantile lower bound
Col.	0.9827	0.0089	0.9913
Bck.	0.6672	0.1565	0.7853
Fw.	0.8063	0.1515	0.6846

Table 5.6 – MAC criterion and the respective uncertainties, under a turbulent wind

Table 5.6 summarizes the MAC and uncertainties of each mode. For the Collective and Backward edge, the value of the identified MAC criterion is once again below the lower bounds of the 95% quantile defined with a chi-square law modeling. This confirms that the mode shapes of the damaged state are different from those of the reference state. Thus, despite the larger uncertainty, it is still possible to detect the damaged state. However, it should be noted that the detectability of a damage depends on two parameters, the process noise (here the turbulence intensity) and the size of the damage. For example, with the selected simulation conditions it is not possible to detect a stiffness loss of 2.5% on a blade. Then, the MAC of the Forward edge mode seems to follow a chi-square law, meaning that the mode shapes are close or similar. Consequently, the uncertainties of the MAC are once again validating the graphical analysis based on the confidence intervals.

Finally, with the obtained results, it can be concluded that the analysis of the edgewise bending mode shapes can be used to detect fault corresponding to a loss of 5% of stiffness in one blade. Also, it is possible to use the amplitudes of the Collective mode shape for fault localization.

5.5 Conclusion

Firstly, an analysis of the changes in the mode shapes of the edge bending eigenmodes has allowed us to validate that the phase shift and the amplitude are highly sensitive to a change of the stiffness or the mass of one blade. Secondly, the uncertainty computation for the phase shift and the amplitude has been defined and validated with a Monte Carlo simulation using the academic model of a wind turbine. Secondly, a fault detection method has been presented, with the comparison of the phase and amplitude jointly with the respective uncertainties. This method can detect a fault in a blade, on a realistic example with a loss of 5% of stiffness on one blade. This work has been presented during the conference ISMA [24].

The method must be improved to develop a metric to quantify the probability of change in a mode shape. To do so, methods based on the local approach presented in Section 2.4 will be explored.

Chapter 6

ROTOR FAULT DETECTION BASED ON THE LOCAL APPROACH

Abstract

In this Chapter, damage detection is pursued with the adaptation of the Stochastic Subspace-based Damage Detection, by defining a residual using the phase shift and amplitude of the edge bending mode shapes. Then, it is applied with a gradually increasing difficulty, from the detection and localization of a loss of stiffness of one blade of the academic model to the detection and localization of a global loss of stiffness of one blade of the DTU 10MW wind turbine model under a realistic variable wind. To continue and to increase the damage detectability using measurements with a fixed length and without concatenating the data, the mean residual is defined, conjointly with the associated impact on the covariance of the residual. The mean residual is then used in a range of applications, showing that it is possible to detect and localize local losses of stiffness, additions of mass, and pitch errors. The effect of the number of sensors, and their location, is also highlighted.

6.1 Introduction

In the previous Chapter, efficient damage indicators of rotor faults have been defined with the associated uncertainties, namely the phase shift and amplitude of the mode shapes of the Fourier harmonics of edge bending. Then an OMA-based damage detection has been presented to show that they can be used for damage detection. However, the presented method needs to compute the uncertainty of the damage features for each identification, which can be time consuming for continuous monitoring. Also to obtain a metric that quantifies the difference between the mode shapes, the only option is to estimate the associated probabilities with a Monte-Carlo method, which is also time consuming, as the MAC criterion gives just binary results for the comparison of the mode shapes. Finally, the method does not provide any localization and estimation of the damage. Consequently, the Stochastic Subspace-based Damage Detection based on the local approach presented in Section 2.4 will be used and adapted for the detection of wind turbine rotor fault. As presented in Section 2.4, since this data-driven method uses model information, it should be possible to perform damage localization and quantification.

The Chapter is organized as follows. First, the new residual designed for the monitoring of wind turbine rotors is presented. Then, the damage detection, localization, and quantification are validated with the detection of a loss of stiffness of one blade of the academic model of a wind turbine. To continue, the method is performed on data computed with the DTU 10MW wind turbine model, with different complexity of the wind modeling. After that, the mean residual is defined, to use several measurements to perform damage detection and then increase the damage detectability. Then, the newly defined residual is tested and the performance is verified, with an application on the academic model of wind turbine. Afterward, the mean residual is used to perform damage detection for the detection of local losses of stiffness on blades of the DTU 10MW wind turbine model. To finish, it is shown that the method can be used to detect the other types of fault that occur on a wind turbine rotor, namely the addition of mass and the pitch error. Also, it is shown that damage detection can also be performed without the model information.

6.2 Definition of a new residual for the Stochastic Subspace-based Damage Detection and localization

The damage detection method defined in the previous Chapter (Section 5.4) enables to identify a global loss of stiffness of one blade through an analysis of the phase shift and amplitude (in general the mode shape) of the edge bending Fourier harmonics. However, it is necessary to compute the uncertainty at every identification, and there is no metric for damage localization. Therefore, the damage detection and localization method presented in Section 2.4 will be used, with a residual based on the phase shifts and the amplitudes of the Fourier harmonics of edge bending.

Let us define the vector v_i that gathers the phase shifts and the amplitudes of the i–th mode shape (defined with r outputs)

$$v_i = \begin{bmatrix} p_2^i & p_3^i & \dots & p_r^i & a_2^i & a_3^i & \dots & a_r^i \end{bmatrix}^T . \tag{6.1}$$

With this vector, it is possible to express a new residual

$$\zeta_i = \sqrt{N}\left(\hat{v}_i - v_i\right) \in \mathbb{R}^{2(r-1)}, \tag{6.2}$$

where $\hat{v}_i$ is an estimate of v_i using a data of length N. It has to be noted that this residual is defined with $r-1$ phases and amplitudes because one needs to be used to set the reference (phase equal to 0 and amplitude equal to 1). Then, a residual that gathers the information of n mode shapes can be defined, such that

$$\zeta = \begin{bmatrix} \zeta_1^T & \dots & \zeta_n^T \end{bmatrix}^T = \sqrt{N}\left(\hat{V} - V\right) \in \mathbb{R}^{2n(r-1)}, \tag{6.3}$$

where $V = \begin{bmatrix} v_1^T & \dots & v_n^T \end{bmatrix}^T$ is the vector regrouping the phases and amplitudes of n mode shapes (which can be called the damage sensitive vector). The phase and amplitude of the identified mode shapes can be described with a Gaussian distribution, as they are a function of the mode shapes which are described by a Gaussian distribution. This is confirmed in Section 5.3, with the definition of the uncertainties of the phase and amplitude based on the first-order delta method, assuming that the phase and amplitude are described by a Gaussian distribution.

In real operational conditions, it can be difficult to know the theoretical value of V, so an estimate ($\hat{V}^0$) of this quantity in the reference state can be used instead. In this thesis, an average of (n_f) different estimates is used, such that

$$\hat{V}^0 = \frac{1}{n_f}\sum_{j=1}^{n_f}\hat{V}^{(j)}, \tag{6.4}$$

where $\hat{V}^{(j)}$ is an estimate of V using the j–th of the n_f data sets. From this, similarly to [136], a residual $(\tilde{\zeta})$ function of the estimated reference can be defined,

$$\tilde{\zeta} = \sqrt{N}\left(\hat{V} - \hat{V}^0\right) = \zeta - \sqrt{N}\left(\hat{V}^0 - V\right). \tag{6.5}$$

$\hat{V}$ is an estimate of V using data of length N. Then, the distribution of the residual ζ (Equation (6.3)) is defined by the following distribution

$$\zeta = \sqrt{N}\left(\hat{V} - V\right) \sim \begin{cases}\mathcal{N}\left(0, \Sigma\right) : H_0 \\ \mathcal{N}\left(\mathcal{J}\delta, \Sigma\right) : H_1\end{cases}, \tag{6.6}$$

with the assumption that the effect of the parameter change on V is linear.

Now, let us take into account the estimated reference into the distribution of the residual ($\tilde{\zeta}$ in Equation (6.5)). First, as $\hat{V}^{(j)}$ is computed using a data set of length N

$$\sqrt{N}\left(\hat{V}^{(j)} - V\right) \sim \mathcal{N}\left(0, \Sigma\right). \tag{6.7}$$

As the different estimates are computed with disjointed data, they are independent, so,

$$\sum_{j=1}^{n_f}\sqrt{N}\left(\hat{V}^{(j)} - V\right) \sim \mathcal{N}\left(0, n_f\Sigma\right). \tag{6.8}$$

Consequently, using Equation (6.4) the distribution of the estimated reference is

$$\sqrt{N}\left(\hat{V}^0 - V\right) \sim \mathcal{N}\left(0, \frac{\Sigma}{n_f}\right). \tag{6.9}$$

Finally, as the data used for the computation of the estimates $\hat{V}$ and $\hat{V}^0$ are different, $\hat{V}$ and $\hat{V}^0$ are independent. So, the distribution of the residual $\tilde{\zeta}$ is

$$\tilde{\zeta} \sim \begin{cases}\mathcal{N}\left(0, \Sigma\left(1 + \frac{1}{n_f}\right)\right) : H_0 \\ \mathcal{N}\left(\mathcal{J}\delta, \Sigma\left(1 + \frac{1}{n_f}\right)\right) : H_1\end{cases}. \tag{6.10}$$

With this new residual, it will be possible to perform damage detection and localization on operating wind turbine rotors using the Stochastic Subspace-based Damage Detection method. To validate the use of this new residual, damage detection and localization will be performed on the academic model of a wind turbine.

6.3 Application to the academic model of wind turbine

In this example, the damage detection and localization method will be used to detect a loss of stiffness on a blade DOF of the academic model of a wind turbine. The simulated measurements will be computed for a model with a rotational speed of 1.4 rad/s under Gaussian noise, with a signal 600 s long data sampled at 25 Hz.

6.3.1 Preliminary study

The first step is to compute the matrices that are needed to perform the different tests, as it is shown in the flowchart Figure 2.5. So, with the system matrices, the sensitivity of the phase shift and amplitude of the mode shape of the Fourier harmonics regarding a loss of stiffness of each blade can be computed (leading to $\nu = 3$). In this example, the first-order Taylor approximation is used with $\Delta G = -0.1\%$. Then, the covariance matrix of the residual needs to be estimated. Here, the covariance matrices of phases and amplitudes of the mode shapes is estimated using the method presented in the previous Chapter (Section 5.3), where the identification is performed using the accelerations of the rotor DOF. Consequently, with the sensitivity and covariance matrices, the Fisher matrix (Equation (2.63)) can be computed. Thus, it is possible to estimate the minimum 95%-level detectable parameter change (Equation (2.72)) and estimate the probability of detection of specific changes (Equation (2.73)), as a function of the number of data sets used for the estimation of the reference (n_f in Equation (6.4)).

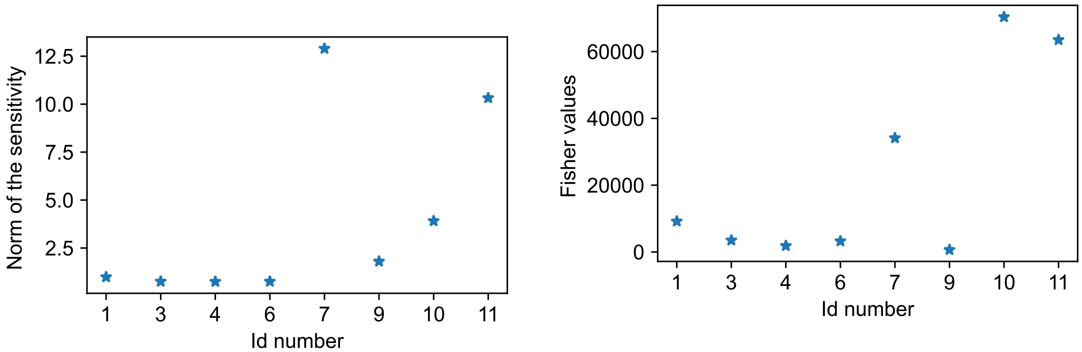

(a) Norm of the sensitivity matrix

(b) Sum of the diagonal values of the Fisher matrix

Figure 6.1 – Contribution of each identifiable Fourier harmonic to the damage detection of the academic model of wind turbine

Before assessing the performance of the damage detection, the Fourier harmonics that will be used to construct the residual need to be selected. To do so, the sensitivity matrix of each identifiable harmonic will be studied. In Figure 6.1a, the norm of the sensitivity of each harmonic is displayed. And one can see, that the harmonics 7, 9, 10, and 11 have the highest sensitivities. However, the covariance of each harmonic needs to be taken into account. In Figure 6.1b, the sum of the diagonal values of the Fisher matrix of each Fourier harmonic is displayed. And one can see that three harmonics are corresponding to a value higher than the others, namely the 7, 10, and 11. Those harmonics are the harmonics of rotor flap bending of the Floquet modes of Backward, Forward, and Collective flap (see Table 3.1). So the residual will be composed of those harmonics, namely 7, 10 and 11.

Once the residual has been designed, it is possible to compute the minimum 95%-level detectable parameter change and the probability of detection (POD) of some damages, function of the number of files used to compute the reference. In Table 6.1, the minimum 95%-level detectable parameter change and the probability of detection of different changes in the parameters are assessed. For simplicity, the relative change in one parameter component ($\overline{\Delta\theta} = \Delta\theta/\theta_0$) will be used in this section. With Table 6.1, it can be seen that increasing the accuracy of the reference estimate has an impact on the minimum 95%-level detectable parameter change (which is the same for all the parameter components) and on the probabilities of detection. But it can be seen that from $n_f = 25$, increasing further the accuracy of the reference does not improve significantly the minimum 95%-level detectable parameter change and the POD estimations, with a maximum gain of 0.03% on $\overline{\Delta\theta}_{min}$. So, a reference estimated with $n_f = 25$ will be used in this section. Also, the minimum identifiable parameter change and the probability of detection are coherent: as 1.5% is below $\overline{\Delta\theta}_{min}$, the probability of detection is below 95%, and in contrast 2% and 2.5% are higher than $\overline{\Delta\theta}_{min}$, with an associated POD higher than 95%.

n_f	$\overline{\Delta\theta}_{min}$	POD(1.5%)	POD(2%)	POD(2.5%)
5	1.94%	77.24%	96.12%	99.74%
10	1.86%	81.09%	97.43%	99.88%
25	1.81%	83.44%	98.08%	99.93%
50	1.79%	84.22%	98.27%	99.94%
100	1.78%	84.61%	98.37%	99.95%
200	1.78%	84.80%	98.41%	99.95%

Table 6.1 – Minimum 95%-level detectable change ($\overline{\Delta\theta}_{min}$) and probabilities of detection (POD) function of the number of data sets used for the estimation of the reference (n_f)

In Section 2.4.4, the minmax localization method has been presented, but to apply this method, the sensitivity matrix of the residual needs to be full rank. Unfortunately, with the studied problem, the sensitivity matrix is not full rank, indeed the sensitivities of the parameters are linearly dependent, with $\mathcal{J}_1 + \mathcal{J}_2 + \mathcal{J}_3 = 0$ (where $\mathcal{J}_i$ is the sensitivity of the i–th blade). The physical meaning is that the anisotropy is identical if one blade has a drop of stiffness, or if the two other blades have the opposite change of stiffness. Consequently, for the study of the wind turbine rotors with the selected residual, it will be not possible to use the minmax localization method.

The minimum 95%-level detectable parameter change and the probability of detection have been assessed. Now, damage detection will be performed to validate the previous theoretical study. To do so, the test is performed on data corresponding to 4 states of the model, namely the reference one and three different damaged states, with a graduated stiffness reduction of G_3, precisely 1.5%, 2%, and 2.5%.

6.3.2 Damage detection

Before presenting the results the designation of the test in the figures have to be explained:

— Reference test: Distribution of the damage detection test performed on data corresponding to the reference and healthy structure

- Reference 95% quantile: Value of the upper bound of the 95% quantile of the damage detection test performed on data corresponding to the reference and healthy structure
- Damaged test: Distribution of the damage detection test performed on data corresponding to a damaged structure

After performing the damage detection test (1000 times per damaged state), the parameter change is detected 790 times for the first damaged state, 973 times for the second, and 999 times for the third, corresponding to empirical POD of 79.0%, 97.3%, and 99.9%, respectively. Those results are in agreement with the theoretical POD computed *a priori* (see Table 6.1 at $n_f = 25$) for $\overline{\Delta G_3} = -2\%$ and -2.5%. For $\overline{\Delta G_3} = -1.5\%$, the empirical POD is lower than the theoretical one, it might be due to the value of the simulated change being lower than the 95%-level detectable parameter change. Also, with the histograms of those tests, it is possible to compare them with the theoretical distributions of the tests, see Figure 6.2. With this figure, it can be seen, that for each state of the structure, the histograms of the tests are matching with the theoretical distributions. Also, the mean of the tests can be studied. In Table 6.2, the theoretical and empirical means are compared. For the different structure states, the theoretical and empirical means are close, which confirms the theoretical statistical modeling. Consequently, from the POD, the histograms, and the tests means, the damage detection test is assessed to perform as predicted.

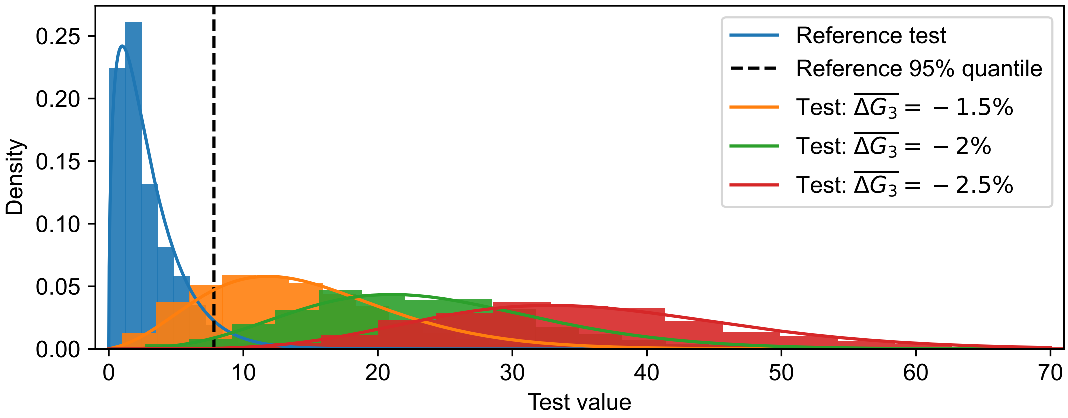

Figure 6.2 – Comparison of the theoretical distributions and the histograms of the damage detection tests

	Reference	$\overline{\Delta G_3} = -1.5\%$	$\overline{\Delta G_3} = -2\%$	$\overline{\Delta G_3} = -2.5\%$
$\bar{t}_{th}$	3	14.83	24.03	35.86
$\bar{t}_{emp}$	2.79	13.67	22.94	35.25

Table 6.2 – Theoretical and empirical means of the damage detection tests, $\bar{t}_{th}$ and $\bar{t}_{emp}$ respectively

6.3.3 Damage localization

To continue the application, the damage localization presented in Section 2.4.4 is performed. Two cases can be studied, one with a POD lower than 95% ($\overline{\Delta G_3} = -1.5\%$) and one with a POD higher than 95% ($\overline{\Delta G_3} = -2\%$). In Table 6.3, the means of the localization tests corresponding to 1.5% and 2% of stiffness loss of the third blade are compared with the theoretical means. One can see that in both cases, the empirical and theoretical means are close. Consequently, it confirms that the mean of the localization test is coherent with the theoretical distribution for all the considered cases.

Simulated damage		Tested parameter G_1	G_2	G_3
$\overline{\Delta G_3} = -1.5\%$	$\bar{t}_{h\ th}$	3.66	4.61	12.83
	$\bar{t}_{h\ emp}$	3.36	3.88	11.67
$\overline{\Delta G_3} = -2\%$	$\bar{t}_{h\ th}$	5.72	5.63	22.03
	$\bar{t}_{h\ emp}$	5.50	6.29	20.89

Table 6.3 – Theoretical and empirical means of the damage localization tests, $\bar{t}_{h\ th}$ and $\bar{t}_{h\ emp}$ respectively, function of the tested parameters

So, the localization test is performing as it theoretically should. Also, to perform the damage localization, the distributions of the different tests can be compared. In Figure 6.3, the box plots of the localization test corresponding to the three different blades for the two first simulated damages are displayed. In addition to a higher mean, the distribution of the test corresponding to the damaged blade is much more shifted, which is the consequence of the χ^2 distribution, where the mean of the distribution depends on the non-centrality parameter which characterizes the mean of the distribution.

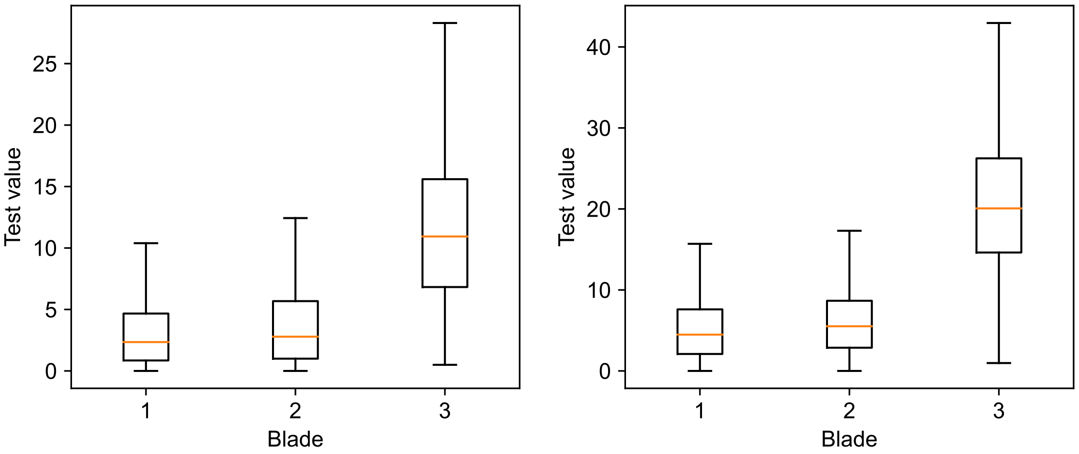

(a) $\overline{\Delta G_3} = -1.5\%$ (b) $\overline{\Delta G_3} = -2\%$

Figure 6.3 – Box plot of the damage localization tests, for the two first simulated damages

6.3.4 Damage quantification

Once the damage localization is performed, it can be confirmed with the damage quantification (Equation (2.80)). In Table 6.4, the mean values of the damage quantification with the associated 95% confidence intervals (computed based on the central limit theorem, remind in Appendix B.2) are reported. Firstly, one can see that only the parameter G_3 is associated with a loss of stiffness, which confirms that the parameter has really changed. This difference in sign is the consequence of the Fisher matrix, where the non diagonal values are all negative. Secondly, the estimated damage in G_3 is close to the simulated damage for both studied simulated damages. So, for this model, the assumption of a linear effect of the parameter changes on the residual is respected. Finally, the standard deviation of the damage quantification is around 0.43% for the different estimations, and theoretically, it should be 0.42% ($\sqrt{1/F_{33}}$ obtained based on the distribution Equation (2.81)). This confirms that the damage quantification test is performing as it theoretically should.

Simulated damage	G_1	G_2	G_3
$\overline{\Delta G_3} = 1.5\%$	0.68 ± 0.03 %	0.72 ± 0.03 %	-1.43 ± 0.03 %
$\overline{\Delta G_3} = 2.\%$	0.93 ± 0.03 %	0.99 ± 0.03 %	-1.95 ± 0.03 %

Table 6.4 – Mean values of the damage, associated with their 95% confidence interval

With the application of the damage detection, localization, and quantification method on the academic model of a wind turbine, it has been confirmed that the method can be used to detect and localize a fault in a rotating wind turbine rotor. To continue the validation, the method will be performed on data from the DTU 10MW wind turbine model, with a wind load of different complexity.

6.4 Application to the DTU 10 MW wind turbine model, hub height wind

6.4.1 Simulation parameters

To continue with the validation, the damage detection and localization is performed on data computed with the DTU 10MW model of wind turbine, to have data closer to real measurements. The objective is to propose a framework that works continuously during the lifetime of a wind turbine, so its robustness towards realistic environmental conditions must be ensured, which can change a lot. For this purpose, real wind data are taken here. So, for each data set, the external load, which is the wind, is computed based on in-filed data. The filed data are 10 minutes mean wind speed from a *Météo France* buoy located in the golf of Gascony (See Figure 6.4). Those data have been collected in 2021 and are free to use [92]. Based on the mean wind speed, the "Hub Height" wind filed is computed using the software *Turbsim* (see Section 1.4.1), where the turbulence intensity is automatically defined based on the IEC B norm.

The simulated data are 600 s long and sampled at 50 Hz as it is common in the wind turbine field but the first 100 s are not used to remove the start up of the wind turbine, so $N = 25000$. To have an operating wind turbine and to avoid any change in the structure, especially the pitch angle of the blades, the mean wind speeds are selected between 4 and 11 m/s (see Figure 1.8 for the pitch evolution of wind turbine model). This range contains almost 70% of the speed values, as it is shown in Figure 6.5, with a histogram of all the wind speed values and an evolution of the wind speed over one month. So, it can be concluded that the selected mean speed range represents mainly the conditions of a wind turbine.

Then, to perform the identification and the different statistical tests, the edge bending Fourier harmonics of the rotor will be identified using the edge bending blade root moments. Those

Figure 6.4 – Localization of the meteorological buoys of Météo-France with accessible data [92], the used buoy is circled

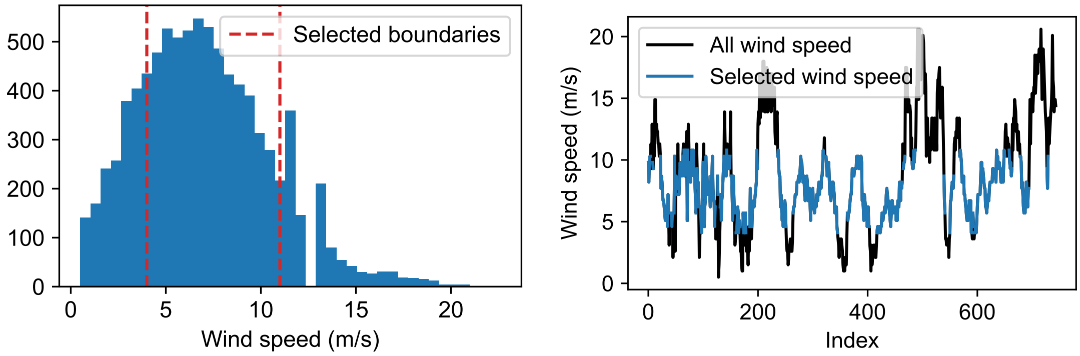

(a) Histogram of the wind speed, year 2021 (b) Wind speed evolution, January 2021

Figure 6.5 – Wind speed values for the Gascogne buoy

outputs are used because it is easier to install sensors close to the hub. Finally, the simulated damage will be a global stiffness reduction of the third blade of the rotor, along flap and edge. So, there will be three parameters in the damage parametrization, one for the stiffness of each blade.

6.4.2 Preliminary study

The first step of the preliminary study is to compute the sensitivities with the First order Taylor approximation. To do so, the Floquet modes are computed for a small change of stiffness for each blade (1% in the present case). Then, the identification can be performed using a reference data set corresponding to an undamaged rotor, composed of 100 data sets, so $n_f = 100$. Then, from the study in Section 5.2, to build the residual, the phase shift and amplitude of the Backward, Forward, and Collective edge bending mode shapes will be used.

In Figure 6.6a, the diagonal values of the Fisher matrix are displayed, where the residual is built using each harmonic or all the Fourier harmonics of edge bending. From this Figure, it is clear that the Collective edge is the harmonic that provides much information and the Backward edge the least. But the damage detectability is better when all the Fourier harmonics are selected. This is confirmed with the POD of different stiffness losses in Table 6.5, especially with the lower damage. Indeed, for 1% of stiffness loss, the POD is almost two times higher with a residual constructed with all the harmonics, compared to the residual with only the Collective edge. The POD of the last column of Table 6.5, can be visualized in Figure 6.6b, with the theoretical distributions of the damage detection, for a residual composed of all the Fourier harmonics of edge bending. This last residual will be used in the following.

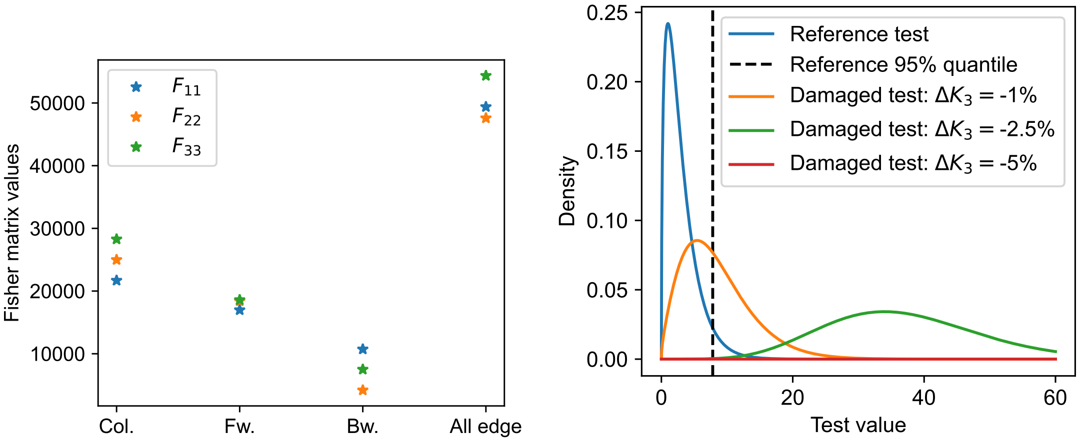

(a) Diagonal values of the Fisher matrix function of the Fourier harmonics that compose the residual

(b) Theoretical distribution of the statistical test for different system states, residual composed of all the edge bending harmonics

Figure 6.6 – Theoretical study of the damage detection applied to the DTU 10MW wind turbine model

Stiffness loss (%)	Col.	Bw.	Fw.	All egde
1	26.04	18.11	9.80	47.54
2,5	95.59	82.75	41.55	99.95
5	100.00	100.00	96.61	100.00

Table 6.5 – Theoretical probability of detection (%) for different stiffness losses and different construction of the residual

Now, as the construction of the residual is stated and the associated theoretical performed assessed, damage detection can be performed. For this damage detection, an estimated reference will be used with $n_f = 100$, as the data sets used for the computation of the covariance matrix are used for the estimation of the reference.

6.4.3 Damage detection

Before assessing the performance of the damage detection test, it has to be verified that the test follows its theoretical distribution for the training state (i.e. undamaged structure). In Figure 6.7a, the test values are displayed against the mean wind speed during the simulation used to compute the residual. In this figure, there is no clear correlation between the test and the wind speed, with an estimated correlation coefficient of 0.19. Then, the distribution of the test can be assessed; in Figure 6.7b, the histogram of the test is compared with the theoretical distribution. It can be seen, that the shape of the histogram is close to the theoretical distribution. However, there are more outliers in the test than it is predicted, this might be the consequence of identification errors. Consequently, it seems that there it is possible to perform damage detection with variable wind conditions.

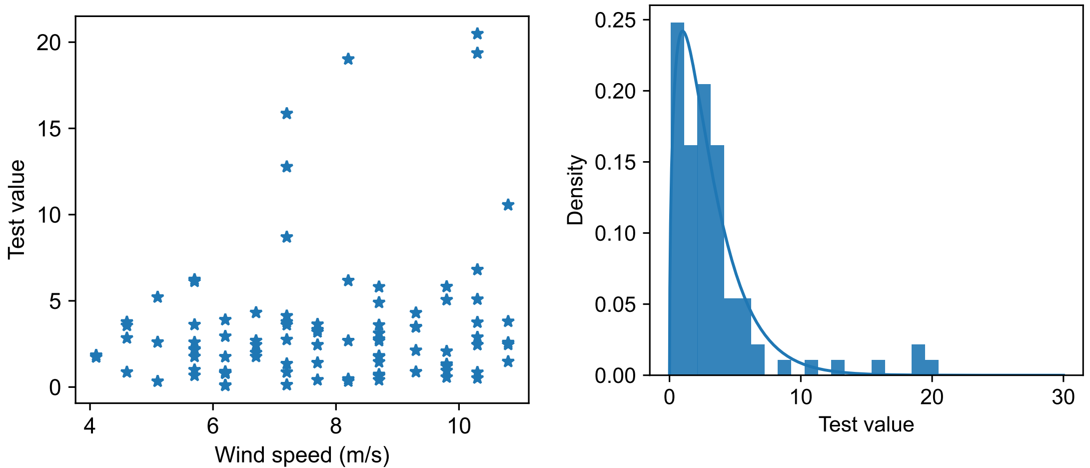

(a) Test value against the mean wind speed during the simulation

(b) Comparison of the theoretical distribution and the histogram of the test computed with the training data set

Figure 6.7 – Study of the performance of the damage detection test

After that, the damage detection test is performed on three data sets, corresponding to a different stiffness loss of the third blade, 1%, 2.5%, and 5%. In Figure 6.8, the histograms of the test performed on each data set are displayed. First, it can be seen that the distribution shifts to the right when the damage increases. But the shift for the tests corresponding to 1% and 2.5% of stiffness loss seems to be reduced compared to the theory in Figure 6.6b. This is confirmed by the empirical POD, with a probability of 15%, 89% for 1% and 2.5% of stiffness loss, compared to 47.54% and 99.95% theoretically (last column of Table 6.5). The gap between the empirical and theoretical POD can be also explained by the outliers in the tests, which are increasing the estimated value of t_{crit}, 11.7 against 7.8 theoretically. Nevertheless, the stiffness loss of one blade has been detected and the performance can be considered close to the theory with $\Delta K_3 = -2.5\%$ and $\Delta K_3 = -5\%$. So, the damage localization can be performed, to verify if the position of the simulated damage is well isolated.

6.4.4 Damage localization and quantification

To assess the performance of the localization test, the cases corresponding to 2.5% and 5% of stiffness losses are studied, as the damage is not enough detected for a loss of 1% of stiffness. In Figure 6.9 the box plot of the localization is displayed for the two considered damages. With this figure, it is clear that for both damages, the third blade is the parameter that is reacting the most to the localization test. To confirm the localization, the quantification results can be studied. In Table 6.6, the mean values of the quantification tests for all the parameters are reported, with the values associated with their 95% confidence interval. With those mean values, it can be seen that the estimated damage is negative only for the test corresponding to the third blade. So, it confirm the results of the localization test.

To study more precisely the damage quantification results (Table 6.6), the results obtained

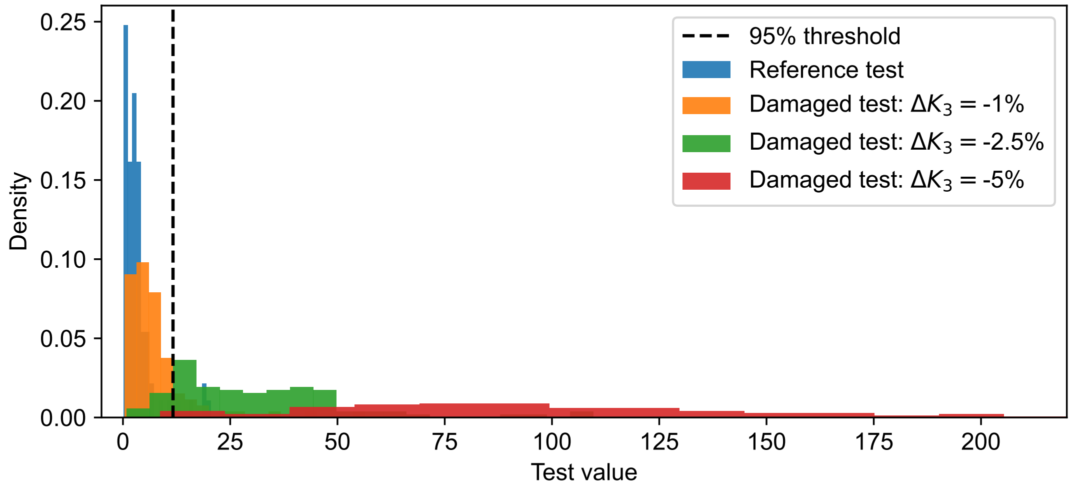

Figure 6.8 – Histograms of the damage detection test

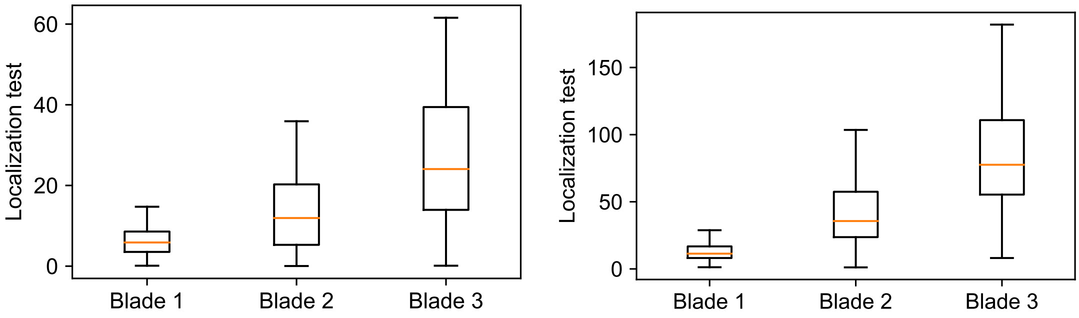

(a) 2.5% of stiffness drop

(b) 5% of stiffness drop

Figure 6.9 – Box plot of the damage localization for the two studied cases

also for the data sets with $\Delta K_3 = -1\%$ can be studied. Looking at the mean values of the quantification, it can be seen that there is a gap between those values and the simulated ones. The gap is increasing more as the stiffness drop rises because the assumption of linear impact of the damage is less accurate. Nevertheless, the damage quantification is a good estimation of the simulated damage. Looking at the standard deviation of the damage quantification, it should be 0.45% theoretically ($\sqrt{1/F_{33}}$ based on the distribution Equation (2.81)). For the first data set corresponding to the first simulated damage, the mean standard deviation is 0.46%. However, for the two other data sets, the mean standard deviation is respectively 0.62% and 0.77%. It seems that the more the damage is important, the more the standard deviation increases, which is due

Stiffness loss (%)	Blade 1	Blade 2	Blade 3
1	0.66 ± 0.09 %	0.53 ± 0.09 %	-0.83 ± 0.10%
2.5	1.22 ± 0.08 %	1.50 ± 0.15 %	-1.98 ± 0.14 %
5	1.73 ± 0.09 %	2.65 ± 0.18 %	-3.47 ± 0.19 %

Table 6.6 – Mean values of the damage quantification with the associated 95% confidence intervals

to the change in the covariance of the residual. So, the assumption of a constant covariance of the residual is not verified for important damage.

To conclude this application of the damage detection method, it can be seen that it is possible to detect and localize a global stiffness reduction of a blade, from data computed with an aero-servo-elastic model of a wind turbine, even if all the assumptions of the method are not respected.

6.5 Application to the DTU 10 MW wind turbine model, full field wind

To continue the application of the damage detection, the damage detection will be performed on data computed with a model where the wind is changed to full field modeling (see Section 1.4.1), to simulate data closer to the reals ones.

6.5.1 Preliminary study

First, the impact of the new wind modeling on damage detectability will be assessed, with the same study performed in the last section. So, the covariance matrix is estimated, as it was done in Section 6.4.2. To begin, with the diagonal values of the Fisher matrix function of the Fourier harmonics in Figure 6.10a, it can be seen that the change of load had an important impact on the Collective edge, with an increase of the covariance. For the two other harmonics, there is less evolution of the covariance. The increase in the covariance can be understood by comparing the "hub height" and the full field wind. As the full field wind add spatial turbulence, the noise increase, which means that covariance increases. Consequently, the diagonal values of the Fisher matrix for a residual composed of all the Fourier harmonics are reduced by almost 40%.

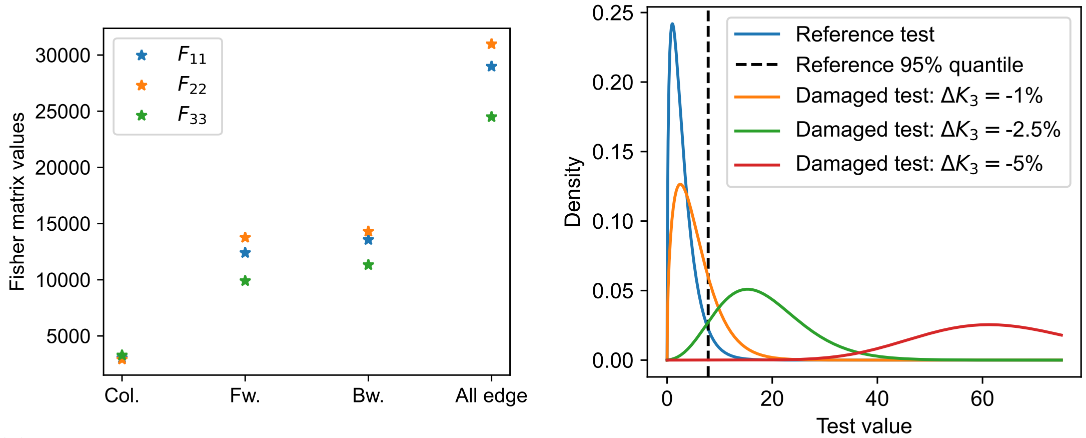

(a) Diagonal values of the Fisher matrix function of the Fourier harmonics that compose the residual

(b) Theoretical distribution of the statistical test for different system states

Figure 6.10 – Study of the performance of the damage detection test, full field wind simulated

The reduction of the Fisher values has a direct impact on damage detection. In Figure 6.10b, the theoretical distribution of the damage detection test is displayed. Compared to previous wind modeling Figure 6.6b, it is clear that the shift of the test has reduced. Which is logic, as the shift is a direct function of the Fisher matrix ($\lambda = \delta_h^2 F_{hh}$). Following the reduction of the shift in the distribution, there is a reduction in the probability of detection. In Table 6.7, the POD for the different configurations of the residual are displayed and when they are compared to the previous case (Table 6.5) the probabilities have reduced.

Stiffness loss (%)	Col.	Bw.	Fw.	All egde
1	7.00	11.49	12.52	22.87
2,5	19.61	53.16	59.45	92.96
5	66.59	99.25	99.73	100.00

Table 6.7 – Theoretical probability of detection (%) for different stiffness loss and different construction of the residual

Now that the preliminary study has been carried out, damage detection can be performed, with the same simulated damages that have been presented in the previous section. For this application, the residual constructed with the phase shift and the amplitudes of the three edge bending modes shapes is once again used.

6.5.2 Damage detection

To verify the performance of the damage detection under the full field wind, the method is applied to different data sets with the same damage presented in the previous section. For those data sets, the environmental variability is again based on the real data of *Météo-France*. In Figure 6.11 the histograms of the damage detection test applied to the different states of the structure are displayed. Compared to the theoretical distributions in Figure 6.10b, two main differences can be seen. First, there is less shift than expected and the histogram corresponding to a loss of 5% of stiffness has a wider spread. This is the consequence of the two main assumptions of the method that are not fully respected, namely the linear effect of the damage on the residual and the stability of the covariance matrix of the residual.

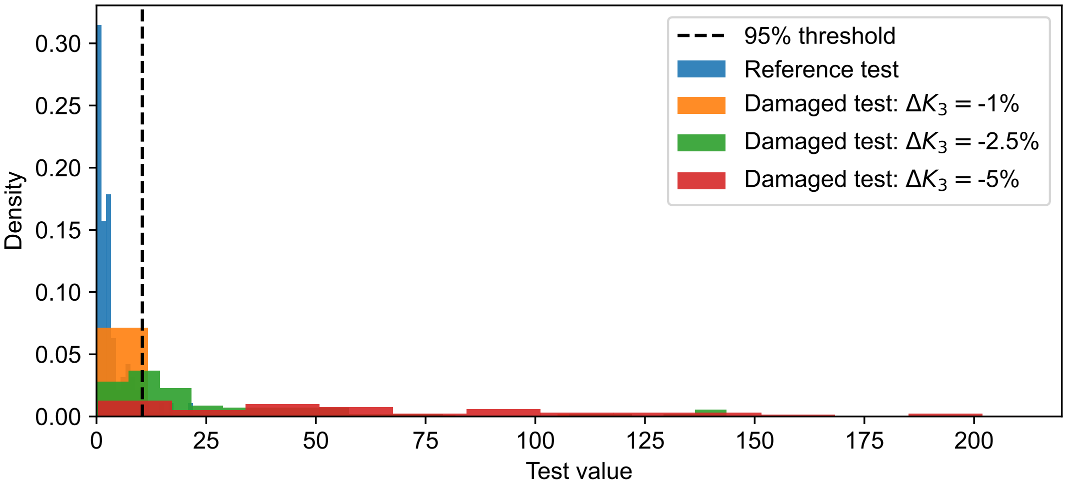

Figure 6.11 – Histograms of the damage detection test, full field wind modeling

Then, the empirical POD can be computed, with 16%, 67%, and 84% for respectively 1%, 2.5% and 5% of loss of stiffness. Compared to the theoretical values in Table 6.7 (last column), for 2.5% and 5% of loss of stiffness, there is an important gap. This is the consequence of the less important shift of the test corresponding to the damaged rotor, exactly like the previous application with the other modeling of the wind. Despite this, it has been possible to detect a loss of stiffness of one blade. To continue the damage localization will be performed.

6.5.3 Damage localization and quantification

As in the previous application, only the cases with a loss of 2.5% and 5% of loss of stiffness are studied to assess the performance of the damage localization. In Figure 6.12 the box plot of the localization tests of both simulated damages is displayed. The results are similar to the previous application, with a much more important shift for the third blade, which is the damaged blade in the simulations.

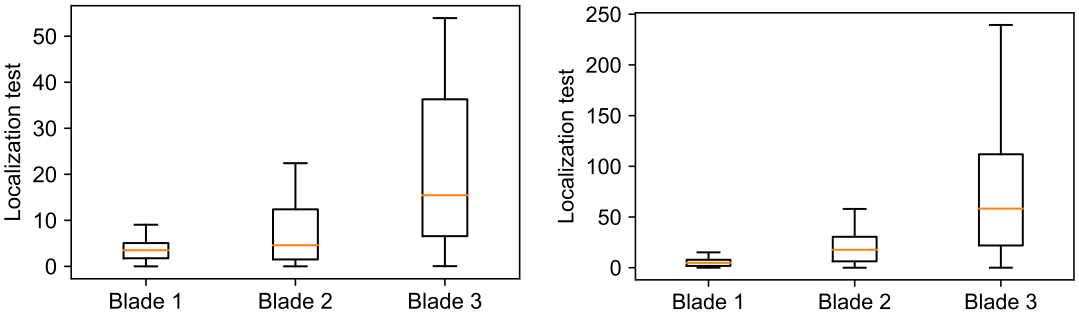

(a) 2.5% of stiffness drop

(b) 5% of stiffness drop

Figure 6.12 – Box plot of the damage localization for the two studied cases, full field wind modeling

Then the damage quantification is performed, to confirm the localization results. In Table 6.8, the mean estimated damage with the associated 95% confidence intervals are displayed. Once again, the quantification is confirming the localization, where only the third blade is associated with a loss of stiffness. But, looking at the value, as for the previous application, it can be seen that there is a gap between the estimated and the simulated damage. This is related to the lower shift, which is directly linked to the estimated damage.

Stiffness loss (%)	Blade 1	Blade 2	Blade 3
1	0.26 ± 0.09 %	0.25 ± 0.17 %	-0.44 ± 0.21%
2.5	0.74 ± 0.08 %	1.50 ± 0.25 %	-2.12 ± 0.34 %
5	0.83 ± 0.11 %	2.28 ± 0.18 %	-3.44 ± 0.56 %

Table 6.8 – Mean values of the damage quantification with the 95% confidence intervals, full field wind modeling

To conclude this application, it can be stated that it has been possible to detect and localize the damage simulated on the blades of the rotor. The impact of the new wind modeling has been seen with an increase in the covariance of the residual, as the full field modeling adds spatial turbulence. Also, whereas the assumption of a linear impact of the damage and the stability in the covariance of the residual are not respected in the application, it is possible to use the Stochastic Subspace-based Damage Detection method. To be closer to the theory, smaller damages can be searched, and to do so the damage detectability has to be increased. From the theory of the damage detection method, the minimum parameter change that can be detected directly depends on the length of the signal used for the identification of the residual. In the next section, it will be shown how to increase damage detectability coupling identification results instead of increasing the signal length.

6.6 Definition of the mean residual

6.6.1 Residual distribution

With the presented method, the value of the minimum detectable parameters changes depends on two quantities, the covariance which is related to the external noise, which cannot be changed, and the length of the signal. The latter can be adapted according to a targeted value. However, in the wind turbine field, it is common to have a fixed length of the measurement to be synchronized with the SCADA data. One option to is to concatenate the data and then identify the residual. Another option is to identify the residual with all the data sets and then compute a mean residual, which leads to an equivalent change in the distribution of the residual. The last option is chosen because it allows to use residuals that have already been computed and the formalism is equivalent to the estimation of the reference that has been introduced in Section 6.2.

The mean residual, function of the phase shifts and amplitudes of the edge bending modes is defined as

$$\bar{\zeta} = \sqrt{N}\left(\bar{V} - V\right) \in \mathbb{R}^{2n(r-1)}, \tag{6.11}$$

with

$$\bar{V} = \frac{1}{nb_f}\sum_{j=1}^{nb_f}\left(\hat{V}\right)_j, \tag{6.12}$$

the mean of the phase shifts and amplitudes, computed with the values identified using nb_f N long files.

Let us define the distribution of this new residual, as it has been done in the previous Section

$$\sqrt{N}\left(\frac{1}{nb_f}\sum_{j=1}^{nb_f}\left(\hat{V}\right)_j - \frac{1}{nb_f}\sum_{j=1}^{nb_f}V\right) \sim \begin{cases}\mathcal{N}\left(0, \dfrac{\Sigma}{nb_f}\right) : H_0\\ \mathcal{N}\left(\mathcal{J}\delta, \dfrac{\Sigma}{nb_f}\right) : H_1\end{cases}, \tag{6.13}$$

then

$$\bar{\zeta} \sim \begin{cases}\mathcal{N}\left(0, \dfrac{\Sigma}{nb_f}\right) : H_0\\ \mathcal{N}\left(\mathcal{J}\delta, \dfrac{\Sigma}{nb_f}\right) : H_1\end{cases} \tag{6.14}$$

the distribution of the mean residual, computed with nb_f identified residuals. Thereafter, the minimum 95% detectable fault associated with the mean residual can be expressed as a function of the minimum detectable fault defined in Equation (2.71),

$$\bar{\delta}_{h\ min} = \frac{\delta_{h\ min}}{\sqrt{nb_f}}. \tag{6.15}$$

Consequently, nb_f can be adjusted to detect a specific fault or parameter change.

Analogously, a mean residual computed using nb_f identified residuals with a reference estimated with n_f identifications is defined as

$$\bar{\zeta}^* \sim \begin{cases} \mathcal{N}\left(0, \Sigma\left(\frac{1}{nb_f} + \frac{1}{n_f}\right)\right) : H_0 \\ \mathcal{N}\left(\mathcal{J}\delta, \Sigma\left(\frac{1}{nb_f} + \frac{1}{n_f}\right)\right) : H_1 \end{cases}. \tag{6.16}$$

Now, as this new residual as been defined, it will be tested on data computed with the academic model of wind turbine.

6.6.2 Application to the academic model of wind turbine

To start, the theoretical performance of the damage detection test and the impact of the number of files used to compute the mean residual will be assessed, with this time the use of a theoretical reference in the computation of the residual. Table 6.9 presents the minimum 95% delectable fault and the probability of detection of a reduction of 0.5% of G_3 function of the number of files used to compute the mean residual. With this Table, it is clear that using several files to compute the mean residual will improve the damage detectability. In Figure 6.13, the evolution of the distribution of the detection test function of nb_f is displayed and one can see that as the damage detectability increases the shift increases also (and vice versa).

nb_f	1	2	5	10	15	20	25	50
δ_{min}	1.77%	1.25%	0.79%	0.56%	0.46%	0.40%	0.35%	0.25%
POD($\overline{\Delta G_3} = -0.5\%$)	14.27	25.23	57.81	88.82	97.80	99.65	99.95	> 99.9

Table 6.9 – Minimum detectable fault and probability of detection function of the number of files used in the mean residual (nb_f)

To validate the mean residual, the damage detection will be performed with the modeling of a change of -0.5% in G_3. Before that, the optimal nb_f has to be found, and looking at Table 6.9, $nb_f = 15$ seems to be the ideal parameter to choose,as it is a good compromise between the POD (equal to almost 98%) and the number of data to manipulate.

Here, 1500 simulations of the wind turbine model are computed, both for the reference and damaged state ($\overline{\Delta G_3} = 0.5\%$). To compute the mean residual, the 1500 residuals of each system state are separated into 100 sets, to have completely independent mean residuals. In Figure 6.14, the histograms of the damage detection tests using the mean residual are displayed, conjointly with their theoretical distributions. Firstly, the histogram of the damage test corresponding to the reference structure fits well with the theoretical distribution, although the limited number

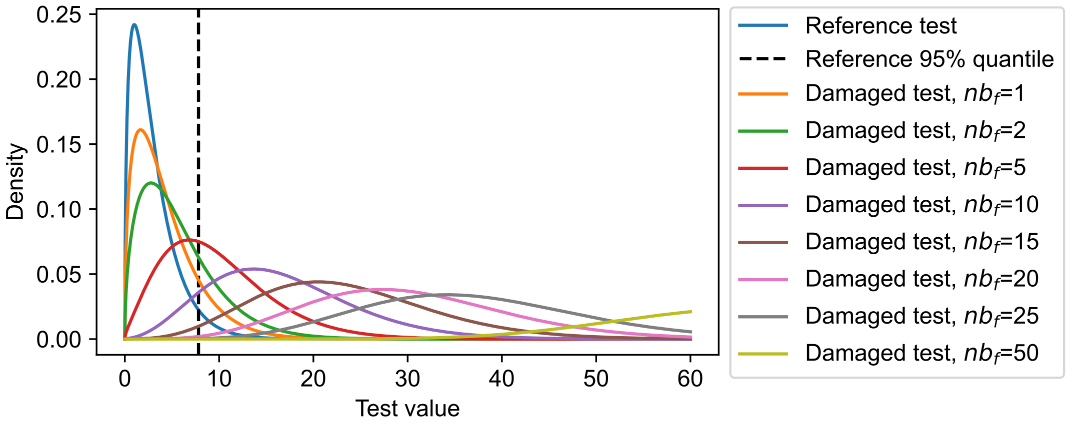

Figure 6.13 – Theoretical distribution of the damage detection test for $\Delta G_3 = -0.5\%$ and different values of nb_f

of tests is not sufficient to totally assess the distributions. Secondly, it can be seen that there is a shift for the case corresponding to a change of 0.5% of G_3, and this shift is corresponding to the theoretical one, with an empirical POD of 97% compared to 97.8% theoretically. Those two remarks are confirmed by looking at the mean of the damage detection in Table 6.10, where the means of both tests are close to the theoretical values. So, it can be concluded that the damage detection using the mean residual is performing as it should. Also, the positive effect of the mean residual on the damage detectability can be assessed with the histogram of the test when $\Delta G_3 = -0.5\%$ (see Figure 6.14), where the shift of the distribution is similar to the one obtained with the test using initial residual for $\Delta G_3 = -2\%$ (see Figure 6.2).

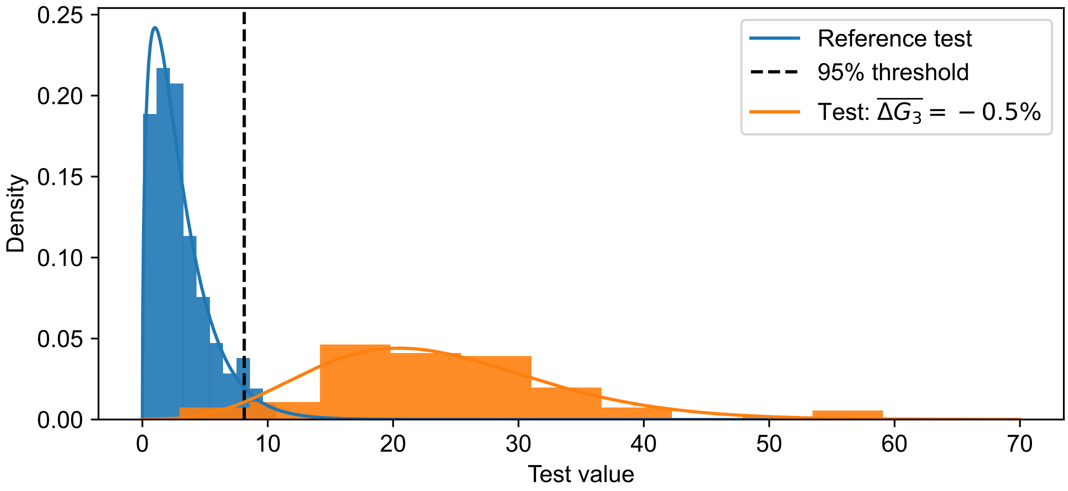

Figure 6.14 – Comparison of the theoretical distributions and the histograms of the damage detection tests using the mean residual

Thereafter, the damage localization and quantification are performed. In Table 6.11, the mean results are reported and clearly, the localization test is in agreement with its theoretical distribution. Also, the damaged blade has been detected and the simulated parameter change has been well estimated, with an empirical standard deviation of 0.11% equal to the theoretical one. This example confirms the use of the localization and quantification test with the mean

	Reference	$\overline{\Delta G_3} = -0.5\%$
$\bar{t}_{th}$	3	23.50
$\bar{t}_{emp}$	3.04	24.20

Table 6.10 – Theoretical and empirical means of the damage detection tests using the mean residual, $\bar{t}_{th}$ and $\bar{t}_{emp}$ respectively

residual.

	Tested parameter		
	G_1	G_2	G_3
$\bar{t}_{h\ th}$	5.69	6.54	21.5
$\bar{t}_{h\ emp}$	6.78	5.77	22.31
$\bar{\delta}_h$	0.27 ± 0.02	0.23 ± 0.02	-0.51 ± 0.02%

Table 6.11 – Theoretical and empirical means of the damage localization and quantification tests using the mean residual, function of the tested parameters

It has been shown that a mean residual over several data sets can be used to perform damage detection and localization and improve damage detectability equivalently to increase the length of the signal. However, in the studied case, the number of residuals and tests is not sufficient to get a good estimation of the histogram. To improve this estimation, the bootstrapping and the moving average methods are tested in the following.

6.6.3 Bootstrapping and moving average

To increase the number of mean residuals (and the number of tests) with a finite number of identified damage sensitive vectors ($1500/nb_f$= 100 in the previous Section), it is needed to increase the number of combinations used to compute the mean residual. In Section 6.6.1 the distribution of the mean residual is defined with independent damage sensitive vectors, so there is no restriction on the combinations that are used, and one damage sensitive vector can be used to compute several mean residuals. In this thesis, two methods are used, bootstrapping (with N random combinations selected, 1000 or 250 in the following example) to validate the method and the simple moving average to practice continuous monitoring.

To begin, the bootstrapping method is performed two times, one where the combinations are made among 1000 residuals and the other among 250 residuals. In Figure 6.15 the histograms associated with the two examples are displayed. Compared to the histogram obtained without bootstrapping (see Figure 6.14), the histograms of both cases are closer to the theoretical distributions, with a better match when the bootstrapping is performed using 1000 residuals to construct the mean residuals. Then, the associated POD are 98.4% and 96.5%, respectively for mean residual computed among 1000 and 250 damage sensitive vectors out of the available 1500. Those two values are close to the theoretical one (97.8%) and close to the one obtained without bootstrapping (97%). Consequently, bootstrapping can be used to compute more mean residuals to have a better estimation of the distribution of the tests, even if the number of damage sensitive vectors is low. Concerning the mean value of the damage detection tests, $\bar{t}_{h\ emp}$ is equal to 2.99 for the reference state and 23.58 for the damaged state when 1000 residuals are used to compute all the mean residuals. While, $\bar{t}_{h\ emp}$ is equal to 3.00 and 21.5 for the reference state and damaged state, respectively, when 250 residuals are used. In both cases, the mean test values are close to those obtained without the bootstrapping, and it has to be noted that the combinations are random, as are the means values of the tests and the POD.

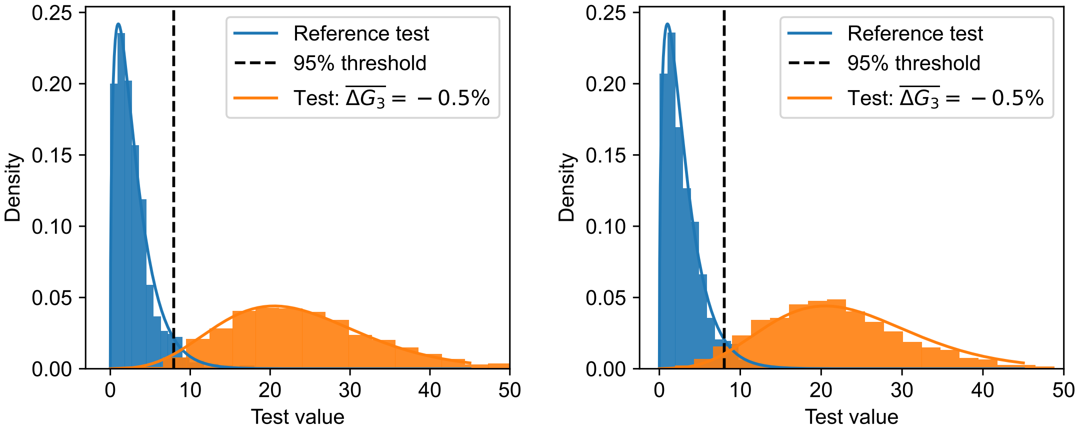

(a) Use of 1000 residuals

(b) Use of 250 residuals

Figure 6.15 – Histograms of the damage detection test for the two system states, with different numbers of residuals to construct the mean residual with the bootstrapping

Then, the moving average can be performed using 1000 residuals. As $nb_f = 15$, it means that 986 mean residuals are computed for each system state. The mean residual is computed such that

$$\bar{\zeta}(k) = \frac{1}{nb_f} \sum_{p=0}^{nb_f - 1} \zeta_{k+p}, \ k \in [1, 1000 - (nb_f - 1)] \,. \tag{6.17}$$

Once the mean residuals have been computed, the damage detection test can be performed. As the moving average is performed, the time evolution of the test can be displayed, in Figure 6.16a the end of the reference state and the beginning of the damaged state are displayed, with the last 60 damage sensitive vectors of the reference state and the first 60 of the damaged state. With this figure, the shift of the distribution when the system is damaged can be clearly seen. Also, during continuous monitoring, a mean residual corresponding to two different states of the system can be computed. In Figure 6.16a, this transition is displayed in grey and each test has its own distribution depending on the ratio between the number of residuals corresponding to the reference state or the damaged state. Then the distribution of the damage detection can be studied: in Figure 6.16b, the histograms computed with the mean residuals of the two system states are displayed. For both system states, the histograms of the damage detection tests are close to the theoretical distributions, with an empirical probability of detection of 98.28%. Finally, as with the use of bootstrapping, the mean values of the different tests are close to the mean of the tests obtained in the previous section, with a mean value of the test equal to 3.05 and 24.84 for respectively the reference and the damaged state.

With the two presented methods, it has been shown that using different combinations of identified residuals to compute the mean residual can be useful to have more damage detection tests. With both methods, the damage detection and localization test are following their theo-

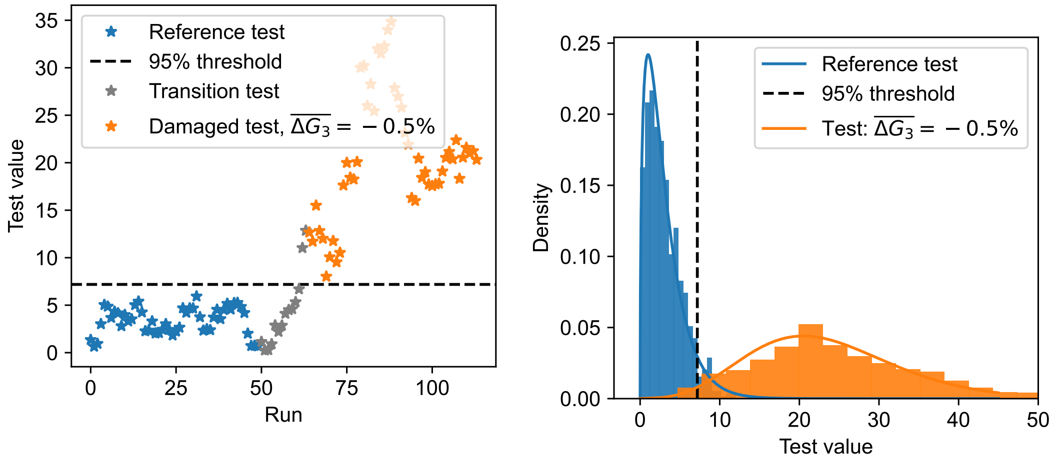

(a) Time evolution of the damage detection test

(b) Histograms of the damage detection test

Figure 6.16 – Results of the damage detection using the mean residual and a moving average

retical distribution. However, it has to be reminded that both methods do not add information, with negligible changes in the mean of the different tests. For the next studies, the mean residual will be computed using the moving average, to replicate continuous monitoring.

6.7 Modeling of a local loss of stiffness on the DTU 10MW wind turbine model

The mean residual presented in the previous section, enables the detection of small damages, using more information to compute each test. Consequently, it will be possible to detect more physical damages on the model of the DTU 10MW wind turbine. As presented in Section 2.5 there are many damages that can affect the wind turbine blades and as presented in [91], those damages can be linked to local loss of stiffness. To do so, in this thesis, it is chosen to define a fault parametrization with ten stiffness parameters per blade, each corresponding to 10% of the blade length.

6.7.1 Computation of the sensitivities

Before the computation of the sensitivities of the new damage parametrization, the local loss of stiffness has to be modeled. As presented in Section 1.4.5 the modeling is based on the modal decomposition, built with the eigenmodes of each component of the system. Consequently, to compute the sensitivities, the eigenmodes of a blade for all the damage locations have to be computed. After that, the model of a wind turbine with a damaged rotor can be defined and the Floquet mode decomposition and the approximation can be performed.

Once the Floquet modes have been computed for all the different locations of the damage, the associated sensitivities can be computed, here a change of 5% of the stiffness is used. In Figure 6.17, the sensitivities of the phase shift and amplitude of the edge bending mode shapes are displayed, associated with the sensitivities of the frequencies. Firstly, one can see that the phase shift and amplitude are much more sensitive than the frequencies, which was also the case

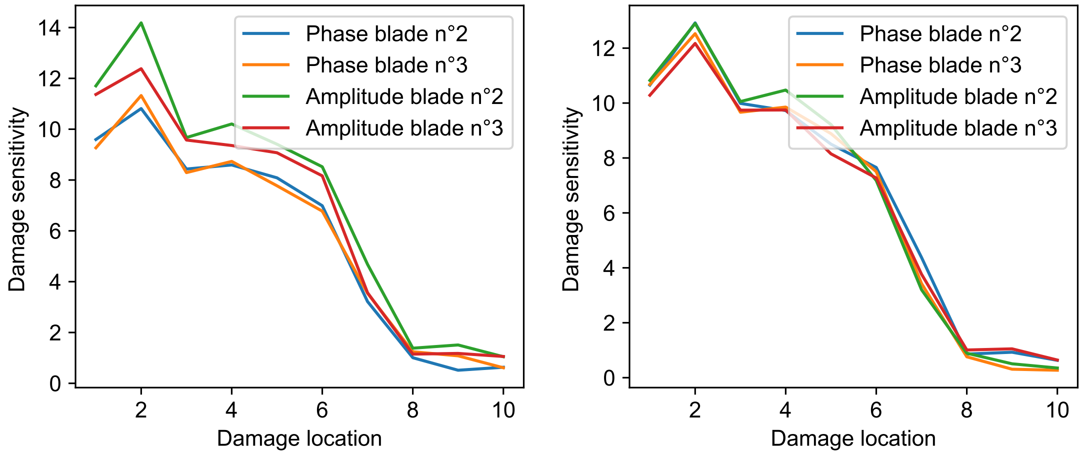

(a) Backward (b) Forward

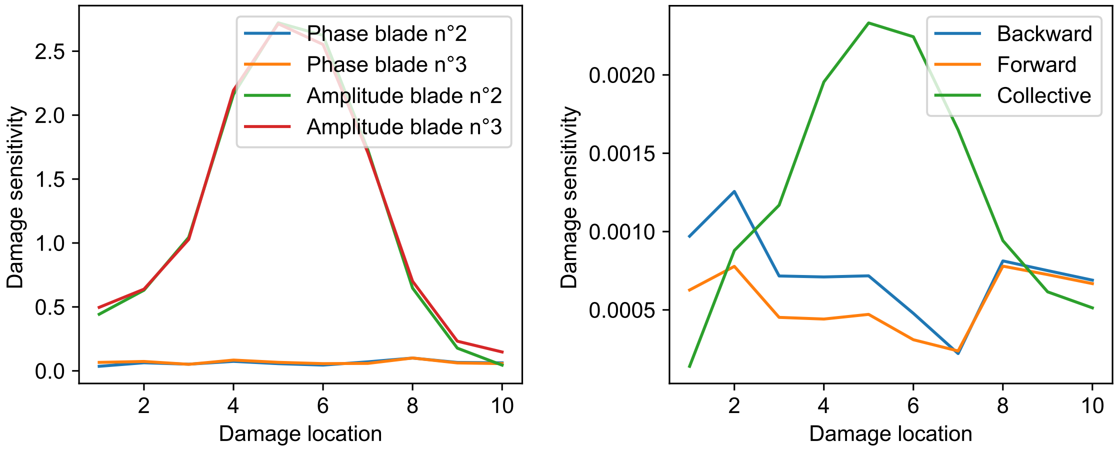

(c) Collective (d) Frequencies

Figure 6.17 – Absolute values of the sensitivities of the phase shift and amplitude of the edge bending modes shapes and the sensitivities of the associated frequencies against the damage location on the blade

for the global loss of stiffness (Section 5.2). Secondly, the three edge bending Fourier harmonics do not have the same sensitivities, with the Backward and the Forward having almost decreasing sensitivities as the damage is located close to the end of the blade. For the Collective, the sensitivities of the amplitude are maximum when the damage is located around half of the blade. Finally, the sensitivities of a local loss of stiffness are lower than the sensitivities corresponding to a global loss of stiffness, which are around five times higher than the highest sensitivities, for each harmonic. Also, the sum of the sensitivities of the local losses of stiffness has the same order of magnitude than the global loss of stiffness.

To continue the study, a Fisher matrix using those new sensitivities can be computed. To do so, the residual is composed of the phase shift and amplitude of the three edge bending modes with the same wind condition as in Section 6.5. Also, all those parameters are numbered section by section and in the order of the blades. So the number of the parameter of section i of blade j is $3i + j$, with $i \in [0, 9]$ and $j \in [0, 2]$. In Figure 6.18a, the color map of the Fisher matrix is displayed. As a reminder, the higher the value of a Fisher coefficient of a parameter, the more

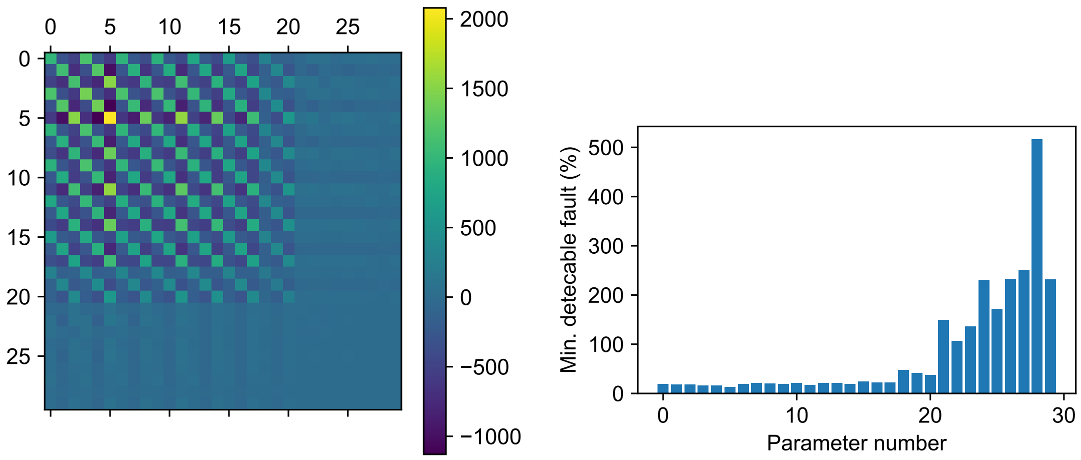

(a) Color-map of the Fisher matrix (b) Minimum 95% detectable faults

Figure 6.18 – Preliminary study using the full damage parametrization

sensitive the test will be to a variation in that parameter, since the non-centrality of the damage detection test depends on that value. It can be seen that for parameters 21 to 29, the associated matrix coefficients are lower. These components correspond to the parameters at the end of the blades. Moreover, as the detectable fault directly depends on the Fisher matrix components (see Equation (2.71)), the minimum detectable faults will be higher for these parameters. This is shown in Figure 6.18b, where the values of the minimum detectable fault for each parameter are given (computed from Equation (2.72)). One can see that the values are higher for parameters 21 to 29, with minimum detectable damages that represent a variation of more than 100% of the healthy value. Consequently, with the selected residual, measurements, and signal length, it is not possible to detect a loss of stiffness in the last 30% of the blades. As a consequence, the corresponding parameters are removed from the parametrization in the following, leading to 21 parameters representing the stiffness of the first 70% of the three blades. The incapacity of detecting a fault with these measurements (blade root moments corresponding to the edge bending) and this approach on the last 30% of the blades is a drawback. However, as presented in [77], the end of the blade is much more subjected to erosion instead of crack appearance, with a review on the prevention of blade erosion presented in [89].

From the 21 parameters, some can be redundant. So, the clustering method presented in Section 2.4.5 is used to reduce the parametrization.

6.7.2 Clustering of the redundant parameters

To avoid redundant parameters over the 21 used in the parametrization of the model, clustering is performed to group parameters of similar sensitivity based on the method detailed in Section 2.4.5. Results are displayed with a dendrogram given in Figure 6.19a, where the distance displayed is the cumulative one to provide a better visualization of the clustering. From the clustering, three main clusters can be distinguished, each one gathering the stiffness of a blade. Smaller clusters are not distant enough to define a more refined localization. The final parametrization is composed of three parameters and is displayed in Figure 6.19b. It can be concluded from the clustering that it should be possible to localize the damaged blade. However, it should not be possible to asses which part of the blade is damaged as the sensitivity of parameters on the same blade are too similar. Those assumptions will be confirmed in the next sections.

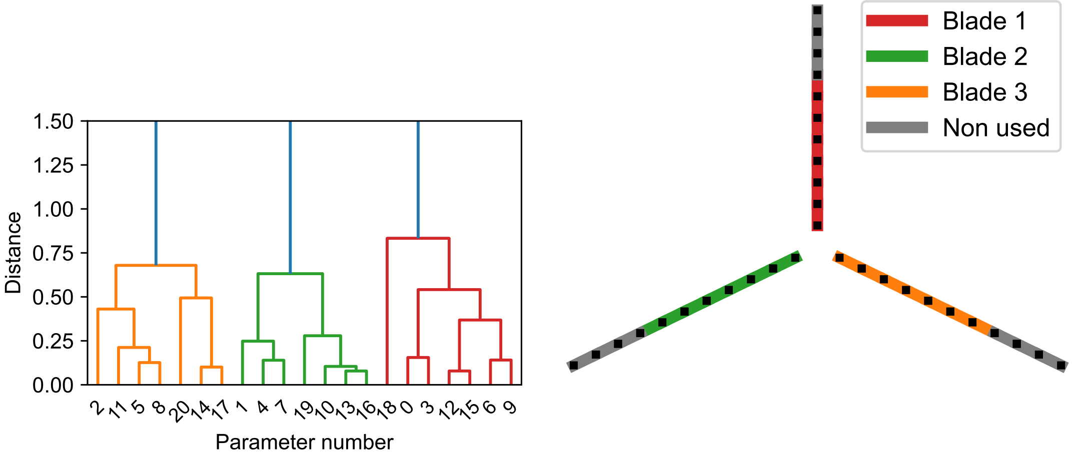

(a) Dendrogram of the clustering

(b) Representation of the clustering of the rotor stiffness parameters

Figure 6.19 – Results of the clustering of the rotor stiffness parameters

6.8 Detection and localization of local losses of stiffness

Once the damage parametrization is defined, it is possible to detect and localize different damages. Here, it is chosen to simulate a loss of 7.5% of stiffness at different locations, namely in the second section on the third blade, in the fifth section on the second blade, and between the third and fourth section on the first blade, denoted $\Delta K_{2,3}$, $\Delta K_{5,2}$, and $\Delta K_{3/4,1}$ respectively. The purpose of this selection of simulated damages is to test the capacity of the method to detect and localize damages on different locations of the blade. For the last damage, it will also be checked if the damage detection can deal with damages that are not following the damage parametrization. The order of magnitude of the stiffness losses can be linked to a shear web debonding, as it is presented in [91].

So, 100 data sets corresponding to each different damage will be used to compute the residual. The reference and training data sets are those used in Section 6.5. Also, the covariance matrix estimated in the aforementioned Section has been computed using 200 data sets, so as the estimated reference, leading to $n_f = 200$.

Looking at the values of the minimum 95% detectable faults (Figure 6.18b), the values are higher than 15%. Therefore, the mean residual is needed to detect the simulated damages, where $nb_f = 10$ is used in the following. The objective of this application is to show that a local loss of stiffness can be identified but also to replicate continuous monitoring. So, the moving average method will be used.

6.8.1 Damage detection

To begin, the performance of the damage detection can be assessed with the empirical POD. In Table 6.12, all those probabilities are reported and one can see that while the values of damage are the same, the POD are not the same. However, based on a preliminary study, the theoretical POD of each damage should be higher than 99%. It means that the damage detection test is not performing as well as it should, at least for two of the three damage cases.

Damage	$\Delta K_{2,3}$	$\Delta K_{3/4,1}$	$\Delta K_{5,2}$
POD(%)	72.53	46.15	100

Table 6.12 – Empirical probability of detection

Those probabilities are illustrated in Figure 6.20, with the evolutions of the damage detection tests and their associated histograms (computed using bootstrapping to have a better estimation of the tests distribution). With those figures, it is clear that the shift of the damage detection test is not the same considering the location of the loss of stiffness. For the first and second damages, the shift of the damage detection is lower than expected with the theory, which explains why the associated POD are lower than expected.

Despite the lower shifts than expected, it has been possible to detect different local losses of stiffness, namely $\Delta K_{2,3}$ and $\Delta K_{5,2}$. However, for such a complex model, it is difficult to stay under the assumption of the linear effects of the damage on the residual, which is why a lower shift than expected can be obtained and why it is difficult to detect a damage scenario not included in the parametrization. Moreover, the use of the mean residual to increase damage detectability has enabled the identification of small damages, when empirical POD lower than 20% are obtained without the mean residual. To continue this example, damage localization and quantification are performed.

6.8.2 Damage localization and quantification

Along with the damage detection, the damage localization test has been computed, where each cluster (i.e. each blade) is tested. Also, the damage quantification is performed jointly with the localization. The results of those tests are summarized in Table 6.13. Firstly, it can be seen that for the first and the third simulated damages, the test with the highest shift is corresponding to the damaged blade in the simulations. Also for those two simulated damages, the estimated damage associated with the localization is negative, with a value close to the simulated one for the third damage (on the second blade). For the second damage, the localization is not conclusive, the localization test corresponding to the first blade is not the test with the highest mean. Looking at the mean values, two parameters are associated with a stiffness loss.

Looking at the mean quantification values corresponding to the damaged blade in each simulation, it is possible to explain the shift of the damage detection of the first and second damages. As the estimated damage is directly linked to the shift ($\lambda = \delta^T F \delta$), if an estimated damage is lower than the simulated one, the shift is also lower than the theoretical one. These differences can be explained by the non-linear effects of the damages on the mean of the residual.

To conclude this application, it has been possible to detect local losses of stiffness in two

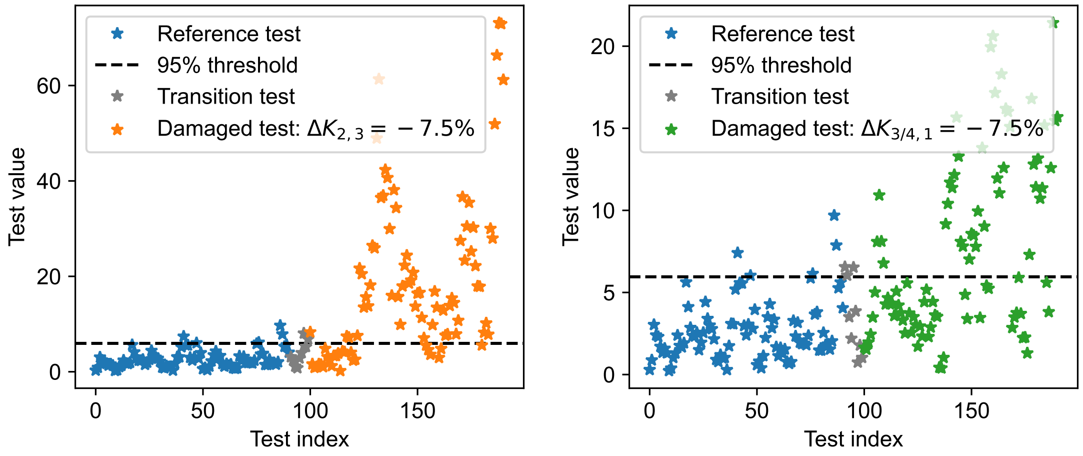

(a) $\Delta K_{2,3}$

(b) $\Delta K_{3/4,1}$

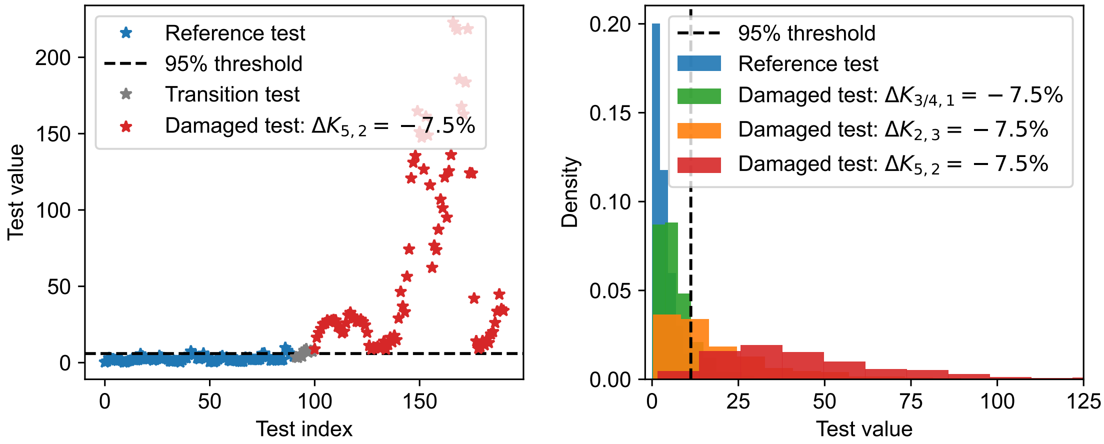

(c) $\Delta K_{5,2}$

(d) Histograms of the damage detection tests

Figure 6.20 – Evolutions of the damage detection test using the mean residual ($nb_f = 10$) for the different simulated damages, associated with the histogram obtained using bootstrapping

different locations and localize the damaged blade. After, it has been tested to localize more precisely the damage using the direct localization test considering the full parametrization (without the last 30% of the blades). As the localization using the first parametrization gives the damaged blade, only the parameters of that blade are tested in the new localization. In Figure 6.21, the results of this localization are displayed for the third simulated damage ($\Delta K_{5,2} = -7.5\%$). Firstly, the distribution of the localization test shows that all the tests have a non-negligible distribution shift. Secondly, the mean values of the damage quantification are all negative, which means that there is no false positive. Consequently, it is not possible to determine the exact position of the damage on the blade. Similar results are obtained with the localization test on the third blade for $\Delta K_{2,3} = -7.5\%$, where it is not possible to assess the precise location of the damage on the third blade.

Also, it has been tested to detect and localize a loss of stiffness of the last section of one blade, with a stiffness loss of 25% simulated. Even with a use of a mean residual with $nb_f = 20$, it has not been possible to detect and localize such damage, which confirms the study on the Fisher matrix. This is due to the negligible impact of a loss of stiffness at the end of the blade

Damage	Test	Blade 1	Blade 2	Blade 3
$\Delta K_{2,3}$	Localization	3.70	7.50	16.28
	Quantification	1.68 ±0.27%	2.62 ±0.38%	-3.42±0.46%
$\Delta K_{3/4,1}$	Localization	1.76	3.64	2.67
	Quantification	-0.78±0.26%	-0.99±0.41%	1.20±0.24%
$\Delta K_{5,2}$	Localization	3.77	38.62	9.00
	Quantification	2.00±0.15%	-6.52±0.64%	2.59±0.33%

Table 6.13 – Mean values of the localization and quantification tests, with the 95% confidence intervals for the quantification

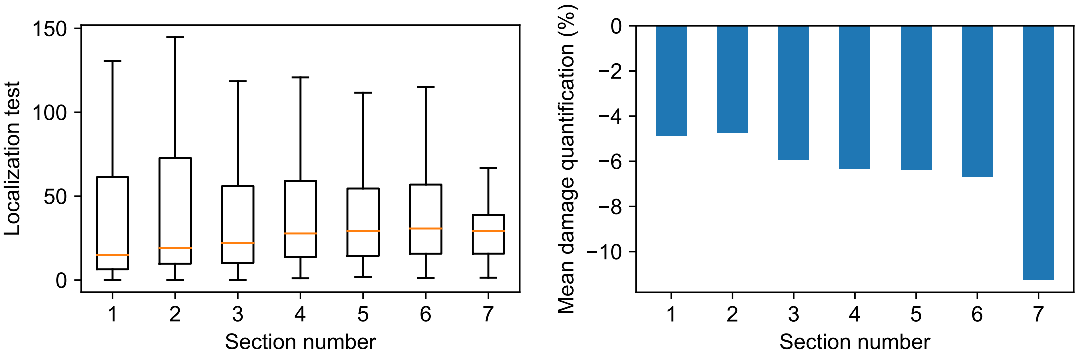

(a) Box plot of the localization tests

(b) Mean values of the damage quantification

Figure 6.21 – Results of the localization and quantification on the parameters of the second blade, $\Delta K_{5,2} = -7.5\%$

on the considered residual.

6.9 Alternative selection of sensors

The previous results have been obtained using the blade root moments as unique sensors. However, both detection and localization strongly depend on the sensor choice. The benefit of completing the instrumentation will be demonstrated by using accelerations of the blades, along edge, at 40% and 80% of the blade span. It is expected to get better results in terms of detectability and localization as more information is available and more distributed along the blades.

Today, it is not possible to install accelerometers on the wind turbine blade as the centrifugal force is too important. But the recent progress in sensing based on computer vision [28, 88], will perhaps enable the measurements of the displacements along the blades of a wind turbine.

6.9.1 Parametrization and clustering

The first step is to perform the clustering once again, as the sensitivities depend on the sensor type and their location. In Figure 6.22a, the dendrogram of the hierarchical clustering is displayed. Firstly, one can see that there is the same sub cluster in the three main clusters, which means that it seems that it is possible to define more than one cluster inside a blade, leading to future more accurate localization. Secondly, the distance between the clusters is much more

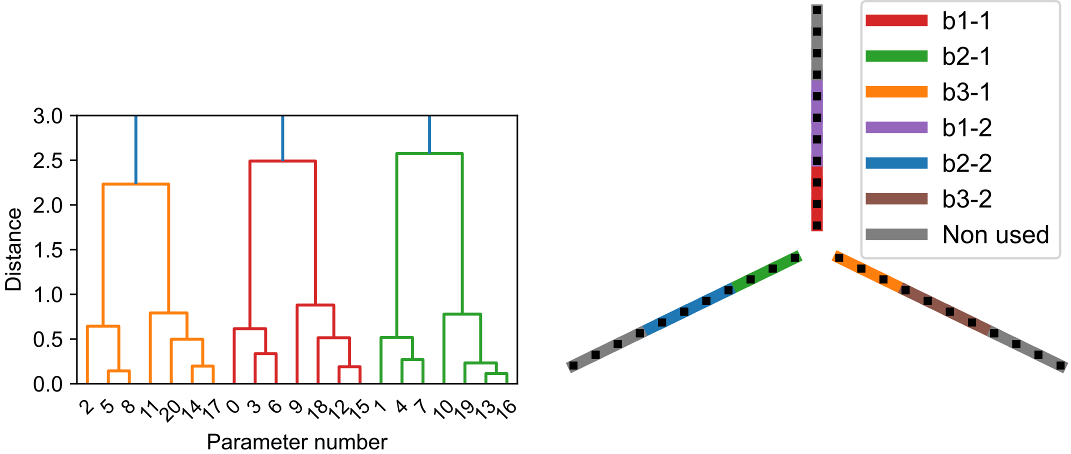

(a) Dendrogram of the clustering

(b) Representation of the clustering of the rotor stiffness parameters

Figure 6.22 – Results of the clustering of the rotor stiffness parameters, use of accelerations

important with this instrumentation compared to the previous one (see Figure 6.19a), which means that the sensitivities are less collinear than with the moments. So, it is chosen to define two clusters per blade, as illustrated in Figure 6.22b. Also, as with the previous instrumentation, the theoretical minimum 95% detectable faults for the last 30% of the blades are too important (more than 100%), so associated parameters are removed of the parametrization, which means that a loss of stiffness at the end of one blade have a negligible effect on this new residual as well. In general, such fault have a negligible effect on the mode shapes of the edge bending Fourier harmonics.

6.9.2 Damage detection and localization

Once the parametrization has been defined, the damage detection can be performed, once again with an estimated reference with $n_f = 200$ and a mean residual with $nb_f = 10$. Here only the first and third simulated damages simulated in Section 6.8 are studied ($\Delta K_{2,3}$ and $\Delta K_{5,2}$ respectively), as the final objective is to compare the localization results. Once the test is performed, an empirical POD of 100% is obtained for the two simulated damages. Histograms are given in Figure 6.23, where the shift between the distributions is obvious. Compare to the previous instrumentation (see Figure 6.20d), the shift of the test corresponding to the damaged structure is more important and always over the 95% threshold. This means that using two accelerations per blade instead of one root moment gives more information and gives better damage detectability.

The final step is to confirm that the localization has been improved. From the clustering, it has been chosen that the parametrization will be composed of two clusters per blade. So, for the damage localization, each cluster is tested using Equation (2.77), with conjointly the estimation of the associated parameter change. In Figure 6.24, the results of the damage localization and quantification of one damage case are displayed. Thus, it can be seen that the damage has been well localized, as the cluster which includes the position of the simulated damage is the cluster with the maximum shift. Also, the damage quantification gives an equivalent estimation of the

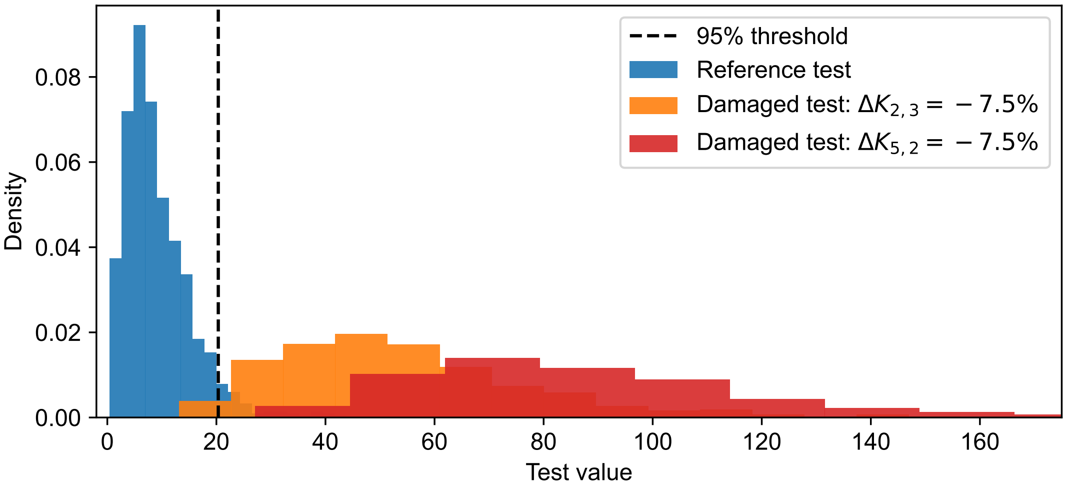

Figure 6.23 – Histograms of the damage detection tests, use of the blade accelerations, obtained using bootstrapping

damage compared to the use of the moment, which is close to the simulated damage. Similar results are obtained for the second simulated damage, with the localization of the cluster which includes the position of the simulated damage and an associated quantification close to the one obtained with the moments.

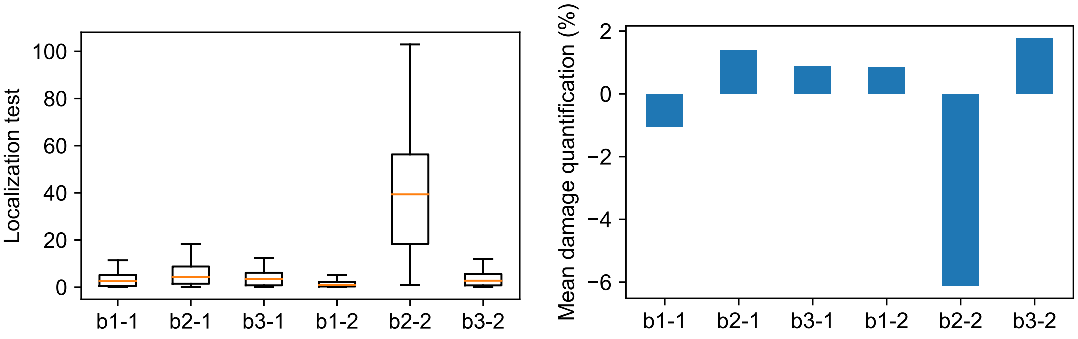

(a) Box plot of the localization tests

(b) Mean values of the damage quantification

Figure 6.24 – Results of the damage localization and quantification for a loss of 7.5% of stiffness in the section 5 of the second blade, use of the accelerations

The localization test has also been performed using the full parametrization, to try to have a more precise localization inside the damage cluster. For both simulated damages, the localization tests corresponding to every parameter of the damaged cluster have equivalent shifts and the associated estimated damage is negative. So, it is not possible to assess more precisely the damage position.

From this study, it can be concluded that, with more and different sensors, it is possible to improve the damage detectability and to localize the damage with a precision of almost half of a blade. Furthermore, it shows that despite a limited number of sensors, the blade root moment gives an equivalent damage detectability and enables the localization of the damaged blade. It also has been tested to couple blade root moments and accelerations. If one acceleration per blade is used with the moments (at 40% or 80%), there is no major improvement in the damage detection and the damage localization is equivalent to the one obtained using only the blade root moments. Then it has been tested to couple the blade root moments with both accelerations at 40% and 80%. The damage detection and localization are equivalent to those obtained using only both accelerations on the blades, with just a higher shift of the damage detection test. So, using both accelerations on each blade (with or without the blade root moments) is the only configuration that enables localizing the damage with the best resolution.

6.10 Detection and localization of mass and pitch imbalance

In this chapter, works presented so far were focused on stiffness anisotropy, with the detection of global or local stiffness losses. However, as presented in Section 2.5, in addition to stiffness loss, other faults can occur in a wind turbine. The two other faults are the addition of mass and pitch misalignment, also called mass and pitch imbalance. In this section, it will be tested to perform damage detection and localization of mass and pitch imbalance on the DTU 10MW wind turbine model. To perform damage detection, the sensors used are the edge bending blade root moments.

6.10.1 Mass imbalance

As the studied damage is different from the previous applications, the sensitivities have to be adjusted to the simulated damage. In Section 5.2.2 it has been shown that an addition of mass is equivalent to a loss of stiffness. Consequently, the sensitivities of the global loss of stiffness can be used for the addition of mass. But, in Section 6.8 a parametrization composed of the local stiffness of the blades has been used, and it is important to see if this parametrization can be used to detect and localize an addition of mass. To do so, the cosine between the sensitivities of the global loss of stiffness and the clusters regrouping the local stiffness of each blade is computed, with

$$\cos\left(\mathcal{J}_i, \mathcal{J}_j\right) = \frac{\tilde{\mathcal{J}_i}^T \tilde{\mathcal{J}_j}}{\|\tilde{\mathcal{J}_i}\| \|\tilde{\mathcal{J}_j}\|}, \tag{6.18}$$

with $\tilde{\mathcal{J}} = \Sigma^{-1/2}\mathcal{J}$. For the sensitivities of each blade, the cosine value is higher than 0.99, which means that the clusters of the sensitivities of local losses and the sensitivities of the global losses are collinear. So the damage detection and localization should be equivalent using both parametrizations, with the only difference in the damage quantification.

To apply the damage detection, simulated data of the DTU 10MW model under full-field wind are used. The reference and training data sets are those used in Section 6.5. Then a global addition of mass is simulated with three different data sets composed of 100 simulations, with an increase of the third blade density of 0.5%, 1%, and 2.5%. Those values have been used in the application of the rotor imbalance detection method presented in Section 2.5.1.

With the sensitivities of the global loss of stiffness, let us compute the theoretical probability of detection of the simulated damages, to find an appropriate value of nb_f. The probabilities are reported in Table 6.14, using $nb = 1$ and $nb_f = 10$. As the probabilities of detecting additions of 0.5% or 1% of mass are low, it can be concluded that it is needed to use the mean residual, and $nb_f = 10$ seems to be an appropriate value to detect the simulated values. It has to be noted that to have a probability higher than 95% for an addition of mass of 0.5%, a mean residual with $nb_f > 25$ is needed.

nb_f	$\Delta M_3 = 0,50\%$	$\Delta M_3 = 1\%$	$\Delta M_3 = 2,50\%$
1	9.44	25.73	95.33
10	56.46	99.56	> 99.9

Table 6.14 – Theoretical POD of mass additions function of the number of files used to compute the residual

The objective is to show that it is possible to detect and localize other damages than a loss of stiffness. Therefore, the bootstrapping method is used to evaluate the performance of the mean residual, with 1000 combinations to compute the mean residual for each simulated damage and the training.

Sensitivity	$\Delta M_3 = 0,50\%$	$\Delta M_3 = 1\%$	$\Delta M_3 = 2,50\%$
Cluster of local losses	9.6%	43.3%	99.8%
Global loss	13.4%	48%	99.3%

Table 6.15 – Empirical POD of mass additions function of the sensitivities used to compute the test. Obtained using bootstrapping

In Table 6.15, the empirical POD depending on the sensitivities are reported. First, it can be seen that the difference between the probabilities using one or the other parametrization is small, which is consistent with the collinearity analysis performed at the beginning of the section. Also, it can be seen that the POD are lower than the theoretical ones for the two different sensitivities. This is the consequence of a lower shift than what is obtained in the theory. In Figure 6.25 the histograms of the damage detection tests are displayed and it can be seen that the shift associated with the two smallest additions of mass is low. Also, it can be seen that the distribution of the damage test corresponding to an addition of 2.5% of mass has an important spread. This is the consequence of an increase of the covariance, as it has been experienced in Section 6.5.

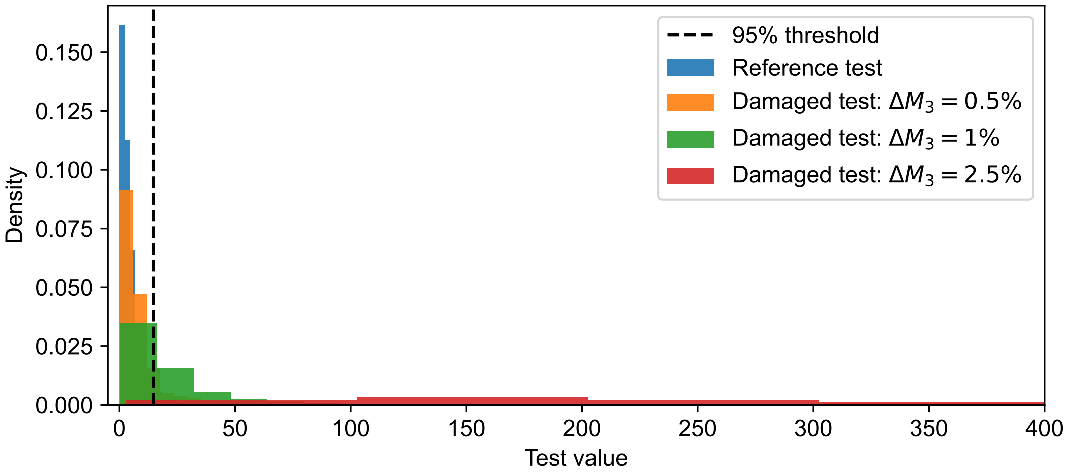

Figure 6.25 – Histogram of the damage detection for an addition of mass, using the mean residual ($nb_f = 10$) and the bootstrapping

To continue, the damage localization can be performed. In Table 6.16 the results of the damage localization and quantification are reported, where those results are obtained using the sensitivities of the global loss of stiffness. First, the low shifts obtained with the two first damages are confirmed, where the mean estimated damages are lower than the simulated ones. However, for the three simulated additions of mass, the damage is well localized, where the test corresponding to the third blade has the highest value. Also, the associated estimated damages are negatives, which corresponds to an addition of mass. Moreover, the change in the covariance with the increase in the damage is confirmed by an increase in the standard deviation of the estimated damages, when and addition of mass of 2.5% is simulated.

Damage	Test	Blade 1	Blade 2	Blade 3
$\Delta M_3 = 0.5\%$	Localization	1.62	1.80	3.27
	Quantification	0.05±0.01%	-0.07±0.02%	-0.07±0.02%
$\Delta M_3 = 1\%$	Localization	4.36	5.27	17.72
	Quantification	0.27±0.01%	0.32±0.02%	-0.54±0.02%
$\Delta M_3 = 2.5\%$	Localization	21.04	72.79	194.37
	Quantification	0.64±0.01%	1.50±0.03%	-2.02±0.04%

Table 6.16 – Mean values of the localization and quantification tests on data with simulations of additions of mass, with the 95% confidence intervals for the quantification

To finish the application, the localization results obtained with the sensitivities of the global loss of stiffness are compared to those obtained with the sensitivities of the local losses of stiffness. To be concise, only the results of the addition of 1% of mass are compared, with all the values reported in Table 6.17. Looking at the mean values, one can see that the mean values of the localization tests are close. And as was explained at the beginning of the Section, the main difference is obtained with the damage quantification. Compared to the mean damage estimated using the sensitivities of a global loss, the mean damage is around 6 times higher when the cluster of the local losses of stiffness is used.

Sensitivity	Test	Blade 1	Blade 2	Blade 3
Cluster of local losses	Localization	4.15	5.31	15.67
	Quantification	1.74±0.06%	2.09±0.11%	-3.34±0.13%
Global loss	Localization	4.36	5.27	17.72
	Quantification	0.27±0.01%	0.32±0.02%	-0.54 ±0.02%

Table 6.17 – Comparison of the mean values of the localization and quantification tests with two different sensitivity matrices, applied on data with an addition of 1% of mass

To conclude this application, it has been shown that it is possible to use Stochastic Subspace-based Damage Detection to detect and localize an addition of mass on a blade, with a performance equivalent to the detection and localization of a global loss of stiffness on one blade. Also, the detection and localization can be performed using the sensitivity of local or global losses of stiffness. However, it must be noted that with the used method, it is not possible to differentiate add of mass or loss of stiffness, but it can be done with a study of the tower or nacelle accelerations, with the presence or not of the 1P harmonic along Side-Side.

6.10.2 Pitch imbalance

After the loss of stiffness and the mass imbalance, the pitch imbalance is the other common fault that occurs in a wind turbine rotor. A pitch error is different from a loss of stiffness or an addition of mass, so the sensitivities corresponding to a pitch error are computed, using once again the first-order Taylor approximation, with the computation of the Floquet modes for a pitch error of 1°. Then, the cosine between the sensitivities of the pitch error and the clusters of the sensitivities of the local loss of stiffness is computed and the values obtained are -0.3, 0.1, and -0.4 for the first, second, and third blades, respectively. Consequently, the sensitivities of a pitch error and a loss of stiffness are different, which means that the sensitivities of the pitch error are needed to perform the detection and localization of such damage.

To continue, the theoretical performance of the detection test can be assessed, to then define the damage scenarios according to those results. Using a single file to compute the residual, the minimum 95% detectable fault is 4.78°, this value is higher than what is performed in the bibliography. With $nb_f = 10$ the minimum 95% detectable fault becomes 1.35°, which is closer to the value obtained in the bibliography [20]. Consequently, three data sets are computed with 100 simulations of 600 s sampled at 50 Hz, with different pitch errors of the third blade, namely a pitch error of 2°, -2°, and 4°. With the mean residual computed with $nb_f = 10$, all the damage should be detected. Also, as the pitch error can be negative or positive, a negative pitch error is simulated to check if the sensitivities can take into account a negative pitch error. As for the previous damage case, the objective is to show that it is possible to detect and localize other damages than a loss of stiffness. Consequently, the bootstrapping method is used to assess the performance of the mean residual, with 1000 combinations to compute the mean residual for each simulated damage and the training.

In Table 6.18 the empirical POD are obtained using the sensitivities of the local losses of stiffness or the sensitivities of the pitch error. With those probabilities, it can be seen that when the sensitivities of the pitch error are used, the POD are higher (for the pitch error of 2° and 4°) than the ones obtained with the sensitivities of the local losses of stiffness. This show that it is important to use the sensitivities of the studied damage for damage detection. Then in Figure 6.26, the histograms of the damage detection test using the sensitivities of the pitch error are displayed. With this Figure, it can be seen that the shift of the test for a pitch error of 2° is more important than the one for an error of -2°. This show that the effect of the pitch error on the residual is not linear. Also, with the important spread of the distribution for the test corresponding to an error of 4°, it is clear that the covariance has changed compared to the reference and training state (as for the global stiffness loss and the addition of mass). However, it has been possible to detect a pitch error on one blade.

Sensitivity	$\Delta p_3 = 2°$	$\Delta p_3 = -2°$	$\Delta p_3 = 4°$
Cluster of local stiffness losses	37%	35%	80%
Pitch error	92%	38%	99%

Table 6.18 – Empirical POD of a pitch error function of the sensitivities used to compute the test. Obtained using bootstrapping

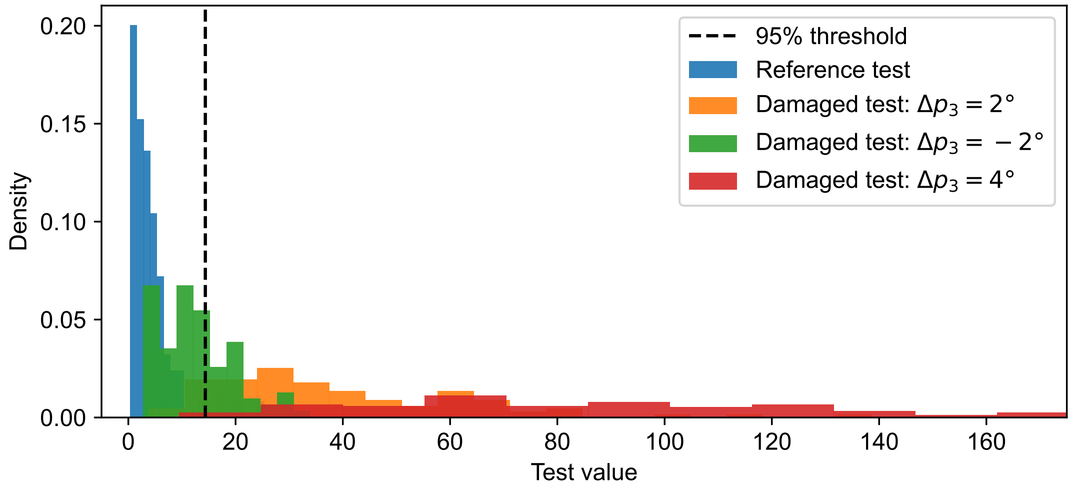

Figure 6.26 – Histograms of the damage detection test for a pitch error, using the mean residual ($nb_f = 10$) and the bootstrapping

To continue, the localization and quantification tests are performed with the both sensitivities, to once again show that it is important to use the sensitivities corresponding to the studied fault. But first, let us evaluate the performance using the sensitivities corresponding to the pitch error. In Table 6.19 the mean results of the localization test and the associated damage quantification are detailed. Looking at the localization results, for each simulated pitch error, the test corresponding to the third blade (which is the damaged one) is the test with the higher mean. For $\Delta p_3 = -2°$, the difference between the mean is small, because the shift due to the damage is low. Then, the quantification can be studied. For the first pitch error, the mean estimated damage is close to the simulated one. However, for the two others, there is a gap of around 1° between the estimated and the simulated pitch error. As for the other examples, it is because the assumption of the linear effect of the damage on the residual is not respected. Also, it explains why the shift of the damage detection test is lower than expected for $\Delta p_3 = -2°$. Nevertheless, for the three simulated pitch errors, the damaged blade has been localized and the associated damage has the same order of magnitude as the simulated one.

Damage	Test	Blade 1	Blade 2	Blade 3
$\Delta p_3 = 2°$	Localization	13.91	3.22	30.25
	Quantification	-0.91±0.04°	-0.34±0.04°	1.70±0.04°
$\Delta p_3 = -2°$	Localization	5.94	1.27	8.08
	Quantification	0.60±0.03°	-0.01±0.03°	-0.88±0.02°
$\Delta p_3 = 4°$	Localization	49.07	4.37	81.99
	Quantification	-1.97±0.05°	0.14±0.05°	2.87±0.06°

Table 6.19 – Mean values of the localization and quantification tests on data with simulation of pitch errors, with the 95% confidence intervals of the quantification

To finish this application, the localization and quantification using the sensitivities of the local losses of stiffness can be studied and compared to the one presented before. In Table 6.20 the results obtained using the two different sensitivities for the data set with a pitch error of 2° are detailed. To begin, the mean value of the localization test corresponding to the third blade obtained with the sensitivities of the local losses of stiffness is six times lower than the other. This is linked to the lower shift obtained with damage detection (see the first line of Table 6.19). So, it can not be stated that the third blade is damaged, even if the test corresponding to the third blade has the highest shift. Then, the estimated damage associated with the localization test is not related to the simulated damage, so it is difficult to use them to validate the localization results.

Sensitivity	Test	Blade 1	Blade 2	Blade 3
Cluster of local stiffness losses	Localization	2.35	1.78	5.65
	Quantification	-0.40±0.05%	1.03±0.08%	-1.33±0.12%
Pitch error	Localization	13.91	3.22	30.25
	Quantification	-0.91±0.04°	-0.34±0.04°	1.70±0.04°

Table 6.20 – Comparison of the mean values of the localization and quantification tests with two different sensitivity matrices, applied on data with a pitch error of 2°

In conclusion of this application, it can be stated that it is also possible to detect and localize pitch angle errors on the rotor blades. Indeed, using the sensitivities related to the studied damage, it has been possible to detect, localize and estimate the angle of an error of at least 2° on one blade. However, it has been shown that the performance of the method decreases if the sensitivities corresponding to the losses of stiffness are used. So, during continuous monitoring, the detection and localization tests can be performed with both sensitivities and select the right one function of the amplitude of the 1P harmonic along Fore-Aft in the measurement of the tower and nacelle or if a decrease in the electricity production has been detected.

6.11 Performance of the non-parametric test

To perform the damage detection using the Stochastic Subspace-based Damage Detection and localization, it is needed to have the sensitivity of the residual regarding the parameters of the studied system. This means that it is necessary to have a model corresponding to the studied system, which can not be possible sometimes. Consequently, the non-parametric test (Equation (2.66)) has to be used to perform damage detection, with

$$t_{np} = \zeta^T \Sigma^{-1} \zeta. \tag{6.19}$$

Also, as said in the previous section, different types of damage can occur on a structure with different associated sensitivities. So, the non-parametric test can be used without making any assumption on the damage and the selection of the sensitivities. Then, based on other information, perform the localization and quantification test using the appropriate sensitivities.

Here it is chosen to compare the empirical POD obtained in the previous Section obtained with the parametric test, with the empirical POD obtained with the non-parametric test. The non-parametric test has been performed with the same parameters used in the parametric test, namely $n_f = 200$ and $nb_f = 10$. The bootstrapping method is used to have a better estimation of the empirical probabilities. In Table 6.21, the empirical probabilities obtained for the three types of simulated damages are reported. For each simulated damage, the POD obtained with the non-parametric test are close to those obtained with the parametric test.

Damage	$\Delta K_{2,3} = -7.5\%$	$\Delta K_{3/4,1} = -7.5\%$	$\Delta K_{5,2} = -7.5\%$
Non-parametric	53,20%	18,10%	92,90%
Parametric	63,9%	19,6%	97,8%
Damage	$\Delta M_3 = 0,50\%$	$\Delta M_3 = 1\%$	$\Delta M_3 = 2,50\%$
Non-parametric	20%	44%	100%
Parametric	9,6%	43,3%	99,8%
Damage	$\Delta p_3 = 1°$	$\Delta p_3 = -2°$	$\Delta p_3 = 4°$
Non-parametric	87%	56%	100%
Parametric	92%	38%	99%

Table 6.21 – Empirical POD of the different simulated damages using the non-parametric test, compared to the probabilities obtained with the parametric test

From those examples, it can be concluded that the non-parametric test can also detect damages of the same order of magnitude as the parametric test. So, the non-parametric test can be used if there is no available sensitivity or if the type of damage is unknown. However, it should be kept in mind that with this test it is not possible to localize the damage.

6.12 Conclusion

In this Chapter, the Stochastic Subspace-based Damage Detection based on the local approach has been adapted to the problem of the rotor faults, with the definition of a new residual function of the most sensitive damage indicators, namely the phases shift and amplitudes of the Fourier harmonics of edge bending. Then, this residual and the application of the damage detection and localization method are validated with the detection and localization of a stiffness loss of one blade, on data with a gradual complexity. Also, it has been demonstrated that the residual (therefore the damage detection and localization) is not affected by the rotational speed. This means that the damage detection can be performed during continuous monitoring, using blade root sensors. The definition of the new residual and the detection and localization of a rotor fault applied to the academic model of wind turbine has been presented at the Conference IFAC World Congress [22].

Then to improve damage detectability, the mean residual is defined, to use several measurements to compute the damage detection tests. The theory behind this new residual has been validated on data computed with the academic model of wind turbine. Also, techniques to improve the estimation of the test distribution and the probabilities of detection have been validated. Then, after the modeling of the local loss of stiffness of the blades, it has been shown that it is possible to detect and localize such damages, using the mean residual. Also, an alternative instrumentation of the blades has been tested, to show that the performance of the method relies on the measurements used and that the method can be adapted to future measurement techniques.

Finally, it has been shown that damage detection can be used to detect and localize the other type of damage of wind turbine rotor, namely the addition of mass and the pitch error. With the applications, it has been concluded that the mass addition can be detected and localized using the sensitivities of the local losses of stiffness, whereas the pitch error can be properly detected and localized using the appropriate sensitivities. Then, it is shown that it is possible to detect the three types of damage without any model information (i.e. the sensitivities) using the non-parametric damage detection test.

In the different applications of the method on data computed with the DTU 10MW wind turbine model, some limitations have been seen, especially with the assumption of the linear impact of the damage on the residual. This limitation is inherent to the method and when it is not respected it impacts mainly the shift of the distribution and the damage quantification. To have a better estimation of the damage, other methods have to be used, such that the model updating [52, 51, 57]. Nevertheless, the results of the quantification can be used as an initialization point, of such methods.

As said previously, the presented method uses measurements on the rotor, but as it is a rotating part it could be difficult to monitor it. Consequently, it is useful to define damage detection methods for rotor faults using tower and nacelle measurements. To do so, in the next Chapter, the best damage indicators of the rotor using tower and nacelle measurements will be searched, and associated damage detection methods will be defined.

Chapter 7

DETECTION OF DAMAGE OF THE ROTOR USING MEASUREMENT FROM THE FIXED FRAME

Abstract

In the previous chapters, the damage detection of the rotor was performed using rotor measurements. However, since it may be difficult to monitor the rotor, in this Chapter, damage detection is also performed using only the tower and nacelle measurements as this instrumentation is very common nowadays. So, to define a damage detection method, the most sensitive damage features are searched and identified as the appearance of new Fourier harmonics and the frequencies of the Fourier harmonics of edge and Side-Side bending. Then, a damage detection method is presented for each damage sensitive feature. For the appearance of new Fourier harmonics, an existing method is studied. This method is based on the coherence of a signal and its modulation with rotor speed. It is shown that this method is more suitable for rotor imbalance detection. Finally, the Stochastic Subspace-based Damage Detection method is adapted, with the definition of a residual using the frequencies of the selected damage sensitive Fourier harmonics. With this method, it is possible to detect smaller rotor stiffness losses than with the coherence and to distinguish between rotor and tower faults.

7.1 Introduction

In the previous Chapters, efficient damage indicators of rotor faults using rotor measurements were used and damage detection using those damage indicators has been defined. However, the instrumentation of the rotor is difficult as it is a rotating part. So, it is easier to install sensors on the tower and the nacelle (also called fixed frame) than on the rotor. Consequently, it has to be assessed if it is possible to perform damage detection of rotor fault using measurements from the fixed frame in order to propose a methodology adapted to current instrumentation.

The Chapter is organized as follows. To begin, efficient damage indicators are searched, with a focus on the evolutions of the Floquet modes and the Fourier harmonics with the rotor anisotropy. Then, a damage detection method of the literature using the coherence will be tested. To finish, the Stochastic Subspace-based Damage Detection will be used, with a residual defined with the frequencies of the Fourier harmonics that can be identified.

7.2 Search for sensitive damage indicators

The first step before performing damage detection is to find the best damage indicators. As the studied systems are modeled as linear time periodic systems, let us study first the evolution of the Floquet modes and their associated approximation using only the tower/nacelle DOF.

7.2.1 Floquet modes evolution

To start the study, the academic model of wind turbine in the isotropic configuration is studied, where the approximation is computed using the two DOF of the nacelle (θ_x and θ_z in Figure 1.7). In Table 7.1, all the Fourier components of the Floquet modes are reported, using the same id Number as the approximation using all the DOF (Table 3.1). All the Fourier components reported in the Table 7.1 can be seen in Figure 3.1 with the PSD of the tower DOF. With the approximation, it can be seen that there is no Fourier components corresponding to the Floquet mode of Collective flap.

Floquet mode	id Number	Participation factor (ϕ^y)	Frequency (Hz)	Damping (%)
Yaw motion	2	1.000	1.470	0.794
Pitch/tilt motion	5	1.000	1.590	0.682
Forward flap	8	1.000	0.864	0.240
Collective flap			None	
Backward flap	12	1.000	0.448	0.344

Table 7.1 – Fourier harmonics of Floquet modes, with a minimum participation factor of 1%, for a rotational speed of 1.4 rad/s using the nacelle DOF, academic model of a wind turbine with an isotropic rotor

Then the same study can be performed on the same system but where one blade is damaged with a loss of stiffness of 5%. In Table 7.2 all the Fourier harmonics of the Floquet modes of the approximation are detailed. One can see that there are three new Fourier harmonics in the approximation, with the appearance of two Fourier harmonics for the Collective flap and one for the Backward flap. Also, it seems that the evolution of the participation factor is much more important than the evolution of the frequencies. In Figure 7.1, the evolution of the frequencies of the principal Fourier harmonic and the evolution of the participation factor of the Backward flap are presented against the stiffness loss of one blade up to 10%. With this Figure, it is clear that the evolution of the participation factor is much more important than the evolution of the associated frequency. So, it seems that the appearance of the new Fourier harmonics is a better damage indicator than the evolutions of the frequencies.

This appearance of the new Fourier harmonics needs to be confirmed with identifications of the damaged system. To do so, the academic model of a wind turbine is identified with a gradual reduction of the stiffness of one blade, from 0.99% to 90% of stiffness with a step of 1%. Then, it can be seen from which stiffness reduction new Fourier harmonics are identified. The first new harmonic is identified from a stiffness of 95% and the second from a stiffness of 91%, in Table 7.3 the frequencies of the identified new harmonics are reported for different simulated stiffness with the associated estimated standard deviation. The first identified new harmonic is one harmonic of the Backward flap Floquet mode and the second is one of the Collective Floquet mode. In Figure 7.1, it has been shown that the participation factor of one new harmonic increases, meaning that the amplitude of this new harmonic also increases. Consequently, it should be easier to identify the new harmonics. This is confirmed by the estimated standard deviation of

Floquet mode	id Number	Participation factor (ϕ^y)	Frequency (Hz)	Damping (%)
Yaw motion	2	1.000	1.466	0.797
Pitch/tilt motion	5	1.000	1.587	0.684
Forward flap	8	0.999	0.861	0.238
Collective flap	New	0.916	0.963	0.207
	New	0.083	0.518	0.384
Backward flap	12	0.639	0.444	0.350
	New	0.361	0.889	0.175

Table 7.2 – Fourier harmonics of Floquet modes, with a minimum participation factor of 1%, for a rotational speed of 1.4 rad/s using the nacelle DOF, academic model of wind turbine with a stiffness reduction of 5% one one blade

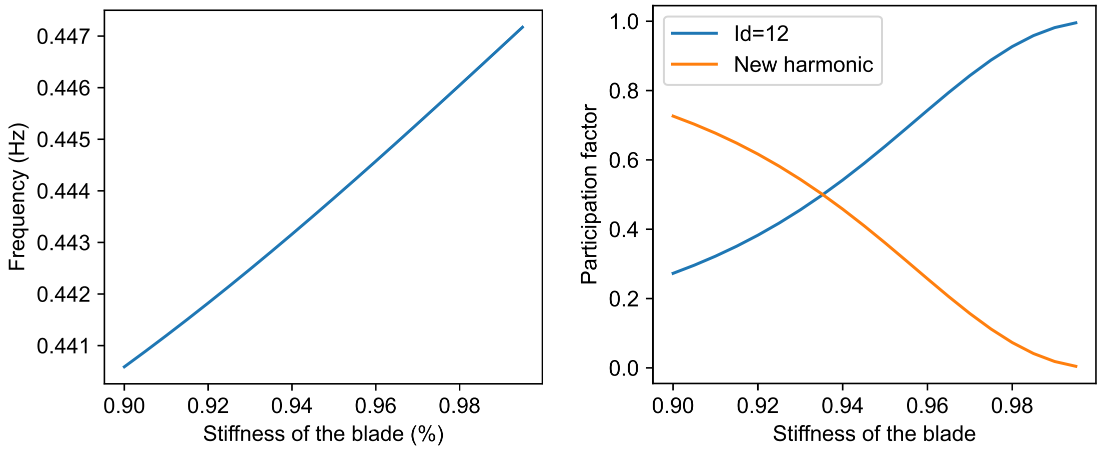

(a) Evolution of the frequencies of the 12–th Fourier harmonic

(b) Evolution of the participation factor of harmonics the of the fifth Floquet mode

Figure 7.1 – Evolution of the Backward flap Floquet against the stiffness of one blade, academic model of wind turbine

the identified frequencies. Indeed, for the first new harmonic, the standard deviation is divided by five between the first time it is identified and the last simulation. So, with this example, it has been shown that the appearance of new Fourier harmonics can be used to detect rotor faults using nacelle measurement. To confirm it, the evolution of the Floquet modes of the DTU 10MW wind turbine model will be studied, using tower and mid-tower FA and SS accelerations.

Stiffness (%)	0.95	0.93	0.91		0.9	
Identified frequencies (Hz)	0.894	0.890	0.964	0.886	0.958	0.885
σ_f (Hz)	0.010	0.004	0.006	0.003	0.004	0.002

Table 7.3 – New harmonics identified function of the simulated stiffness of one blade, associated with the estimated standard deviation of the frequency (σ_f)

With the example of the academic model of a wind turbine, it has been shown that a loss of stiffness of one blade can be detected with the appearance of new harmonics in the Floquet modes. However, it happens only with the Floquet modes of rotor bending along flap, which are the only blade bending modes in the academic model. For the DTU 10MW wind turbine model, there are the edge and flap bending modes, but as the damping of all the flap bending modes is too high, only the edge bending modes can be identified. Thus, three Floquet modes have to be studied, namely the Collective, Backward, and Forward edge. Looking at the Collective edge, there are no new harmonics that appear with a loss of stiffness of one blade, which is perhaps coming from the unchanging phase shift regarding the loss of stiffness of one blade (see Figure 5.1c). The two other Floquet modes can be studied: the participation factors of both Floquet modes function of the stiffness of one blade are displayed in Figure 7.2. With the two evolutions of the participation factor, it can be seen that a new Fourier harmonic is appearing in both Floquet modes at $h = 2$ for the Backward edge and $h = -2$ for the Forward edge.

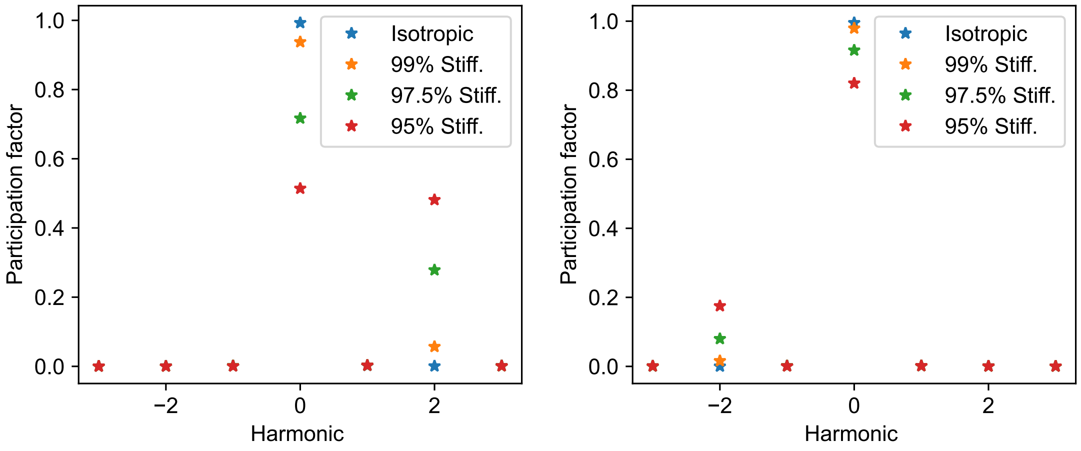

(a) Backward edge

(b) Forward edge

Figure 7.2 – Participation factor of edge bending Floquet modes using only tower accelerations function of the stiffness of one blade

However, the frequencies of the new Fourier harmonics are close to the frequency of other Fourier harmonics. For the Backward edge, the harmonic $h = 0$ has a frequency of around 0.9 Hz, and the new harmonic ($h = 2$) is around 1.1 Hz. Whereas for the Forward edge, it is the opposite, the harmonic $h = 0$ has a frequency around 1.1 Hz and the other new is around ($h = -2$) 0.9 Hz. In Figure 7.3 PSD of mid-tower accelerations along Side-Side are compared, with one from accelerations computed using a model with an isotropic rotor and one from accelerations computed using a model where one blade has a loss of stiffness of 5%. With this Figure, it can be seen that only one peak has been split, which means that two harmonics are merged in a peak around 0.9 Hz. Also, the mode shapes of the harmonics with close frequencies are very similar, with a MAC over 0.99. So, it will not be possible to distinguish the different harmonics with identification for small damages. Indeed, for a global loss of stiffness of 10% on one blade (which is large) and with the environmental conditions used in Section 4.4, it has been possible to identify a new Fourier harmonic, but not for lower losses of stiffness. With this global stiffness loss of 10%, the major harmonic of the Forward edge is identified with a frequency of 1.108 Hz and another harmonic is identified with a frequency of 1.073 Hz which is corresponding to the new harmonics of the Backward edge Floquet modes. So, the identification of a new Fourier harmonic in the fixed frame is a sign of a highly damaged rotor, since it means that there is a strong increase in the modal amplitude of the new harmonics associated with a significant shift in frequencies.

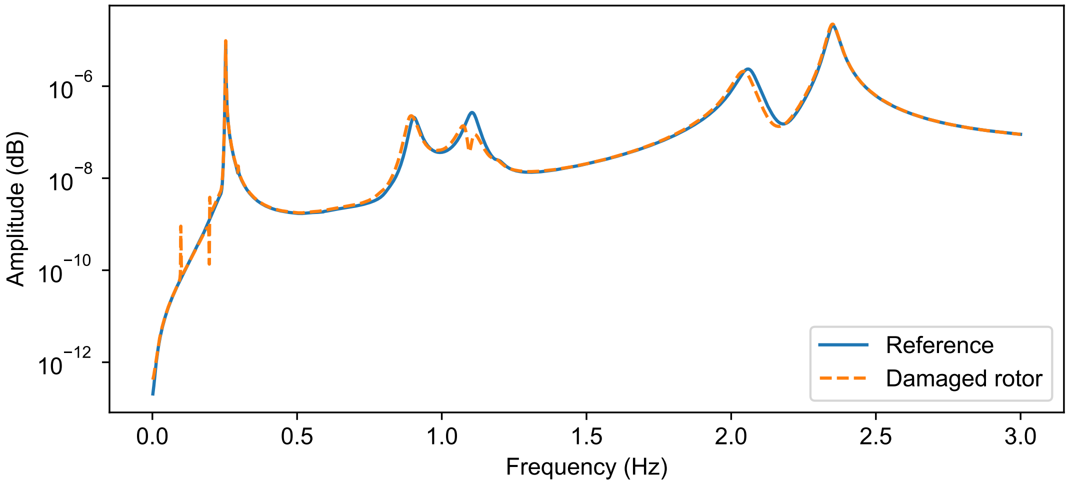

Figure 7.3 – Comparison of the PSD of the acceleration at mid-tower along Side-Side with accelerations from a model with an isotropic rotor and from a model where one blade has a loss of stiffness of 5%. Accelerations obtained from a simulation with a constant wind speed

With this study, it has been concluded that damage on one blade can be detected with a change in the Floquet modes with the appearance of new harmonics. However, it is not possible to identify these harmonics with the DTU 10MW wind turbine model for small damages. So, the evolution of the mode shapes and frequencies of the harmonics have to be studied for this wind turbine model to find out if they are better damage indicators.

7.2.2 Evolution of the modes shapes and frequencies of the DTU 10MW

To find damage sensitive parameters, let us focus on the mode shapes and frequencies of the Fourier harmonics of the DTU 10MW wind turbine model. So, first, let us compute the sensitivity of the modes shapes along the tower DOF regarding a loss of stiffness of one blade of all the identifiable Fourier harmonics. Once the sensitivities of the mode shapes are computed, it can be seen that the order of magnitude is small, with around 10^{-2} at the maximum, which is low compared to the sensitivities of the phase shift and amplitude computed in the Section 6.7. To confirm this, the MAC criterion is computed between the mode shapes obtained with a model with an isotropic rotor and the mode shapes obtained with a model where one blade has a stiffness loss of 5%. In Table 7.4, all the MAC are reported and one can see that the MAC is close to 1 for all the Fourier harmonics. It means that the mode shapes of the Fourier harmonics along the tower are not good damage sensitive parameters because they do not evolve enough with the damage.

Names	1-SS	1-FA	Bck. edge	Fw. edge	Col. edge	2-FA	2-SS
MAC	>0.9999	>0.9999	0.9958	0.9992	>0.9999	>0.9999	>0.9999

Table 7.4 – MAC between the mode shapes of the DTU wind turbine model with an isotropic rotor and the mode shapes of the DTU wind turbine model where a blade has a stiffness loss of 5%, identifiable Fourier harmonics using tower accelerations along Side-Side and Fore-Aft

The frequencies can then be studied, with first the study of the sensitivities. In Table 7.5 the sensitivities of the frequency of the different Fourier harmonics are detailed. One can see that the sensitivity is maximum for the harmonics of edge bending and that the order of magnitude is lower than the order of magnitude of the sensitivities of the amplitude and phase shift obtained in Section 6.7. But, the covariance of the estimation of the frequencies is lower than the covariance of the identified mode shape. As the damage detectability is a ratio between sensitivity and covariance, the damage detectability may be equivalent. For the second tower bending harmonics, the sensitivities are lower, with an order of magnitude around 10^{-2}, but can give information on the rotor damage. However, the sensitivities of the first tower bending harmonics are too low to give information on the rotor damage.

Names	1-SS	1-FA	Bck. edge	Fw. edge	Col. edge	2-FA	2-SS
Sensitivity	$6.12\ 10^{-5}$	$-2.40\ 10^{-3}$	$2.26\ 10^{-1}$	$1.10\ 10^{-1}$	$3.08\ 10^{-1}$	$2.34\ 10^{-2}$	$2.25\ 10^{-2}$

Table 7.5 – Sensitivities of the frequencies of the identifiable Fourier harmonics using tower accelerations (Ω=6 rpm)

To finish the study, it has to be noted that the frequencies of the Fourier harmonic can vary with the rotational speed (see Section 1.5.3). In Table 7.6, all the frequencies function of the rotational speed are reported. In the evolution, 4.9 rpm is chosen instead of 5 rpm because at 5 rpm the 3p harmonic is at 0.25 Hz (close to 1-FA and 1-SS) and the controller of the DTU 10MW wind turbine model is designed to avoid 5 rpm. Looking at the values, one can see that two Fourier harmonics have an important evolution, namely the Backward and Forward edge. For those Fourier harmonics, the frequencies are linearly dependant on the rotational speed with theoretically

$$f_{bck} = \bar{f}_{bck} - \frac{\Omega}{2\pi} \quad \text{and} \quad f_{fw} = \bar{f}_{fw} + \frac{\Omega}{2\pi}. \tag{7.1}$$

Where $\bar{f}_{bck}$ and $\bar{f}_{fw}$ are the frequencies of the Fourier harmonics that can be identified using rotor sensors, with both frequencies around 1.0 Hz for the studied model. Then two other frequencies are varying with an order of magnitude close to the sensitivity, namely the two Fore-Aft bending Fourier harmonics. So, a change in the rotational speed can be seen as a fault, which prevents the use of those harmonics. To conclude, the frequencies that can be used to perform damage detection are the Fourier harmonic of the second Side-Side bending and all the Fourier harmonics of edge bending, but with a correction using the rotational speed for the Backward and the Forward edge.

In the previous Chapter (Section 5.2), it has been stated that the sensitivities of the frequencies were small, however as there are no other damage indicators, the frequencies are the best damage indicators when the system is monitored using only tower accelerations.

7.2.3 Additivity of the effects of the damage

In the previous Chapter, the damage detection was based on anisotropy tracking, which means that there is no damage additivity in the damage indicators. Indeed, if the three blades of the rotor have the same loss of stiffness, the rotor is still isotropic, so there are no changes in the phase shift and the amplitudes compared to those of the non-damaged case. It is the same

Rotational speed (rpm) Name	4	4.9	6	7	8	9	9.6
2-FA	2.300	2.287	2.279	2.273	2.270	2.268	2.266
2-SS	2.351	2.351	2.351	2.351	2.351	2.351	2.351
Col. edge	2.059	2.060	2.062	2.063	2.065	2.066	2.068
Fw. edge	1.075	1.089	1.107	1.123	1.140	1.156	1.166
Bck. egde	0.934	0.918	0.901	0.883	0.865	0.849	0.839
1-FA	0.252	0.254	0.257	0.258	0.259	0.260	0.260
1-SS	0.253	0.253	0.253	0.253	0.253	0.253	0.253

Table 7.6 – Frequencies of the identifiable Fourier harmonics using tower accelerations function of the rotational speed (Hz)

for the appearance of the new Fourier harmonics, it is linked to the rotor anisotropy. Thus, the additivity of the effects of rotor damages on the frequencies of the Fourier harmonics has to be assessed. To do so, the Floquet modes of the DTU 10MW wind turbine model are computed for different stiffness losses in the rotor, all for a rotational speed of 6 rpm. In Figure 7.4, the evolutions of the frequencies of the selected Fourier harmonics function of different stiffness loss are displayed. First, it can be seen that the effect of the damage seems to be additive for the Collective edge and the 2-SS, where the frequency of the harmonics for a loss of stiffness of 5% on one blade or distributed on two blades are close. Then, with the evolution of the frequency of the Backward and Forward edge, it can be seen that there is no damage additivity for both Fourier harmonics. But the behaviors are different than the one obtained with the anisotropy. In other words, it will not be possible to distinguish a loss of stiffness on one blade from a loss of stiffness distributed on the rotor.

To conclude this study, it has been stated that the appearance of Fourier harmonics, is directly linked to the rotor anisotropy, so with these damage indicators there is no damage additivity. Then for the frequency of the Fourier harmonics, for one part of the harmonics, it seems that the effects of the damages on the frequencies are additive and not for the other part. So there is no true damage additivity with the frequencies, but using the sensitivities computed for a stiffness loss of one blade, it is possible to have an estimation of the order of magnitude of the global damage in the rotor, as it is not possible to assess the distribution of the damage on the different blades. Damage detection based on the monitoring of the frequencies is presented in Section 7.4. First, in the following section, a method to detect the appearance of the new Fourier harmonics from the literature is tested.

7.3 Use of the coherence to detect new Fourier harmonics

In the previous Section, it has been shown that with the example of the DTU 10MW wind turbine model, with anisotropy new Fourier harmonics are appearing but with a frequency close to frequencies of harmonics that can be identified for a system with an isotropic rotor. In [125], the author presents a method to detect the appearance of new Fourier harmonics, even when these harmonics are close in the frequency space (and spatial space), using tower acceleration, with an application to an academic model of a wind turbine. To detect the appearance of new Fourier harmonics, the acceleration is modulated and the coherence is computed between the

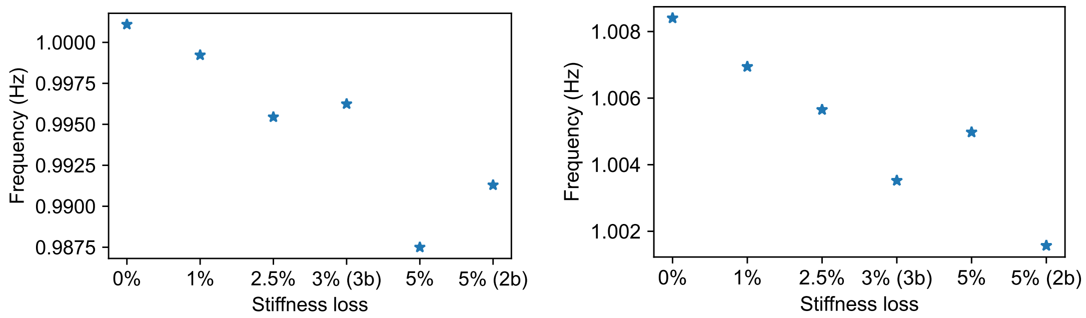

(a) Backward edge (b) Forward edge

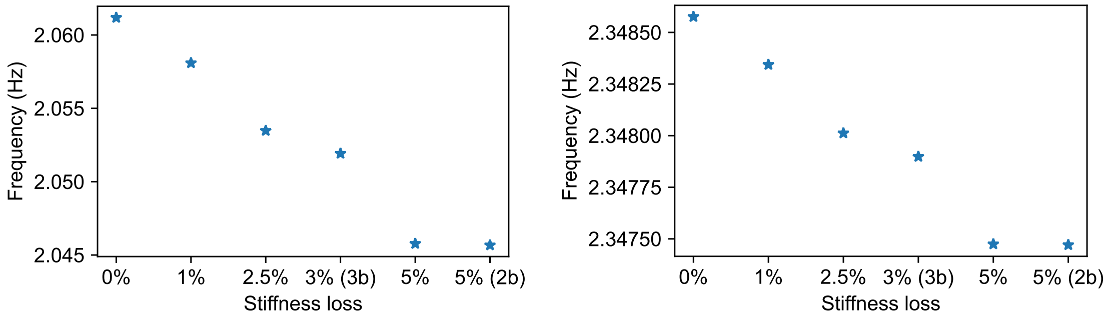

(c) Collective edge (d) 2-SS

Figure 7.4 – Evolutions of the frequencies of the Fourier harmonics sensitive to a rotor damage function of different stiffness losses in the rotor. 2b:= two damaged blades and 3b:= three damaged blades

reference signal and the modulated one. The appearance of new Fourier harmonics should gives new peaks in the coherence spectrum.

7.3.1 Description of the method

The method is designed knowing that the frequencies of the Fourier harmonics of the Backward and Forward edge are separated by $2\Omega/2\pi$ in the fixed frame. Consequently, a signal measured on the tower and the same signal with modulation of $\pm 2\Omega$ will have common frequency contents. The k–th modulation of a signal $y(t)$ is

$$\begin{aligned} y_k(t) &= y(t)\exp\left(-ik\Omega t\right) \\ &= y(t)\exp\left(-ik\psi(t)\right) \end{aligned}, \tag{7.2}$$

where Ω is the rotational speed and $\psi(t)$ the azimuth angle of the rotor. In Figure 7.5 the frequency content for a reference signal and a modulated ($k = 2$) one are displayed, for an isotropic and an anisotropic rotor, with the example of the DTU 10MW wind turbine model at 6 rpm. In this Figure, it can be seen that when the rotor is isotropic, two frequencies are common in the complex spectrum of a signal and its modulation. Then, for a signal from a model with an anisotropic rotor, new frequencies are matching between the modulated and the reference signal. First, with the appearance of the first harmonic of the rotational speed (1P, see Section 2.5.1) three frequencies are in common: two near the negative forward edge and two near the backward edge. Then with the appearance of new Fourier harmonics, 4 other frequencies are in common. Consequently, new peaks should appear in the coherence spectrum when the rotor is anisotropic.

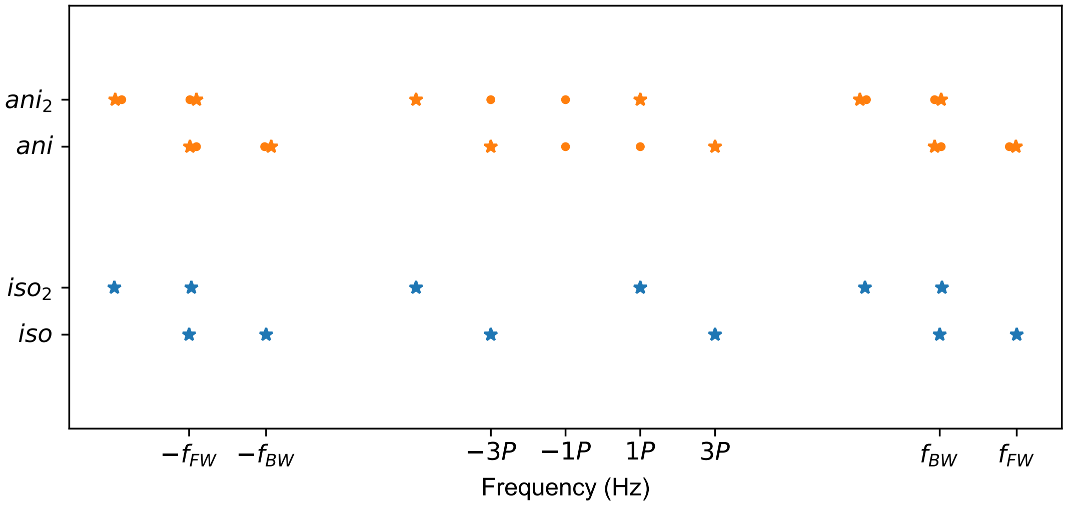

Figure 7.5 – Visualization of the frequencies of interest in the original and modulated signal ($k = 2$), for an isotropic and anisotropic rotor (5% stiffness loss on one blade). ●:= Frequency of a new Fourier harmonic or harmonic of the rotational speed that is appearing with anisotropy

The coherence between two signals (real or complex) $x(t)$ and $y(t)$ is defined such that

$$\gamma_{xy}(\omega) = \frac{|G_{xy}(\omega)|^2}{G_{xx}(\omega)\, G_{yy}(\omega)}, \tag{7.3}$$

with $G_{xy}(\omega)$ the cross-spectrum between $x(t)$ and $y(t)$, $G_{xx}(\omega)$ the power spectral density of $x(t)$ and $G_{yy}(\omega)$ the power spectral density of $y(t)$. All spectra are estimated using the Welch method [141]. The coherence has values between 0 and 1, where 1 means that both signals have the same frequency content at the frequency ω ($|G_{xy}(\omega)|^2 = G_{xx}(\omega)\, G_{yy}(\omega)$).

7.3.2 Distribution of the coherence

Before testing the damage detection using the coherence, the associated distribution need to be studied to have a better understanding of the impact of the rotor anisotropy on the coherence spectrum. To do so, the study is performed using a synthetic signal

$$x(t) = 0.01\cos(2\pi 25t) + 0.05\cos(2\pi 35t) + w_x \tag{7.4}$$

$$y(t) = 0.01\cos(2\pi(25 + 0.002)t) + 0.05\sin(2\pi 35 + 0.002)t) + w_y, \tag{7.5}$$

where w_x and w_y are zero mean Gaussian noise, with a standard deviation of 0.02 and 0.05, respectively. To estimate the distribution of the coherence, a Monte Carlo simulation is performed with 1000 computations of the coherence. In Figure 7.6 the mean coherence spectrum of the Monte-Carlo with the estimated empirical 95% confidence interval is displayed. First, one can see that the coherence spectrum is composed of two peaks, with associated frequencies corresponding to the frequencies of the harmonics that compose $x(t)$ and $y(t)$. Then, as the coherence is bounded by zero, the lower bound of the confidence interval is close to 0 except for the peaks. So, it seems that the distribution of the coherence depends on the value of the coherence, with a peak or noise.

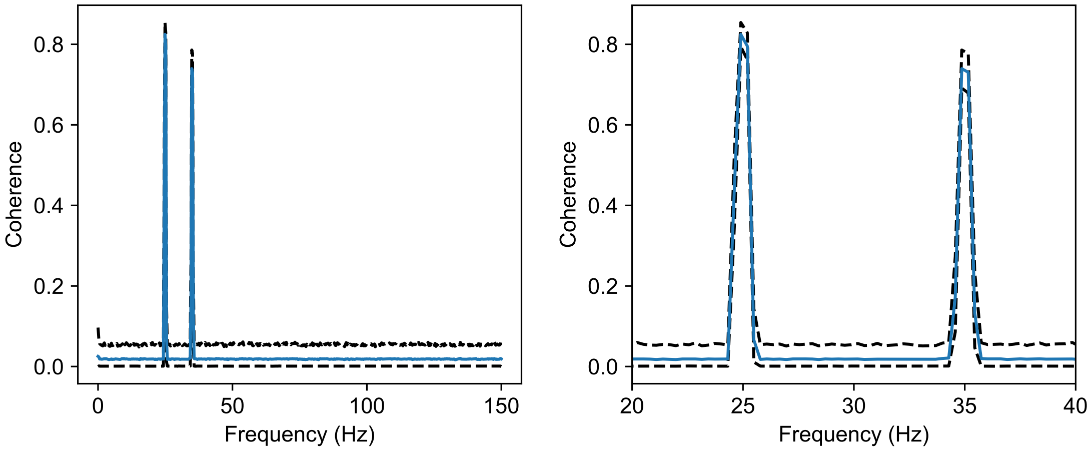

(a) full coherence spectrum

(b) Zoom on the peaks

Figure 7.6 – Mean coherence spectrum, with the 95% estimated confidence interval (- - -), 1024 values in the spectrum

To confirm the previous assumption, the histogram of the coherence is studied, with the coherence at a frequency corresponding to a peak or to the noise. In Figure 7.7, the histograms are displayed conjointly with a fit of an associated distribution, a χ^2 for the noise, and a normal law for a peak.

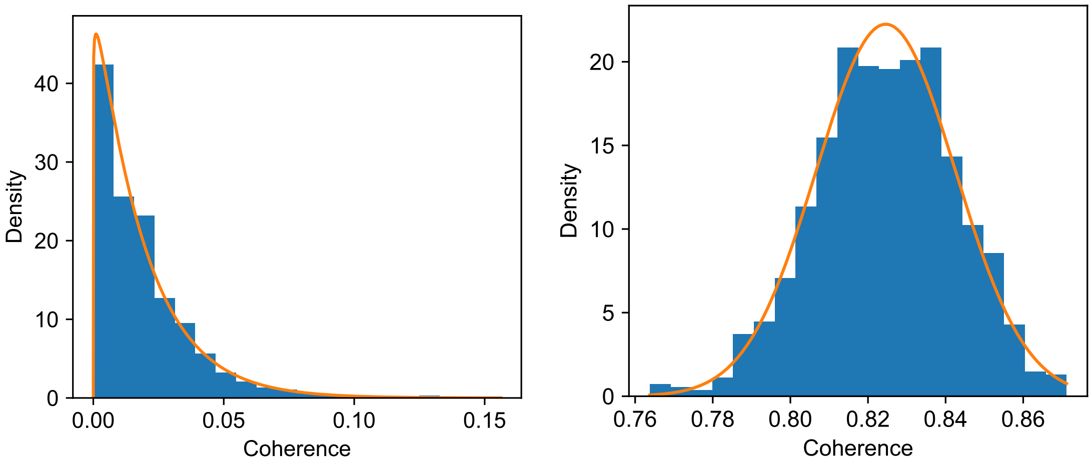

(a) f=100.19 Hz, fit of a χ^2 law

(b) f=25.195, fit of a normal law

Figure 7.7 – Histograms of the coherence for a frequency corresponding to a peak and a frequency corresponding to the noise, with a fit of a distribution

With this Figure, it is clear that there is a good agreement between the fit and the histogram for both cases, so it can be concluded that the coherence can be described by a normal law when it is corresponding to a peak and described by a χ^2 law when it is corresponding to the noise. Consequently, if a peak appears in the coherence spectrum, the coherence at the associated frequency will shift from a χ^2 distribution to a normal distribution.

In the next section, the coherence will be used to detect a stiffness loss of one blade, with an application on data computed with the DTU 10MW wind turbine model with a gradual complexity.

7.3.3 Application: detection of a stiffness loss on one blade

To test the approach, the method is applied on tower top Side-Side accelerations computed with the DTU 10MW wind turbine model for different configurations of the rotor (600 s long sampled at 50 Hz). The first study is performed with a wind defined as white noise with a mean value of 7 m/s leading to a mean rotational speed of around 6 rpm and a 1P around 0.1 Hz. The modulation is performed with $k = 2$ and the azimuth angle $\psi(t)$ is estimated by time integration using the rotational speed sampled at 1 Hz (the rotational speed has often not the same sampling rate as the other measurements). The coherence between the acceleration and the modulated one is computed with a spectrum composed of 2048 values, giving a frequency resolution of around 0.025 Hz.

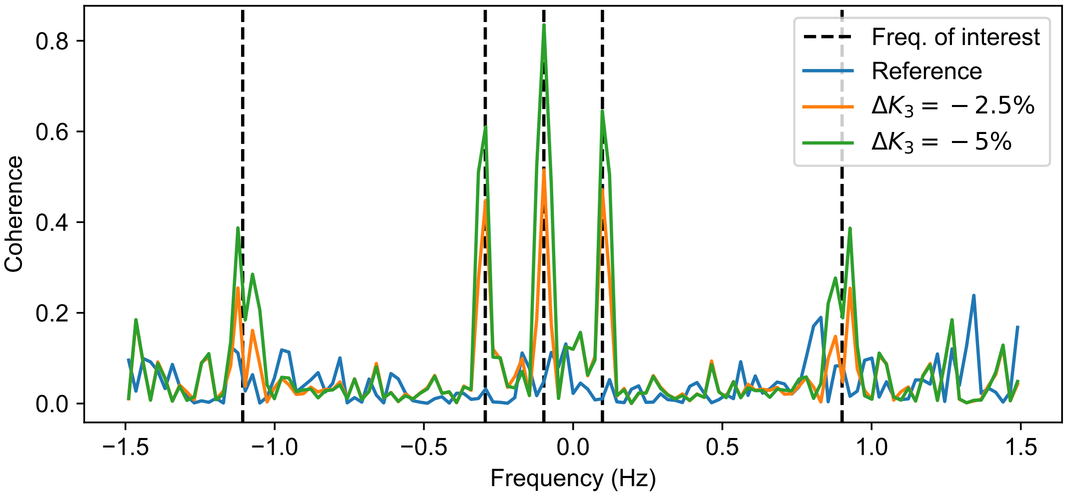

(a) Coherence spectrum

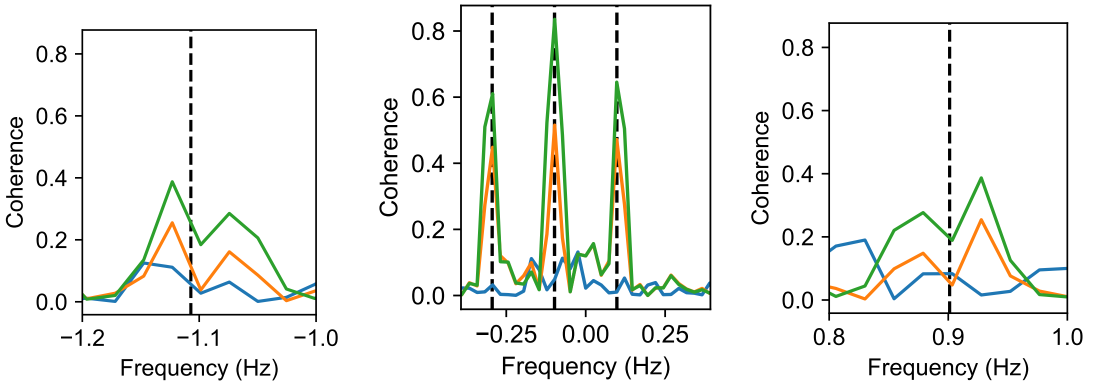

(b) Zoom around the frequency of the Forward edge

(c) Zoom around the harmonics of the rotational speed

(d) Zoom around the frequency if the Backward edge

Figure 7.8 – Coherence between the acceleration tower-top along Side-Side and the modulated one, wind turbine model under white noise wind

In Figure 7.8 the coherence spectrum is displayed for different signals corresponding to different stiffness loss of one blade, with the zoom around the frequencies of interest of the spectrum. First, looking around the harmonics of the rotational speed (Figure 7.8c), it can be seen that three peaks appear with the loss of stiffness of one blade, with an increase of the amplitude conjointly with the increase of the stiffness loss. The frequency of the peaks are corresponding to the harmonic of the rotational speed as it was expected (see Figure 7.5). Then, new peaks are appearing close to the frequency of the Backward and Forward edges. However, the amplitude of those new peaks is low compared to the peaks around the harmonics of the rotational speed, but it seems that two peaks appear around each frequency.

To continue the study, the method is applied once again on acceleration on the tower top along Side-Side, but on data computed under turbulent wind (modeled as "hub-height"), to test the method on more realistic data. In Figure 7.9, the coherence spectrum using the new simulated accelerations, for the different states of the rotor is displayed, with zooms around the frequencies of interest.

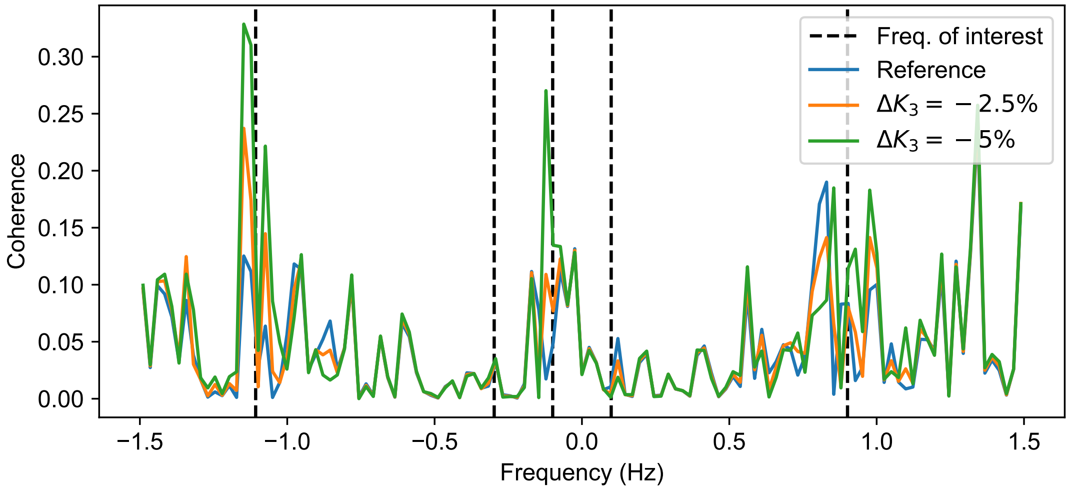

(a) Coherence spectrum

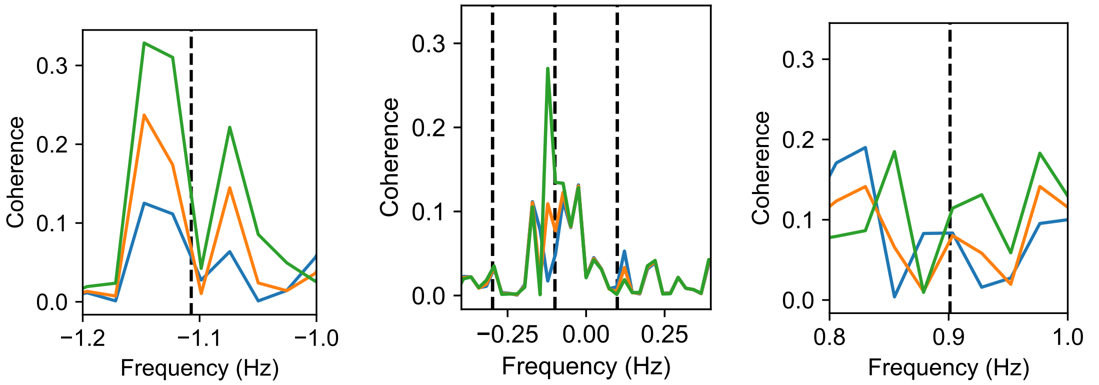

(b) Zoom around the frequency of the Forward edge (c) Zoom around the harmonics of the rotational speed (d) Zoom around the frequency if the Backward edge

Figure 7.9 – Coherence between the acceleration tower-top along Side-Side and the modulated one, wind turbine model under turbulent wind

Compared to the previous spectrum (Figure 7.8), the main difference is around the harmonics of the rotational speed, where the only remaining peak is corresponding to the modulation of the

1P and -1P (-1P in the coherence spectrum). Also, the amplitude of the peak has been reduced, from 0.8 to below 0.3. This might be due to the highly variable rotational speed, which leads to time varying harmonics. Then, there are no more peaks around the frequency of the Backward edge. But two peaks near the frequency of the Forward edge remain. Consequently, to detect the loss of stiffness of one blade, the focus might be on the values of the coherence with a frequency near the -1P and the Forward edge.

Finally, a complete study can be performed similarly to what has been done in Section 6.4. Thus the method is performed first on accelerations computed with the DTU 10MW wind turbine model under a variable turbulent wind (modeled as "hub-height"). Then, the method is performed on accelerations computed with a wind turbine model, where one blade has a loss of stiffness of 5%, with 100 data sets for each rotor configuration. As the mean wind speed is variable, the frequencies of interest are not the same for each simulation. So, to follow the evolution of the coherence, the focus will be around the peaks of the Forward and Backward edge and the -1P, $\pm 2\Delta f$ (Δf: the coherence spectrum resolution) because the peaks in the coherence spectra do not exactly correspond to the studied frequencies. The frequencies of interest are estimated with an identification using the tower accelerations of each data set. With the mean coherence spectrum displayed in Figure 7.10, it can be seen that there are no more coherence peaks around the harmonics of the rotational speed. Then, one can see that the peaks around the Backward and Forward edge have increased. So, the impact of the blade stiffness loss has been detected with the coherence, using all the data sets available. Now the distributions of the coherence will be studied, to see if there is a shift in the distributions.

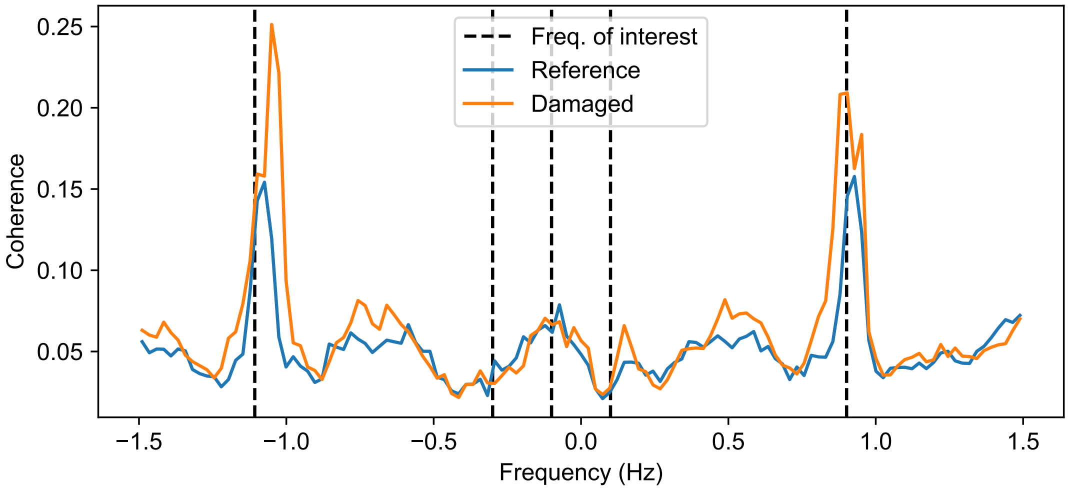

Figure 7.10 – Mean Coherence spectrum of each rotor configuration, with the dashed lines corresponding to he frequencies of interest

Since there are no more coherence peaks around the harmonics of the rotational speed, the study of the coherence will be focused on the Forward and Backward edge. In Figure 7.11 the histograms of the coherence spectra are compared around the frequencies of the Backward and Forward edge. For the Forward edge (Figure 7.11a), the shift of the distribution at the frequency $f_{fw} - \Delta f$ and $f_{fw} + 2\Delta f$ can be seen. However, the distributions are not completely distinct. The same can be stated with the coherence at the frequencies around the Backward edge at $f_{bw} - 2\Delta f$ and $f_{bw} - 2\Delta f$ in Figure 7.11b, where the distributions have shifted, but not enough to be distinct. So, with this application, it can be concluded that it might be possible to detect a stiffness loss of one blade using tower accelerations thanks to a change in the mean of the coherence spectrum. But, other sophisticated methods need to be used conjointly to perform damage detection during continuous monitoring (for example to have an automatic detection of change in the coherence spectrum). This is due to the high noise in the spectra, impeding the distinction between distributions associated with the reference and damaged states. Consequently, the presented method seems not to be adapted to the detection of stiffness losses. In the next section, the method will be used to detect mass imbalances, to find out whether it is better suited to this problem.

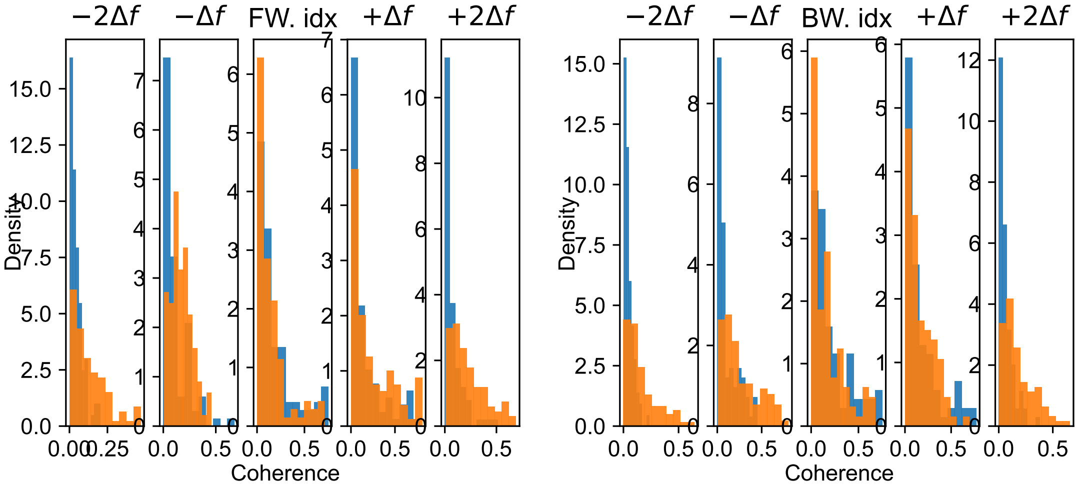

(a) Forward edge

(b) Backward edge

Figure 7.11 – Histograms of the coherence around the frequencies of the Backward and Forward edge, 🟦 := histogram computed from accelerations of the reference rotor, 🟧:= histogram computed from accelerations of the damaged rotor

7.3.4 Application: detection of a addition of mass on one blade

To continue the application of the coherence to detect rotor imbalance using the measurement from the fixed frame, the mass imbalance is studied. The main difference between the spectrum of acceleration between a mass and stiffness anisotropy is the amplitude of the 1P harmonic along Side-Side (see Figure 5.2). So, the first study is performed on an acceleration computed under turbulent wind ("hub-height") from a wind turbine model with an isotropic rotor and a damaged rotor with two different mass additions of 2.5% and 5%, respectively. Then it will be compared to the results obtained in Figure 7.9, as the difference between the coherence spectra should be localized around the harmonics of the rotational speed. So, in Figure 7.12, the coherence spectra of each rotor configuration are displayed. The main difference between these spectra and those obtained in Figure 7.9 is the amplitude of the peak at the frequency of -1P, which corresponds to the coherence between the harmonic of the 1P of the acceleration. Also, it can be seen that the value of the coherence is almost equal for this peak between an addition of mass of 2.5% or 5%. It means that the mass imbalance can be detected with the coherence at the frequencies of the harmonics of the rotational speed, and not at the frequencies of the Backward and Forward edge.

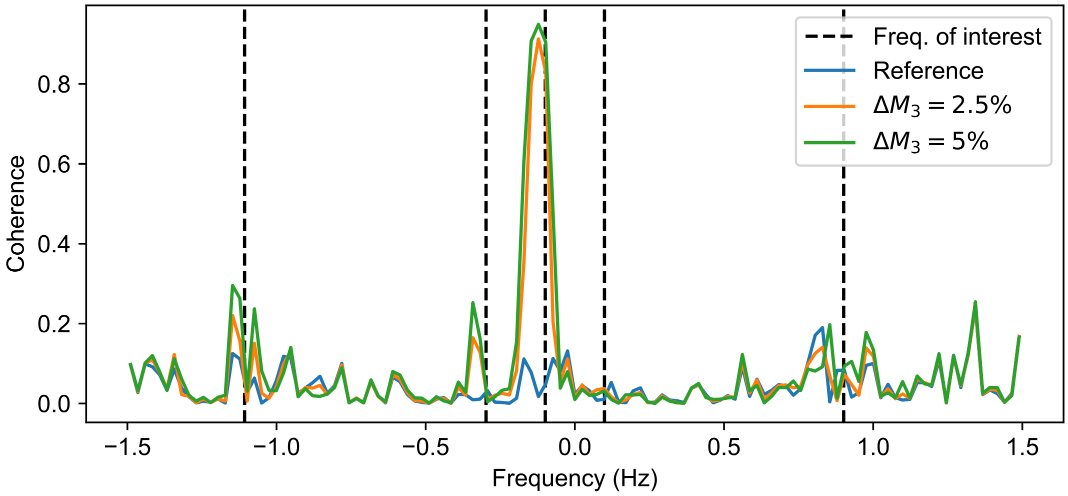

(a) Coherence spectrum

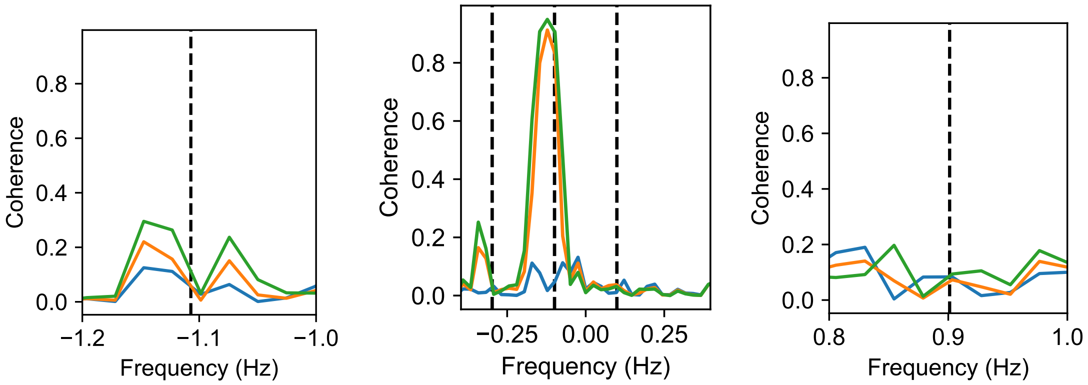

(b) Zoom around the frequency of the Forward edge

(c) Zoom around the harmonics of the rotational speed

(d) Zoom around the frequency if the Backward edge

Figure 7.12 – Coherence between the acceleration tower-top along Side-Side and the modulated one, wind turbine model under turbulent wind with an addition of mass

Then, a complete study can be performed similarly to the previous Section. So, the coherence is computed first on accelerations computed with the reference wind turbine model under a variable turbulent wind (modeled as "hub-height") with a total of 100 data sets. Then, the method is performed on accelerations computed with a wind turbine model, where one blade has an addition of mass of 1% (also 100 data sets) to have a damage value close to what has been detected with the method in the literature.

In Figure 7.13a the mean coherence spectra are displayed around the harmonics of the rotational speed. With this Figure, it is clear that a peak is appearing at the frequency of -1P. Another one also appears close to the 1P but with a smaller amplitude. The second peak comes from the modulation of the 1P and the 3P. Since the 3P has a lower amplitude than the 1P, it can explain the lower amplitude of the second peak. It confirms that it is easier to detect the mass imbalance than the stiffness imbalance due to the amplitude of the harmonic of the 1P. Then, the distributions of the coherence can be studied. In Figure 7.13b, the histograms of the coherence values at the frequencies around the 1P are shown. For the coherence values at the frequency of the 1P and below, the distributions have shifted, especially for the value at the frequency of the 1P. Consequently, from this example, it can be concluded that the coherence can be used to detect mass imbalance of the rotor, with the appearance of the 1P peak. However, as for the detection of a stiffness loss, the study needs to be continued to have an automatic detection of rotor imbalance, with the definition of an associated automatic detection method like it is done for the study of the PSD (presented in Section 2.5.1).

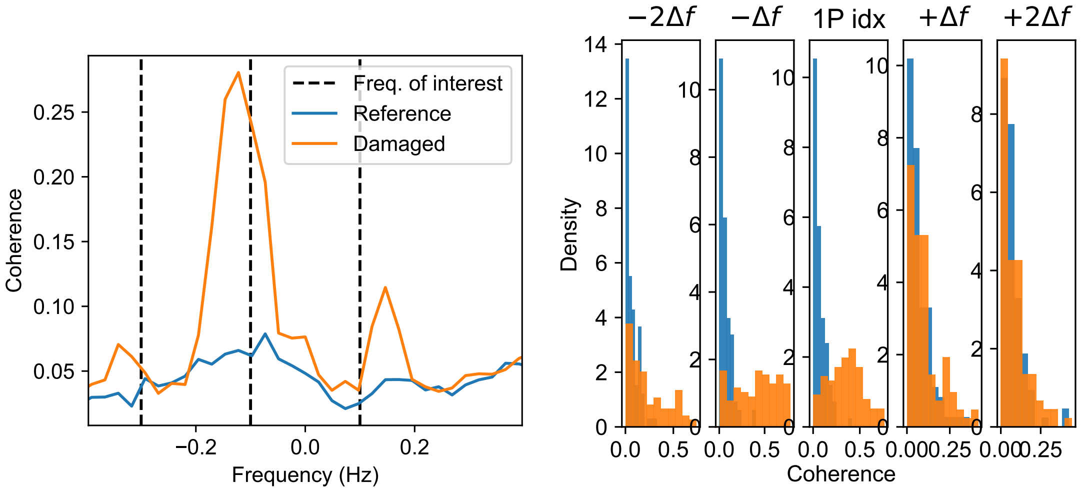

(a) Mean coherence spectrum around the harmonics of the rotational speed

(b) Histograms of the coherence values around the 1P frequency

Figure 7.13 – Coherence results using the tower-top acceleration along Side-Side, addition of mass on one blade

With this example, it can be seen that it is easier to detect an addition of mass than a loss of stiffness with this method, as the addition of mass leads to the appearance of the 1P peak. It is a preliminary work, but it seems that it is difficult to detect a small loss of stiffness with this approach. Therefore, based on the previous study on the damage indicators, the detection of stiffness losses of the rotor must be based on the monitoring of the frequencies.

7.4 Damage detection based on the frequencies

In Section 7.2, with the appearance of new Fourier harmonics in the Floquet modes, the other damage indicators were the frequencies of the identifiable Fourier harmonics. To perform damage detection using the frequencies, the stochastic subspace identification is used as it was done in [59].

7.4.1 Definition of a residual

To perform damage detection with the Stochastic Subspace-based Damage Detection, a residual has to be defined. Based on the study performed in Section 7.2.2, the residual is composed of the damage sensitive harmonics that are not varying with the rotational speed. So, the residual is defined as

$$\zeta = \sqrt{N}\begin{bmatrix}\hat{f}_{1SS}-f_{1SS} & \hat{f}^*_{bw}-f^*_{bw} & \hat{f}^*_{fw}-f^*_{fw} & \hat{f}_{col}-f_{col} & \hat{f}_{2SS}-f_{2SS}\end{bmatrix}^T, \tag{7.6}$$

where $\hat{f}_k$ the estimation of the frequency f_k and the normalized frequencies defined such that

$$f^*_{bw} = f_{bw} + \frac{\Omega}{2\pi} \quad \text{and} \quad f^*_{fw} = f_{fw} - \frac{\Omega}{2\pi}. \tag{7.7}$$

In the same way, as for the previous residual in the previous Chapter, this residual can be expressed function of an estimated reference. Also, it will be possible to use the mean residual to reduce the covariance, and thus detect smaller damages. From this new residual, it will be possible to define the statistical test using the sensitivities computed in Section 7.2.2. But as some of the frequencies are also sensitive to tower damage it is chosen to add the associated sensitivities. Also, it should be possible to distinguish a rotor fault from a tower fault. So, the considered parametrization is composed of two parameters.

7.4.2 Theoretical performance

From the definition of the residual and the sensitivities, the Fisher matrix can be then computed. To do so, the covariance matrix needs to be estimated. In this study, the simulated data computed in Section 6.5 are used (simulations with turbulent full filed wind based on *Météo-France* measurement, 600 s long sampled at 50 Hz), except that the tower top accelerations along Fore-Aft and Side-Side are used to perform the identification instead of the blade root moments. In Figure 7.14a, the diagonal values of the Fisher matrix function of the frequencies used to construct the residual are displayed. With those diagonal values, it can be seen that the Fourier harmonics corresponding to the Floquet modes of edge bending give the best detectability of the rotor damage. Whereas, for the tower damage, the Fourier harmonics of the Floquet modes of tower bending give the best detectability. Then, using the Fourier harmonics of all the Floquet modes of the rotor and tower bending gives the best damage detectability of rotor and tower damage.

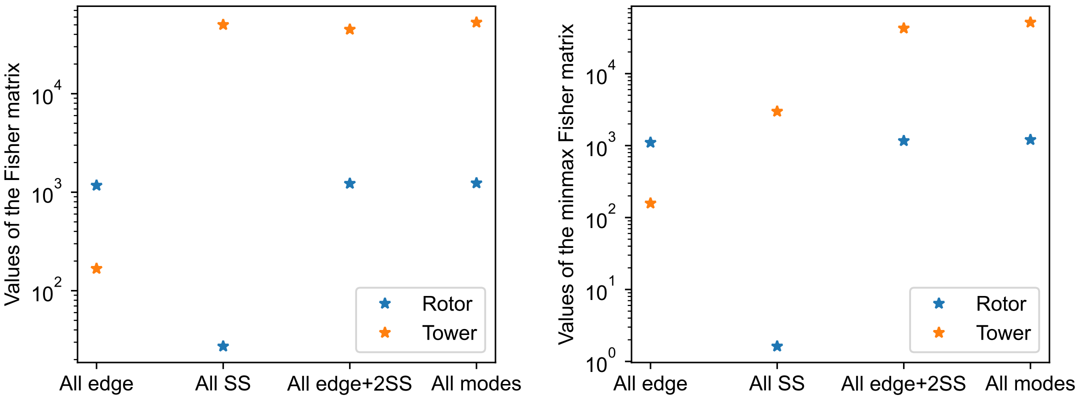

(a) Diagonal values of the Fisher matrix (b) Values of the minmax Fisher matrix

Figure 7.14 – Values of the Fisher matrix function of the considered residual

With this parametrization, it is possible to use the minmax damage localization and quantification method, as the sensitivity matrix is full column rank. This is confirmed in Figure 7.14b, where the diagonal values of the Fisher matrix and the values of the minmax Fisher matrix (defined in Equation (2.86)) have the same order of magnitude. This was not the case in the previous Chapter, for example, where the sensitivities of the parameters were linearly dependent.

To finish the study of the theoretical performance, the probabilities of detection of some simulated damages can be computed considering different residuals. The values are reported in Table 7.7. First, the probabilities confirm the statement made at the beginning of the Section, with the Fourier harmonics of the Floquet modes of edge bending giving the best damage detectability of rotor fault and the Fourier harmonics of the Floquet modes of tower bending the best damage detectability of tower fault. Then, for the different residual construction, the probabilities are low. It means that the damage detectability needs to be improved. As it was done in the previous Chapter, the mean residual can be used. To obtain a probability of detection over 95% for a stiffness loss of 5% on a blade and 1% on the tower considering a residual composed of all the Fourier harmonics, $nb_f = 10$ can be chosen.

Damage	All edge	All SS	All edge+2SS	All modes
$\Delta K_3 = -1\%$	5.89%	5.02%	5.93%	5.94%
$\Delta K_3 = -2.5\%$	10.92%	5.13%	11.20%	11.27%
$\Delta K_3 = -5\%$	31.45%	5.51%	32.71%	33.02%
$\Delta K_{tower} = -0.5\%$	5.03%	15.54%	14.36%	16.20%
$\Delta K_{tower} = -1\%$	5.13%	50.43%	45.93%	52.82%

Table 7.7 – POD of different stiffness reductions of the tower or the rotor function of the definition of the residual

7.4.3 Application: detection of different damage scenarios

As presented in the previous Section, the mean residual is used with $nb_f = 10$ and as the objective is to assess the possibility to use the frequency to perform damage detection, bootstrapping is used. Also, the estimated reference is computed with the data-sets used during the computation of the covariance matrix, with $n_f = 200$.

To perform the damage detection, a residual composed of all the edge bending harmonics and the second Side-Side harmonic is used. The first Side-Side harmonic is removed because its frequency is close to the frequency of the third harmonic of the rotational speed in some simulations, which happens when the rotational speed is close to 5.05 rpm. Nevertheless, the first Side-Side harmonic does not give a lot of information on the damage as the probabilities of detection and Fisher values for a residual constructed with all the harmonics or without the 1-SS are close (Figure 7.14 and Table 7.7). So, the performance of the damage detection is not significantly affected by the removal of the first Side-Side harmonic.

To validate the damage detection using the frequencies, the test is performed on different data sets. First, the same training data set as in Section 6.5 is used (with a wind modeled as "nub-height"). Then, on data sets with different stiffness reductions of one or two blades. And, to finish on data sets with a stiffness reduction of the tower and with stiffness reductions of the tower and a blade.

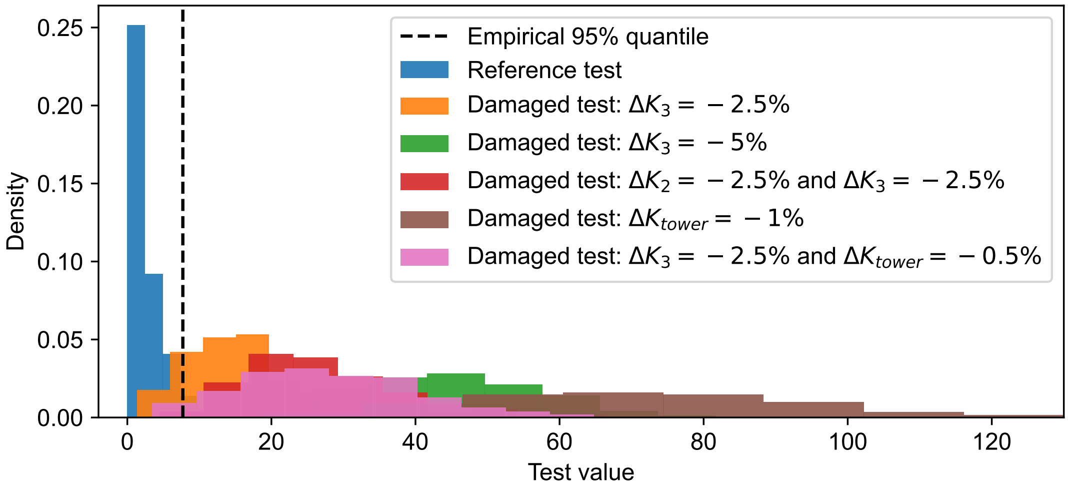

Figure 7.15 – Histogram of the damage detection test for the different simulated damage scenarios, using the mean residual ($nb_f = 10$) and bootstrapping (1000 combinations)

In Figure 7.15, the histogram of the test performed on the different data sets is displayed. To begin, it can be seen that the shift of the distribution is important for all the tests computed on data sets corresponding to a damaged structure. Then, the associated empirical probabilities of detection are close to the theoretical ones for the stiffness reduction of one blade of 5% and the stiffness reduction of the tower of 1%, with a value over 99.9% (100% theoretically). For a stiffness loss of 2.5%, the empirical probability is 85.2%, which is over the theoretical one of 70%. This gap can be the consequence of the assumption of the linear effect of the damage which is not respected. Then, for the test computed on data where the tower and a blade are damaged, the empirical probability is around 96.4% whereas the theoretical one is about 97.9%. The empirical and theoretical probabilities are close, which means that the effect of loss of stiffness of the tower and a blade are additive. Finally, looking at the results corresponding to the data set where two blades are damaged, it can be seen with Figure 7.15 that the shift of the distribution is lower than the one obtained for a loss of stiffness of 5% but higher than the one obtained for a loss of stiffness of 2.5%. This result confirms the study performed in Section 7.2.3, where the damage additivity is not perfect, but the assumption gives a good estimate of the order of magnitude of the rotor damage. This will also be verified with the results of the quantification test.

In Table 7.8, the mean values of the localization and quantification tests are reported, with the mean values of the quantification test associated with their empirical 95% confidence interval. Let us start with the localization test. When the simulated damage is only on the rotor or the tower, the damage is well localized for each simulated damage. The difference between the mean values corresponding to the damaged parameter and the other is important because the minimax test is used and theoretically only the localization test corresponding to the damaged parameter should have a shift. For the test where damage is simulated on the rotor and on the tower, the mean values of the two localization tests have the same order of magnitude.

Finally, the performance of the quantification test can be assessed. As the quantification is linked to the shift of the distribution and as the empirical probabilities of detection are close to the theoretical ones, it should be the same for the estimated damage. For the test corresponding

Simulated damage	Test	Rotor	Tower
$\Delta K_3 = -2.5\%$	Localization	13.917	2.855
	Quantification	-3.37±0.04%	0.17±0.01%
$\Delta K_3 = -5\%$	Localization	41.377	3.808
	Quantification	-5.92±0.04%	0.20±0.01%
$\Delta K_2 = -2.5\%$ and $\Delta K_3 = -2.5\%$	Localization	20.639	2.747
	Quantification	-4.13±0.04%	-0.16±0.01%
$\Delta K_{tower} = -1\%$	Localization	1.093	64.848
	Quantification	-0.18±0.04%	-1.22±0.01%
$\Delta K_3 = -2.5\%$ and $\Delta K_{tower} = -0.5\%$	Localization	9.976	12.609
	Quantification	-2.75±0.05%	-0.49±0.01%

Table 7.8 – Damage localization and quantification results using the minmax test

to a loss of stiffness of one blade or the tower, the estimated damage is close to the simulated one, but higher. This is in agreement with the empirical probabilities of detection that are higher than the theoretical ones. For the test corresponding to a simulation of a loss of stiffness of two blades, the estimated damage is lower than the simulated one, as the shift of the distribution of the damage detection test is lower than the theoretical one. Then, when the damage is simulated on one blade and on the tower, the estimation of each damage is close to the simulated one, thanks to the minmax test that gives an unbiased estimator.

To conclude, with the use of the frequencies of the identifiable Fourier harmonics, it has been possible to detect and localize faults on the rotor and the tower, based on the model sensitivities and signal processing. But, the performance of the damage detection is lower than the one based on the phase shift and the amplitude (see Section 6.5), where a loss of stiffness of 5% on one blade is detected without the use of the mean residual.

7.5 Conclusion

To conclude, using only measurements from the fixed frame, two main damage indicators have been found. With the appearance of new Fourier harmonics and the evolutions of the frequencies.

Whereas the new Fourier harmonics appear close to existing ones, which does not make it possible to directly identify it for small damages, the use of coherence might be a solution. With the use of coherence, it is theoretically possible to detect the appearance of the new Fourier harmonics even if the associated frequencies are close to other ones. But, the method is sensitive to the variable rotational speed. Consequently, the method is more suitable for the detection of an addition of mass than a loss of stiffness, as the addition of mass leads to the appearance of harmonics of the rotational speed. However, the detection of mass imbalance with the coherence is close to the imbalance detection based on the appearance of the 1P in the PSD in the fixed frame (with the methods briefly presented in Section 2.5.1). Consequently, a machine learning method can be used jointly to perform imbalance detection with coherence.

Finally, the Stochastic Subspace-based Damage Detection based on the local approach has been used using the frequencies of the Fourier harmonics to define a residual. With this method, it has been possible to detect loss of stiffness of the rotor, with different combinations of damaged blades. Also, thank to the minmax test, it is possible to differentiate rotor damages and tower damages.

This Chapter is a preliminary work for damage detection using the measurements of the fixed frame to assess the potential of the damage indicators. To continue this work, both methods that have been tested need to be applied to data computed under a full field wind and potentially on real measurements.

However, damage detection using the frequencies can not be performed directly on a real structure. Indeed, the frequencies of a structure are impacted by the temperature, as it is shown in [145] on civil engineering structures and in [45] on a wind turbine. Consequently, to perform the presented damage detection method, a correction of the temperature effect has to be performed first, as it is done in [50] based on the Gaussian process.

CONCLUSION AND PERSPECTIVES

Conclusion

In this thesis, the first objective was to define a new identification approach to perform Operational Modal Analysis (OMA) on operating wind turbines. The second objective was to define a fault detection method associated with the identification (i.e. the OMA methods), with a focus on rotor faults. The main problem is that the rotation of the rotor of a wind turbine breaks the Linear Time Invariant (LTI) hypothesis, and these systems should rather be modeled as Linear Time Periodic (LTP) systems. Since the basic assumptions of OMA are no longer fulfilled, these LTI-based OMA methods need to be extended to LTP systems. The approach that is chosen in the thesis was to define the identification procedure based on the physics behind the studied system. For damage detection, it is chosen to construct the method with the most sensitive damage features that can be obtained with the new identification procedure.

To begin, the first Part was dedicated to the state of the art, to understand the modeling of an operating wind turbine and the problem of performing OMA on it. Looking at the OMA methods of the state of the art, the main challenge comes from the modeling of the operating wind turbine, which goes against one of the assumptions of the OMA methods. Thus, some methods have been developed to adapt the OMA methods to the problem of rotating machines and LTP systems in general, but all those methods have non-negligible drawbacks and cannot be used for the monitoring of operating wind turbines. Then, looking at the damage detection methods designed for operating wind turbines, many methods are dealing with rotor imbalance detection (mass or aerodynamic), but there are only few methods for the detection of structural faults. Therefore, this problem is assessed in the thesis.

To continue, in the second Part, the problem of the identification of LTP systems is treated, where it is chosen to approximate the eigenmodes of the LTP systems (called Floquet modes) as a finite sum of eigenmodes of LTI systems. Precisely, each Floquet mode is approximated as the sum of its Fourier harmonics with a non-zero amplitude. Then, this approximation is validated with the example of an academic model of wind turbine and a physical meaning is given to the Fourier harmonics of the Floquet modes. To continue, the validity of the identification of the Fourier harmonics of the Floquet modes with the Stochastic Subspace Identification (SSI) is demonstrated, based on the definition of the state-space representation of the approximation, which is an LTI system under non-stationary inputs, precisely inputs with periodic moments. Finally, the identification is performed using data from simulations of rotating wind turbines, with a gradual complexity. In every case, the modes identified with the SSI are corresponding to the Fourier harmonics of the Floquet modes of the model.

To finish, in the third Part, fault detection is treated, with the aim of using the identification results as a basis. Also, based on the results of the state of the art, it is chosen to define the damage detection method based on rotor anisotropy tracking. For this purpose, the parameters of the identified Fourier harmonics that are the most sensitive to the rotor anisotropy are sought, and defined as the phase shift and the amplitude of the mode shapes of the edge bending (i.e. in the rotor plane) Fourier harmonics. Firstly, it is shown that those damage indicators can be used to detect rotor anisotropy with a single identification using the associated uncertainties. Secondly, those damage indicators are used to define a new residual to adapt the Stochastic Subspace-based Damage Detection to the detection of rotor faults. This damage detection method is then applied with the detection and localization of a stiffness loss of one blade, on data with a gradual complexity. For each application, it has been possible to detect a stiffness loss, assess which blade is damaged, and estimate the order of magnitude of the damage. To continue, and to improve damage detectability using fixed length measurements, the mean residual is defined and validated with an application on data of an academic model of a wind turbine. After that, using the mean residual, different local losses of stiffness simulated with an aero-servo-elastic wind turbine model have been detected, as the damaged blade. Also, it is shown that the performance of the damage detection and even more the damage localization depends on the sensors used in the identification to construct the residual, with the example of the damage detection and localization using an ideal instrumentation composed of two measurements of accelerations per blade (mid and end of the blade) along the edge direction. Finally, the problem of wind turbine rotor damage detection using fixed frame (nacelle and tower) measurement is assessed. Considering the parameter of the identifiable Fourier harmonic, the most sensitive indicators are the shift of frequencies and the appearance of new Fourier harmonics. The last indicator is difficult to monitor even with dedicated methods from the literature. For the shift of the frequencies, the Stochastic Subspace-based Damage Detection can be used by defining a residual function of the frequencies. This damage detection is applied to data computed with an aero-servo-elastic model of a wind turbine, with a simulated loss of stiffness of one blade.

To conclude, the two objectives of the thesis have been achieved thanks to the definition of the approximation of the Floquet modes as a sum of eigenmodes of time invariant system, with its associated state-space representation, allowing the use of the SSI. This has made it possible to monitor the operating wind turbines through the identification of Fourier harmonics of the Floquet modes.

Perspectives

From the work that has been carried out and the results obtained during the thesis, some perspectives can be seen:

- Apply the identification procedure to real data from the rotor. To confirm that the identification procedure can be used for a continuous monitoring of an operating wind turbine.
- In addition to the identification, apply the damage detection methods defined in Chapter 6 and Chapter 7. One of the objectives will be to confirm that the damage detection test based on phase shifts and amplitudes is not sensitive to wind conditions and especially to temperature. For the temperature, since the residual is a function of the rotor anisotropy and the rotor is exposed to the same temperature field, the test may be insensitive to the temperature. For the damage detection based on the frequencies, it should be possible

to estimate the effect of the temperature on the identified frequencies and try to remove the effect, as it is mentioned in the conclusion of Chapter 7.

- Use model updating after the damage detection, localization, and quantification, to have a better estimate of the state of the wind turbine, to avoid any assumptions on the features used to perform the damage detection. However, there is a major challenge with the model updating. Indeed, if the damage features are based on the harmonics of the Floquet modes, it will be necessary to compute the Floquet modes of the model during the optimization process, which is a costly operation. One option might be to use a meta-model for the optimization.

PART IV

Appendices

Appendix A

Aerodynamic loads modelling with the BEM theory

Here the theory of the Blade Element Momentum (BEM) is presented. In order to compute the aerodynamic load from the properties of the wake and the wind turbine.

Actuator disc concept

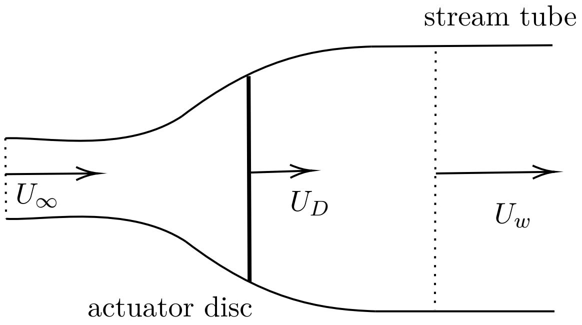

Figure A.1 – Stream tube of a wind turbine

To begin, let's determine the power extracted from the wind by the wind turbine, considered as a uniform disk. To do this, let's define a stream tube Figure A.1. Thus, we can define a flow and deduce a relationship between the different speeds, according to the conservation of energy of a non-compressible fluid:

$$U_\infty A_\infty = U_D A_D = U_w A_w, \tag{A.1}$$

where A_∞ is the considered surface at the beginning of the steam tube, A_d is the surface swept by the rotor and A_w the surface considered at the end.

The parameter a, the axial flow induction factor, is defined to quantify the change in speed between the incident wind and the wind at the rotor, with $U_D = U_\infty(1-a)$. With the momentum theory, it is possible to express In the same way the wind speed downstream of the rotor :

$$U_w = (1 - 2a)U_\infty. \tag{A.2}$$

Thus, the change in momentum of the flow (ΔM), with ρ the air density, is defined as:

$$\Delta M = (U_\infty - U_w)\, \rho A_D U_D. \tag{A.3}$$

The change in momentum can be related to the force differential at the rotor, so we get

$$\left(p_D^+ - p_D^-\right) A_D = \left(U_\infty - U_w\right) \rho A_D U_\infty (1-a), \tag{A.4}$$

with p_D^+ and p_D^- respectively the pressure ahead and behind the rotor. Finally, the power due to the wind forces on the rotor can be expressed :

$$P = F U_D = 2 \rho A_D U_\infty^3 a (1-a)^2. \tag{A.5}$$

Furthermore, the theoretical power coefficient of a wind turbine can be defined:

$$C_p = 4a(1-a)^2, \text{ with } \; P = \frac{1}{2} C_p \rho A_D U_\infty^3. \tag{A.6}$$

From the definition of the power coefficient, it is possible to calculate the theoretical maximum, called the Betz limit

$$\frac{dC_p}{da} = 4(1-a)(1-3a) \tag{A.7}$$

$$= 0 \;\; \text{for } a = \frac{1}{3}. \tag{A.8}$$

Thus, the maximum power coefficient is $C_{p\ max} = 0.593$.

Rotor disc theory

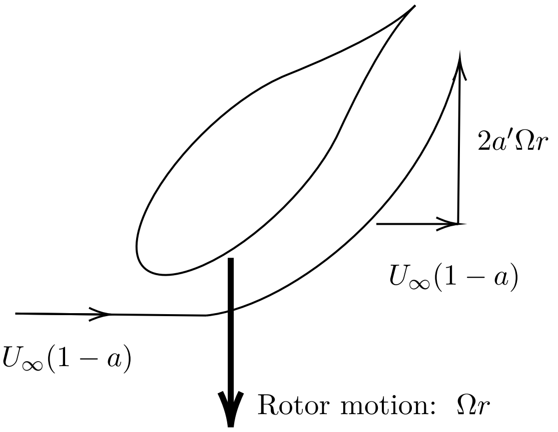

Figure A.2 – Tangential velocity across the rotor

Now let us consider the rotation of the rotor, which induces a rotation of the flow (Figure A.2). To begin, let's define the tangential flow velocity, as a function of the rotational speed Ω, the radius r and the tangential flow induction factor a' :

$$V_t = 2 \Omega r a'. \tag{A.9}$$

Once the two velocity components are defined, it is possible to define the torque produced by the wind. The torque transmitted to the wind turbine can be defined as the change in angular momentum of the flow.

Assuming that each annular ring of radius r and of radial width δr is independent, the torque increment associated with this element is equal to the momentum of the tangential velocity by the radius of the considered element

$$\delta Q = \rho \delta A_D U_\infty (1-a) 2\Omega r a' r \tag{A.10}$$

with δA_D the elementary surface swept by the surface element associated to the radius increment.

From the torque increment, we can express the associated power $\delta P = \delta Q \Omega$. Reusing the definition of power,the relation between axial and tangential flow induction factor is

$$\delta P = 2\rho \delta A_D U_\infty^3 a(1-a)^2. \tag{A.11}$$

We then obtain the following equality

$$U_\infty^2 a(1-a) = \Omega^2 r^2 a'. \tag{A.12}$$

By setting $\lambda_r = \frac{\Omega r}{U_\infty}$ the *local speed ratio* we obtain the relation

$$a(1-a) = \lambda_r^2 a'. \tag{A.13}$$

Finally, we can express the power of the flow through a rotor element

$$\delta P = \left(\frac{1}{2}\rho U_\infty^3 2r^2 \delta r\right) 4a'(1-a)\lambda_r^2, \tag{A.14}$$

with two distinct parts, the power of the flow through the elementary ring $(\frac{1}{2}\rho U_\infty^3 2r^2 \delta r)$ and the efficiency of the wind turbine $(\eta_r = 4a'(1-a)\lambda_r^2)$.

Rotor blade theory

Once the speeds are obtained, we can calculate the aerodynamic loads on a blade section, from the drag and lift loads. First, let's define the relative speed of a blade at radius r

$$w = \sqrt{U_\infty^2 (1-a)^2 + \Omega^2 r^2 (1+a')^2}. \tag{A.15}$$

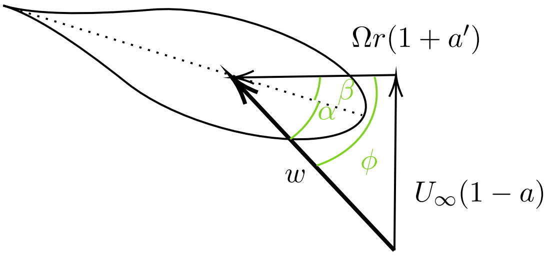

Figure A.3 – Blade element velocities

The angle of attack is defined as $\alpha = \phi - \beta$ (see Figure A.3), where β represents the pitch of the blade and ϕ is defined by the following equations:

$$\sin\phi = \frac{U_\infty(1-a)}{w} \tag{A.16}$$

$$\cos\phi = \frac{\Omega r(1+a')}{w}. \tag{A.17}$$

Finally, we can express the lift and drag forces for each element of length δr and chord c

$$\delta L = \frac{1}{2}\rho w^2 c C_L \delta r, \tag{A.18}$$

$$\delta D = \frac{1}{2}\rho w^2 c C_D \delta r \tag{A.19}$$

with C_L and C_D respectively the lift and drag coefficients of the aerodynamic profile for the angle of attack α. This gives us the axial load and the torque on an element for N blades

$$\delta T = \delta L\cos\phi + \delta D\sin\phi = \frac{1}{2}\rho w^2 Nc\left(C_L\cos\phi + C_D\sin\phi\right)\delta r, \tag{A.20}$$

$$\delta Q = \delta T\Omega. \tag{A.21}$$

Blade Element Momentum (BEM)

Once the different loads are defined, the velocity field must be determined. For this the Blade Element Momentum theory (BEM) [19] is used. This theory, widely used, considers that each element of a blade interacts only with the flow passing through this part.

First, the variation of the axial momentum of the flow passing through the swept annular can be written as:

$$\rho U_\infty(1-a)2\pi r\delta r 2aU_\infty = 4\pi\rho U_\infty^2 a(1-a)r\delta r. \tag{A.22}$$

Then the loss of pressure of the flow downstream of the rotor inducing an additional load on the annular is considered

$$F_{\Delta p} = \frac{1}{2}\rho(2a'\Omega r)^2 2\pi r\delta r. \tag{A.23}$$

Consequently

$$\frac{1}{2}\rho w^2 Nc\left(C_L\cos\phi + C_D\sin\phi\right)\delta r = 4\pi\rho\left(U_\infty^2 a(1-a) + (a'\Omega r)^2\right) r\delta r, \tag{A.24}$$

by simplifying the equation

$$\frac{w^2}{U_\infty^2}N\frac{c}{R}\left(C_L\cos\phi + C_D\sin\phi\right) = 8\pi\left(a(1-a) + (a'\lambda\mu)^2\right)\mu, \tag{A.25}$$

with $\mu = \frac{r}{R}$, $\lambda = \frac{\Omega R}{U_\infty}$ the tip speed ratio and R the rotor radius.

In a second step, let us express the axial torque generated by an element of the rotor

$$\left(\delta L\sin\phi - \delta D\cos\phi\right) r = \frac{1}{2}\rho w^2 Nc\left(C_L\sin\phi - C_D\cos\phi\right) r\delta r. \tag{A.26}$$

Using the angular momentum variation of the flow we obtain:

$$\frac{w^2}{U_\infty^2}\frac{Nc}{R}\left(C_L\sin\phi - C_D\cos\phi\right) = 8\pi\lambda\mu^2 a'(1-a). \tag{A.27}$$

Usually we define

$$\begin{aligned} C_L\cos\phi + C_D\sin\phi &= C_X \\ C_L\sin\phi - C_D\cos\phi &= C_Y. \end{aligned} \tag{A.28}$$

Finally from the equations A.25 and A.27, we can obtain the flow induction factors a and a'

$$\frac{a}{1-a} = \frac{\sigma_r}{4\sin^2\phi}\left(C_X - \frac{\sigma_r}{4\sin^2\phi}C_Y^2\right) \tag{A.29}$$

$$\frac{a}{1+a'} = \frac{\sigma_r C_Y}{4\sin\phi\cos\phi}, \tag{A.30}$$

with $\sigma_r = \frac{Nc}{2\pi\mu R}$ the chord solidity. To determine the velocity field and thus obtain the forces exerted on the rotor, the equations A.29 and A.30 must be solved iteratively for each rotor element.

Appendix B

LEMMA AND THEOREM USED

B.1 Law of large numbers [30]

Let $X = \{X_1, X_2, \ldots, X_n, \ldots\}$ a sequence of independent random variable define with a mean μ and a variance σ^2. The sample average of X is defined as

$$\bar{X}_n = \frac{1}{n}\sum_{i=1}^{n} X_i \tag{B.1}$$

Weak law: The weak law of large numbers (also called law of Khinchin) states that the sample average converges in probability towards the expected value

$$\bar{X}_n \to \mu \quad \text{when} \quad n \to \infty. \tag{B.2}$$

So, for any positive number ε

$$\lim_{n\to\infty} \mathbb{P}\left(\left|\bar{X}_n - \mu\right| < \varepsilon\right) = 1. \tag{B.3}$$

Strong law: The strong law of large numbers (also called law of Kolmogorov) states that the sample average converges almost surely to the expected value

$$\bar{X}_n \overset{\text{a.s.}}{\to} \mu \quad \text{when} \quad n \to \infty. \tag{B.4}$$

That is,

$$\mathbb{P}\left(\lim_{n\to\infty} \bar{X}_n = \mu\right) = 1. \tag{B.5}$$

B.2 Central limit theorem [30]

Let $X = \{X_1, X_2, \ldots, X_n, \ldots\}$ a sequence of independent random variable define with a mean μ and a variance σ^2. Then as n approaches infinity, the random variable $\sqrt{n}\left(\bar{X}_n - \mu\right)$ converge to a normal distribution $\mathcal{N}\left(0, \sigma^2\right)$:

$$\sqrt{n}\left(\bar{X}_n - \mu\right) \sim \mathcal{N}\left(0, \sigma^2\right). \tag{B.6}$$

B.3 Lemma 3 of [12]

Let $(v_k)_{k\geq 0}$ and $(z_k)_{k\geq 0}$ be two sequences of square integrable vector valued random variables defined over some probability space $(\Omega, \mathcal{G}, \mathbb{P})$ and let $(\mathcal{G}_k)_{k\geq 0}$ be an increasing family of sub-σ-

algebras of $\mathcal{G}$ such that:

$$\sup_{k\geq 0}\mathbb{E}\left(\|v_k\|^2\right)\leq C<\infty,\text{ and }\lim_{N\to\infty}\sum_{k=0}^{N}\|z_k\|^2=+\infty\ w.p.1 \tag{B.7}$$

v_k and z_k are $\mathcal{G}_k$-measurable, and $\mathbb{E}\left(v_k|\mathcal{G}_{k-1}\right)=0$. Then, for any $j>0$, the following holds:

$$\lim_{N\to\infty}\frac{\sum_{k=j}^{N}v_j z_{k-j}^T}{\sum_{k=0}^{N}\|z_k\|^2}=0\ w.p.1. \tag{B.8}$$

If $\frac{1}{N}\sum_{k=0}^{N}\|z_k\|^2\leq C<\infty$, Equation (B.8) is equivalent to

$$\lim_{N\to\infty}\frac{1}{N}\sum_{k=j}^{N}v_j z_{k-j}^T=0\ w.p.1. \tag{B.9}$$

B.4 Theorem: Convergence of finite sum

Let x_n $n\in\mathbb{N}$ a random variable with $\sup_{k\geq 0}\mathbb{E}\left(\left\|x_k x_k^T\right\|^2\right)\leq C<\infty$, with $\|\cdot\|$ a p-norm $(1<p<\infty)$. Let us define a new variable with

$$X_n=\left\|\frac{1}{n}\sum_{k=n}^{n+a}x_k x_k^T\right\|,\ a\text{ constant and }<\infty. \tag{B.10}$$

Using the Chebyshev inequality, with $\varepsilon\in\mathbb{R}>0$

$$\mathbb{P}\left(|X_n|\geq\varepsilon\right)\leq\frac{\mathbb{E}\left(|X_n|^2\right)}{\varepsilon^2}, \tag{B.11}$$

using the definition of X_n

$$\begin{aligned}\mathbb{P}\left(X_n\geq\varepsilon\right)&\leq\frac{1}{\varepsilon^2}\frac{1}{n^2}\mathbb{E}\left(\left\|\sum_{k=n}^{n+a}x_k x_k^T\right\|^2\right) && \text{(B.12)}\\&\leq\frac{1}{\varepsilon^2}\frac{1}{n^2}\mathbb{E}\left(\left(\sum_{k=n}^{n+a}\left\|x_k x_k^T\right\|\right)^2\right) && \text{(B.13)}\\&\leq\frac{1}{\varepsilon^2}\frac{1}{n^2}\mathbb{E}\left(a\sum_{k=n}^{n+a}\left\|x_k x_k^T\right\|^2\right) && \text{(B.14)}\\&\leq\frac{a^2}{\varepsilon^2}\frac{1}{n^2}\sup_{k\geq 0}\mathbb{E}\left(\left\|x_k x_k^T\right\|^2\right) && \text{(B.15)}\end{aligned}$$

Consequently, using Equation (B.15)

$$\begin{aligned}\lim_{N\to\infty}\sum_{i=1}^{N}\mathbb{P}\left(X_i\geq\varepsilon\right)&\leq\lim_{N\to\infty}\sum_{i=1}^{N}\frac{a^2}{\varepsilon^2}\frac{1}{i^2}\sup_{k\geq 0}\mathbb{E}\left(\left\|x_k x_k^T\right\|^2\right) && \text{(B.16)}\\&\leq\frac{a^2}{\varepsilon^2}\sup_{k\geq 0}\mathbb{E}\left(\left\|x_k x_k^T\right\|^2\right)\sum_{i=1}^{N}\frac{1}{i^2}<\infty && \text{(B.17)}\end{aligned}$$

using the Borel-Cantelli lemma

$$\lim_{n\to\infty} X_n = \lim_{n\to\infty} \left\| \frac{1}{n} \sum_{k=n}^{n+a} x_k x_k^T \right\| = 0 \ \forall \ a \in \mathbb{N} < \infty. \tag{B.18}$$

Appendix C

MATHEMATICAL PROOFS

C.1 Proof: Convergence of $o(1)$

First using Equation (3.49)

$$S_{m,n}(N) = \hat{H}_{m,n} - \tilde{\mathbf{C}}\tilde{\mathbf{A}}^{m+n-2}\frac{1}{N}\sum_{k=0}^{N-1}\left(\tilde{\mathbf{A}} z_{k_n} z_{k_n}^T \tilde{\mathbf{C}}^T + \mathbf{B}_{k_n} v_{k_n} v_{k_n}^T \mathbf{D}_{k_n}^T\right) \tag{C.1}$$

let us prove the convergence to zero of all parts of $S_{m,n}(N)$, using Lemma 3 of [12]. $S_{m,n}(N)$ can be separated as follows

$$S_{m,n}(N) = S_{m,n\ z}(N) + S_{m,n\ v}(N) + S_{m,n\ vB}(N) + S_{m,n\ vD}(N) + S_{m,n\ w}(N). \tag{C.2}$$

First

$$S_{m,n\ v}(N) = \tilde{\mathbf{C}}\tilde{\mathbf{A}}^{m+n-2}\frac{1}{N}\sum_{k=0}^{N-1}\left(\mathbf{B}_{k_n} v_{k_n} z_{k_n}^T \tilde{\mathbf{C}}^T + \mathbf{B}_{k_n} v_{k_n} \tilde{w}_{k_n}^T\right) \tag{C.3}$$

Assuming N is a multiple of T_d, similarly to (3.53)

$$S_{m,n\ v}(N) = \tilde{\mathbf{C}}\tilde{\mathbf{A}}^{m+n-2}\frac{1}{T_d}\sum_{l=1}^{T_d}\mathbf{B}_l\frac{T_d}{N}\sum_{k_l}\left(v_{k_l} z_{k_l}^T \tilde{C}^T + v_{k_l}\tilde{w}_{k_l}^T\right), \tag{C.4}$$

where k_l denotes the indices at the same discrete time l in the period. Expressing z_{k_l} function of z_{k_l-1}

$$S_{m,n\ v}(N) = \tilde{\mathbf{C}}\tilde{\mathbf{A}}^{m+n-2}\frac{1}{T_d}\sum_{l=1}^{T_d}\mathbf{B}_l\frac{T_d}{N}\sum_{k_l}\left(v_{k_l} z_{k_l-1}^T \tilde{\mathbf{A}}^T\tilde{\mathbf{C}}^T + v_{k_l} v_{k_l-1}^T \mathbf{B}_{l-1}\tilde{\mathbf{C}}^T + v_{k_l}\tilde{w}_{k_l}^T\right). \tag{C.5}$$

v_{k_l} and z_{k_l} are square integrable random variables such that $\sup_{k\geq 0}\mathbb{E}\left(v_{k_l} v_{k_l}^T\right) \leq C < \infty$ and $\lim\limits_{N\to\infty}\frac{1}{N}\sum_{k_l}\|z_{k_l}\|^2 \leq C < \infty$ (proof in Appendix C.2). Also, they are $\mathcal{Y}_k$-measurable and $\mathbb{E}\left(v_k|\mathcal{Y}_{k-1}\right) = 0$, where $\mathcal{Y}_{k-1}$ denotes the family of variables y_0 to y_{k-1}. So using Lemma 3 of [12]

$$\lim_{N\to\infty}\tilde{\mathbf{C}}\tilde{\mathbf{A}}^{m+n-2}\frac{1}{T_d}\sum_{l=1}^{T_d}\mathbf{B}_l\frac{T_d}{N}\sum_{k_l} v_{k_l} z_{k_l-1}^T\tilde{\mathbf{A}}^T\tilde{\mathbf{C}}^T = 0. \tag{C.6}$$

v_k is a Gaussian white noise, so it is a sequence of independent variables with zero mean

$$\lim_{N\to\infty}\tilde{\mathbf{C}}\tilde{\mathbf{A}}^{m+n-2}\frac{1}{T_d}\sum_{l=1}^{T_d}\mathbf{B}_l\frac{T_d}{N}\sum_{k_l} v_{k_l} v_{k_l-1}^T\mathbf{B}_{l-1}\tilde{\mathbf{C}}^T + v_{k_l}\tilde{w}_{k_l}^T = 0. \tag{C.7}$$

Finally, leading to

$$\lim_{N\to\infty} S_{m,n\ v}(N) = 0. \tag{C.8}$$

Secondly, following the same steps as above,

$$\begin{aligned} S_{m,n\ vB}(N) = \frac{1}{N}\sum_{k=0}^{N-1}\sum_{j=1}^{m+n-2} \tilde{\mathbf{C}}\tilde{\mathbf{A}}^{j-1}\Big(&\mathbf{B}_{k_m-j}v_{k_m-j}z_{k_n}^T\tilde{\mathbf{C}}^T + \mathbf{B}_{k_m-j}v_{k_m-j}v_{k_n}^T\mathbf{D}_{k_n}^T \\ &+\mathbf{B}_{k_m-j}v_{k_m-j}\tilde{w}_{k_n}^T\Big). \end{aligned} \tag{C.9}$$

Leading to

$$S_{m,n\ vB}(N) = \frac{1}{N}\sum_{j=1}^{m+n-2}\sum_{k=0}^{N-1} \tilde{\mathbf{C}}\tilde{\mathbf{A}}^{j-1}\left(\tilde{v}_{k_m-j}z_{k_n}^T\tilde{\mathbf{C}}^T + \tilde{v}_{k_m-j}v_{k_n}^T\mathbf{D}_{k_n}^T + \tilde{v}_{k_m-j}\tilde{w}_{k_n}^T\right), \tag{C.10}$$

where $\mathbf{B}_k v_k = \tilde{v}_k$. z_{k_n} and $\tilde{v}_k$ are square integrable variables such that $\sup_{k\geq 0}\mathbb{E}\left(\tilde{v}_k\tilde{v}_k^T\right) \leq C < \infty$ and $\lim\limits_{N\to\infty}\frac{1}{N}\sum_{k_l}\|z_{k_l}\|^2 \leq C < \infty$. Also they are $\mathcal{Y}_k$-measurable and $\mathbb{E}\left(\tilde{v}_k|\mathcal{Y}_{k-1}\right) = 0$. $k_m - j > k_n$ for $1 < j < m+n-2$, so using Lemma 3 of [12]

$$\lim_{N\to\infty}\frac{1}{N}\sum_{j=1}^{m+n-2}\sum_{k=0}^{N-1} \tilde{\mathbf{C}}\tilde{\mathbf{A}}^{j-1}\left(\tilde{v}_{k_m-j}z_{k_n}^T\tilde{\mathbf{C}}^T\right) = 0. \tag{C.11}$$

v_k and $\tilde{w}_k$ are independent Gaussian process, so

$$\lim_{N\to\infty} S_{m,n\ vB}(N) = 0. \tag{C.12}$$

Following with $S_{m,n\ vD}(N)$,

$$S_{m,n\ vD}(N) = \frac{1}{N}\sum_{k=0}^{N-1}\left(\bar{v}_{k_m}z_{k_n}^T\tilde{\mathbf{C}}^T + \bar{v}_{k_m}v_{k_n}^T\mathbf{D}_{k_n}^T + \bar{v}_{k_m}\tilde{w}_{k_n}^T\right), \tag{C.13}$$

where $\bar{v}_k = \mathbf{D}_k v_k$. With the same arguments used for the previous part $\lim\limits_{N\to\infty} S_{m,n\ vD}(N) = 0$.

Continuing with $S_{m,n\ w}(N)$

$$S_{m,n\ w}(N) = \frac{1}{N}\sum_{k=0}^{N-1}\left(\tilde{w}_{k_m}z_{k_n}^T\tilde{\mathbf{C}}^T + \tilde{w}_{k_m}v_{k_n}^T\mathbf{D}_{k_n}^T + \tilde{w}_{k_m}\tilde{w}_{k_n}^T\right), \tag{C.14}$$

z_{k_n} and $\tilde{w}_{k_n}$ are square integrable variables such that $\sup_{k\geq 0}\mathbb{E}\left(\tilde{w}_k\tilde{w}_k^T\right) \leq C < \infty$, and $\lim\limits_{N\to\infty}\frac{1}{N}\sum_{k_l}\|z_{k_l}\|^2 \leq C < \infty$. Also they are $\mathcal{Y}_k$-measurable and $\mathbb{E}\left(\tilde{w}_k|\mathcal{Y}_{k-1}\right) = 0$. So using Lemma 3 of [12] (as $k_m > k_n\ \forall k$)

$$\lim_{N\to\infty}\frac{1}{N}\sum_{k=0}^{N-1}\left(\tilde{w}_{k_m}z_{k_n}^T\tilde{\mathbf{C}}^T\right) = 0. \tag{C.15}$$

Also $\tilde{w}_{k_n}$ and v_k are Gaussian white noise, so they are independent and with zero mean, thus

$$\lim_{N\to\infty} S_{m,n\ w}(N) = 0. \tag{C.16}$$

Finally,

$$S_{m,n\ z}(N) = \tilde{\mathbf{C}}\tilde{\mathbf{A}}^{m+n-2}\frac{1}{N}\sum_{k=0}^{N-1}\left(z_{k_n}v_{k_n}^T\mathbf{D}_{k_n}^T + \tilde{\mathbf{A}}z_{k_n}\tilde{w}_{k_n}^T\right), \tag{C.17}$$

expressed as function of the step $k_n - 1$

$$\begin{aligned} S_{m,n\ z}(N) = \tilde{\mathbf{C}}\tilde{\mathbf{A}}^{m+n-1}\frac{1}{N}\sum_{k=0}^{N-1} & \left(\left(\tilde{\mathbf{A}}z_{k_n-1} + \mathbf{B}_{k_n-1}v_{k_n-1}\right)v_{k_n}^T\mathbf{D}_{k_n}^T \right. \\ & \left. + \left(\tilde{\mathbf{A}}z_{k_n-1} + \mathbf{B}_{k_n-1}v_{k_n-1}\right)\tilde{w}_{k_n}^T\right). \end{aligned} \tag{C.18}$$

Using $\tilde{v}_k$ and $\bar{v}_k$,

$$S_{m,n\ z}(N) = \tilde{\mathbf{C}}\tilde{\mathbf{A}}^{m+n-1}\frac{1}{N}\sum_{k=0}^{N-1}\left(\left(\tilde{\mathbf{A}}z_{k_n-1} + \tilde{v}_{k_n-1}\right)\bar{v}_{k_n}^T + \left(\tilde{\mathbf{A}}z_{k_n-1} + \tilde{v}_{k_n-1}\right)\tilde{w}_{k_n}^T\right). \tag{C.19}$$

$\tilde{\mathbf{A}}z_{k_n-1} + \tilde{v}_{k_n-1}$, $\tilde{v}_{k_n}$ and $\tilde{w}_{k_n}$ are square integrable variables such that $\sup_{k\geq 0}\mathbb{E}\left(\tilde{w}_k\tilde{w}_k^T\right) \leq C < \infty$, $\sup_{k\geq 0}\mathbb{E}\left(\tilde{v}_k\tilde{v}_k^T\right) \leq C < \infty$ and $\lim_{N\to\infty}\frac{1}{N}\sum_{k=0}^{N-1}\|\tilde{\mathbf{A}}z_k + \tilde{v}_k\|^2 \leq C < \infty$. Also they are $\mathcal{Y}_k$-measurable, with $\mathbb{E}\left(\tilde{w}_k|\mathcal{Y}_{k-1}\right) = 0$ and $\mathbb{E}\left(\tilde{v}_k|\mathcal{Y}_{k-1}\right) = 0$. Thus, using the Lemma 3 of [12] presented in Section B.3

$$\lim_{N\to\infty} S_{m,n\ z}(1) = 0. \tag{C.20}$$

All the parts converge to zero, consequently $S_{m,n} = o(1)$ converges to zero.

C.2 Proof of the convergence of $\frac{1}{N}\sum_{k=0}^{N} z_k z_k^T$

Let us express the state vector at the index $k + T_d$ as a function of the inputs and the state vector at the index k,

$$z_{k+T_d} = \tilde{\mathbf{A}}^{T_d}z_k + \sum_{j=1}^{T_d}\tilde{\mathbf{A}}^{j-1}\mathbf{B}_{k+j-1}v_{k+j-1}. \tag{C.21}$$

Let us define the extended state vector

$$Z_k = \begin{bmatrix} z_k^T & z_{k+1}^T & \dots & z_{k+T_d-1}^T \end{bmatrix}^T \in \mathbb{R}^{\tilde{n}T_d}, \tag{C.22}$$

also the extended input vector can be defined as

$$V_k = \begin{bmatrix} v_k^T & v_{k+1}^T & \dots & v_{k+T_d-1}^T \end{bmatrix}^T \in \mathbb{R}^{mT_d}. \tag{C.23}$$

Using Equation (C.21) for any index a

$$Z_{a+T_d} = \mathbb{A}Z_a + \mathbb{B}V_a, \tag{C.24}$$

with

$$\mathbb{A} = \begin{bmatrix} \tilde{\mathbf{A}}^{T_d} & 0 & \dots & 0 \\ 0 & \tilde{\mathbf{A}}^{T_d} & \dots & 0 \\ \vdots & \vdots & \ddots & \vdots \\ 0 & \dots & & \tilde{\mathbf{A}}^{T_d} \end{bmatrix} \text{ and } \mathbb{B} = \begin{bmatrix} \tilde{A}^{T_d-1}\mathbf{B}_a & \tilde{A}^{T_d-2}\mathbf{B}_{a+1} & \dots & \mathbf{B}_{a+T_d-1} \\ \tilde{A}^{T_d-1}\mathbf{B}_{a+1} & \tilde{A}^{T_d-2}\mathbf{B}_{a+2} & \dots & \mathbf{B}_a \\ \vdots & \vdots & \ddots & \vdots \\ \tilde{A}^{T_d-1}\mathbf{B}_{a+T_d-1} & \tilde{A}^{T_d-2}\mathbf{B}_a & \dots & \mathbf{B}_{a+T_d-2} \end{bmatrix}. \tag{C.25}$$

From Equation (C.24), it is possible to express an LTI relation

$$Z_{K+1} = \mathbb{A}Z_K + \mathbb{B}V_K, \tag{C.26}$$

where

$$Z_K = \begin{bmatrix} z^T_{a+KT_d} & z^T_{a+KT_d+1} & \dots & z^T_{a+KT_d+T_d-1} \end{bmatrix}^T, \tag{C.27}$$

and similarly for V_K. In other words, the new index K denotes the period index and a the initial index in the vector Z_0. Equation (C.26) defines an LTI-system of size $\tilde{n}T_d$ where the matrix $\mathbb{B}$ had a lines arrangement depending of a, thus,

$$\lim_{\tilde{N}\to\infty} \frac{1}{\tilde{N}} \sum_{K=0}^{\tilde{N}} Z_K Z_K^T = \mathbb{E}\left(Z_K Z_K^T\right). \tag{C.28}$$

To prove that $\frac{1}{N}\sum_{k=0}^{N} z_k z_k^T$ converges, Equation (C.28) will be used. First,

$$Z_K Z_k^T = \sum_{l=0}^{T_d-1} z_{a+KT_d+l} z^T_{a+KT_d+l}. \tag{C.29}$$

Consequently,

$$\frac{1}{\tilde{N}} \sum_{K=0}^{\tilde{N}} Z_k Z_k^T = \frac{1}{\tilde{N}} \sum_{K=0}^{\tilde{N}} \sum_{l=0}^{T_d-1} z_{a+KT_d+l} z^T_{a+KT_d+l} \tag{C.30}$$

$$= T_d \frac{1}{N} \sum_{k=0}^{N} z_{a+k} z^T_{a+k}, \text{ with } N = T_d\tilde{N}, \tag{C.31}$$

as $\frac{1}{\tilde{N}}\sum_{K=0}^{\tilde{N}} Z_k Z_k^T$ converges, $\frac{1}{N}\sum_{k=0}^{N} z_{a+k} z^T_{a+k}$ also converges. Now let us prove that it converges to the same limit $\forall a > 0$. Let us define $a' \neq a$, so

$$\frac{1}{N}\sum_{k=0}^{N} z_{a+k} z^T_{a+k} - \frac{1}{N}\sum_{k=0}^{N} z_{a'+k} z^T_{a'+k} = \begin{cases} \dfrac{1}{N}\left(\displaystyle\sum_{k=N+a'}^{N+a} z_k z_k^T - \sum_{k=a'}^{a} z_k z_k^T\right), \ a > a' \\ \dfrac{1}{N}\left(-\displaystyle\sum_{k=N+a}^{N+a'} z_k z_k^T + \sum_{k=a}^{a'} z_k z_k^T\right), \ a < a' \end{cases}. \tag{C.32}$$

$\sup_{k\geq 0} \mathbb{E}\left(\|z_k z_k^T\|^2\right) \leq C < \infty$, consequently, using the Chebyshev inequality and the Borel-Cantelli lemma

$$\lim_{N\to\infty} \left(\frac{1}{N}\sum_{k=0}^{N} z_{a+k} z^T_{a+k} - \frac{1}{N}\sum_{k=0}^{N} z_{a'+k} z^T_{a'+k}\right) = 0 \tag{C.33}$$

Finally, $\frac{1}{N}\sum_{k=0}^{N} z_{a+k} z_{a+k}^{T}$ converges to the same limit $\forall a \geq 0$.

Appendix D

PROOF: MOMENTS AND ACCELERATIONS COUPLING WITH SSI

The objective is to prove that bending moments can be used with other quantities such as displacements, velocities, or accelerations as data in the SSI method.

First let us recall the state-space model and the system matrices

$$\begin{cases} x_{k+1} = \mathbf{A}x_k + \mathbf{B}\mathbf{v}_k \\ y_k = \mathbf{C}x_k + \mathbf{D}\mathbf{v}_k \end{cases}, \tag{D.1}$$

where the observation matrix is defined as

$$\mathbf{C} = \begin{bmatrix} C_d - C_a\mathcal{M}^{-1}\mathcal{K} & C_v - C_a\mathcal{M}^{-1}\mathcal{C} \end{bmatrix} \in \mathbb{R}^{r\times n}. \tag{D.2}$$

Where C_a,C_v and C_d are the selection matrices of the degrees of freedom corresponding to the different outputs, respectively for the acceleration, velocity and displacement associated with the observations

$$y(t) = C_a \frac{d^2\ u(t)}{dt^2} + C_v \frac{d\ u(t)}{dt} + C_d u(t) \in \mathbb{R}^r. \tag{D.3}$$

Now let us express the definition of the moments. With the Euler–Bernoulli beam theory, the bending moment is defined as

$$M_i = -EI_i \frac{\partial \theta_i}{\partial x}, \tag{D.4}$$

where E depends on the material properties, I_i depends on the geometrical properties and θ_i denotes the rotation along the axis i (x is the parameter defining the distance along the neutral axis). Also, the torsional moment is defined as

$$M_x = GJ\theta_x, \tag{D.5}$$

where G depends on the material properties, J depends on the geometrical properties and θ_x denotes the torsional angle. As in finite element modeling, a linear operator between displacements and moments T, a function of the material and geometrical properties can be defined,

$$M = Tu, \tag{D.6}$$

where M gathers all the bending moments, u the displacements of the system and T the linear operator.

From this, the observation considering the moments can be expressed as

$$y(t) = C_a \frac{d^2\ u(t)}{dt^2} + C_v \frac{d\ u(t)}{dt} + C_d u(t) + C_m T u(t), \tag{D.7}$$

where C_m denotes the selection matrix of the moments, then expressed as a function of the system matrices

$$\begin{aligned} y(t) &= (C_d + TC_m)\, u(t) + C_v \frac{d\ u(t)}{dt} + C_a \left(\mathcal{M}^{-1} v(t) - \mathcal{M}^{-1}\mathcal{C} \frac{d\ u(t)}{dt} - \mathcal{M}^{-1}\mathcal{K} u(t) \right) && \text{(D.8)} \\ &= \left(C_d + TC_m - C_a \mathcal{M}^{-1}\mathcal{K} \right) u(t) + \left(C_v - C_a \mathcal{M}^{-1}\mathcal{C} \right) \frac{d\ u(t)}{dt} + C_a \mathcal{M}^{-1} v(t) && \text{(D.9)} \\ &= \left[C_d + TC_m - C_a \mathcal{M}^{-1}\mathcal{K} \quad C_v - C_a \mathcal{M}^{-1}\mathcal{C} \right] x(t) + C_a \mathcal{M}^{-1} v(t) && \text{(D.10)} \\ &= \mathbf{C} x(t) + \mathbf{D} v(t). && \text{(D.11)} \end{aligned}$$

Comparing the new definition of the observation matrix (Equation D.10) with the reference definition (Equation D.2), there is just a new term function of u, TC_m.

Finally, let us study the identified mode shapes, depending on the type of output. With the identified mode shapes defined as $\phi_y = C\Psi$, with $r = n$ (all the DOF are measured).

$$\begin{aligned} \phi_y &= \phi \ \text{ when } \ C_d = I_n,\ C_v = 0,\ C_a = 0 \text{ and } C_m = 0 && \text{(D.12)} \\ \phi_y &= i\,[\mu]\,\phi \ \text{ when } \ C_d = 0,\ C_v = I_n,\ C_a = 0 \text{ and } C_m = 0 && \text{(D.13)} \\ \phi_y &= -\,[\mu]^2\,\phi \ \text{ when } \ C_d = 0,\ C_v = 0,\ C_a = I_n \text{ and } C_m = 0, && \text{(D.14)} \end{aligned}$$

with $[\mu]\,\phi$ the amplitude of velocities and $[\mu]^2\,\phi$ the amplitude of accelerations.

Now, with moments and accelerations together

$$\begin{aligned} \phi_y &= C_m T \phi + C_a\, [\mu]^2\, \phi && \text{(D.15)} \\ &= \begin{bmatrix} C_m T \phi \\ -C_a \mu^2 \phi \end{bmatrix} && \text{(D.16)} \end{aligned}$$

Adding moments into the data does not affect the mode shapes of the output corresponding to the accelerations. So, moments and accelerations can be used together with the SSI method and with subspace methods in general.

Appendix E

EXTRACTION OF THE IDENTIFIED EIGENMODES FROM THE STABILIZATION DIAGRAM

From the theory of the stochastic subspace identification, the system should be identified at his theoretical order. However, for a complex model or a real structure the theoretical order is unknown, so the stabilization diagram is used, which gives the values of the identified modal parameters for several orders. The next question is how to extract the model parameters of the stabilization diagram? The simplest answer is to extract the modal parameters at a specific order, but it is difficult to select the order, even more for automated identification.

Many papers propose methods to extract the modal parameters from the stabilization diagram, with most of them based on the clustering of the identified modes [106, 114, 102]. So, in this thesis the extraction method is based on the clustering of the identified modes at selected range of model order, based on the one presented in [81].

Extraction of the modal parameters of a stabilization diagram

1. Initialization of the cluster with the eigenmodes of the maximum order of the selected range.
2. Loop on the cluster, with a descending order:
   (a) For all the eigenmodes of the order compute the following distance with the existing order
   $$d = 1 - MAC + \Delta f, \tag{E.1}$$
   with the MAC is computed between the mode shape of the eigenmode and the mode shape of the cluster and Δf the relative gap between the frequency of the eigenmode and the frequency of the cluster.
   (b) If there is no distance lower than a defined minimum value (d_{min}), the eigenmodes define a new cluster.
   (c) Otherwise, the eigenmodes is added with the cluster associated with the minimum distance and a new cluster center is computed with the mean of the frequency, damping, eigenvalue and MAC between the eigenmodes of the cluster.
3. To finish, the cluster with of number of eigenmodes below a minimum values are deleted, in order to remove the eigenmodes corresponding to the noise.

Then, an example of the extraction results is presented, with the identification of the academic model of a wind turbine, presented in Section 4.3.1. In this example the range of model order is between the order 2 and 20, the minimum distance is set to $d_{min} = 0.01$ and the minimum eigenmodes per cluster is set to 2. In Figure E.1, the result of the extraction is displayed, where each bar represents a cluster with the mean frequency and the number of eigenmodes that compose the cluster.

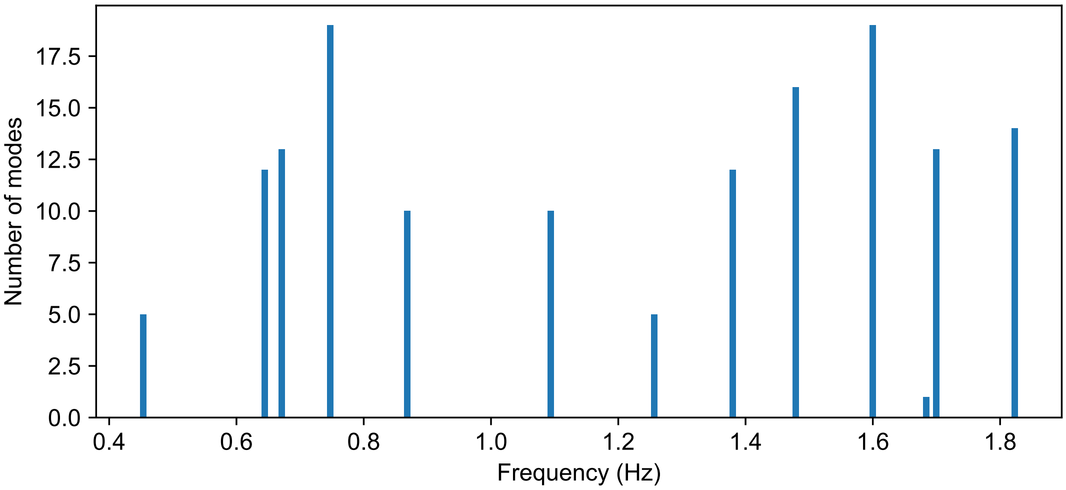

Figure E.1 – Results of the extraction of the eigenmodes of the stabilization diagram, for the identification of the academic model at a constant rotational speed

BIBLIOGRAPHY

[1] Gizem Acar and Brian F. Feeny. « Floquet-based analysis of general responses of the Mathieu equation ». In: *Journal of Vibration and Acoustics* 138.4 (2016).

[2] Saeid Allahdadian, Michael Döhler, Carlos Ventura, and Laurent Mevel. « Towards robust statistical damage localization via model-based sensitivity clustering ». In: *Mechanical Systems and Signal Processing* 134 (2019), p. 106341.

[3] Matthew S. Allen, Michael W. Sracic, Shashank Chauhan, and Morten Hartvig Hansen. « Output-only modal analysis of linear time-periodic systems with application to wind turbine simulation data ». In: *Mechanical Systems and Signal Processing* 25.4 (2011), pp. 1174–1191.

[4] Yonghui An, Eleni Chatzi, Sung-Han Sim, Simon Laflamme, Bartlomiej Blachowski, and Jinping Ou. « Recent progress and future trends on damage identification methods for bridge structures ». In: *Structural Control and Health Monitoring* 26.10 (2019), e2416.

[5] Estefania Artigao, Sergio Martín-Martínez, Andrés Honrubia-Escribano, and Emilio Gómez-Lázaro. « Wind turbine reliability: A comprehensive review towards effective condition monitoring development ». In: *Applied energy* 228 (2018), pp. 1569–1583.

[6] Onur Avci, Osama Abdeljaber, Serkan Kiranyaz, Mohammed Hussein, Moncef Gabbouj, and Daniel J. Inman. « A review of vibration-based damage detection in civil structures: From traditional methods to Machine Learning and Deep Learning applications ». In: *Mechanical Systems and Signal Processing* 147 (2021), p. 107077.

[7] Christian Bak, Frederik Zahle, Robert Bitsche, Taeseong Kim, Anders Yde, Lars Christian Henriksen, Morten Hartvig Hansen, Jose Pedro Albergaria Amaral Blasques, Mac Gaunaa, and Anand Natarajan. « The DTU 10-MW reference wind turbine ». In: *Danish wind power research 2013*. 2013.

[8] Michele Basseville. « Information criteria for residual generation and fault detection and isolation ». In: *Automatica* 33.5 (1997), pp. 783–803. ISSN: 0005-1098.

[9] Michele Basseville, Maher Abdelghani, and Albert Benveniste. « Subspace-based fault detection algorithms for vibration monitoring ». In: *Automatica* 36.1 (2000), pp. 101–109. ISSN: 0005-1098.

[10] Michèle Basseville, Laurent Mevel, and Maurice Goursat. « Statistical model-based damage detection and localization: subspace-based residuals and damage-to-noise sensitivity ratios ». In: *Journal of sound and vibration* 275.3-5 (2004), pp. 769–794.

[11] Albert Benveniste, Michele Basseville, and G. Moustakides. « The asymptotic local approach to change detection and model validation ». In: *IEEE Transactions on Automatic Control* 32.7 (1987), pp. 583–592. ISSN: 0018-9286.

[12] Albert Benveniste and Laurent Mevel. « Nonstationary consistency of subspace methods ». In: *IEEE Transactions on Automatic Control* 52.6 (2007), pp. 974–984. ISSN: 0018-9286.

[13] Gunjit Bir. « Multi-Blade Coordinate Transformation and its Application to Wind Turbine Analysis ». In: *46th AIAA Aerospace Sciences Meeting and Exhibit.* [Reston, VA]: [American Institute of Aeronautics and Astronautics], 2008. ISBN: 978-1-62410-128-1.

[14] Gunjit Bir. *User's guide to BModes (software for computing rotating Beam-coupled Modes)*. Tech. rep. National Renewable Energy Lab.(NREL), Golden, CO (United States), 2005.

[15] Marc Boeswald, Dennis Goege, Ulrich Fuellekrug, and Yves Govers. « A review of experimental modal analysis methods with respect to their applicability to test data of large aircraft structures ». In: *Proc. of the international conference on noise and vibration engineering ISMA*. 2006, pp. 2461–2482.

[16] Carlo Luigi Bottasso and Stefano Cacciola. « Model-independent periodic stability analysis of wind turbines ». In: *Wind Energy* 18.5 (2015), pp. 865–887. ISSN: 10954244.

[17] Rune Brincker and Carlos Ventura. *Introduction to operational modal analysis.* Chichester West Sussex: Wiley, 2015.

[18] Rune Brincker, Lingmi Zhang, and Palle Andersen. « Modal identification of output-only systems using frequency domain decomposition ». In: *Smart materials and structures* 10.3 (2001), p. 441.

[19] Tony Burton, David Sharpe, Nick Jenkins, and ERvin Bossanyi. *Wind energy handbook.* John Wilez And Sons, LTD, 2001.

[20] Stefano Cacciola, I. Munduate Agud, and Carlo Luigi Bottasso. « Detection of rotor imbalance, including root cause, severity and location ». In: *Journal of Physics: Conference Series.* IOP Publishing, 2016, p. 072003. ISBN: 1742-6596.

[21] Ambroise Cadoret, Enora Denimal, Jean-Marc Leroy, Jean-Lou Pfister, and Laurent Mevel. « Linear Time Invariant Approximation for Subspace Identification of Linear Periodic Systems Applied to Wind Turbines ». In: *11th IFAC Symposium on Fault Detection, Supervision and Safety for Technical Processes - SAFEPROCESS.* Pafos, Cyprus, 2022.

[22] Ambroise Cadoret, Enora Denimal, Jean-Marc Leroy, Jean-Lou Pfister, and Laurent Mevel. « Modal-Based Anisotropy Early Warning in Wind Turbine Rotor ». In: *IFAC World Congress.* Yokohama, Japan, 2023.

[23] Ambroise Cadoret, Enora Denimal, Jean-Marc Leroy, Jean-Lou Pfister, and Laurent Mevel. « Periodic System Approximation for Operational Modal Analysis of Operating Wind Turbine ». In: *EWSHM 2022 - 10th Workshop on Structural Health Monitoring.* Palermo, Italy, 2022.

[24] Ambroise Cadoret, Enora Denimal, Jean-Marc M Leroy, Jean-Lou L Pfister, and Laurent Mevel. « Mode shape phase change detection in wind turbine under anisotropy variation ». In: *ISMA 2022-International Conference on Noise and Vibration Engineering.* Leuven, Belgium, 2022.

[25] Debora Cevasco, J Tautz-Weinert, U Smolka, and A Kolios. « Feasibility of machine learning algorithms for classifying damaged offshore jacket structures using SCADA data ». In: *Journal of Physics: Conference Series*. Vol. 1669. IOP Publishing. 2020, p. 012021.

[26] Debora Cevasco, Jannis Tautz-Weinert, Mark Richmond, Adam Sobey, and AJ Kolios. « A damage detection and location scheme for offshore wind turbine jacket structures based on global modal properties ». In: *ASCE-ASME Journal of Risk and Uncertainty in Engineering Systems, Part B: Mechanical Engineering* 8.2 (2022), p. 021103.

[27] Robert P Coleman. *Theory of self-excited mechanical oscillations of hinged rotor blades.* Tech. rep. NASA, 1943.

[28] Jordan Curt, Matteo Capaldo, François Hild, and Stéphane Roux. « Modal analysis of a wind turbine tower by digital image correlation ». In: *Journal of Physics: Conference Series*. Vol. 1618. 2. IOP Publishing. 2020, p. 022002.

[29] Swagato Das, P Saha, and SK Patro. « Vibration-based damage detection techniques used for health monitoring of structures: a review ». In: *Journal of Civil Structural Health Monitoring* 6 (2016), pp. 477–507.

[30] Frederik Michel Dekking, Cornelis Kraaikamp, Hendrik Paul Lopuhaä, and Ludolf Erwin Meester. *A Modern Introduction to Probability and Statistics: Understanding why and how.* Vol. 488. Springer, 2005.

[31] Frédéric Delbos, Fabien Caleyron, and Jean-Marc Leroy. « Transfer Learning of Model-Based Neural Network for Transfer Function Inversion and Load Monitoring of Wind Turbines ». In: *Journal of Physics: Conference Series*. Vol. 2265. IOP Publishing. 2022, p. 032081.

[32] Technical University of Denmark DTU. *dtu-10mw-rwt*. `https://rwt.windenergy.dtu.dk/dtu10mw/dtu-10mw-rwt`. Accessed: 2021-06-03.

[33] Massimiliano Deon, Ilmar F. Santos, and Giuliano Coppotelli. « Application of OMA techniques to LTP systems ». In: *8th International Operational Modal Analysis Conference*. 2019, pp. 577–589.

[34] Emilio Di Lorenzo. « Operational Modal Analysis for rotating machines ». PhD thesis. University of Naples" Federico II, 2017.

[35] Emilio Di Lorenzo, S Manzato, B Peeters, V Ruffini, and MM Luczak. « Modal analysis of wind turbine blades with different test setup configurations ». In: *Topics in Modal Analysis & Testing, Volume 8: Proceedings of the 37th IMAC, A Conference and Exposition on Structural Dynamics 2019*. Springer. 2020, pp. 143–152.

[36] Emilio Di Lorenzo, Simone Manzato, BART Peeters, and Francesco Marulo, eds. *Modal Parameter Estimation for Operational Wind Turbines*. 2014.

[37] Emilio Di Lorenzo, Simone Manzato, BART Peeters, Frederik Vanhollebeke, Wim Desmet, and Francesco Marulo. « Order-Based Modal Analysis: a modal parameter estimation technique for rotating machineries ». In: *6th International Operational Modal Analysis Conference Proceedings*. EDICIONES UNIV OVIEDO, 2015, pp. 325–332. ISBN: 8416046808.

[38] Nikolay Dimitrov and Anand Natarajan. « From SCADA to lifetime assessment and performance optimization: how to use models and machine learning to extract useful insights from limited data ». In: *Journal of Physics: Conference Series*. Vol. 1222. IOP Publishing. 2019, p. 012032.

[39] Michael Döhler, Falk Hille, Laurent Mevel, and Werner Rücker. « Structural health monitoring with statistical methods during progressive damage test of S101 Bridge ». In: *Engineering Structures* 69 (2014), pp. 183–193.

[40] Michael Döhler and Laurent Mevel. « Efficient multi-order uncertainty computation for stochastic subspace identification ». In: *Mechanical Systems and Signal Processing* 38.2 (2013), pp. 346–366.

[41] Michael Döhler and Laurent Mevel. « Fast multi-order computation of system matrices in subspace-based system identification ». In: *Control Engineering Practice* 20.9 (2012), pp. 882–894. ISSN: 0967-0661.

[42] Michael Döhler, Laurent Mevel, and Falk Hille. « Subspace-based damage detection under changes in the ambient excitation statistics ». In: *Mechanical Systems and Signal Processing* 45.1 (2014), pp. 207–224.

[43] Michael Döhler, Laurent Mevel, and Qinghua Zhang. « Fault detection, isolation and quantification from Gaussian residuals with application to structural damage diagnosis ». In: *Annual Reviews in Control* 42 (2016), pp. 244–256. ISSN: 1367-5788.

[44] Ying Du, Shengxi Zhou, Xingjian Jing, Yeping Peng, Hongkun Wu, and Ngaiming Kwok. « Damage detection techniques for wind turbine blades: A review ». In: *Mechanical Systems and Signal Processing* 141 (2020), p. 106445.

[45] R. Ernst, P. Lauridsen, C. Klein, and B. Buffetti. « The effect of damage position on Operational Modal Analysis of wind turbine blades for SHM ». In: *Journal of Physics: Conference Series*. IOP Publishing, 2022, p. 032099. ISBN: 1742-6596.

[46] Wind Europe. *Wind energy in Europe: 2022 Statistics and the outlook for 2023-2027*. 2022.

[47] David J Ewins. *Modal testing: theory, practice and application*. John Wiley & Sons, 2009.

[48] Elia Favarelli and Andrea Giorgetti. « Machine learning for automatic processing of modal analysis in damage detection of bridges ». In: *IEEE Transactions on Instrumentation and Measurement* 70 (2020), pp. 1–13. ISSN: 0018-9456.

[49] Gaston Floquet. « Sur la théorie des équations différentielles linéaires ». In: *Annales Scientifiques de L'École Normale Supérieure*. Vol. 8. 1879, pp. 3–132.

[50] David García Cava, Luis David Avendaño-Valencia, Artur Movsessian, Callum Roberts, and Dmitri Tcherniak. « On explicit and implicit procedures to mitigate environmental and operational variabilities in data-driven structural health monitoring ». In: *Structural Health Monitoring Based on Data Science Techniques*. Springer, 2022, pp. 309–330.

[51] Guillaume Gautier, Laurent Mevel, Jean-Mathieu Mencik, Roger Serra, and Michael Döhler. « Variance analysis for model updating with a finite element based subspace fitting approach ». In: *Mechanical Systems and Signal Processing* 91 (2017), pp. 142 –156.

[52] Guillaume Gautier, Roger Serra, and J-M Mencik. « Vibratory diagnosis by finite element model updating and operational modal analysis ». In: *Mechanics & Industry* 14.2 (2013), pp. 145–149.

[53] Szymon Gres. « Vibration-based monitoring of structures: Algorithms for fault detection and uncertainty quantification of modal indicators ». PhD thesis. Aalborg Universitetsforlag, 2019.

[54] Szymon Greś, Michael Döhler, Palle Andersen, and Laurent Mevel. « Kalman filter-based subspace identification for operational modal analysis under unmeasured periodic excitation ». In: *Mechanical Systems and Signal Processing* 146 (2021), p. 106996.

[55] Szymon Greś, Michael Döhler, Palle Andersen, and Laurent Mevel. « Uncertainty quantification for the Modal Phase Collinearity of complex mode shapes ». In: *Mechanical Systems and Signal Processing* 152 (2021), p. 107436.

[56] Szymon Greś, Michael Döhler, Niels-Jørgen Jacobsen, and Laurent Mevel. « Uncertainty quantification of input matrices and transfer function in input/output subspace system identification ». In: *Mechanical Systems and Signal Processing* 167 (2022), p. 108581.

[57] Szymon Greś, Michael Döhler, and Laurent Mevel. « Statistical model-based optimization for damage extent quantification ». In: *Mechanical Systems and Signal Processing* 160 (2021), p. 107894.

[58] Szymon Greś, Michael Döhler, and Laurent Mevel. « Uncertainty quantification of the Modal Assurance Criterion in operational modal analysis ». In: *Mechanical Systems and Signal Processing* 152 (2021), p. 107457.

[59] Szymon Gres, Alexander Mendler, Niels-Jørgen Jacobsen, Palle Andersen, and Michael Döhler. « Statistical damage detection and localization with Mahalanobis distance applied to modal parameters ». In: *IOMAC 2022-9th International Operational Modal Analysis Conference*. 2022.

[60] Patrick Guillaume, Peter Verboven, and Steve Vanlanduit. « Frequency-domain maximum likelihood identification of modal parameters with confidence intervals ». In: *Proceedings of the international seminar on modal analysis*. Vol. 1. Katholieke Universiteit Leuven. 1998, pp. 359–366.

[61] Martin Otto Laver Hansen, Jens Nørkær Sørensen, S. Voutsinas, Niels Sørensen, and H. Aa Madsen. « State of the art in wind turbine aerodynamics and aeroelasticity ». In: *Progress in aerospace sciences* 42.4 (2006), pp. 285–330. ISSN: 0376-0421.

[62] Morten H. Hansen. « Aeroelastic instability problems for wind turbines ». In: *Wind Energy* 10.6 (2007), pp. 551–577. ISSN: 10954244.

[63] Morten Hartvig Hansen. « Improved modal dynamics of wind turbines to avoid stall–induced vibrations ». In: *Wind Energy* 6.2 (2003), pp. 179–195. ISSN: 10954244.

[64] Morten Hartvig Hansen. « Modal dynamics of structures with bladed isotropic rotors and its complexity for two-bladed rotors ». In: *Wind Energy Science* 1.2 (2016), pp. 271–296.

[65] Morten Hartvig Hansen and Lars Christian Henriksen. « Basic DTU wind energy controller ». In: *DTU Wind Energy E No. 0028* (2013).

[66] Erich Hau. *Wind turbines: fundamentals, technologies, application, economics.* Springer Science & Business Media, 2013.

[67] Guilherme R. Hübner, H. Pinheiro, C. E. de Souza, C. M. Franchi, L. D. Da Rosa, and J. P. Dias. « Detection of mass imbalance in the rotor of wind turbines using Support Vector Machine ». In: *Renewable Energy* 170 (2021), pp. 49–59. ISSN: 0960-1481.

[68] George H James III, Thomas G Carne, and James P Lauffer. *The natural excitation technique (NExT) for modal parameter extraction from operating wind turbines.* Tech. rep. Sandia National Labs., Albuquerque, NM (United States), 1993.

[69] Ahmed Jhinaoui. « Subspace-based identification and vibration monitoring algorithms for rotating systems ». PhD thesis. Université Rennes 1, 2014.

[70] Ahmed Jhinaoui, Laurent Mevel, and Joseph Morlier. « A new SSI algorithm for LPTV systems: Application to a hinged-bladed helicopter ». In: *Mechanical Systems and Signal Processing* 42.1-2 (2014), pp. 152–166.

[71] Ahmed Jhinaoui, Laurent Mevel, and Joseph Morlier. « Extension of Subspace Identification to LPTV Systems: Application to Helicopters ». In: *Topics in Modal Analysis I, Volume 5.* Ed. by R. Allemang, J. de Clerck, C. Niezrecki, and J. R. Blough. Conference Proceedings of the Society for Experimental Mechanics Series. New York, NY: Springer New York and Imprint: Springer, 2012, pp. 425–433. ISBN: 978-1-4614-2425-3.

[72] Ahmed Jhinaoui, Laurent Mevel, and Joseph Morlier. « Subspace instability monitoring for linear periodically time-varying systems ». In: *IFAC Proceedings Volumes* 45.16 (2012), pp. 380–385. ISSN: 1474-6670.

[73] Ahmed Jhinaoui, Laurent Mevel, and Joseph Morlier. « Uncertainties quantification for subspace identification of rotating systems ». In: *IFAC Proceedings Volumes* 46.12 (2013), pp. 35–40. ISSN: 1474-6670.

[74] Bonnie J Jonkman. *Turbsim user's guide v2. 00.00.* Tech. rep. National Renewable Energy Lab.(NREL), Golden, CO (United States), 2014.

[75] Jason M Jonkman and Bonnie J Jonkman. « FAST modularization framework for wind turbine simulation: full-system linearization ». In: *Journal of Physics: Conference Series.* Vol. 753. IOP Publishing. 2016, p. 082010.

[76] Jer-Nan Juang and Richard S Pappa. « An eigensystem realization algorithm for modal parameter identification and model reduction ». In: *Journal of guidance, control, and dynamics* 8.5 (1985), pp. 620–627.

[77] Panida Kaewniam, Maosen Cao, Nizar Faisal Alkayem, Dayang Li, and Emil Manoach. « Recent advances in damage detection of wind turbine blades: A state-of-the-art review ». In: *Renewable and Sustainable Energy Reviews* 167 (2022), p. 112723.

[78] J C Kaimal, JCJ Wyngaard, Y Izumi, and OR Coté. « Spectral characteristics of surface-layer turbulence ». In: *Quarterly Journal of the Royal Meteorological Society* 98.417 (1972), pp. 563–589.

[79] Josh Kusnick, Douglas E. Adams, and D. Todd Griffith. « Wind turbine rotor imbalance detection using nacelle and blade measurements ». In: *Wind Energy* 18.2 (2015), pp. 267–276. ISSN: 10954244.

[80] Dongsheng Li, Siu-Chun M Ho, Gangbing Song, Liang Ren, and Hongnan Li. « A review of damage detection methods for wind turbine blades ». In: *Smart Materials and Structures* 24.3 (2015), p. 033001.

[81] Filipe Magalhães, Álvaro Cunha, and Elsa Caetano. « Online automatic identification of the modal parameters of a long span arch bridge ». In: *Mechanical Systems and Signal Processing* 23.2 (2009), pp. 316–329.

[82] Hassan Malekzehtab and Ali A Golafshani. « Damage detection in an offshore jacket platform using genetic algorithm based finite element model updating with noisy modal data ». In: *Procedia Engineering* 54 (2013), pp. 480–490.

[83] Philippe Mellinger. « Estimation d'incertitudes d'identification modale avec et sans entrées connues: théorie, validation, application ». PhD thesis. Université Rennes 1, 2014.

[84] Philippe Mellinger, Michael Döhler, and Laurent Mevel. « Variance estimation of modal parameters from output-only and input/output subspace-based system identification ». In: *Journal of Sound and Vibration* 379 (2016), pp. 1–27.

[85] Alexander Mendler. « Minimum diagnosable damage and optimal sensor placement for structural health monitoring ». PhD thesis. University of British Columbia, 2020.

[86] Alexander Mendler, Michael Döhler, Carlos Ventura, and Laurent Mevel. « Clustering of Redundant Parameters for Fault Isolation with Gaussian Residuals ». In: *IFAC 2020 - 21st International Federation of Automatic Control World Congress*. Berlin, Germany, July 2020.

[87] Alexander Mendler, Michael Döhler, and Carlos E. Ventura. « A reliability-based approach to determine the minimum detectable damage for statistical damage detection ». In: *Mechanical Systems and Signal Processing* 154 (2021), p. 107561.

[88] Boualem Merainani, Bian Xiong, Vincent Baltazart, Jean Dumoulin, Michael Döhler, and Qinghua Zhang. « Experimental investigation of structural modal identification using pixels intensity and motion signals from video-based imaging devices: performance, comparison and analysis ». In: *SPIE Optical Metrology 2021*. Virtual, United States: SPIE, June 2021.

[89] Leon Mishnaevsky Jr, Charlotte Bay Hasager, Christian Bak, Anna-Maria Tilg, Jakob I Bech, Saeed Doagou Rad, and Søren Fæster. « Leading edge erosion of wind turbine blades: Understanding, prevention and protection ». In: *Renewable Energy* 169 (2021), pp. 953–969.

[90] Artur Movsessian, David Garcia Cava, and Dmitri Tcherniak. « An artificial neural network methodology for damage detection: Demonstration on an operating wind turbine blade ». In: *Mechanical Systems and Signal Processing* 159 (2021), p. 107766.

[91] Noah Myrent, Douglas E Adams, and D Todd Griffith. « Wind turbine blade shear web disbond detection using rotor blade operational sensing and data analysis ». In: *Philosophical Transactions of the Royal Society A: Mathematical, Physical and Engineering Sciences* 373.2035 (2015), p. 20140345.

[92] Météo-France. *Observations en mer.* `https://donneespubliques.meteofrance.fr/?fond=produit&id_produit=95&id_rubrique=32`. Accessed: 2022-04-27.

[93] Jenny Niebsch, Ronny Ramlau, and Thien T. Nguyen. « Mass and aerodynamic imbalance estimates of wind turbines ». In: *Energies* 3.4 (2010), pp. 696–710.

[94] National Renewable Energy Laboratory NREL. *OpenFAST v2.5.0.* `https://github.com/OpenFAST/openfast/releases/tag/v2.5.0`. Accessed: 2021-06-03.

[95] Gary W Oehlert. « A note on the delta method ». In: *The American Statistician* 46.1 (1992), pp. 27–29.

[96] Gustavo Oliveira, Filipe Magalhães, Álvaro Cunha, and Elsa Caetano. « Continuous dynamic monitoring of an onshore wind turbine ». In: *Engineering Structures* 164 (2018), pp. 22–39.

[97] Gustavo Oliveira, Filipe Magalhães, Álvaro Cunha, and Elsa Caetano. « Vibration-based damage detection in a wind turbine using 1 year of data ». In: *Structural Control and Health Monitoring* 25.11 (2018), e2238. ISSN: 15452255.

[98] Miroslav Pastor, Michal Binda, and Tomáš Harčarik. « Modal Assurance Criterion ». In: *Procedia Engineering* 48 (2012), pp. 543–548. ISSN: 1877-7058.

[99] Bart Peeters and Guido de Roeck. « Reference-based stochastic subspace identification for output-only modal analysis ». In: *Mechanical Systems and Signal Processing* 13.6 (1999), pp. 855–878.

[100] Bart Peeters and Herman van der Auweraer. « PolyMax: a revolution in operational modal analysis ». In: *1st International Operational Modal Analysis Conference* (2005).

[101] Principia and IFP énergies nouvelles. *Deeplines V5.5.* 2020.

[102] Johann Priou, Szymon Gres, Matthieu Perrault, Laurent Guerineau, and Michael Döhler. « Automated uncertainty-based extraction of modal parameters from stabilization diagrams ». In: *IOMAC 2022-9th International Operational Modal Analysis Conference.* 2022.

[103] Kevin Qu, David Garcia Cava, Stuart Killbourn, and Alasdair Logan. « Operational modal analysis for scour detection in mono-pile offshore wind turbines ». In: *European Workshop on Structural Health Monitoring: EWSHM 2022-Volume 2.* Springer. 2022, pp. 668–678.

[104] Oscar Ramirez Requeson, Dmitri Tcherniak, and Gunner Chr Larsen, eds. *Comparative study of OMA applied to experimental and simulated data from an operating Vestas V27 wind turbine.* 2015.

[105] Edwin Reynders. « System identification methods for (operational) modal analysis: review and comparison ». In: *Archives of Computational Methods in Engineering* 19 (2012), pp. 51–124.

[106] Edwin Reynders, Jeroen Houbrechts, and Guido De Roeck. « Fully automated (operational) modal analysis ». In: *Mechanical systems and signal processing* 29 (2012), pp. 228–250.

[107] Edwin Reynders, Kristof Maes, Geert Lombaert, and Guido de Roeck. « Uncertainty quantification in operational modal analysis with stochastic subspace identification: Validation and applications ». In: *Mechanical Systems and Signal Processing* 66-67 (2016), pp. 13–30.

[108] Edwin Reynders, Rik Pintelon, and Guido de Roeck. « Uncertainty bounds on modal parameters obtained from stochastic subspace identification ». In: *Mechanical Systems and Signal Processing* 22.4 (2008), pp. 948–969.

[109] Edwin Reynders and Guido de Roeck. « Reference-based combined deterministic–stochastic subspace identification for experimental and operational modal analysis ». In: *Mechanical Systems and Signal Processing* 22.3 (2008), pp. 617–637.

[110] Riccardo Riva. « Stability Analysis of Wind Turbines through System Identification Techniques ». PhD thesis. Politecnico di Milano, 2017.

[111] Riccardo Riva, Stefano Cacciola, and Carlo Bottasso. « Periodic stability analysis of wind turbines operating in turbulent wind conditions ». In: *Wind Energy Science* 1 (2016), pp. 177–203.

[112] Callum Roberts, David Garcia Cava, and Luis David Avendaño-Valencia. « Understanding the influence of environmental and operational variability on wind turbine blade monitoring ». In: *European Workshop on Structural Health Monitoring: Special Collection of 2020 Papers-Volume 1*. Springer. 2020, pp. 109–118.

[113] J Ros, A Olcoz, and A Plaza. « Along-the-path exponential integration for Floquet stability analysis of wind turbines ». In: *Journal of Physics: Conference Series*. Vol. 2265. IOP Publishing. 2022, p. 032026.

[114] João Santos, Christian Crémona, and Paulo Silveira. « Automatic Operational Modal Analysis of Complex Civil Infrastructures ». In: *Structural Engineering International* 30.3 (2020), pp. 365–380. ISSN: 1016-8664.

[115] Brian J Schwarz and Mark H Richardson. « Experimental modal analysis ». In: *CSI Reliability week* 35.1 (1999), pp. 1–12.

[116] S. Sinha, R. Pandiyan, and J. Bibb. « Liapunov-Floquet Transformation: Computation and Applications to Periodic Systems ». In: *Journal of Vibration and Acoustics* 118 (1996).

[117] Peter Fisker Skjoldan. « Aeroelastic modal dynamics of wind turbines including anisotropic effects ». PhD thesis. Danmarks Tekniske Universitet, Risø Nationallaboratoriet for Bæredygtig Energi, 2011.

[118] Peter Fisker Skjoldan and Morten Hartvig Hansen. « Implicit Floquet analysis of wind turbines using tangent matrices of a non–linear aeroelastic code ». In: *Wind Energy* 15.2 (2012), pp. 275–287. ISSN: 10954244.

[119] Peter Fisker Skjoldan and Morten Hartvig Hansen. « On the similarity of the Coleman and Lyapunov–Floquet transformations for modal analysis of bladed rotor structures ». In: *Journal of Sound and Vibration* 327.3 (2009), pp. 424–439.

[120] Andrea Staino and Biswajit Basu. « Dynamics and control of vibrations in wind turbines with variable rotor speed ». In: *Engineering Structures* 56 (2013), pp. 58–67.

[121] Andrea Staino, Biswajit Basu, and S.R.K. Nielsen. « Actuator control of edgewise vibrations in wind turbine blades ». In: *Sound and vibration* 331.6 (2012), pp. 1233–1256. ISSN: 0022-460X.

[122] IEC Standard. *61400-1; WindTurbines—Part 1: Design requirements.* 2005.

[123] Karl Stol, Hans-Georg Moll, Gunjit Bir, and Hazim Namik. « A comparison of multiblade coordinate transformation and direct periodic techniques for wind turbine control design ». In: *47th AIAA Aerospace Sciences Meeting including The New Horizons Forum and Aerospace Exposition.* 2009, p. 479.

[124] Jannis Tautz-Weinert and Simon J Watson. « Using SCADA data for wind turbine condition monitoring–a review ». In: *IET Renewable Power Generation* 11.4 (2017), pp. 382–394.

[125] Dmitri Tcherniak. « Detection and identification of a damaged blade using only a tower sensor, without stopping the wind turbine ». In: *Proceedings of ISMA2016 including USD2016.* 2016.

[126] Dmitri Tcherniak. « Rotor anisotropy as a blade damage indicator for wind turbine structural health monitoring systems ». In: *Mechanical Systems and Signal Processing* 74 (2016), pp. 183–198.

[127] Dmitri Tcherniak, Shashank Chauhan, and Morten Hartvig Hansen. « Applicability limits of operational modal analysis to operational wind turbines ». In: *Structural Dynamics and Renewable Energy, Volume 1.* Springer, 2011, pp. 317–327.

[128] Dmitri Tcherniak and Gunner Chr Larsen, eds. *Application of OMA to an Operating Wind Turbine: now including Vibration Data from the Blades.* 2013.

[129] Dmitri Tcherniak and Lasse L Mølgaard. « Active vibration-based structural health monitoring system for wind turbine blade: Demonstration on an operating Vestas V27 wind turbine ». In: *Structural Health Monitoring* 16.5 (2017), pp. 536–550.

[130] Dmitri Tcherniak, S Yang, and Matthew S. Allen. « Experimental characterization of operating bladed rotor using harmonic power spectra and stochastic subspace identification ». In: *Proc. International Conference on Noise and Vibration Engineering (ISMA).* 2014.

[131] Martin D Ulriksen, Dmitri Tcherniak, and Lars Damkilde. « Damage detection in an operating Vestas V27 wind turbine blade by use of outlier analysis ». In: *2015 IEEE Workshop on Environmental, Energy, and Structural Monitoring Systems (EESMS) Proceedings*. IEEE. 2015, pp. 50–55.

[132] Martin Dalgaard Ulriksen. « Damage Localization for Structural Health Monitoring: An Exploration of Three New Vibration-based Schemes ». PhD thesis. Aalborg Universitetsforlag: Aalborg Universitetsforlag, 2018.

[133] Gijsbrecht Jan van der Veen. « Identification of wind energy systems ». PhD thesis. Delft University of Technology, 2013.

[134] Peter van Overschee and B. L. de Moor. *Subspace identification for linear systems: Theory—Implementation—Applications*. Springer Science & Business Media, 2012. ISBN: 1461304652.

[135] Peter van Overschee and Bart de Moor. « Subspace algorithms for the stochastic identification problem ». In: *Automatica* 29.3 (1993), pp. 649–660. ISSN: 0005-1098.

[136] Eva Viefhues, Michael Döhler, Falk Hille, and Laurent Mevel. « Statistical subspace-based damage detection with estimated reference ». In: *Mechanical Systems and Signal Processing* 164 (2022), p. 108241.

[137] Aemilius AW van Vondelen, Sachin T Navalkar, Alexandros Iliopoulos, Daan C van der Hoek, and Jan-Willem van Wingerden. « Damping identification of offshore wind turbines using operational modal analysis: a review ». In: *Wind Energy Science* 7.1 (2022), pp. 161–184.

[138] Gustavo B. Wagner, Damien Foiny, Rubens Sampaio, and Roberta Lima, eds. *Operational modal analysis under wind load using stochastic sub-space identification*. 2017.

[139] Wout Weijtjens, Tim Verbelen, Emanuele Capello, and Christof Devriendt. « Vibration based structural health monitoring of the substructures of five offshore wind turbines ». In: *Procedia engineering* 199 (2017), pp. 2294–2299.

[140] Wout Weijtjens, Tim Verbelen, Gert de Sitter, and Christof Devriendt. « Foundation structural health monitoring of an offshore wind turbine—a full-scale case study ». In: *Structural Health Monitoring: An International Journal* 15.4 (2016), pp. 389–402. ISSN: 1475-9217.

[141] Peter Welch. « The use of fast Fourier transform for the estimation of power spectra: a method based on time averaging over short, modified periodograms ». In: *IEEE Transactions on audio and electroacoustics* 15.2 (1967), pp. 70–73.

[142] Norman M. Wereley. « Analysis and control of linear periodically time varying systems ». PhD thesis. Massachusetts Institute of Technology, 1990.

[143] Norman M. Wereley and Steven R. Hall. « Linear time periodic systems: transfer function, poles, transmission zeroes and directional properties ». In: *American Control Conference*. IEEE, 1991, pp. 1179–1184. ISBN: 0879425652.

[144] B Wondra, J Rupfle, A Emiroglu, and CU Grosse. « Analysis of Icing on Wind Turbines by Combined Wireless and Wired Acceleration Sensor Monitoring ». In: *European Workshop on Structural Health Monitoring: EWSHM 2022-Volume 1*. Springer. 2022, pp. 143–155.

[145] Yong Xia, Bo Chen, Shun Weng, Yi-Qing Ni, and You-Lin Xu. « Temperature effect on vibration properties of civil structures: a literature review and case studies ». In: *Journal of civil structural health monitoring* 2 (2012), pp. 29–46.

[146] Shifei Yang, Dmitri Tcherniak, and Matthew S. Allen. « Modal analysis of rotating wind turbine using multiblade coordinate transformation and harmonic power spectrum ». In: *Topics in Modal Analysis I, Volume 7*. Springer, 2014, pp. 77–92.

COLLEGE DOCTORAL BRETAGNE
MATHS, TELECOMS
INFORMATIQUE, SIGNAL
SYSTEMES, ELECTRONIQUE

Université de Rennes

Titre : Analyse modale opérationnelle pour le suivi de santé structurelle des éoliennes

Mots clés : Vibrations et analyse modale, Méthodes Sous-espaces, Détection de défaut, Éoliennes

Résumé : Dans cette thèse, l'objectif est de surveiller une éolienne sans avoir à l'arrêter ni à interférer avec son fonctionnement. Ainsi, le problème de la surveillance des éoliennes par analyse modale opérationnelle est traité. Le défi principal provient du fait qu'une éolienne en rotation entraine un caractère périodique au système, ce qui empêche l'utilisation des méthodes d'identification des modes propres définie pour des structures temporellement invariantes telles que celles de génie civil.

Pour permettre l'identification des modes propres des systèmes périodiques, une étude de la dynamique des éoliennes en rotation est réalisée. Ainsi, basée, sur cette étude, une approximation des modes propres des éoliennes en rotation est définie, où ces modes propres sont définis comme une somme de modes propres d'une structure invariante.

Par la suite, il est démontré théoriquement que les méthodes d'identification sous espaces existantes peuvent identifier correctement l'approximation définie précédemment. Puis validé avec différents exemples d'identifications utilisant des données simulées à partir de modèles d'éoliennes.

Pour conclure le travail, la détection de défaut du rotor est traitée, en utilisant des mesures du rotor ou bien de la tour. Pour ces deux cas, les paramètres obtenus par identification les plus sensibles aux défauts sont recherchés et utilisés pour adapter une méthode de détection de défaut de l'état de l'art. Pour les deux situations, il a été possible de détecter une baisse de raideur d'une pale et de déterminer la pale endommagée lorsque des mesures du rotor sont utilisées.

Title: Operational Modal Analysis (OMA) for wind turbines health monitoring

Keywords: Vibration and modal analysis, Subspace methods, Damage detection, Wind turbines

Abstract: In this thesis, the objective is to monitor the wind turbine without stopping or interfering with its operation. So, the monitoring of operating wind turbines with Operational Modal Analysis is studied. The main challenge is the periodic behavior of a wind turbine, which prevent the use of the eigenmodes identification methods from the literature, defined for time invariant structures such as civil engineering ones.

To enable the identification of the periodic system eigenmodes, a study of the dynamical behavior of the rotating wind turbine is carried on. Thus, an approximation of the rotating wind turbine eigenmodes is defined, where those eigenmodes are expressed as a sum of invariant system eigenmodes.

Afterward, it is theoretically demonstrated that the existing subspace identification methods can correctly identify the previously defined approximation. Then, it is validated with different examples of identification using data computed with wind turbine models.

To complete the work, damage detection of the rotor of a wind turbine is treated using rotor or tower measurements. For both cases, the most damage sensitive parameters obtained from the identification are searched and used to adapt a damage detection method from the state-of-the-art. In both configurations, it has been possible to detect a stiffness loss of one blade and asses the damaged blade when rotor measurements are used.